BLOOD FLOW MODULATION OF EMBRYONIC CARDIAC REMODELING AND MALFORMATION

By
Madeline Anne Midgett

A DISSERTATION

Presented to the Department of Biomedical Engineering
of the Oregon Health & Science University
School of Medicine
in partial fulfillment of the requirements for the degree of

Doctor of Philosophy
in Biomedical Engineering

October 2016

School of Medicine
Oregon Health & Science University

CERTIFICATE OF APPROVAL

This is to certify that the PhD dissertation of

Madeline A. Midgett

has been approved

Sandra Rugonyi (Mentor/Advisor)

Monica Hinds (Member/Committee Chair)

Kent Thornburg (Member)

Owen McCarty (Member)

Andras Gruber (Member)

I dedicate this dissertation to my family, for all their support along the way.

Table of Contents

Acknowledgements

Firstly, I would like to express my sincere gratitude to my dissertation advisor, Dr. Sandra Rugonyi, for her mentoring during my graduate study. She has been an incredible advisor. Dr. Rugonyi’s knowledge and guidance provided an essential framework to support my development as a researcher. I am very thankful for her openness to engage in frequent discussions about science, projects, and my personal goals, and how she constantly challenged me to grow and do my very best.

I would also like to extend my gratitude to the rest of my dissertation committee members, Dr. Monica Hinds, Dr. Owen McCarty, and Dr. Kent Thornburg for their support and insightful assessment of my research. Dr. Monica Hinds’ encouragement, experimental observations, and technical writing guidance have been instrumental to my research, and I am very thankful for her willingness to serve as chair of my dissertation defense committee. Dr. Owen McCarty has been a valued mentor since my early undergraduate research summer internship in his lab, as well as a constant source of motivation to strive for the most in my career. My understanding of cardiovascular development has been greatly enhanced by Dr. Kent Thornburg, who always encouraged me to see the big picture and has been extremely helpful with countless manuscript revisions. I also want to thank András Gruber for his perceptive questions and participation in my dissertation defense committee. I feel honored to have had the mentorship of such an exceptional group of researchers.

I had the privilege of working with an outstanding network of people at OHSU and beyond. I want to thank Dr. Joe Gray, Dr. Claudia López, Dr. Jonathan Lindner, and Dr. Skip Rochefort for insightful input on my research projects and their critical reviews of manuscripts and grant applications. I am very grateful to Dr. Monique Rennie, Dr. Devon

Scott-Drechsel, Dr. Sevan Goenezen, Dr. Jaime Zelaya, Dr. Keshav Chivukula, Dr. Ly Phan, Stephanie Stovall, Stephan Haller, Katherine Courchaine, and Taylor Lawson for being an incredible group of co-workers and friends. I also want to thank interns who have joined the lab over the years, Curran Gahan, Calder Dorn, Samantha Wallace, Megan Caruso, Brianna Cowin, Madison Hayes-Lattin, Evan Davis, Abigail Griffiths, Sabrina Angel, Mary Root, Batya Beard, Kevin Cho, Molly Carpenter, and Matthew Stephens for their hard work and contributions to my projects. Additionally, I want to acknowledge my previous mentors that helped ignite my passion for learning, including but not limited to Dr. Patrick Rousche, Dr. Philip Harding, Dr. Joe McGuire, Dr. Adam Higgins, Walt Pebley, and Dr. Mike Fitzpatrick.

Finally, I thank my family for their years of support and encouragement, especially in this phase of my career. And lastly, I extend my deepest thanks to my husband, Ryan for his constant motivation, unwavering confidence, and limitless support.

List of Figures

List of Tables

List of Abbreviations

AV: atrioventricular
CFD: computational fluid dynamics
CHD: Congenital heart disease
CON: surgical sham embryo control
D: Dean number
DORV: double outlet right ventricle
EMT: endothelial-mesenchymal transition
Erbb3: Receptor tyrosine-protein kinase erbB-3, also known as HER3 (human epidermal growth factor receptor 3)
FIB-SEM: focused ion beam scanning electron microscopy
KLF2: Krüppel-Like Factor 2
HH: Hamburger and Hamilton development stage
HLHS: hypoplastic left heart syndrome
LAL: left atrial ligation
LHH: left heart hypoplasia
LTR: LysoTracker Red
LV: left ventricle
NL: normal embryo control
OCT: optical coherence tomography
OFT: outflow tract
OTB: outflow tract banding
PAA: pharyngeal arch arteries
PDA: patent ductus arteriosus
PIV: particle image velocimetry
Re: Reynold’s number
SEM: scanning electron microscopy
SV: stroke volume
TEM: transmission electron microscopy
TGFβ: transforming growth factor beta
TMT: tandem mass tagging
TUNEL: terminal deoxynucleotidyl transferase dUTP nick end
W: Womersley number
WSR: wall shear rate
VSD: ventricular septal defect
VEGF: vascular endothelial growth factor
VVL: vitelline vein ligation

Abstract

Blood Flow Modulation of Embryonic Cardiac Remodeling and Malformation

Madeline A. Midgett

Department of Biomedical Engineering
School of Medicine
Oregon Health & Science University

October 2016
Dissertation Advisor: Sandra Rugonyi, PhD

Normal hemodynamic forces associated with blood flow are essential for proper cardiac development, as abnormal blood flow conditions trigger detrimental cardiac growth and remodeling that eventually result in heart defects seen in congenital heart disease. Although it is clear that hemodynamics play an important role in heart morphogenesis, the ways in which perturbed blood flow dynamics in the early embryo lead to later cardiovascular malformation remain unclear. The work presented in this dissertation uses novel combinations of imaging techniques and analysis methods to precisely characterize the effects of abnormal hemodynamics on cardiac development. Specifically, this dissertation uses a chicken embryo model to characterize the dynamic blood flow patterns in the early embryonic heart, define the range of altered hemodynamics induced by surgical interventions, elucidate the effects of abnormal hemodynamics on cellular remodeling of primitive heart tissue, and determine the extent to which the mechanical stimuli produced by altered blood flow in early development predict distinct cardiac defect phenotypes. Overall, this research more definitively than ever before demonstrates that embryonic cardiac malformation is finely regulated by the hemodynamic environment. These findings emphasize the importance of early diagnostic imaging of embryonic circulation to help guide future pregnancy management decisions to possibly revert or prevent cardiac malformation.

CHAPTER 1: Introduction

1.1 Research field summary

Heart formation is a finely orchestrated interplay between genetic and environmental factors. The heart is the first functional organ in the embryo, and starts beating and pumping blood as soon as the primitive tubular heart is formed. The early heart tube is transformed during development through a series of looping and septation processes into the mature complex, four-chambered structure [1]. Blood flow during early embryonic stages plays a critical role in heart morphogenesis, as constant interactions between blood and cardiac tissues generate hemodynamic forces that modulate cardiac growth and remodeling [2-6]. Hemodynamics can become abnormal in human embryos and fetuses by genetic anomalies and environmental exposures that induce structural cardiovascular malformation, contractile deficiencies, and inadequate vascularization of the placental and vitelline beds. Abnormal hemodynamics interfere with regular embryonic tissue remodeling, which can eventually lead to major heart defects [3, 7-14].

Congenital heart disease (CHD) is the most common and lethal structural disease present at birth [15], affecting nearly 1% of newborns in the United States [16, 17]. Additionally, surgical repair of congenital heart defects is associated with a yearly economic burden of approximately $2.2 billion [18]. CHD research has traditionally focused on unraveling the signaling pathways of genetic disorders associated with cardiac defects. However, since genetic anomalies only account for a small portion of CHD cases and known cardiac-defect inducing genetic mutations do not affect individuals equally [19], investigations have recently expanded to include contributions from alternative influences to explain complex cardiac malformations [15, 20]. The

National Birth Defects Prevention Network in collaboration with the Centers for Disease Control and Prevention, compiled data from population-based birth defect surveillance programs conducted in the United States between 1997 and 2011. This data has recently been used to identify factors that increase the risk of CHD affected pregnancies, which include maternal obesity [21], diabetes [22], and smoking [23]. The obesity epidemic in the United States is of particular concern, since the Centers for Disease Control and Prevention estimate that 20% of women are obese (BMI> 30kg/m^2) at the beginning of pregnancy [24] with increased risk of further pregnancy complications like gestational diabetes, hypertension, and preeclampsia [25]. While the harmful developmental processes that underlie the association between these risk factors and CHD are largely unknown, other investigations have shown that these environmental conditions can alter the normal fetal blood flow patterns by inducing placental vascular dysfunction [25-27]. Placental insufficiency creates abnormally high resistance of the placental bed that can lead to a compensatory response of the developing heart in order to maintain cardiac function. This abnormal adjustment is marked by fetal blood flow redistribution and increased loading of the ventricles [28-31]. Numerous studies have shown that mechanical stimuli from surgically altered blood flow alone in animal models results in a spectrum of cardiac defects similar to those seen in CHD [7-10, 32, 33]. Ultimately, flow perturbations may underlie many of the CHD cases that are most often associated with specific genes and teratogens. Despite the undisputable importance of blood flow conditions in cardiac development, the mechanisms by which altered hemodynamic forces lead to congenital heart defects are unknown. Understanding the role of abnormal blood flow in CHD is essential for future prevention, early diagnostics, and treatment in order to build healthier lives, free of cardiovascular disease.

1.2 Dissertation summary

While animal models have been used to show that surgically modified blood flow ultimately leads to cardiac defects [7-10, 32, 33], the spectrum of malformation is very wide and largely undefined. The research in this dissertation combines imaging techniques on several scales to create a unique and valuable view of the developing heart in order to thoroughly characterize the relationship between abnormal blood flow and cardiac malformation. Using chicken embryo models of cardiac development, this work shows that the level of mechanical stimuli produced by precisely controlled blood flow patterns during early cardiac morphogenesis drives the expression of tissue remodeling and cardiac defect phenotypes. These results explicitly demonstrate that cardiac malformations are finely regulated by the specific hemodynamic environment.

This dissertation used chicken embryos as a biological model of human heart development because of ease of accessibility in the egg for surgical manipulation to alter blood flow without maternal interferences, and the substantial conservation of basic cardiovascular development mechanisms between avian and mammalian species [34-36]. Furthermore, the positioning of the heart in the egg permitted the implementation of a variety of *in vivo* imaging techniques (such as optical coherence tomography and high frequency ultrasound) to measure hemodynamic and functional conditions following surgical interventions. Research focused on the development of the outflow tract portion of the embryonic chick heart beginning at Hamburger and Hamilton (HH) stage 18 (~3 days of incubation) [37], which corresponds to approximately 4 weeks of human gestation. The outflow tract is of interest at this stage because it is very sensitive to hemodynamic perturbation and later gives rise to the aorta, pulmonary trunk, interventricular septum, and semilunar valves, which are often involved in congenital heart defects [3, 10, 38].

Chapter 2 provides a background for the studies presented in the following chapters, and discusses biomechanical regulation of heart morphogenesis, animal models of cardiac development, normal heart formation, and surgical interventions in the chick embryo that produce altered hemodynamics, detrimental tissue remodeling, and cardiac defects. Chapter 3 details a study that characterized the normal blood flow changes through the cardiac outflow tract during early looping stages using optical coherence tomography to acquire high-resolution blood velocity and structural information of the developing heart *in vivo*. Similar techniques were used in Chapter 4 to define the hemodynamic conditions induced by a well-established intervention, outflow tract banding, which constricts the diameter of the early embryonic outflow tract of the heart and increases hemodynamic load (pressure and shear stresses) on cardiac tissues. While previous studies have not considered the range of hemodynamic change induced by surgical interventions, this study determined that the amount of hemodynamic change due to outflow tract banding can be controlled by the degree of band tightness.

The remaining chapters use varied band tightness and other surgical interventions to produce a defined range of hemodynamic perturbations that demonstrate how the developing cardiovascular system adjusts and remodels in response to diverse hemodynamics loads. The work presented in Chapter 5 elucidates the effects of altered blood flow on the initial detrimental remodeling of the outflow tract cushions (which serve as primitive valves). Finally, Chapter 6 characterizes the role of specific blood flow patterns induced during early embryogenesis in the formation of cardiac defect phenotypes in late developmental stages when the heart has four chambers and valves.

The results from this work provide clear evidence that mechanical stimuli drive the expression of cardiac phenotypes and valuable insight into the contributing role of hemodynamics in the development of CHD. The studies detailed in this dissertation help define the ways in which hemodynamic patterns underlie cardiac morphogenesis and congenital heart defects.

CHAPTER 2: Background

Congenital heart malformations induced by hemodynamic altering surgical interventions

Madeline Midgett & Sandra Rugonyi

2.1 Abstract

Embryonic heart formation results from a dynamic interplay between genetic and environmental factors. Blood flow during early embryonic stages plays a critical role in heart development, as interactions between flow and cardiac tissues generate biomechanical forces that modulate cardiac growth and remodeling. Normal hemodynamic conditions are essential for proper cardiac development, while altered blood flow induced by surgical manipulations in animal models result in heart defects similar to those seen in humans with congenital heart disease. This review compares the altered hemodynamics, changes in tissue properties, and cardiac defects reported after common surgical interventions that alter hemodynamics in the early chick embryo, and shows that interventions produce a wide spectrum of cardiac defects. Vitelline vein ligation and left atrial ligation decrease blood pressure and flow; and outflow tract banding increases blood pressure and flow velocities. These three surgical interventions result in many of the same cardiac defects, which indicate that the altered hemodynamics interfere with common looping, septation and valve formation processes that occur after intervention and that shape the four-chambered heart. While many similar defects develop after the interventions, the varying degrees of hemodynamic load alteration among the three interventions also result in varying incidence and severity of cardiac defects, indicating that the hemodynamic modulation of cardiac developmental processes is strongly dependent on hemodynamic load.

This review was originally published by *Frontiers in Physiology*. Midgett M & Rugonyi S. Congenital heart malformations induced by hemodynamic altering surgical interventions. *Front Physiol*. 2014; 5:287. Reprinted with permission.

2.2 Introduction

Hemodynamics play an important role in regulating early cardiovascular development [39]. Numerous studies have shown that surgically altered blood flow conditions in embryos result in a spectrum of cardiac defects that resemble those found in human babies with congenital heart disease (CHD) [7, 8, 10-12, 32, 33, 40-47]. During normal development, cardiac performance progressively improves to meet the rising metabolic demands of the growing embryo under increased hemodynamic loading conditions [48]. Hemodynamic loads on cardiac tissues, which are blood pressures and wall shear stresses exerted by blood flow, modulate cardiac development and are required for proper heart formation [3, 8, 13, 49]. When hemodynamic parameters are altered by surgical manipulations, normal cardiac morphogenesis is disrupted and this disruption results in cardiac malformations/defects. Cardiac anomalies observed after surgical manipulations that alter blood flow conditions in embryonic animal models are thought to result from incorrect looping, septation and valve formation, as well as improper growth and remodeling during heart development. Despite the undisputable importance of blood flow conditions on cardiac development, the mechanisms by which hemodynamic forces lead to malformations seen in CHD remain unclear.

2.3 Biomechanical regulation of development

The embryonic cardiovascular system is dramatically affected by changes in hemodynamic load. The embryonic heart, the main driver of hemodynamic loads, acutely adapts passive ventricular properties and contractile function in response to altered loads [50-52], and proceeds to undergo abnormal growth and morphogenesis that later result in cardiac defects [8-12]. Studies have shown that mechanical stresses and strains in the myocardium regulate ventricular growth and remodeling, and trigger endothelial cell organization and signaling [3, 13, 49], as well as changes in geometry and passive properties to offset the effects of altered wall stresses and/or strain [14]. Changes in wall shear stresses, which result from changes in blood flow velocities, have also been shown to alter endocardial cell expression of shear-responsive genes [53], which are important for proper endothelial response and further cardiovascular development. Altered hemodynamic conditions are tightly linked to cardiac defects: cardiac malformations not only occur due to altered blood flow, but also cardiac anomalies unrelated to altered blood flow (e.g. due to genetic mutations, teratogens, etc) affect hemodynamics and are responsible for secondary cardiovascular malformations beyond those of the original cardiac defect.

2.4 Animal models of cardiac development

Several embryonic animal models have been used to study cardiac development and better understand the origins of congenital heart disease. Vertebrate species, in particular, are favorite models since developmental processes are highly conserved among them. Typically studied models include the mouse, the zebra fish, and the chicken (or in general avian) embryos. Due to the availability of knockouts, mouse models are typically used to assess the effects of genes on cardiac development and cardiovascular disease [54, 55]. Further, because mice are mammals, mouse models are also used to assess the effects of mother’s nutrition or cardiovascular conditions, as well as placental development, on embryonic growth and cardiac formation [56-58]. Mouse embryos, however, are not ideal models to study the effects of hemodynamics on cardiac development because they are very difficult to image and manipulate inside their mother’s womb, and cannot develop beyond early stages outside the womb [59]. Zebra fish and avian embryonic models have therefore been more extensively used to monitor hemodynamic conditions during development [1, 3, 60, 61]. Chick embryos, in particular, are often used as a biological model of cardiac development because of ease of accessibility in the egg, including easy access for surgical manipulations to alter blood flow, and developmental similarities with human embryos (including the formation of a four-chamber heart). The availability of advanced *in vivo* imaging techniques (such as optical coherence tomography and high frequency ultrasound) has allowed access to measuring and monitoring embryonic hemodynamic conditions over developmental stages, and to assess acute changes in hemodynamics after interventions that alter blood flow conditions [33, 62-65]. The chicken embryo has therefore been extensively used to study the effects of hemodynamic alterations on cardiac development.

Hemodynamic interventions in the chick embryo are designed to alter preload, afterload, and blood flow volume and velocities. The three main surgical cardiac interventions investigated in the chick embryo are vitelline vein ligation (VVL), left atrial ligation (LAL), and outflow tract banding (OTB), and are summarized in Figure 2-1. After intervention, the induced hemodynamic alterations produce changed heart wall mechanical properties and a spectrum of cardiac defects following the completion of septation and valve formation. The three hemodynamic manipulations result in similar defects, with varying degrees of incidence and severity. VVL redirects the path of blood flow and briefly decreases hemodynamic load on the heart [40, 66-69]. LAL restricts the blood flow entering the primitive ventricle effectively reducing hemodynamic load on the heart. As the heart develops into chambers, decreased load and delayed development on the left side of the heart is compensated by the right side of the heart, leading to left heart hypoplasia, and other associated defects [12, 33, 48, 51, 70]. OTB constricts the diameter of the heart outflow tract, and increases the hemodynamic load on the heart generating high-shear and high-pressure flow conditions [9, 51, 52, 63]. OTB produces some of the largest incidences of defects, as well as the most severe malformations among the surgical procedures including double outlet right ventricle and persistent truncus arteriosus.

This chapter summarizes the normal heart formation process, and clinical significance of congenital heart defects that have been reported after hemodynamic interventions. We will mainly focus on research performed on avian embryos, as they are the favorite model in studying the effects of altered blood flow conditions, and thus extensive studies and available data can be easily compared. We will thus summarize the reported hemodynamic response after surgical interventions, altered cardiac mechanical properties observed, and the final defects of the four-chambered heart after VVL, LAL, and OTB in the chick embryo.

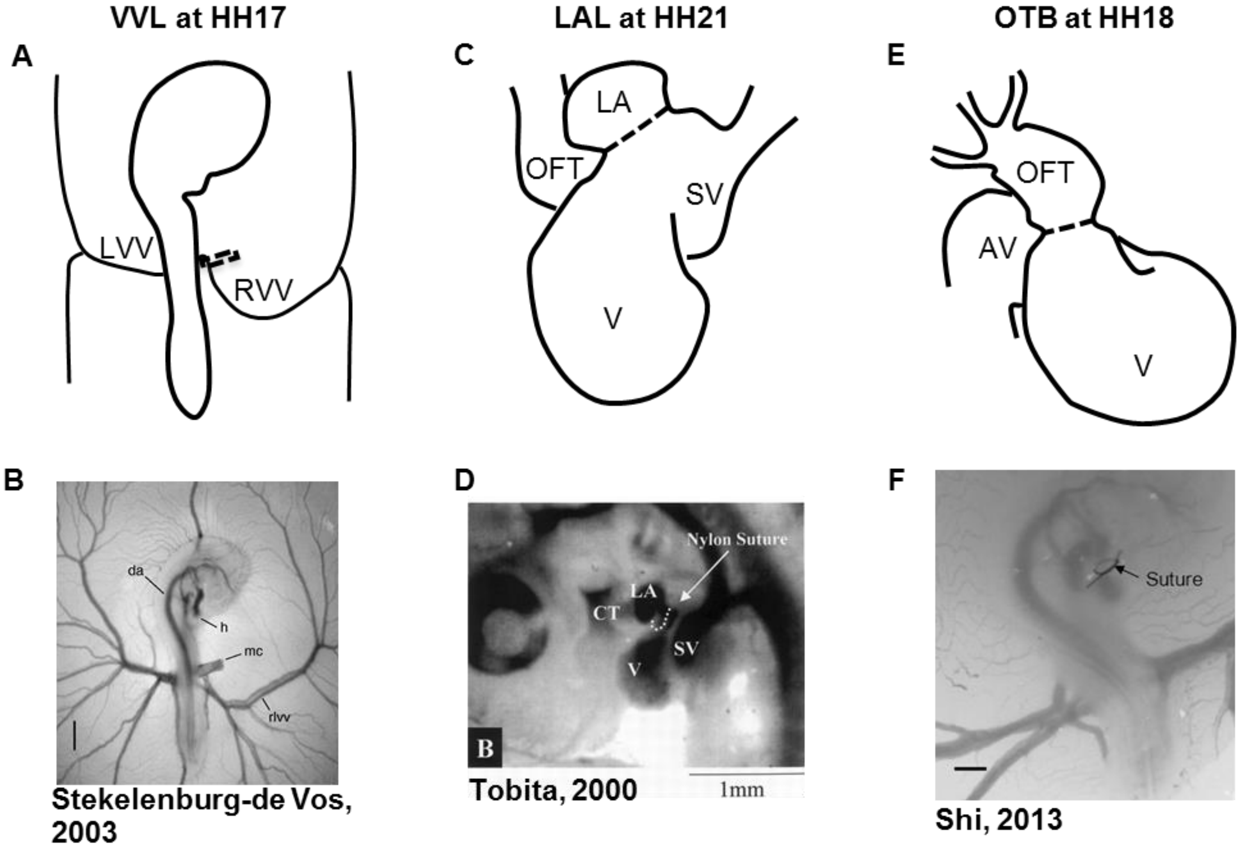

VVL at HH17

LAL at HH21

OTB at HH18

Stekelenburg-de Vos, 2003

Tobita, 2000

Shi, 2013

Figure 2-1. Schematic and experimental photos of the three surgical interventions. (**A&B**) right VVL at HH17. The dotted line represents the point of manipulation where either a clip or suture obstructs the flow of blood back to the heart. (**C&D**) LAL at HH21. The dotted line shows where the suture is tied around the left atrium to reduce its size and restrict flow. (**E&F**) OTB at HH18. The dotted line represents where the suture is tied around the outflow tract to reduce its cross-sectional area. AV, atrioventricular canal; CT, conotruncus , or heart outflow tract; DA, dorsal aorta; H, heart; LA, left atrium; LVV, left vitelline vein; MC, microclip; OFT, outflow tract; RLVV, right lateral vitelline vein or RVV; RVV, right vitelline vein, SV, sinous venosus; V, primitive ventricle. Image reproduced with permission from [12, 52, 66].

2.5 Normal heart formation

The cardiovasculature is one of the earliest systems to form in the embryo, starting with just very thin walls that then grow and remodel over the course of development. Most of the heart morphogenesis processes occur under blood flow conditions, implying an intrinsic interaction between cardiac development and hemodynamics [1, 3, 42, 71, 72]. In this review, we describe the initial heart tube morphogenesis into the four-chambered mature heart focusing on the developmental processes that are influenced by hemodynamics.

2.5.1 Heart tube and looping

Initial heart tube formation starts after fusion of the paired primordia at Hamburger and Hamilton (HH) stage 9 [37], after which the heart tube is formed down the embryonic midline. The primary heart field is the first wave of mesodermal cells that form the initial heart tube. The second heart field additionally contributes to the arterial and venous poles of the heart tube, consisting of progenitor cells that give rise to myocardium, smooth muscle cells, and endothelial cells [73-77]. The early heart tube is composed of three tissue layers: the outer myocardium layer, the inner monolayer of endocardium, and a thick middle layer of largely extracellular matrix, also known as the cardiac jelly. Looping begins at HH9-10, where the initially straight cardiac tube bulges, rotates to the right, and wraps into a loop [42, 71, 78]. After the primitive ventricular region forms a bend in the c-shaped loop at HH11-12, three morphologically distinct cardiac regions emerge: the primitive atrium, the primitive ventricle, and the primitive outflow tract [71]. The heart tube coordinates contractions without the mature pacemaking and conduction system as early as HH10 [1]. The simple c-shaped loop continues to change direction and position until it transforms into an s-shaped loop that is complete by HH24, in which the outflow tract moves over the atrioventricular (AV) canal [1, 71]. Many groups have investigated the mechanisms driving the looping process, and have presented evidence suggesting that looping is mediated by a combination of asymmetric expression of genetic and molecular markers [79, 80], intrinsic forces from differential growth of the heart tube [81, 82], and extrinsic forces of neighboring tissues [83, 84]. Throughout the looping process, the outflow tract and AV canal develop endocardial cushions, which are regional wall thickenings of the cardiac jelly layer, as depicted in Figure 2-2. Cardiac cushions serve as primitive valves that block blood flow upon contraction of the myocardium by closing the lumen. Endocardial cushions play an important role on later valve and septa formation.

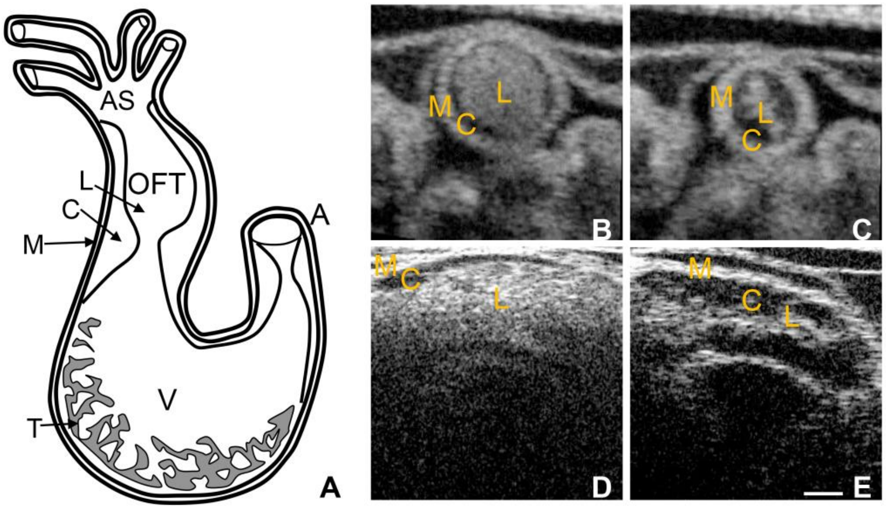

Figure 2-2. Chick heart structure at HH18. (**A**) Heart schematic showing the outflow tract cushions at the inlet of the outflow tract. (**B-E**) Representative optical coherence tomography images of the outflow tract. Cardiac jelly appears darker in between the lighter myocardium and lumen. (**B**) Cross-sectional 2D image at maximal expansion. (**C**) Cross-sectional 2D image at maximal contraction. (**D**) Longitudinal 2D image at maximal expansion. (**E**) Longitudinal 2D image at maximal contraction. A, atrium; AS, aortic sac; C, cardiac jelly; M, myocardium; L, lumen; T, trabeculae; V, ventricle. Scale bar =200 microns.

Trabeculation is initiated in the primitive ventricle during the late stages of looping. Initial trabeculation starts when the cardiac jelly is displaced from the outer curvature of the ventricle and endocardial pouches grow toward the myocardium layer, creating a fine trabecular spongy network with small intertrabecular spaces [82, 85-87], see Figure 2-2. Because trabecular density increases with load, trabeculae have been linked to aiding in cardiac contraction and ventricular output flow direction. Further, because trabeculation increases ventricular luminal surface area, it has been associated to increase in the passive diffusion of oxygen to the myocardial tissue [17, 88, 89]. Trabeculae are important components of early heart development and later chamber formation.

The transitional zones between the primitive regions that emerge during cardiac looping are of interest concerning congenital heart malformations. These areas are brought closer together during the looping process to eventually form portions of the septa, valves, and fibrous heart matrix [38]. Most surgical interventions discussed in this chapter are performed at the later stages of looping (HH17-HH21) and therefore affect subsequent septation and valve formation and the late stages of looping.

2.5.2 Pharyngeal arch artery (PAA) formation

The primitive arterial system develops through vasculogenesis, angiogenesis, and connection with the cardiogenic plates until it eventually transforms into the mature arterial system. Initially, the heart tube connects to the bilateral dorsal aortae through the first pair of PAA. During chick embryo development, a total of six pairs of PAA emerge, remodel, and transform into the mature arteries. Initial formation of the six-paired PAA in the chick embryo is similar to that of human embryos, but the involution pattern is different. In both human and chick embryos, the mature brachiocephalic arteries are derived from the third pair of arches, the aortic arch is derived from the right fourth arch, while the pulmonary arteries and the ductus arteriosus are derived from the sixth arch pair [38, 90]. The fifth arch pair have been have been termed to describe arteries that are only temporarily present in early development of the chick embryo, and are not considered a major PAA [91]. Proper arch formation depends on programmed processes but is also regulated by blood flow conditions [92-94].

2.5.3 Septation and chamber formation

Subsequent to looping, internal septa divisions and valve leaflets develop in the primitive atrial and ventricular chambers, the outflow tract, and the AV canal between stages

HH21-36 [1]. The individual septa join in the center of the heart to complete the transformation into a four-chambered heart. Correct looping is essential for normal cardiac septation. Septation occurs via combinations of merging and fusion of endocardial cushions, compaction of trabeculae, and ballooning of the ventricles [38, 42, 95, 96].

Right and left AV orifices are created once the AV cushions meet and fuse, and eventually transform into the mitral and tricuspid AV valves. The atrial septum starts forming and grows from the atrial roof downward to merge with the AV cushions. Final closure of the atrial septum occurs shortly after birth/hatching [97]. The interventricular septum develops as a common wall between the primitive right and left ventricles by merging and compaction of ventricular outer curvature trabeculae. The aorto-pulmonary septum (mesenchymal tissue) originates between the fourth and sixth PAA, divides the aortic sac, and extends and fuses to the right and left ventricles so that each communicate exclusively with the designated artery. The upstream portion of the outflow tract including the cushions are transformed into the ventricular outflows and the aortic and pulmonary semilunar valves, while the downstream portion of the outflow tract is remodeled to contribute to the proximal portion of the aorta and pulmonary trunks [42, 95, 98].

2.6 Common heart defects following hemodynamic interventions

Nearly 1% babies born have some form of a congenital heart defect [16]. Heart defects found in humans are similar to defects that develop after surgically altering embryonic hemodynamic conditions in animal models. In this section of the review we will summarize the definitions, prevalence, and current treatment options in human patients, of the heart defects that have been observed after hemodynamic manipulations in chicken embryos.

2.6.1 Ventricular septal defects (VSD)

Ventricular septal defect (VSD) is the most common cardiac defect, occurring in 40-50% of all babies with CHD [99, 100]. VSD is a cardiac abnormality in which there is a hole in the ventricular septum that separates the left and right ventricles. VSD is classified by the muscular/fibrous location of the defect within the septum, and its size. Communication between the ventricles caused by VSD forces oxygen-rich blood from the left side of the heart through the defect to mix with the oxygen-poor blood from the right ventricle, with corresponding right ventricle volume overload. The presence of a VSD can result in pulmonary hypertension (from having more blood to be pumped to the pulmonary vessels) and can force the left ventricle to work harder to pump the needed blood to the body. VSD can also cause difficult breathing and heart murmurs [100, 101].

Many factors influence the hemodynamic significance of VSDs, including VSD size, ventricular pressures, and pulmonary resistance. Doppler echocardiography can diagnose VSD early in development, but sometimes VSDs reduce in size or disappear shortly after birth [99, 102]. If the VSD is small enough, it can close on its own without surgery. In addition, small VSDs can be asymptomatic and not be discovered until later in life, without significantly affecting an individual’s health. If the VSD is large, surgical closure is necessary. To close a VSD a patch of fabric or pericardium is sewn over the hole, and eventually the patch gets covered by normal heart tissue. Catheter closure has also emerged as an attractive VSD treatment method [103, 104]. Time of repair depends on the size and location of the VSD.

2.6.2 Pharyngeal arch artery malformation

Many different malformations of the six-paired PAA can occur. Cardiac developmental progression establishes flow patterns through the heart that are directed into the developing PAA. The altered hemodynamics following surgical interventions also disturb aortic blood flow, which affect normal muscularization patterns and morphogenesis of the aorta. Anomalies of the aortic arch are often indicators of other congenital cardiovascular diseases [105, 106].

Common cardiac defects associated with arch malformations include: double aortic arch, interrupted aortic arch, patent ductus arteriosus, and persistent truncus arteriosus. Double aortic arch is rare and occurs when the ascending aorta divides into two arch arteries, which funnel into the descending aorta. Because one of the aortic arches is close to the trachea and/or esophagus, symptoms are associated with trachea/esophagus compression [107]. Surgery is performed in symptomatic patients.

Interrupted aortic arch is also a rare condition that occurs when there is regression of both of the right and left fourth aortic arches, and as a result the ascending and descending aorta are not connected [106]. Because an interrupted aortic arch affects blood flow to the lower body, it must be treated with surgery soon after birth.

Patent ductus arteriosus (PDA) occurs when the ductus arteriosus that typically closes after birth does not close, resulting in abnormal blood flow between the aorta and pulmonary arteries [108]. Incidence rates range from 1 in 500 births [109] to 1 in 2000 births (accounting for about 5-10% of all congenital heart defects) [110], varying as some reports choose to include clinically silent cases that are discovered incidentally. The ductus arteriosus, which connects the aorta with the pulmonary artery, contains cushions made up of elastic fibers and smooth muscle cells that normally close at the junction of the aorta after birth [72, 111]. When it fails to close, the opening permits oxygen-rich blood from the aorta to mix with oxygen-poor blood from the pulmonary artery. This can strain the heart and increase blood pressure in the pulmonary arteries causing pulmonary hypertension. Sometimes the PDA closes on its own, but if it remains open, a transcatheter closing device is used. Surgical ligation and surgical division is performed when all other options have failed [108].

Persistent truncus arteriosus [103] occurs when the truncus arteriosus fails to properly divide into the pulmonary trunk and aorta. Thus instead of having outlets from the right and left ventricles, one great vessel arises above a large VSD connecting the ventricles [112]. PTA is rare but severe, and accounts for approximately 1% of CHD cases [113]. Blood flow in the PTA goes to both the body and the lungs. Similar to VSD defects, extra blood is pumped back to the lungs, causing the left side of the heart to work harder with the risk of pulmonary hypertension. Surgery is required to close the VSD and separate the body and lung blood flow. Pulmonary arteries are removed from the great vessel and then connected to a tube with a valve inserted into the right ventricle. The tube and valve need replacement 2-3 times in childhood and into adulthood as needed.

2.6.3 Atrio-ventricular and semilunar valve malformations

Valve morphology abnormalities can result in valve insufficiency and stenosis [114]. Valve insufficiency occurs when the abnormal shape of the valve leaflets prevents the valve from properly closing and allows blood flow regurgitation back across the valve, causing cardiac overload. Valvular stenosis happens when the valvular tissue thickens and becomes more fibrous and stiffer, which narrows the valve opening and reduces blood flow. The fibrous valve interferes with blood flow and produces an increase in blood pressures throughout the cardiovascular system. Bicuspid aortic valve is a common semilunar valve defect, affecting 1-2% of the population, where there are only two complete commissures [16]. AV valve anomalies are associated with aneurysms of the ascending aorta, VSD, and aortic coarctation [115, 116].

Mitral valve prolapse is a common atrio-ventricular valve defect, where a mitral valve leaflet is displaced into the left atrium during systole [117, 118]. This arises when blood flow interacts with an abnormally thickened leaflet, and has been estimated to affect 2-3% of the population [119]. Mitral valve prolapse is associated with mid-systolic clicks, late systolic murmurs, and other serious complications including severe mitral regurgitation and bacterial endocarditis [120]. Symptoms associated with valve insufficiency and stenosis greatly depend on the degree of flow obstruction. Patients can remain asymptomatic for years, but once they become symptomatic rapid detrimental cardiac progression begins, and surgery is recommended. Surgical interventions include repair and reconstruction or valve replacement.

2.6.4 Double outlet right ventricle (DORV)

Double outlet right ventricle (DORV) accounts for approximately 1.5-2.0% of all congenital heart defects (0.03-0.1/1,000 live births) [121]. DORV encompasses a spectrum of malformations where the pulmonary artery and the aorta both arise from the right ventricle. This anomalous cardiac morphology decreases the amount of oxygenated blood that reaches the body. DORV is also always combined with VSD [122]. A variety of surgical options exist to treat DORV. Surgeons can use a patch to form a tunnel through the VSD that connects the aorta to the right ventricle, or perform an arterial switch by detaching the aorta from the right ventricle and attaching it to the left ventricle [123].

2.6.5 Left heart hypoplasia (LHH)

Left heart hypoplasia (LHH), also known as hypoplastic left heart syndrome (HLHS), is a rare manifestation of CHD (3.8% of cases). However, it causes 25% of all CHD mortalities [124], and is one of the most difficult cardiac anomalies to treat. The LHH left ventricle is underdeveloped and unable to support systemic circulation, and LHH is also often associated with mitral and aortic valve anomalies. Infants with LHH may initially be asymptomatic, but become very ill when the ductus arteriosus closes [125]. Surgery involves bypassing the weak left side of the heart and using the right ventricle for all the pumping by attaching a new aorta to the right ventricle (although oxygen-rich and poor blood still mix in the heart), or creating a bi-directional shunt that allows returning oxygen-poor blood to go directly to the lungs so that the blood does not mix in the heart [126-128].

2.7 Surgical interventions to alter hemodynamic conditions in chick embryos and consequences

In this section we present the most common surgical interventions performed in chick embryos to alter blood flow conditions. Further, we summarize the changes in hemodynamic conditions associated with the different surgical interventions (Table 2-1), changes in cardiovascular tissue properties observed after intervention (Table 2-2), and the cardiac defects induced by the intervention (Table 2-3).

2.7.1 Vitelline vein ligation/clipping

Vitelline vein ligation/clipping is a procedure in which one of the vitelline veins that returns blood to the embryonic heart is ligated or clipped, obstructing blood flow [40, 67-69]. Ligation can be performed using a surgical suture, while clipping uses a surgical clip to obstruct flow. The ligation or clipping can be performed on either the right or left vitelline veins. For this review, we will refer to both vitelline vein ligation and clipping as VVL as they both produce the same hemodynamic alterations. The VVL procedure has been usually performed at HH13-HH18, during the looping cardiac stages and before cardiac septation begins, when heart formation is sensitive to blood flow conditions.

<u>VVL Acute Hemodynamics</u>

VVL causes blood flow to reroute into the opposite lateral vitelline vein, temporarily reducing hemodynamic load on the developing heart. This manipulation alters the left/right balance of venous inflow to the heart, without chronically changing circulating blood volume. The major hemodynamic changes are mainly acute (lasting only hours after manipulation), but have been suggested to start a cascade of altered growth and remodeling events that lead to defects in the fully formed heart.

The altered venous return following VVL has been shown to acutely reduce stroke volume as well as dorsal aortic and outflow tract blood flow velocities [62, 66]. After 5 hours of right VVL performed at HH17, dorsal aortic peak systolic blood flow velocity was significantly 36% below the peak velocity of the control group, while stroke volume decreased 14% in manipulated embryos compared to controls [66]. In addition to decreased flow velocities, VVL has also been shown to alter blood flow patterns through the heart. Right VVL caused a small change of the blood flow pattern in the AV canal where the blood flowed more centrally and with shorter streamlines through the left half of the AV canal (as observed in India ink experiments). Left VVL forced blood from the posterior and left lateral yolk sac regions to detour, causing alterations in both the AV canal flow and the inflow portion of the ventricle. Separate from left and right VVL, ligation of the posterior vitelline vein, caused flow changes within the AV canal and ventricle with more central streamlines running through the AV canal [32] (Figure 2-3). Since endothelial and endocardial cells have responsive elements that are activated by shear stress, cardiac blood flow patterns may be important in regulating normal cardiovascular development [3, 13, 49]. In fact it has been shown that VVL alters gene expression patterns of shear sensitive genes (ET-1, KLF2, eNOS) in the heart endocardium [53].

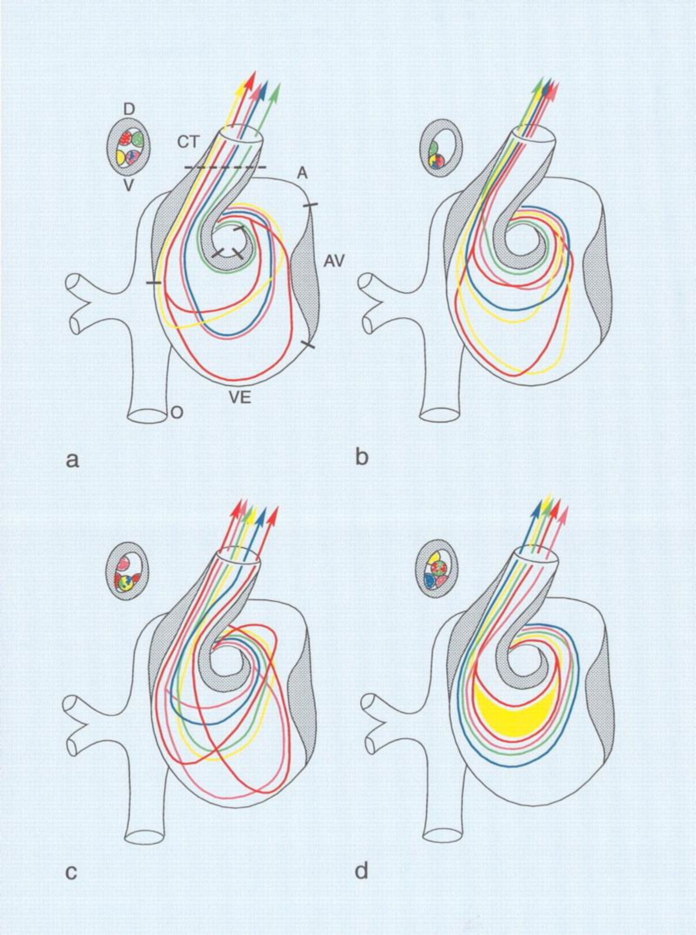

Figure 2-3. Combined schematic representation of intracardiac flow patterns after ligation of the different vitelline veins. Each colored line represents the average flow pattern of one particular yolk sac region. (**a**) Normal flow pattern. (**b**) Flow pattern observed after ligation of the right VVL. There is a reduction of streamlines passing through the left half of the AV canal (red, yellow), and in the outflow tract all streamlines were located along the lateral-most half and also more ventrally. (**c**) Flow pattern observed after ligation of the left VVL. By crossing from the inner curvature to the outer curvature, the pink streamline is added to the left half of the AV canal. Both red streamlines are sharply edged in the left atrium, ventricular inflow and outflow. (**d**) Flow pattern observed after posterior VVL. Most streamlines were running centrally through the AV canal, with hardly any flow along the outer curvature of the ventricle and the inner curvature of the outflow tract. Green=anterior yolk sac region; pink=right lateral yolk sac; blue=left lateral yolk sac; yellow=posterior yolk sac, single streamline; red=posterior yolk sac, double streamline. A, atrium; AV, atrioventricular canal; CT, conotruncus, or heart outflow tract; D, dorsal; V, ventral; VE, ventricle. Image reproduced with permission from [32].

Studies have shown that the acute changes in stroke volume and blood flow velocities subsequently normalize and become comparable to control levels [40, 67-69]. After at least 24 hours of altered flow initiated at HH17, intraventricular end-systolic pressure and end-diastolic pressure are comparable to controls [68], and are increased by HH24 [69]. Pressure-volume loop analysis shows that the increase in pressure at HH24 is accompanied by decreased end-systolic elastance and increased end-diastolic stiffness [69]. The initial increase in pressure after the acute hemodynamic changes followed by a return to normal levels after 24 hours may also impact the final cardiac defects formed.

Little has been reported in the literature about the hemodynamics through the heart following VVL after septation, valve formation and permanent cardiac defects emerge. However, Broekhuizen and colleagues [40] showed that after right VVL at HH17 hemodynamics returned to normal levels by HH24, but then peak systolic blood flow velocity through the dorsal aorta increased by 26% and stroke volume increased by 33% compared to control levels at HH34 [40]. Investigators have proposed that an overcompensating Frank-Starling mechanism develops and leads to a more contractile ventricular myocardium. Nevertheless the observed increase of end-diastolic stiffness at HH24 following VVL manipulation at HH17 [69], suggests there may be additional regulatory mechanisms at play.

Altered tissue properties following VVL

The acute reduced hemodynamic load induced by VVL has been shown to modify the cardiac tissue architecture in terms of endocardial cell arrangement, ventricular compact layer thickness, and ventricular wall stiffness. These anomalies in the heart architecture become evident after acutely altered hemodynamics have returned to normal levels, showing that the effects of VVL continue beyond the initial few hours.

Endocardial cells align in the direction of flow when wall shear stresses reach a critical level and/or when shear stresses are evenly and constantly distributed along the heart walls in the mature and embryonic cardiovascular systems [129-132] . Following the change in hemodynamic forces induced by VVL, endocardial cell arrangement is altered. Normal endocardial cells in the section of the atrial floor that funnels to the AV canal and dorsal wall of the primitive ventricle align with blood flow by HH27 and appear elongated with smooth surfaces and bulging nuclei. Endocardial cells in the dorsal wall of the right atrium, however, remain unaligned by HH27. After left VVL performed at HH13-14, however, endocardial cell orientation emerges in the dorsal wall of the right atrium by HH27: cells appear elongated and in the orientation of the sinus venosus [132]. These results suggest that the altered blood flow patterns after VVL either increase shear stresses on the dorsal wall of the right atrium or create a more constant shear flow than under normal hemodynamic conditions, which align the endocardial cells.

Since cardiac growth is regulated by hemodynamic load [9, 133], the acute reduction of load after VVL is thought to delay the normal ventricular growth progression. Histological sections revealed that the ventricles of VVL embryos were less developed than those of controls: the compact layer of the ventricular myocardium was thinner and ventricular trabeculation was reduced in VVL embryos [134]. Additionally, Steklenburg-de Vos and colleagues found that end-systolic ventricular elastance was significantly lower in VVL embryos (intervention at HH17) with a 52% decrease by HH21 and 61% decrease by HH24 with respect to controls. This change was accompanied by increasingly higher end-diastolic stiffness at HH21 and HH24 [68, 69]. These altered cardiac tissue properties create a less compliant ventricle, which is consistent with normal ventricular tissue at younger developmental stages and suggests that the normal developmental increase in myocardial compliance is also delayed after VVL [68, 135, 136].

VVL Induced Defects

The spectrum of cardiac malformations observed after VVL are hypothesized to stem from impaired heart looping in early developmental stages, and are characterized by increased distance between the inflow and outflow tracts, dextroposed position of the arterial trunk, and disturbed cushion formation [10]. These developmental anomalies cause incomplete fusion of septal components leading to VSD. Most cardiac malformations observed with VVL seem to present a VSD and depend on the location and size of the VSD. Frequently a dextroposed or overriding aorta is found, in which the aorta is positioned directly over a VSD rather than over the left ventricle. Even though the VVL manipulation is fairly reproducible, the magnitude of the flow change could still vary from embryo to embryo, and together with biological variations explain why only varying portions of manipulated embryos develop malformations. See Table 2-3 for cardiac defect incidence in individual studies.

Ventricular septal defect

VSD is a common defect that develops following VVL, with occurrence varying between reported studies. After right VVL at HH17-HH18, 10-72% of VVL embryos developed mild to severe VSDs [10, 32, 40, 41]. Left VVL also showed VSD formation in 18% of the manipulated embryos [32]. VSD is thought to result after VVL from altered hemodynamics and flow patterns that cause the misalignment of septal components [10]. In many cases, VSD accompanies other cardiac malformations including aortic arch defects, valve anomalies, and the double outlet right ventricle defect, all of which are discussed in the following sections. Some reports of VSD in early post-septation stages may provide an over estimation of malformations, since a decrease in VSD malformations was shown between stages HH27-35 and HH36-45, when smaller VSDs spontaneously close on their own during development [32].

Pharyngeal arch artery malformation

PAA malformations consistently developed after right VVL at HH17-18 in about a third of the embryos across reported experiments, and in 9% of the embryos after left VVL [32]. A wide range of anomalies were reported, including arch obliteration, arch interruption, arch persistence, double aortic arch, diameter decrease in the third and sixth arches leading to hypoplastic right brachiocephalic artery, persistent ductus caroticus, and hypoplastic pulmonary artery [10, 32]. Early post-septation stages had more arch malformations combined with VSD, while there were more solitary arch malformations in late post-septation stages [32]. One possible contributor to the spectrum of PAA malformations may be due to the fact that VVL surgical manipulation delays and misdirects the neural crest cell migration from the pharyngeal arch region, evidenced by abnormal condensed positioning of the aorticopulmonary septum mesenchyme [10].

AV valve anomalies

Minor AV valve anomalies have been reported following VVL intervention, always accompanied by VSD [10, 32]. About 8% of manipulated embryos showed AV valve malformations after right VVL, in which some valves had the tricuspid opening dorsal to the aorta instead of to the right and some had developmentally immature AV valves [10].

Semilunar valve anomalies

Semilunar valve anomalies are a common defect that develops following VVL. Approximately a third of manipulated embryos develop a semilunar malformed valve accompanied by VSD [10, 32, 40]. Following right VVL at HH17, anomalies included an additional valve leaflet and fused commissures on both bicuspid aortic valve leaflets and quadricuspid pulmonary valve leaflets [10, 32]. Left VVL specifically affected the pulmonary valve leaflets [32].

Double outlet right ventricle

DORV defects were observed after both right (approximately 1/3 of manipulated embryos) and left VVL [10, 40, 42]. DORV defects were characterized by a dextroposed aorta with a long connection between the base of the aorta and the left ventricle, accompanied by VSD.

2.7.2 Left atrial ligation

In left atrial ligation (LAL), a suture is placed around the left atrium and tied in a knot to constrict the left atrioventricular orifice and decrease the effective volume of the left atrium. LAL has been performed at HH21, during the looping stages and before septation commences [12, 33, 51, 70].

<u>LAL Acute Hemodynamics</u>

LAL causes reduced cardiac preload and blood volume in the ventricle. As a result of LAL there is less blood to flow through the heart outflow tract and the rest of the circulatory system. The partial ligation of the left atrium reduces its size, narrows the inflow area of the left ventricle, and redirects blood flow from the left to the right side of the heart. The redistributed hemodynamic load results in the underdevelopment of the left side of the heart and compensatory overdevelopment of the right side cardiac structures [8, 12].

Preload reduction following LAL has been shown to decrease intraventricular pressure, stroke volume and AV inflow velocities. After LAL at HH21, Tobita and colleagues showed that acute intraventricular peak and end-diastolic pressure decreases in the LAL embryos compared to controls by 11% and 36%, respectively. Pressure remained decreased up to stage HH27, where peak and end-diastolic pressure were each decreased by 18% in manipulated embryos compared to controls [51]. Further, maximum AV inflow velocities immediately decreased after LAL at HH21 by 37% and remained decreased at HH25 by 25% [12]. After LAL at HH21, dorsal aortic stroke volumes also decreased in LAL embryos compared to controls at HH24 [33]. In contrast, Lucitti and colleagues showed that acute end diastolic, systolic, mean, and pulse pressures measured in the dorsal aorta 1 hour after LAL at HH21 were restored and comparable to controls, while stroke volume remained reduced by 55% [70]. By HH24, all dorsal aortic pressure parameters remained similar to controls, while stroke volume was reduced by 33% in LAL embryos compared to controls. Stroke volume in LAL embryos returned to normal levels at HH27 [70]. While it has been shown that arterial pressure increases/decreases with infusion/withdrawal of circulating blood volume [137], the relationship following LAL suggests that arterial pressure maintenance (instead of arterial flow/resistance) may be essential for embryo survival and ensured when balancing circulation deficiencies. This highlights the preservative restoration of the embryonic hemodynamic response, and further suggests that differences in acute wall shear stress may be a major factor leading to cardiac defects after LAL.

Little has been reported in the literature about the hemodynamics of blood flow through the heart following LAL after septation, and after permanent cardiac defects occur. However, Tobita and Keller reported blood flow velocities with right and left ventricular wall deformation patterns after inducing left heart hypoplasia with LAL up until HH31.

Maximum right ventricular inflow velocities were similar to controls, while average inflow velocities were 14% higher after LAL consistent with increased right ventricular filling volumes. Maximum left ventricle inflow velocity was reduced by 19% in LAL embryos, while average left ventricular inflow velocity was comparable to controls. This demonstrates that hemodynamics remained altered after the major malformations developed, which could induce additional secondary malformations and/or detrimental remodeling.

Altered tissue properties following LAL

Chronic reduced preload and ventricular blood volume following LAL have been shown to modify the myocardial architecture prior to the development of cardiac defects. In particular, changes in the myofiber angle distribution, ventricular wall stiffness, compact myocardium thickness, and ventricular dimensions have been documented [33, 43, 44, 51]. These alterations are consistent with delayed developmental growth induced by reduced ventricular hemodynamic load.

Decreased left ventricular dimensions prior to full left heart hypoplasia have been observed as early as 1 hour after LAL [44]. While the immediate (within 1 hour) change in ventricular dimensions is a mechanical consequence of the decreased blood volume filling the heart, ventricular dimensions of LAL embryos remained smaller compared to controls. After LAL at HH21, HH24 ventricular end-systolic volume decreased by 46% and end-diastolic volume decreased by 45% compared to controls [33]. Tobita and colleagues reported that left ventricular major axis lengths were also decreased by 6% compared to controls at HH27, while right ventricular major and minor axis lengths remained similar to controls. These ventricular dimensional changes at HH27 were also associated with a 26% decrease in right ventricular compact myocardium thickness, while left ventricular compact myocardium thickness remained similar to controls. Delayed development in the left side of the heart caused by LAL is further supported by increased myocardial wall stiffness, where left ventricular myocardial stiffness at HH27 was 52% larger in experimental embryos [51].

Myofiber alignment in the embryonic cardiac wall is an important component in the developmental relationship between cardiac architecture and cardiac function. Myofiber alignment has been shown to change in areas of rapid morphogenesis and proliferation [138, 139]. During normal development, the myofiber distribution in the left ventricular compact myocardium changes from a uniform circumferential orientation at HH27 to a longitudinal orientation at HH36. After LAL at HH21, myocardial distribution patterns in the left ventricle remained similar to controls at HH27, but were then developmentally delayed and remained circumferentially oriented at HH31 through HH36 [43] (Figure 2-4). This lack of proper myocardial orientation is associated with altered cardiac function and performance with the underdevelopment of the left side of the heart.

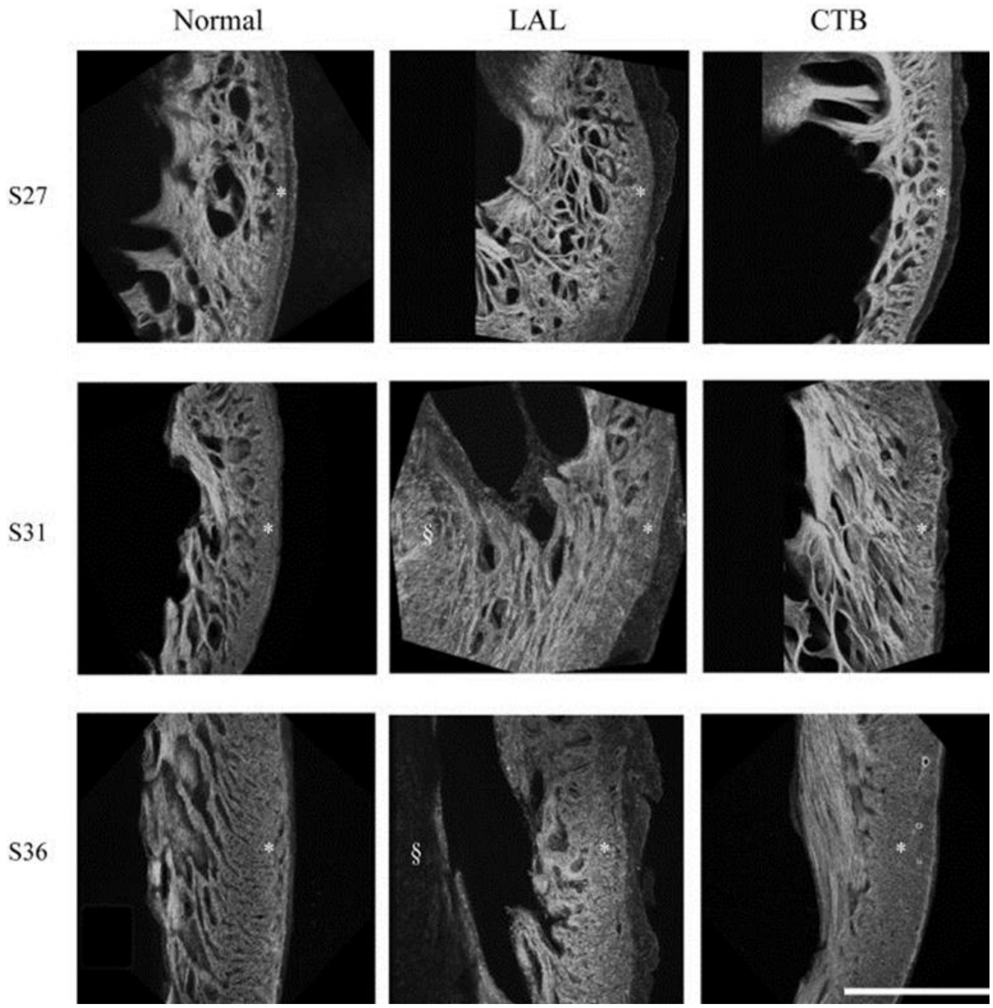

Figure 2-4. Developmental change of the LV myocardium architecture in normal, LAL, and OTB embryos shown by 3D reconstructions of f-actin labeled myocardium. Asterisk, compact myocardium; section symbol, interventricular septum. S27, stage 27 or HH27; S31, stage 31 or HH31; S36, stage 36 or HH36. Scale bar = 500 μm. Image reproduced with permission from [43].

LAL Induced Defects

Reduced ventricular preload and the associated altered flow patterns induced by LAL interfere with normal looping, septation, and valvular formation to produce cardiac malformations. LAL very reproducibly leads to left heart hypoplasia (LHH), which is also associated with varying incidence of VSD, PAA malformation, and abnormal valve morphology. See Table 2-3 for defect incidence in individual studies, and Figure 2-5.

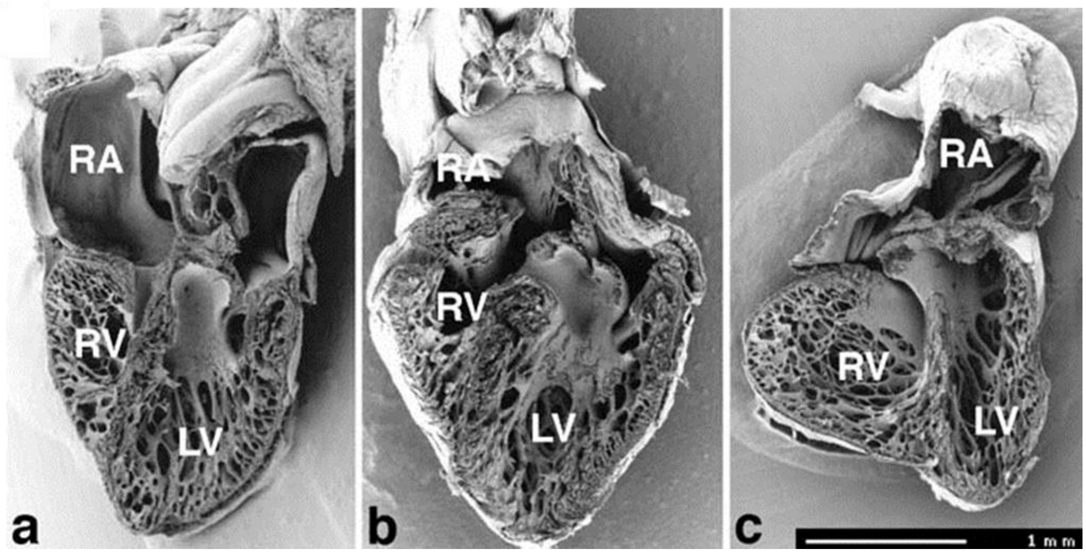

Figure 2-5. Frontal dissection of HH34 sham (**a**), OTB (**b**), and LAL (**c**) hearts. Note distorted atria, changed proportions of the ventricles and defect of interventricular septum in the LAL embryo. The trabeculae in the LV show precocious adherence to the lateral wall and changed orientation with circumferential alignment in the right. The muscular flap-like morphology of the right atrioventricular valve is changed to a bicuspid, mitral-like structure. Ventricular septum defect is seen also in banded heart, where the trabecular compaction is distinctly advanced in both ventricles resulting in thickening of the compact myocardium and interventricular septum and similar modification of right AV valve morphology. Dorsal halves, scale bar = 1 mm. Image reproduced with permission from [8].

Left heart hypoplasia

LHH is the dominant defect produced by LAL, as redistributed blood flow from the left to the right side of the heart leads to underdevelopment of the left cardiac structures. The LAL model is able to induce LHH very reproducibly, with 100% of manipulated embryos that survive to HH34 displaying a form of the defect [33], with the phenotype becoming more pronounced with stage development [8]. After LAL at HH21, the left ventricular area diminished in size by 20% while the right ventricular area enlarged by 40% when compared to controls at HH31 [12]. Right ventricular transverse diameter has been shown to increase as much as 62% [11]. Cardiac shape changes following LAL, which highlight LHH, include a rounded apex of the heart that is mostly fully formed by the right ventricle [11], decreased left ventricular myocardial volume and accelerated trabecular compaction, while the right side compensation has shown chamber dilatation, and thickening of compact myocardium [8].

Further analysis of LHH cases generated by LAL has shown modified functional ventricular composition. Vessels in the hypoplastic left side of the heart are developmentally delayed, without lymphatics in the left ventricle [98]. Cell proliferation also decreased in the hypoplastic left ventricle, while the right ventricular trabeculae showed both advanced proliferation and contractile phenotype differentiation compared to the left ventricle [46].

Ventricular septal defect

VSD was present in about 25% of all LAL hearts [8]. The incidence of VSD following LAL is similar to that of VVL, suggesting that similar hemodynamic factors are at play. Relatively small architectural differences after LAL could be attributed to observed mild VSDs that allow continual intraventricular communication and allow blood to pass to the left ventricle.

Pharyngeal arch artery malformation

About 2/3 of LAL manipulated embryos in reported studies displayed some kind of PAA abnormality. Malformations ranged from abnormal involution patterns, incomplete/interrupted aortic arch formation, asymmetric left side arrangement, smaller left side arterial diameters with twisted appearance, absence of separation between arches (4th and 6th) leading to persistent truncus arteriosus, hypoplastic aortic arch, hypoplastic aortic isthmus, hypoplastic ascending aorta, and patent ductus arteriosus [11, 33]. The most common aortic malformation reported was patent ductus arteriosus [11].

AV valve morphology

Abnormal AV valve morphology commonly accompanied VSD following LAL manipulations. Irregular remodeling of the right atrioventricular valve produced fibrous bicuspid structures resembling a bicuspid valve more than the normal muscular flap-like morphology of the AV valve, the extent of which was related to the degree of left ventricular hypoplasia. Extreme cases also showed dysplastic (thickened) or atretic (completely closed) left atrioventricular valves [8]. Tobita and Keller also noted that after LAL at HH21, the right AV valve appeared larger than the left AV valve at HH31 [12]. These observations indicate that hemodynamic loading is an important determinant in the development of valvular structures.

Semilunar valve morphology

Harh and colleagues reported that stenotic (thickened) aortic valves combined with hypoplastic ascending aorta was evident in 15% of LAL manipulated embryos. Normal valve formation results when endocardial cushion swelling forms a dome-shaped ridge at the primitive site of the valve, which later differentiates into the thin, mature valvular layer. Hypoplastic stenotic aortic valves are thought to result when the early differentiation fails and the valve tissue does not thin [11]. These anomalies and delayed development are attributed to the altered blood flow conditions introduced by LAL.

2.7.3 Outflow tract banding

In outflow tract banding (OTB), a suture is placed around the heart outflow tract and tied to constrict the lumen diameter. OTB has been performed at HH18-HH21, during the looping cardiac stages, by several groups [7-9, 43, 51, 52, 62, 63, 140].

OTB Acute Hemodynamics

OTB constricts/decreases the lumen diameter of the outflow tract so that hemodynamic load is increased in the heart ventricle. Unlike LAL, which decreases cardiac workload on the early embryonic heart, OTB increases cardiac workload on the early heart tube. Banding generates increased blood pressures throughout the embryonic cardiovascular system, and increased blood flow velocity in the region of the band. After OTB, hemodynamics are quickly altered and remain changed throughout development. Peak and end-diastolic intraventricular pressures immediately increase following OTB [51, 52]. After OTB at HH21, peak ventricular pressure increased 36%, and end-diastolic pressure increased 11% compared to controls [51]. Not only does blood pressure increase after banding, but the extent of the increase also depends on band tightness. Shi and colleagues found that both diastolic blood pressure (minimum pressure) and pulse pressure amplitude (and therefore systolic pressure) in the ventricle, aortic sac, and dorsal aorta increased somewhat linearly with band tightness until near 40% band constriction, at which point pressure measures started to increase faster than linearly with band tightness [52]. Differences in hemodynamic response caused by band tightness may be partly responsible for the spectrum of cardiac defects seen after cardiac septation is complete.

Intraventricular pressures remained higher in OTB embryos days after manipulation. After banding at HH21, blood pressure was reported through stage HH27 [9, 51] when peak and end-diastolic intraventricular pressures were 21% and 27% higher than controls, respectively [51]. Increased pressures were accompanied by increased peak blood flow velocities near the band site (and presumably increased wall shear stresses on the lumen walls) [62, 63]. Flow velocities close to the band increased as much as 120% through the outflow tract [63].

Altered tissue properties following OTB

Overload induced by OTB has been shown to modify the myocardial architecture prior to the development of cardiac defects. OTB alters cardiac ventricular dimensions, ventricular compact layer thickness, ventricular mass, ventricular stiffness, and myofiber angle distribution. Ventricle dilation occurs immediately after constricting the outflow tract lumen walls, first as a passive response to increased blood pressure but then through growth and remodeling, as the increased dimensions are sustained until septation [8, 51]. Since banding causes increased resistance to flow at the site where the band is placed, the heart approaches a more 'ideal' spherical shape for efficient pumping with changes in both the right and left ventricles [141]. Tobita et al showed that after OTB at HH21, right ventricle major and minor axis lengths increased by 14% and 17% compared to controls at HH27, respectively, while left ventricle minor axis lengths increased by 10% compared to controls at HH27 and major axis length remained comparable to controls [51]. The increased hemodynamic load imposed on the heart by OTB increased the rate of ventricular growth without changing the overall rate of embryo growth or morphogenesis of the ventricle. Clark et al showed that the increased ventricular mass is due to myocyte hyperplasia (proliferation), since organelle ratios, DNA-to-total protein ratio, and myocyte areas are constant among experimental and control groups [9]. Trabecular compaction in OTB embryos was more advanced than in controls, with increased ventricular compact layer thickness as early as 12 hours after OTB [8], and up to HH27 [51]. Trabeculae also exhibits a spiraled and dense pattern in OTB samples that is not seen in controls, and this spiral pattern is speculated to be part of a mechanism to increase the pumping efficiency of the pressure-overloaded embryonic heart [8].Miller and colleagues reported that passive left ventricular stiffness almost doubled by HH27 after OTB at HH21, with longer exposure to overload resulting in larger stiffness increases. While ventricular compliance normally increases over development, the increased stiffness after OTB may be a result of tissue remodeling to offset increased wall strain induced by OTB [140].

Myofiber alignment is also affected by the banding procedure. OTB produces the opposite myofiber angle distribution response compared to LAL (in which maturation towards normal myocardial distribution patterns is delayed). After OTB at HH21 the myofiber distribution in the compact myocardium remained similar to controls at HH27. Later, myofiber maturation patterns accelerated at stages HH31-36 [43] with myofiber alignment changing rapidly to a longitudinal orientation characteristic of normal HH36 embryos. See Figure 2-4 to compare interventions. These results suggest that myocardial alignment may be regulated by blood pressure: when blood pressure is low (LAL) alignment is delayed; when blood pressure is high (OTB) alignment is accelerated. During normal development, ventricular blood pressure constantly increases, and this increase is perhaps used in the regulation of myofiber alignment.

OTB Induced Defects

Increased ventricular afterload and the associated flow patterns induced by OTB interfere with normal looping, septation, and valvular formation to produce cardiac malformations. OTB produces a wide spectrum of defects with varying incidence depending on the report. These cardiac malformations include VSD, PAA malformation, abnormal valve morphology, and double outlet right ventricle. See Table 2-3 for defect incidence in individual studies, and Figure 2-5.

Ventricular septal defect

VSD is commonly seen after OTB, with incidence ranging from 76-100% in manipulated embryos [7, 8], compared to only ~25% of all LAL hearts developing VSD [8]. Similar to the other surgical interventions, VSD associated with OTB is often combined with other defects including DORV and PAA defects [8, 47]. Total incidence of VSD formation is directly related to duration of outflow tract banding, and increases with longer band placement. Clark and Rosenquist demonstrated that VSD malformation incidence increased with banding duration where after banding for 2 hours, 6 hours, 24 hours, and permanently, incidence was 0%, 44%, 100%, and 76%, respectively (please note, however, that number of embryos in each group varied, in part due to variability in survival rates) [7]. Malformation later in development after only 6 hours of OTB, indicates that hemodynamics play an essential role in regulating growth and morphogenesis and that it is unlikely that cardiac defects result solely from the physical placement of the suture.

Pharyngeal arch artery malformation

A wide spectrum of PAA abnormalities has been observed after OTB. Clark and Rosenquist reported that 56-100% of OTB embryos developed aortic arch malformation depending on the duration of outflow tract constriction. Malformations included complete absence, interruption, and tubular hypoplasia, and were always associated with VSD [7]. Persistent truncus arteriosus, one of the most severe PAA defects, has also been reported following OTB but not in VVL or LAL [8].

AV valve morphology

Abnormal AV valve morphology following OTB shows that loading is an important determinant in valvular development. While incidence was not reported, in some cases, right AV valve morphology changed from normal muscular flap-like to bicuspid valve, and became more similar to the mitral valve [8].

Double outlet right ventricle

DORV was also observed after OTB, although incidence was not reported. Cardiac defects induced by OTB are usually associated with alignment complications of the outflow tract during the looping stages. Looping problems in early development are thought to result in a modified orientation of the aortic and mitral valves, when the separation between the annuli is increased. Severe separation cases can result in DORV, with both great vessels arising from the right ventricle [8, 47].

Table 2-1. Summary of reported hemodynamics after surgical intervention. Interventions were performed between HH17-HH21, and reported hemodynamic conditions were measured between HH21-HH27 (except for noted acute measurements). References correspond to reported change.

Surgical Intervention	DA End-systolic pressure	DA End-diastolic pressure	Ventricular end-systolic pressure	Ventricular end-diastolic pressure	Stroke volume	DA blood velocity	AV canal blood velocity	Outflow tract blood velocity
VVL	**-** Broekhuizen [40]	**-** Broekhuizen [40]	**-** Stekelenburg-De Vos [68] ↑ Stekelenburg-De Vos [69]	**-** Stekelenburg-De Vos [68] ↑ Stekelenburg-De Vos [69]	**↓(acute)** Stekelenburg-De Vos [66] **-** Stekelenburg-De Vos [68], [69] Broekhuizen [40] Ursem [67]	**↓(acute)** Stekelenburg-De Vos [66] **-** Broekhuizen [40]	**-** Ursem [67]	**↓ (acute)** Rugonyi [62]
LAL	**-** Lucitti [70]	**-** Lucitti [70]	↓ Tobita [51]	↓ Tobita [51]	↓ Hu [33] Lucitti [70]		↓ Tobita and Keller [12]	
OTB	↑ Shi [52]	↑ Shi [52]	↑ Clark [51] Tobita [9] Shi [52]	↑ Clark [51] Tobita [9] Shi [52]	**-** McQuinn [63]			↑ McQuinn [63] Rugonyi [62]

↓: decrease in hemodynamic measure in experimental group compared to controls;
-: no significant change in hemodynamic measure in experimental group compared to controls;
↑: increase in hemodynamic measure in experimental group compared to controls

Table 2-2. Summary of reported altered material properties after surgical interventions. Only includes properties that were observed prior to HH36, before the heart has septated chambers and valves. References correspond to reported change.

Surgical Intervention	Increased ventricular dimensions	Decreased ventricular dimensions	Decreased ventricular compact layer thickness	Increased ventricular compact layer thickness	Increased ventricular wall stiffness	Increased ventricular mass	Accelerated myofiber angle distribution	Delayed myofiber angle distribution	Abnormal endocardial cell arrangement
VVL			Hogers [134]		Stekelenburg-de Vos [68], [69]				Icardo [132]
LAL		Tobita [51] Hu [33] deAlmeida [44]	Tobita [51]		Tobita [51]			Tobita [43]	
OTB	Sedmera [8] Tobita [51]			Sedmera [8] Tobita [51]	Miller [140]	Clark [9]	Tobita [43]		

Table 2-3. Summary of reported cardiac defects after surgical intervention. References correspond to reported percentage of embryos with defect.

Surgical Intervention	Ventricular septal defect	Pharyngeal arch artery malformation	Atrioventricular valve malformation	Semilunar valve malformation	Double outlet right ventricle	Left Heart Hypoplasia
VVL	**R:10-72%, L:18%** Hogers [10] *R 57%* Hogers [32] *R10%, L18%* Broekhuizen [40] *R72%* Oscar [41]	**R:~35%, L:9%** Hogers [10] *R35%* Hogers [32] *R32%, L9%* Broekhuizen [40] *R33%*	**R:8%** Hogers [10] *R8%* Hogers[32]	**R:~25%** Hogers [10] *R21%* Hogers [32] *R34%, L36%* Broekhuizen [40] *R39%*	**R:~35%** Hogers [10] *R37%* Broekhuizen [40] *R33%* Icardo [42]	
LAL	**25%** Sedmera [8] 25%	**~66%** Hu [33] 70% Harh [11]* 62%	**X** Tobita and Keller [12] Sedmera [8]	**15%** Harh [11] *15%		**62-100%** Harh [11]*62% Hu [33] *100%* Sedmera [8],[46] Tobita and Keller [12] Tobita [43] deAlmeida [44] Rychter [45]
OTB	**76-100%** Sedmera [8] 100% Clark and Rosenquist [7] *76-100%* Clark [47]	**56-100%** Clark and Rosenquist [7] *56-100%* Sedmera [8]	**X** Sedmera [8]		**X** Clark [47] Sedmera [8]	

*:Obstruction of the left AV canal using suture material- same effect as LAL ; R: right VVL; L: left VVL
X: Incidence was not reported.

2.8 Conclusions and future suggestions

The studies reviewed in this chapter show that surgical interventions that alter hemodynamics in the early chick embryo result in cardiac tissue property changes and produce a wide spectrum of cardiac defects. The main hemodynamic interventions performed in chick embryos are VVL, LAL, and OTB, and they are typically performed during the cardiac looping stages (HH13 to HH21). Further, these interventions are complementary, with VVL and LAL decreasing blood pressure and flow, and OTB increasing blood pressure and flow velocities. Cardiac defect formation is likely very dependent on when the surgical manipulation is performed (stage of development) and what specific developmental processes are interrupted. Tables 2-1, 2-2, and 2-3 summarize outcomes resulting from various embryo manipulations; please refer to the text for specific details. While the stage at which interventions were performed in individual studies varied, the majority of the reviewed manipulations was performed between HH17 and HH21, during the final normal stages of looping and before initial stages of septation and valve formation, and thus results should be comparable. The three surgical interventions discussed result in many of the same cardiac defects, which indicate that the altered hemodynamics interfere with common looping, septation and valve formation processes that occur after intervention and that shape the four-chambered heart. While many similar defects develop after the interventions, the varying degrees of hemodynamic load alteration among the three interventions also result in varying incidence and severity of cardiac defects. Investigations of the effects VVL, LAL, and OTB have all reported VSD, PAA malformations, and valve anomalies. LHH was only reported in LAL, and DORV was only reported in VVL and OTB (see Table 2-3). These results seem to indicate that the hemodynamic modulation of cardiac developmental processes is strongly dependent on hemodynamic load.

Very little has been reported about the hemodynamic conditions of fully developed hearts. Since hemodynamics has been proven fundamental in early development, future investigations should also focus on the effect of sustained hemodynamic alterations in the heart to fully characterize the malformed cardiac deficiencies. In this context, it should also be recognized that even cases in which cardiac malformations originate from disparate factors (e.g. genetic anomalies, teratogen exposure, etc), the altered blood flow patterns that emerge will concomitantly affect cardiac growth, remodeling and morphogenesis. With the same logic, factors that affect blood flow (e.g. by modifying normal cardiac contractility during development) might result in cardiac malformations that are due to flow conditions. Altered flow, in addition, will lead to secondary malformations in the vasculature and changes in tissue properties throughout the cardiovascular system. It is therefore difficult to separate the effect of hemodynamics from the effects of other factors. All aspects (hemodynamics, genetics, exposure) should be considered when evaluating the causes of congenital heart malformations, and when devising treatment options for infants with congenital heart disease.

Little is known about non-genetic mechanisms of cardiac malformation, and in particular the mechanisms by which blood flow modulates cardiac development. Early stages of cardiac malformation and the consequences of altering blood flow need to be more thoroughly investigated. To this end, research that integrates hemodynamic data with biological change in response to hemodynamics, and the mechanisms behind this response, are essential. Several studies to determine hemodynamics in the developing embryonic heart are have been recently published [52, 63, 64, 69, 94], as well as studies to look at remodeling and changes in tissue properties shortly after interventions and flow exposure [53, 142-145]. As these two aspects of cardiac development are put together, a more complete picture of heart formation is emerging where developmental programming plays a substantial role, which needs to be better characterized and studied. Understanding how hemodynamics determines cardiac fate early on will certainly provide clues to design better treatment options and strategies for babies with cardiac malformations.

2.9 Acknowledgements

The authors would like to acknowledge the following funding from the US National Institutes of Health, NIH R01HL094570.

CHAPTER 3: Blood Flow through the Embryonic Heart Outflow Tract during Cardiac Looping Stages

Madeline Midgett, Venkat Keshav Chivukula, Calder Dorn, Samantha Wallace, Sandra Rugonyi

3.1 Abstract

Blood flow is inherently linked to embryonic cardiac development, as hemodynamic forces exerted by flow stimulate mechanotransduction mechanisms that modulate cardiac growth and remodeling. This study evaluated blood flow in the embryonic heart outflow tract during normal development at each stage between HH13-HH18 in chicken embryos, in order to characterize changes in hemodynamic conditions during critical cardiac looping transformations. 2D optical coherence tomography was used to simultaneously acquire both structural and Doppler flow images, in order to extract blood flow velocity and structural information and estimate hemodynamic measures. From HH13 to HH18, peak blood flow rate increased by 2.4-fold and stroke volume increased by 2.1-fold. Wall shear rate and lumen diameter data suggest that changes in blood flow during HH13-HH18 may induce a shear-mediated vasodilation response in the outflow tract. Embryo-specific 4D CFD modeling at HH13 and HH18 complemented experimental observations and indicated heterogeneous wall shear rate distributions over the outflow tract. Characterizing changes in hemodynamics during cardiac looping will help us better understand the way normal blood flow impacts proper cardiac development.

This review was originally published by the *Journal of the Royal Society, Interface*. Midgett M, Chivukula VK, Dorn C, Wallace S, Rugonyi S. Blood Flow through the Embryonic Heart Outflow Tract during Cardiac Looping Stages. *J R Soc Interface*. 2015; 12:111. Reprinted with permission.

3.2 Introduction

Embryonic cardiac formation is a finely orchestrated interplay between genetic and environmental factors. Blood flow plays a critical role in embryonic heart development, as constant interactions between flow and cardiac tissues generate hemodynamic forces that modulate cardiac growth and remodeling [3, 8, 13, 49, 146]**.** Blood flow exerts pressure and shear stresses on heart walls triggering mechanotransduction mechanisms that lead to physical, chemical, and gene regulatory responses in cardiac tissue [147]. Key cardiac morphogenetic events coincide with periods of major hemodynamic change, as the dynamic blood flow environment adjusts to meet the demands of the growing embryo. Normal hemodynamic conditions are essential for proper cardiac development, as several studies have shown that altered blood flow in animal models eventually lead to cardiac defects and malformations [3, 7, 8, 10, 38, 51, 148]**.** Although it is clear that biomechanical forces are fundamental components of heart morphogenesis, the processes that relate blood flow to cardiac development remain unknown.

This study focuses on characterizing normal changes in blood flow through the outflow tract portion of the early embryonic heart. We employed 2D Doppler optical coherence tomography (OCT) to quantify the blood flow environment at each stage during a critical period of cardiac formation from Hamburger and Hamilton (HH) 13 to HH18 in chicken embryos [37]. This developmental period, during which the heart is tubular, includes cardiac looping and the beginning stages of chamber differentiation. The outflow tract connects the primitive ventricle to the arterial vessel system, is very sensitive to hemodynamic perturbation, and later gives rise to the aorta and pulmonary trunks, a portion of the interventricular septum, and the semilunar valves, which are often involved in congenital heart defects [3, 10, 38]. Characterizing the changes in hemodynamics during this period of heart formation will help us better understand the way normal blood flow impacts proper cardiac development, and provide a foundation for future studies that investigate how altered hemodynamics lead to cardiac defects.

Blood starts pumping through the embryonic heart at HH10, long before cardiac morphogenesis is complete [2]. Blood pressure is exerted normal to the wall and results from interactions between the wall and blood flow. During myocardial compression, cardiac walls induce an increase in blood pressure. During myocardial relaxation, however, blood pressure generates a tension stress in the heart tissue. Meanwhile, the frictional force of blood flow creates a wall shear stress that acts tangentially to the endocardium [147]. By HH18, endocardial cushions (regional wall thickenings) at the inflow of the outflow tract function as primitive valves that prevent backflow into the ventricle during diastolic filling [82].

Cardiac looping is an important component of heart morphogenesis. The linear heart tube bends and twists to bring various heart segments into their relative positions to then develop into the four-chambered heart. This process begins soon after beating is initiated and continues through HH16 [82]. Looping is partly mediated by asymmetric gene and molecular expression [79, 80], but animal models have also shown that mechanical forces play a major role in the looping process. Various hypotheses of mechanical looping mechanisms have been proposed, where experiments show that several redundant mechanisms are likely involved [2]. These include compressive axial forces as the heart tube lengthens [149], differential growth on either side of the tube [150], active cell shape change [82], cytoskeletal contractions [151], and extrinsic forces from neighboring tissues [152]. Forces exerted by increasing hemodynamic load during the looping period are likely involved in the structural formation. Abnormal looping can lead to serious structural defects similar to those seen in congenital heart disease (CHD). For example, a transient reduction in hemodynamic load after venous obstruction leads to impaired looping [3, 40] and subsequent ventricular septal and valve defects [3, 10, 32, 67]. Understanding the dynamic blood flow environments during cardiac looping is essential for defining this important developmental event.

Previous work characterizing cardiac development between HH13-HH18 has focused on structural changes over the cardiac cycle and stages. External and internal morphological characteristics have been evaluated using cinephotography and videography images to trace embryonic ventricular borders and calculate cardiac volumes [153, 154]. Others have defined the diastolic filling characteristics of the embryonic heart, including ventricular pressure, dorsal aortic velocity, and atrioventricular blood velocity [48, 155, 156]. More recently, 4D optical coherence tomography has been used in conjunction with computational modeling to analyze the biomechanics through the outflow tract at HH18 [64, 157]. This study focused on hemodynamics in the outflow tract. We measured outflow tract blood flow velocity and lumen diameter from Doppler OCT images and calculated peak velocity (*peak V*), peak flow rate (*peak Q*), stroke volume (*SV*), wall shear rate (*WSR*), cardiac cycle length, and time of flow. Embryo-specific computational fluid dynamics (CFD) simulations were used to complement these measurements and provide additional insights into hemodynamics during the looping stages. This work is the first to report changes in blood flow and *WSR* through the outflow tract during cardiac looping from HH13 to HH18.

3.3 Methods

3.3.1 Chick embryo preparation

Fertilized Brown Leghorn chicken eggs were incubated blunt end up at 37.5 °C and 80% humidity until they reached the desired stage. Embryos at stages HH13 (48-52 hours of incubation), HH14 (50-53 hours), HH15 (50-55 hours), HH16 (51-56 hours), HH17 (52-64 hours), and HH18 (65-69 hours) according to the defined Hamburger and Hamilton structural morphology [37] were used in this study (n=10 at each stage). A small section of the blunt-end shell and the inner shell membrane were removed from above the embryo heart. Any embryos that bled upon membrane removal or had obvious structural defects were discarded. Optical microscopy images were then acquired to record developmental stage, using a Leica M165 C Stereomicroscope light microsocpe with PCO-TECH Inc. sCMOS pco.edge 5.5 rolling shutter camera.

3.3.2 OCT image acquisition

Our custom-made OCT system has been previously detailed and used to image embryonic chicken heart motion and blood flow dynamics [52, 158]. Briefly, the system has a spectral domain configuration consisting of a superluminescent diode centered at 1325 nm from Thorlabs Inc (Newton, NJ) and a 1024 pixel, 92 kHz maximal line-scan rate infrared InGaAs line-scan camera from Goodrich Inc (Charlotte, NC). This system allowed acquisition of 512 x 512 pixel (512 A-scans) 2D images at approximately 140 frames per second with <10µm resolution. Doppler flow phase images were generated together with simultaneous structural images in post-processing by calculating the phase differences between two adjacent A-scans in a B-scan. Doppler velocities (vertical velocities, V_Z) were then computed from phase data, and accuracy of these velocities was recently confirmed with a syringe pump [158]. A thermocouple-controlled heating pad surrounding a ceramic cup filled with water was used to maintain temperature in a plastic box during acquisition. This apparatus kept the embryo near 37.5 °C in order to maintain the normal physiological heart rate.

For 2D analyses, 200 sequential B-scan frames from a longitudinal plane down the center of the outflow tract were acquired for each embryo (~3-4 cardiac cycles; n=10). The embryo was positioned so that the lumen completely filled the outflow tract at maximum expansion and made a slit-like shape in the center of the outflow tract at maximum contraction [64, 159]. A glass capillary tube standard was imaged to calculate a pixel to length conversion factor that was used in all structural analyses. For 4D (3D over time) analyses, cross-sectional B-scan frames were acquired along the outflow tract in a representative embryo at HH13 and at HH18. Separation between adjacent cross-sectional planes was 7.5 µm. Following our previously described procedures, these B-scan frame images were synchronized and reconstructed to generate 4D images [160], and the lumen segmented for computational analysis [161].

3.3.3 2D structural and Doppler OCT image analyses

Custom Matlab code (The MathWorks, Inc. Natick, MA) was used to extract simultaneous structural and Doppler velocity image data sets from the acquired OCT raw data. A summary of optical, structural OCT, and Doppler OCT images acquired at each stage is shown in Figure 3-1. The overall analysis procedure is very similar to the process we reported for blood flow at HH18 in surgically manipulated and control embryos [158]. This process uses structural data to convert vertical velocity from the Doppler phase data to absolute blood flow velocity magnitude, and then employs Poisseuille’s Equation to estimate *peak Q*, *SV*, and *WSR*. Doppler flow combined with structural images show a parabolic-like profile of blood flow through the outflow tract between HH13-HH18, which make these approximations valid (see Figure 3-2). The parabolic profile with low Reynolds (Re <4) and Womersley (W < 0.6) numbers, imply that viscous forces dominate blood flow in the outflow tract. A small Dean number (De<3) implies minor curvature effects in the outflow tract that cause the blood flow profile to slightly skew toward the inner curvature, especially close to the inlet [162].

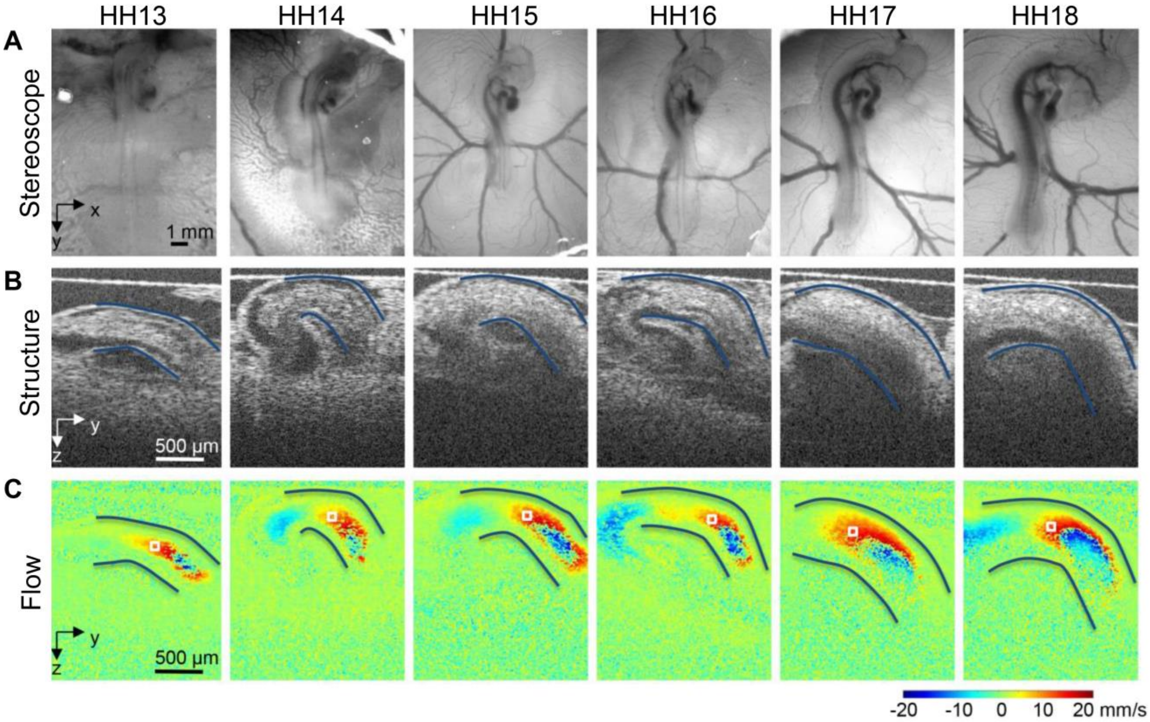

Figure 3-1: Summary of images acquired from the heart of HH13-HH18 chicken embryos. Example (**A**) optical images of the embryo *in ovo* on the top of the egg surface, (**B**) OCT structural 2D longitudinal images of the outflow tract and neighboring structures, and (**C**) corresponding Doppler OCT images. The outflow tract myocardial walls are outlined in A&B, and the velocity measurement location is marked by a box in (**C**).

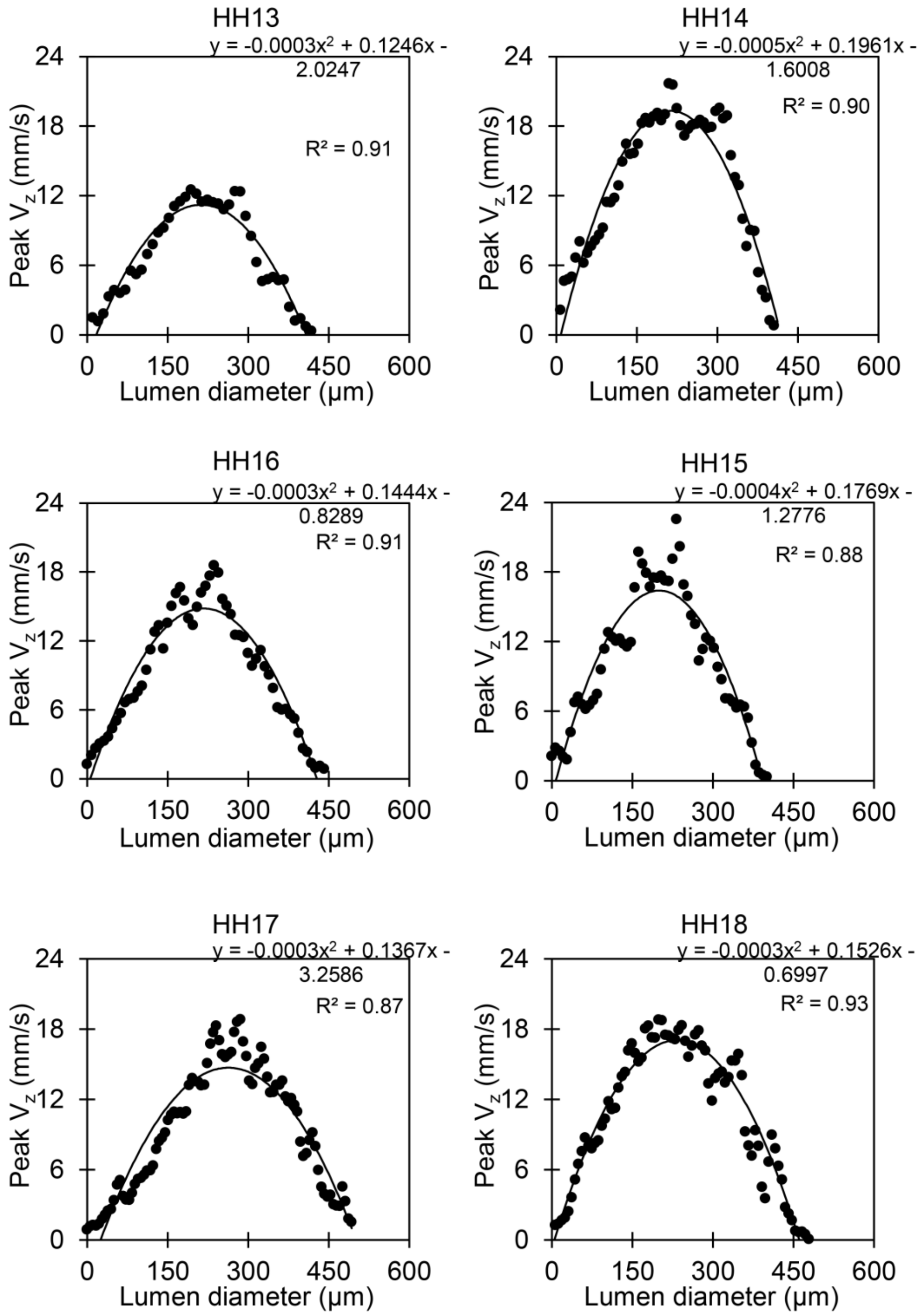

Figure 3-2: Velocity profiles across the diameter of the outflow tract during maximum flow for each stage imaged (HH13 to HH18). Vertical velocity (V_Z), depicted for representative embryos at each stage along a line that passes through the sampling point, shows a parabolic-like profile; a second order polynomial fit and R^2 value are also provided.

Phase wrapping was evident in Doppler images of longitudinal B-scans (Figure 3-1). Wrapping occurs when the phase exceeds ±π, which corresponded to vertical velocities higher than ±23.4 mm/s in our system. Conforming with parabolic-like velocity flow profiles in the outflow tract from HH13-HH18 (Figure 3-2) [62, 157], the fastest flow often wraps in the center of the outflow tract (negative phase enclosed by positive phase), while the slowest/non-wrapped flow develops near the walls. Regions of wrapped and horizontal flow ($V_Z = 0$) in the outflow tract shifted from HH13 to HH18, as the heart tube underwent looping. Consistent non-wrapped, non-horizontal flow regions along the outflow tract centerline were identified at each stage and used for the analysis. Regions directly adjacent or within wrapped flow were not chosen for the measurement location to avoid OCT signal deterioration as well as pixel-averaging errors associated with phase wrapping and corresponding unwrapping algorithms. While there were some differences in specific measurement locations across the stages, all velocity sampling areas were selected near the middle region of the outflow tract. The sampling area used at each stage is shown in Figure 3-1.

Phase shift OCT data within the sampling area were converted to vertical velocity (V_Z) values that were averaged and filtered as previously described [158]. We then calculated the magnitude of the blood flow velocity (*V*) using:

$$V = \frac{V_z}{\cos\theta} \tag{3.1}$$

where θ is the angle between the outflow tract centerline tangent and the vertical direction. Doppler flow and structural images show that blood flow follows the contour of the outflow tract between HH13-HH18, so that θ is a good approximation for the angle between V_Z and the flow direction. For each sampling location θ was measured with a custom Matlab program that calculated the centerline of the outflow tract during maximum flow by finding the midpoint between outlined upper and lower myocardium walls from longitudinal structural images at each position along the tube. The sampling location was chosen along the outflow tract centerline, where maximum velocities occurred, and the average *peak V* was calculated as the maximum absolute velocity at the sampling location over the cardiac cycle. This velocity was compared across all stages.

Outflow tract lumen diameters were measured from M-mode image analysis. M-mode images were generated from a line perpendicular to the outflow tract centerline at the velocity measurement location, and used to display gray scale structure from the chosen line over time (Figure 3-3). The upper and lower lumen interfaces in each M-mode were traced to calculate the lumen diameter (*D*) over the entire cardiac cycle.

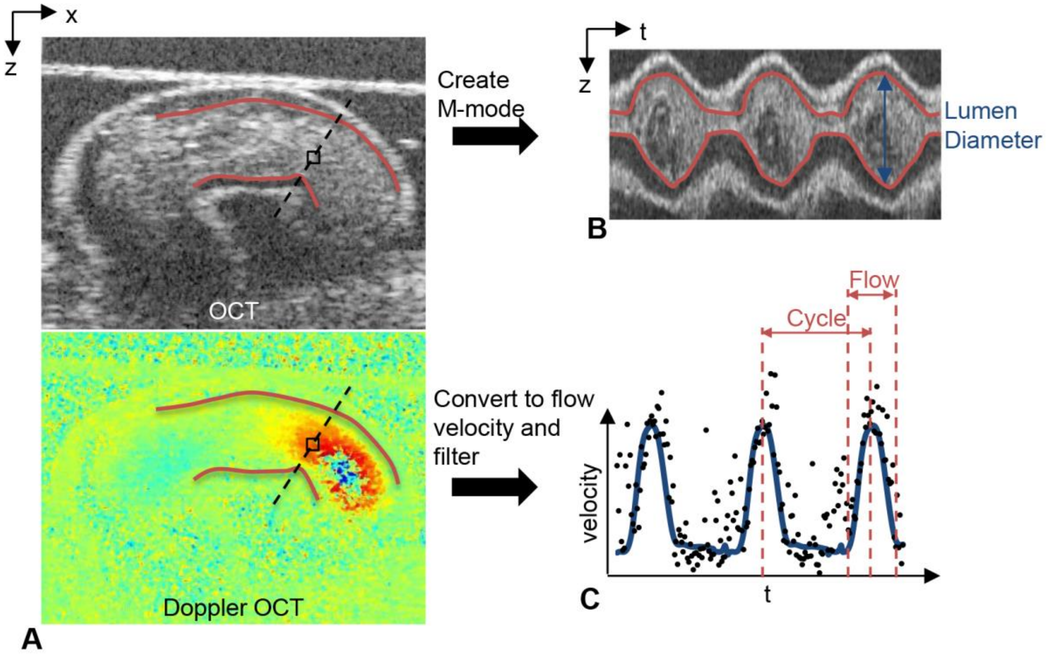

Figure 3-3: Example HH13 images to summarize image analysis procedure. (**A**) Longitudinal planes through the outflow tract were imaged with OCT to acquire simultaneous OCT structural and Doppler OCT images. (**B**) M-mode images were created along the dashed line in the OCT structural image in (**A**) over time, from which we calculated lumen diameter (lumen borders are outlined in red). (**C**) Doppler velocity collected from the box in the Doppler OCT image in (**A**) over time, to display velocity over each cardiac cycle (filtered data shown by blue line), and calculate time of flow.

The length of the cardiac cycle and time of flow were also measured to further characterize the relationship between blood flow and outflow tract wall dynamics at each stage. The length of the cardiac cycle was measured as the time between blood flow velocity peaks, and time of flow was defined as the average percentage of time in the cardiac cycle when the main surge of blood was flowing through the measurement location. The presence of flow was determined from the blood flow velocity versus time trace as clear peaks above the background noise level (Figure 3-3).

Volumetric flow rate over time was calculated using a form of the Poiseuille equation [163, 164]:

$$Q = \frac{\pi D^2 v_c}{8} \tag{3.2}$$

where Q is the blood flow rate through the outflow tract, v_c is the measured outflow tract centerline velocity (absolute value), and D is the outflow tract lumen diameter from each frame. Equation 3.2 assumes that blood is homogeneous, with parabolic, fully developed, and laminar flow, and zero velocity at the outflow tract lumen wall. *SV* was then estimated by summing the forward flowing volume of blood calculated from each frame during flow in a full cardiac cycle:

$$SV = \sum_{i=1}^{N} Q_i \, \Delta t \tag{3.3}$$

where Δt = 1/frame rate (140 fps for our system) and N is the number of frames in one cardiac cycle with forward flowing blood (25-45 frames, depending on the cardiac cycle period and time of flow at each stage).

WSR was calculated using another derivation of the Poisseuille equation [165, 166]:

$$WSR = \frac{4\, v_c}{D} \tag{3.4}$$

Embryonic chick blood has a fairly constant viscosity in the physiological shear rate range [167], so that *WSR* should be proportional to wall shear stress. Al-Roubaie et al reported small changes in viscosity during later development over large periods of developmental time (4 days) [47], indicating that the changes in viscosity between HH13-HH18 (20 hours) are likely minimal, and can be assumed constant. The *WSR* at the time of *peak V* in the cardiac cycle was compared across all developmental stages.

3.3.4 Embryo-specific 4D CFD modeling of hemodynamics in the outflow tract

To complement experimental measurements and determine 3D distributions of flow and *WSR* over time, CFD models of the beating heart outflow tract at HH13 and HH18 were generated. We used 4D embryo-specific geometries of the outflow tract lumen (segmented from OCT images), which consisted of a sequence of meshes that depicted the dynamic motion of the outflow tract walls over the cardiac cycle. Blood was modeled as a Newtonian fluid having density $\rho = 1060\ kg/m^3$ [167] and viscosity $\mu = 0.003$ Pa-s. Embryo-specific blood flow through the outflow tract was modeled using a recently developed inverse method based optimization procedure [168]. Briefly, normal tractions (pressures) at the outflow tract lumen inlet and outlet surfaces (or more practically their difference) were iteratively imposed, until computed and measured Doppler velocities at an optimization point in the interior of the lumen differed by less than 1%. One representative embryo each at HH13 and HH18 were modeled. CFD simulations were performed using the software ADINA (Watertown, MA). *WSR* over the outflow tract lumen surface were obtained and compared to experimentally derived *WSR*, as described earlier.

3.4 Results

Blood flow through the outflow tract was detected in optical and OCT images from HH13-HH18 (Figure 3-1). Optical images show that embryo body size, body curvature, and the surrounding vitelline vessel network make pronounced changes during this development period. OCT structural and Doppler images focus on the outflow tract and show the progression of the cardiac looping process. The HH13 outflow tract is a mostly straight tube near the edge of the embryo body. Consequently, blood flow through the outflow tract at HH13 was mostly horizontal until it reached the downstream half of the tube. As the development stages advance, the outflow tract becomes more curved with larger areas of vertical velocities, the interface between the outflow tract and ventricle becomes more distinct, and the outflow tract endocardial cushions become more visible. Cardiac looping and continued development and growth of the embryo and heart affected blood flow dynamics. Vertical velocity profiles, measured from a line perpendicular to the direction of flow extending from the velocity measurement location, revealed a parabolic-like profile at each stage (Figure 3-2), validating the use of the Poisseuille calculations to estimate Q, SV, and WSR.

3.4.1 Blood flow (peak V, peak Q, and SV)

Peak V, peak Q, *SV*, and *WSR* were measured at each stage between HH13-HH18 and compared across all stages (n=10 for each stage; Figure 3-4). We report embryo group data as the mean ± standard deviation. *Peak V* increased between HH13-HH18 by 1.3-fold from 29.7 ± 2.2 mm/s to 39.3 ±4.4 mm/s, respectively. The largest increase was between HH14-HH16, and was followed by a plateau region between HH16-HH18 (Table 3-1 and Figure 3-4,A). These values correspond to previously published data at various locations in the outflow tract measured through a combination of scanning microscopic particle image velocimetry (PIV), ultrasound, and OCT at HH15 [169], HH17 [170, 171] and HH18 [64, 157, 162, 172]. Since the θ estimation in this study was based on the outline of the myocardium walls from OCT structural images (instead of standard ultrasound angle measuring procedures where θ is manually set by the operator), angle estimations were likely very consistent.

Table 3-1. Summary of average outflow tract flow parameters for each developmental stage (n=10). Data presented as means ± standard deviation. Statistical significance (* denotes p-value<0.05) was determined with a two-sample Student's t-test, reporting two-tail p-values, for HH15 and HH18 values compared to HH13 values.

	HH13	HH14	HH15	HH16	HH17	HH18
Peak V (mm/s)	29.7 ± 2.2	27.8 ± 5.2	36.4 ± 5.5*	39.7 ± 3.9	39.5 ± 4.7	39.3 ±4.4*
Max Diameter(μm)	397 ± 27	399 ± 21	375 ± 24	434 ± 41.9	499 ± 32	533 ± 55*
Peak Q (mm^3/s)	1.8 ± 0.3	1.7 ± 0.3	2.0 ±0.4	3.0 ± 0.6	3.9 ± 0.5	4.4 ± 0.9*
WSR (s^{-1})	301 ± 36	280 ± 57	390 ± 68*	369 ± 52	319 ± 49	299 ± 51
Cardiac Cycle (ms)	599 ± 59	554 ± 58	531 ± 39*	462 ± 66	425 ± 33	419 ±23*
SV (mm^3/beat)	0.22 ± 0.05	0.22 ± 0.04	0.25 ± 0.08	0.31 ± 0.07	0.38 ± 0.07	0.47 ± 0.11*
Time of Flow (%)	41.9 ± 4.3	43.0 ± 6.9	41.4 ± 4.7	44.8 ± 6.1	47.0 ± 6.8	53.3 ± 8.4*

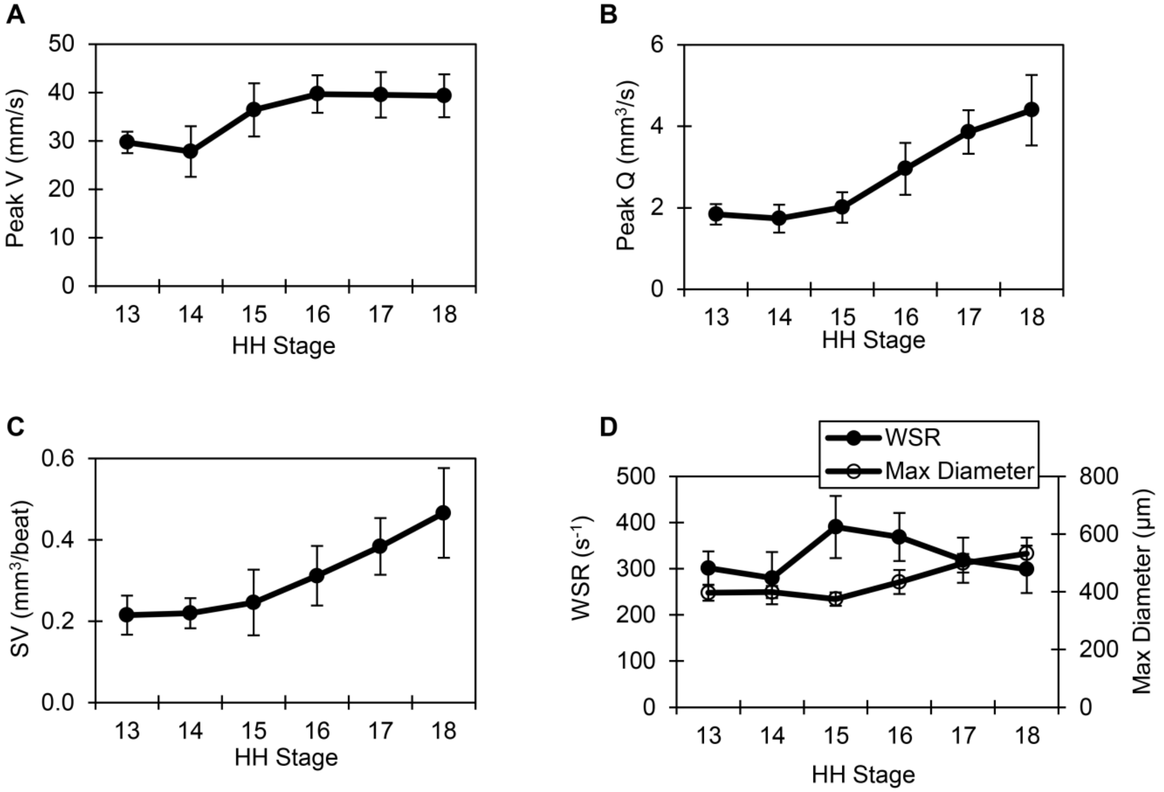

Figure 3-4: Summary of hemodynamic results over advanced developmental stages from HH13-HH18 (n=10 at each stage). (**A**) *Peak V* (mm/s), (**B**) *Peak Q* (mm^3/s), (**C**) *SV* (mm^3/beat), and (**D**) *WSR* (s^{-1}) with maximum diameter (μm) displayed on the secondary y-axis. Average measures are shown at each stage with standard deviation shown as error bars.

Similar to the changes in *peak V* with increased developmental stage, average *peak Q* increased between HH13-HH18 by 2.4-fold from 1.8 ± 0.3 mm^3/s to 4.4 ± 0.9 mm^3/s, respectively, with the largest increase between HH15-HH18 (n=10). These values correspond to previously published data at HH18 [64, 157, 162, 172]. Results are summarized in Table 3-1 and Figure 3-4,B.

Backflow was detected in the downstream portion of the outflow tract in Doppler OCT images in at least a portion of embryos at stages HH13-HH17. All HH14 embryos (n=10) exhibited backflow, while no embryos at HH18 displayed backflow. Backflow was present immediately prior to the systolic ejection phase. The volume of the backflow in each cardiac cycle was very small compared to the forward flow stroke volume (less than 6%) at each stage. Additionally, an initial forward flow surge was detected prior to the main ventricle ejection in 50% of HH17 embryos and 100% of HH18 embryos (Table 3-2 and Figure 3-5).

Table 3-2. Summary of backflow and forward surge flow presence in embryos at each stage (n=10).

Stage	Embryos with Backflow (%)	Embryos with Forward Surge (%)
HH13	60	0
HH14	100	0
HH15	90	0
HH16	50	0
HH17	40	50
HH18	0	100

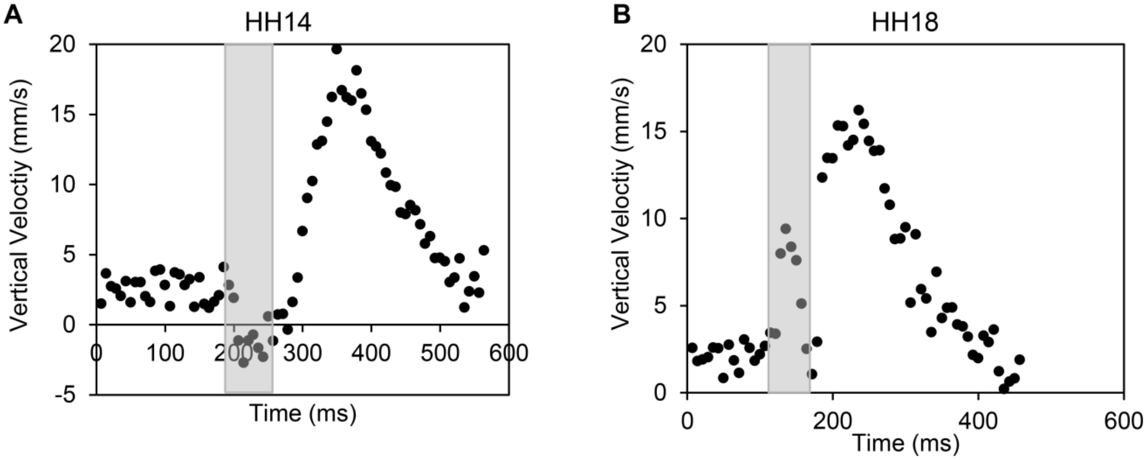

Figure 3-5: Velocity versus time traces of example embryos. (**A**) Vertical flow velocity at HH14 showing backflow (negative velocity, shaded) immediately prior to the systolic phase. (**B**) Velocity at HH18 showing a forward flow surge (shaded) immediately prior to the main flow during the systolic phase.

Average *SV* increased between HH13-HH18 by 2.1-fold from 0.22 ± 0.05 mm^3/beat to 0.47 ± 0.11 mm^3/beat. These values are comparable to previously published data that was estimated with prolate spheroid ventricular volumes [153]. Results are summarized in Table 3-1 and Figure 3-4,C.

WSR at peak blood flow velocity at the sampling location in the outflow tract was calculated at each developmental stage HH13-HH18 (n=10). Average maximum *WSR* across HH13-HH18 embryos was 301 ± 36 s^{-1} and 299 ± 51 s^{-1}, respectively, which is within previously published experimental and computational fluid dynamics model estimates in the chick embryo outflow tract at HH17 [170] and HH18 [64]. While there is no net change in *WSR* from HH13-HH18, *WSR* increased between these stages to return to HH13 levels by HH18. *WSR* peaked at HH15 at 390 ± 68 s^{-1}, which was associated with an increase in *peak V.* Outflow tract lumen diameter remained relatively constant between HH13-HH15, but then also increased between HH15-HH18. Results are summarized in Table 3-1 and Figure 3-4,D.

3.4.2 Cardiac cycle (cardiac cycle length and time of flow)

Cardiac cycle length and time of flow were measured at each stage (HH13-HH18) to compare cycle timing (n=10) (Figure 3-6). The cardiac cycle decreased in length with advanced developmental stage between HH13-HH18 from 599 ± 59 ms to 419 ± 23 ms, respectively. The results are summarized in Table 3-1 and Figure 3-6,A. Cardiac cycle measured in this study corresponds with previously reported values measured from the dorsal aorta, with increased heart rate with advancing developmental stage [48, 155, 156].

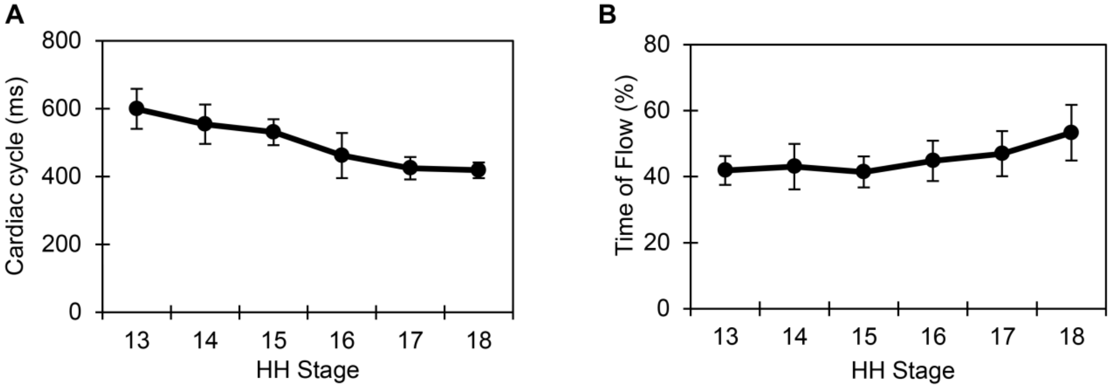

Figure 3-6: Summary of cardiac cycle results over advanced developmental stages from HH13-HH18 (n=10 at each stage). (**A**) Cardiac cycle (ms), and (**B**) Time of flow (%). Average measures are shown at each stage with standard deviation shown as error bars.

The time of flow was measured for all embryos from clearly distinguishable periods of blood flow in the velocity versus time trace from each developmental stage between HH13-HH18 (n=10). Time of flow, the percentage of time in the cardiac cycle when blood was flowing (main surge), was approximately half of the cardiac cycle for all embryos, consistent with our previous observations at HH18 [64]. Time of flow stayed near constant over the analyzed developmental stages and increased slightly between HH13-HH18 from 41.9 ± 4.3% to 53.3 ± 8.4%, respectively. The results are summarized in Table 3-1 and Figure 3-6,B.

3.4.3 CFD modeling of blood flow in the outflow tract

4D embryo-specific CFD modeling of blood flow in the outflow tract revealed the changes in 3D flow profiles between HH13 and HH18 (Figure 3-7, A-B, top rows). Velocity profiles were skewed towards regions of inner curvatures and outflow tract cushions, especially in the HH18 outflow tract. This profile shape was expected due to centrifugal forces created by the curved geometry of the outflow tract. Flow velocities increased as the blood flow approached the outlet of the outflow tract at both HH13 and HH18 due to tapering, although centerline velocities remained higher along the whole length of the outflow tract at HH18. Peak *WSR* was attained at maximal flow conditions with the *WSR* being heterogeneously distributed over the outflow tract wall surface (Figure 3-7,A-B, bottom rows). The overall *WSR* remained similar (~ 330 s^{-1}) for both HH13 and HH18 embryos; however regions of elevated *WSR* (> 900 s^{-1}) were found particularly near the outflow tract cushions closer to the inner curvature at both stages. Velocities and *WSR* results obtained from CFD modeling were consistent with experimentally obtained parameters as described above.

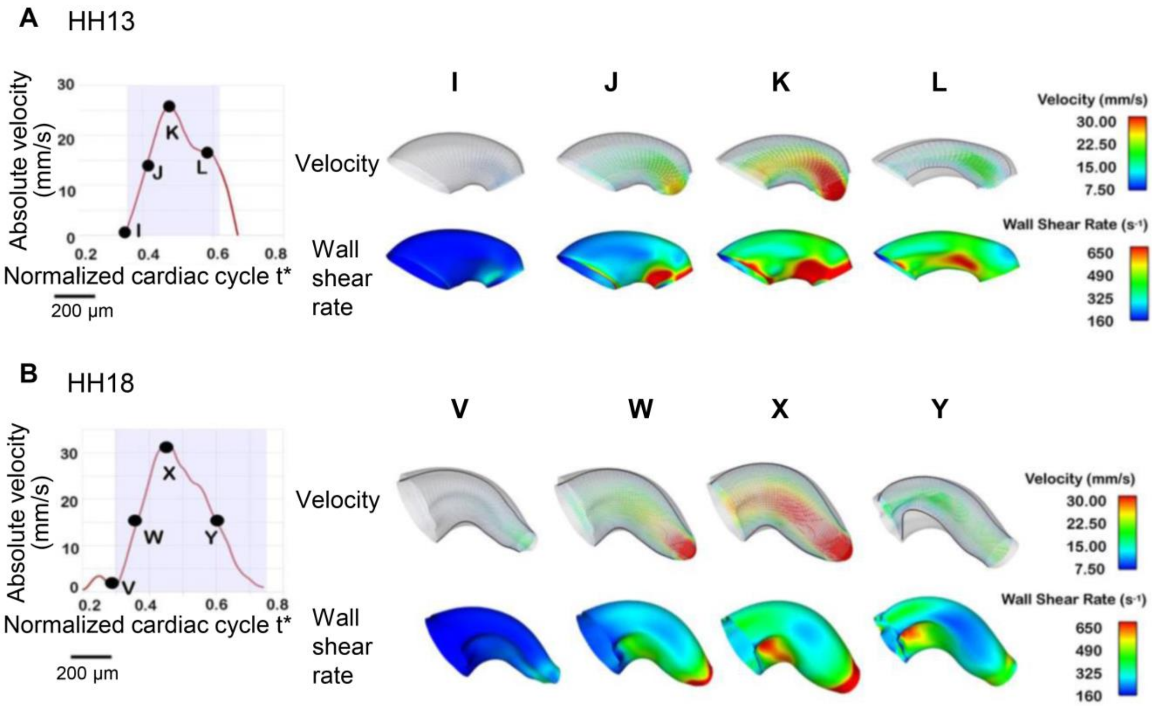

Figure 3-7: Embryo-specific velocity vectors and wall shear rate (WSR) distributions within the outflow tract from CFD models. (**A**) Outflow tract at HH13. (**B**) Outflow tract at HH18. For each case, a normalized cardiac cycle with representative times marked is shown. Velocity magnitudes and WSR are color-coded at the designated time points in the cardiac cycle.

3.5 Discussion

This study characterizes the blood flow forces through the embryonic outflow tract during a critical developmental period, which have been shown to stimulate tissue remodeling that leads to cardiac defects [7-10, 51]. Normal hemodynamic assessment is the first step in elucidating the mechanisms that cause altered blood flow to induce cardiac malformations. The intrinsic relationship between substantial changes in blood flow conditions and structural morphogenesis during cardiac looping highlights the importance of understanding the role of hemodynamics in heart formation.

The 2D OCT longitudinal images acquired in this study allow for an integrated view of blood flow and outflow tract wall movement across a large group of embryos. 4D OCT analyses have been recently used to accurately track the dynamics of myocardial wall motion and blood flow over time [64, 157, 173]. While we also show 4D embryo-specific CFD model examples based on 4D OCT images here, 4D OCT acquisition and image processing is significantly slower and more complex than 2D OCT procedures and does not easily allow for routine embryo scans with large sample sizes. Instead, the variables estimated from 2D longitudinal images in this study compare values at one outflow tract position for *peak V* and *peak Q*, and additionally for only one time point in the cardiac cycle for *WSR*. While simplified, the high reproducibility between samples in the same developmental stage shows our 2D OCT procedure was sufficiently accurate to detect subtle changes in blood flow and structure during looping cardiac development.

Sampling location varied slightly in each stage to allow for accurate Doppler velocity measurement. Our Doppler OCT analysis requires areas of flow that are non-wrapped and non-horizontal. As the looping of the outflow tract and the growth of the cushions change the geometry of the lumen from HH13-HH18, areas of measureable blood flow change position in each developmental stage. Computational models have shown that hemodynamics vary along the length of the outflow tract, so that location will influence outflow tract diameter, blood flow velocity, and wall shear stress. This study compares *WSR* and *D* at the time of *peak V* (and subsequent calculated measures) at each stage, since all sampling locations remained within the middle of the outflow tract and the small changes in positions likely have minor effects. Moreover, *SV* and *peak Q* should be independent of the position chosen for analysis.

3.5.1 Blood flow (peak V, peak Q, SV and WSR)

Looping and cushion generation both contribute to the geometry changes of the outflow tract during the HH13-HH18 development period. This cardiogenesis in turn influences the flow of blood and the resultant hemodynamic environment over the course of development. Since blood flow is expected to increase to meet the demands of the growing embryo, it is not surprising that *peak V* and *peak Q* increased from HH13-HH18. This increase was also captured in CFD embryo-specific models of the outflow tract. In addition, changes in the outflow tract geometry influenced blood flow profiles, which were three-dimensional and skewed towards the inner curvature. The increase in blood flow velocities and flow rates in conjunction with changing curvatures of the developing outflow tract influenced *WSR* distributions obtained from the CFD models.

Overall *WSR* remained relatively constant from HH13-HH14, substantially increased from HH14 to HH15, and then steadily decreased with advanced stage reaching initial HH13 levels by HH18 (Figure 3-4,D). *WSR* was computed at the time of *peak V*, assuming a circular lumen with Equation 3.4, which is a good approximation when the outflow tract walls are fully expanded [64, 159]. The fluctuation in *WSR* from HH13 to HH18 was accompanied by a large increase in lumen maximum diameter between HH15 and HH18, where the initial increase in *WSR* preceded the increase in lumen diameter. One explanation for this response is shear-mediated vasodilation. Vasodilation is a mechanism used in other biological states, including vessel blockage, to expand the lumen and restore shear stress to normal levels [174, 175]. Studies in the chick embryo have shown that the zinc finger transcription factor Krüppel-Like Factor 2 (KLF2) (induced by high shear-stress and an activator of shear-mediated vasodilation [176]) is expressed in early embryonic endocardial cells of the outflow tract [177]. In their study, Groenendijk et al concluded that the spatial expression of KLF2 in relatively narrow portions of the embryonic heart was due to high shear stress flow [177]. The results of our study imply that shear-induced vasodilation may play a role in normal cardiovascular development.

WSR obtained from CFD simulations depicted heterogeneous *WSR* distributions over the outflow tract lumen wall, with regions of higher *WSR* at outflow tract endocardial cushions and inner curvatures. This indicates non-uniform stimuli on the endocardial cells. Proper spatially and temporally varying *WSR* may be important for the normal development of outflow tract endocardial cushions, which are key cardiac structures since they act as primitive valves during looping stages and later give rise to semilunar valves and a portion of the interventricular septum.

Doppler OCT analysis revealed a small volume of backflow in the outflow tract that decreased with advanced developmental stage. Table 3-2 shows that there is a transition in development where all HH14 embryos displayed backflow, while the percentage of embryos with backflow decreased as development approached HH18, at which point no embryos exhibited backflow. Additionally, an initial surge of blood flow through the outflow tract prior to the main flow of the cardiac cycle was evident in HH17 and HH18 embryos. This flow is in the same direction as the major flow but separated from the main surge (Figure 3-5). At the earlier stages, as the ventricle fills with blood during the diastolic phase, it expands possibly exerting a suction pressure on blood flow in the outflow tract [178]. Endocardial cushions help to ensure unidirectional flow in the outflow tract by blocking the flow of blood during diastole. Backflow seen in early stages of development between HH13-HH17 may be caused by incomplete closure of the primitive cushions before they are fully formed. Chamber formation beginning in stages HH17-HH18 may also contribute to more efficient pumping. Additionally, backflow may decrease with advanced developmental stage because of differences in myocardial contractility between HH13 and HH18 (Figure 3-8). While it is critical for adult heart valves to prevent intracardiac retrograde blood flow, studies in the embryonic zebrafish heart suggest that shear stimulus produced by backflow in the developing heart is required for normal valvulogenesis [179]. Our results may therefore reflect a transition in cardiac pumping that is likely essential for proper heart development.

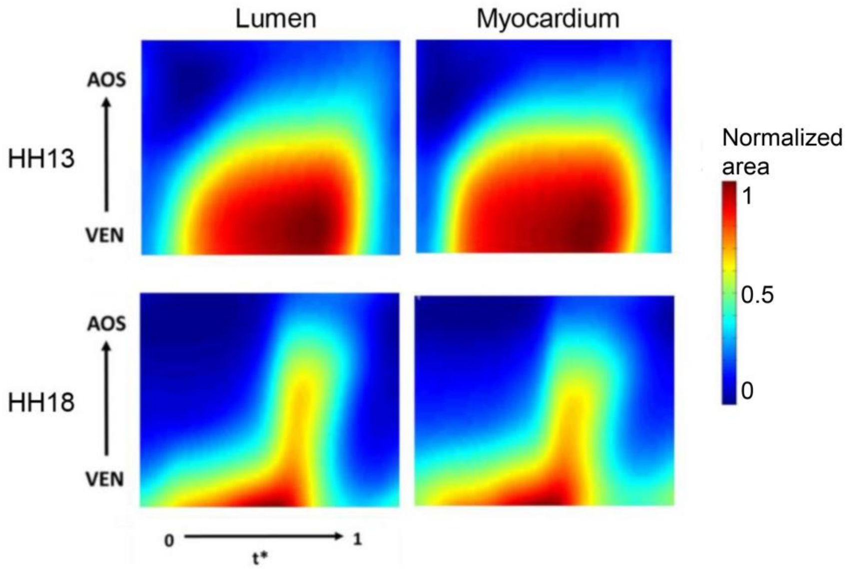

Figure 3-8: Changes in normalized outflow tract lumen and myocardium cross-sectional area. Changes shown over the cardiac cycle (normalized time t*) and outflow tract length (normalized from ventricle, VEN, to the aortic sac, AOS).

This study thoroughly defines the relationship between *SV* and advanced developmental stage during looping by characterizing embryos at each stage between HH13-HH18. This time period only spans 20 hours in chick development, with short time durations between each analysis stage [37]. Increased *SV* throughout the progression of cardiac development reflects an increase in ventricular performance, as the heart adapts to an increased hemodynamic load. According to the Starling law, the heart can generate more force as the contractile muscle fibers stretch toward the optimal sarcomere length [180, 181]. In addition, the ventricle is also developing and growing while increasing its performance. *SV* calculations likely overestimate actual values, since the estimation assumes the outflow tract is a circular cylinder over the entire cardiac cycle. OCT images from a cross-sectional plane of the outflow tract show that while the myocardium concentrically contracts and expands over the cardiac cycle, the lumen is shaped like an ellipse (although almost circular) at maximum expansion and a slit at maximum contraction [64, 159]. Even though this method simplifies the dynamic and complex geometry of the outflow tract, it does account for the changes in lumen diameter and velocity over the cardiac cycle to serve as a comparison of *SV* across developmental stages.

3.5.2 Cardiac cycle (cardiac cycle length and time of flow)

This study also analyzed the timing of the cardiac cycle between HH13-HH18 by measuring the length of the cardiac cycle and the percentage of time in the cardiac cycle with blood flow through the outflow tract. The cardiac cycle decreased by 1.4-fold and the time of flow remained relatively constant from HH13-HH18. These results suggest that the interaction between cardiac cycle length, time of flow, and *SV* are all tightly regulated in normal embryonic cardiovascular development. Using *SV* and cardiac cycle length to calculate cardiac output, our data show that cardiac output increases by 3.1-fold from HH13-HH18. Despite the substantial changes in cardiac cycle and flow, the percentage of time in the cardiac cycle during which there is blood flow stays near 50% over all stages analyzed.

3.6 Conclusions

Chicken embryos provide a valuable biological model of cardiovascular development. This is because of the developmental similarities with humans and the positioning of the embryo in the egg, which permits the implementation of a variety of *in vivo* imaging techniques (such as optical coherence tomography) to measure hemodynamic conditions. The major limitation with the chicken embryo model is the lack of genetic alteration methods available to investigate the signaling mechanisms driving heart development. This study provides an important characterization of blood flow in early development that can be combined with genetic manipulation studies of cardiac formation in other animal models. Previous studies have reported comparable hemodynamic parameters and intrinsic relationships between blood flow and cardiac development in avian, zebrafish, and mammalian embryos [2, 182]. For example, chick embryos and zebrafish exhibit similar ventricular growth patterns and altered blood flow in both organisms lead to impaired cardiac development. Mechanotransduction regulation of cardiac formation is only partially understood. Future work is needed in the cardiovascular development field to link changing blood flow and hemodynamics to mechanotransduction-mediated tissue remodeling. In this regard, the chicken embryo model is ideal for such studies as hemodynamic manipulations in the chick are relatively easy, while the heart is readily accessible for imaging.

Cardiac structure and ventricular performance together generate the hemodynamic environment in the embryonic outflow tract and play a critical role in cardiac formation. The heart undergoes significant structural changes during HH13-HH18 as the heart tube loops and forms a primitive ventricle. For reference, wet embryo weight increases by 3.8-fold between HH14-HH18 [48]. Despite the lack of valves or autonomic innervation in early cardiac development, cardiac function including ventricular blood pressure, stroke volume, and heart rate are tightly regulated [183], as cardiac output increases proportionally to embryo weight [48]. This study used an integrative imaging and modeling approach to characterize the relationship between form and function of the developing heart in order to improve understanding of the processes involved in the development of the cardiovascular system. This new knowledge quantifies normal patterns of hemodynamic change in the early cardiac looping stages, which will be fundamental to future investigations of altered biomechanical environments that lead to cardiac defects.

3.7 Acknowledgements

This work has been supported by grant NIH R01 HL094570 to SR; by a Charles Patrick Memorial scholarship to MM, and Pete and Rosalie Johnson Scholarships to CD and SW. The content is solely the responsibility of the authors and does not necessarily represent the official views of grant giving bodies.

CHAPTER 4: Blood Flow Dynamics Reflect Degree of Outflow Tract Banding in HH18 Chicken Embryos

Madeline Midgett, Sevan Goenezen, Sandra Rugonyi

4.1 Abstract

Altered blood flow during embryonic development has been shown to cause cardiac defects, however the mechanisms by which the resulting hemodynamic forces trigger heart malformation are unclear. This study used heart outflow tract banding to alter normal hemodynamics in a chick embryo model at HH18, and characterized the immediate blood flow response versus the degree of band tightness. Optical coherence tomography was used to acquire 2D longitudinal structure and Doppler velocity images from control (n=16) and banded (n=25, 6-64% measured band tightness) embryos, from which structural and velocity data was extracted to estimate hemodynamic measures. Peak blood flow velocity and wall shear rate initially increased linearly with band tightness ($p<0.01$), but then velocity plateaued between 40-50% band tightness and started to decrease with constriction >50%, whereas wall shear rate continued to increase up to 60% constriction before it began decreasing with increased band tightness. Time of flow decreased with constriction >20% ($p<0.01$), while stroke volume in banded embryos remained comparable to control levels over the entire range of constriction ($p>0.1$). The hemodynamic dependence on the degree of banding reveals immediate adaptations of the early embryonic cardiovascular system, and could help elucidate a range of cardiac adaptations to gradually increased load.

This review was originally published by the *Journal of the Royal Society, Interface*. Midgett M, Goenezen S, Rugonyi S. Blood Flow Dynamics Reflect Degree of Outflow Tract Banding in HH18 Chicken Embryos. *J R Soc Interface*. 2014; 11 (100):20140643. Reprinted with permission.

4.2 Introduction

Hemodynamics play an important role in regulating early cardiovascular development [39], and previous studies have shown that altered flow conditions can result in cardiac defects [3, 7, 8, 10, 38, 51, 148]. Interactions between blood flow and cardiac tissues generate biomechanical stresses and strains which modulate cardiogenesis. Throughout development, blood pressure causes cardiomyocytes to alter their maturation and proliferation [8, 146], and shear stresses (frictional forces exerted by flowing blood on the heart lumen wall) trigger biological responses including endothelial cell organization and signaling [3, 13, 49]. While the resulting defects from abnormal blood flow are known, the mechanisms by which hemodynamic forces lead to congenital heart disease are not clear.

This chapter focuses on the hemodynamics in the outflow tract (outflow tract) portion of the embryonic chick heart, which connects the primitive ventricle to the arterial vessel system during early development at Hamburger and Hamilton (HH) stage 18 [37]. At this early stage, the heart has a tubular structure, with atrium, ventricle and outflow tract connected in series. The outflow tract is frequently studied because it is very sensitive to hemodynamic changes and it later gives rise to the aorta, pulmonary trunk, interventricular septum, and semilunar valves, which are often involved in congenital heart defects [3, 10, 38]. Chick embryos are commonly used as a biological model of cardiac development because of ease of accessibility in the egg and developmental similarities with human embryos. We used a surgical intervention, cardiac outflow tract banding (also called ‘banding’ here for simplicity), to alter hemodynamic conditions through the chick embryo heart. In banding, a suture band is tied around the outflow tract to decrease the cross-sectional area and restrict the motion of the outflow tract wall, resulting in increased resistance to flow, peak ventricular pressure [51, 52], and blood flow velocities [62]. The high-shear and high-pressure flow conditions introduced by banding have been shown to result in a wide spectrum of heart defects in the chick embryo [7-10, 51].

The positioning of the outflow tract in the egg during early developmental stages allows for the implementation of a variety of imaging modalities to study cardiac blood flow and follow the progression of cardiac development. Optical coherence tomography (OCT) is a powerful non-invasive and non-contact tomographic imaging technique, which provides the high resolution, tissue penetration depth, and acquisition rates necessary to capture the beating motion of heart microstructures in early chick heart development. OCT provides a combination of structural and Doppler images with the same spatial and time resolution, which makes OCT a valuable imaging technique to study embryonic blood flow hemodynamics [62, 64, 157, 184, 185]. Further, band tightness can also be measured directly from structural OCT images [52]. OCT detects light reflected back from a low coherence light source to capture structure, and blood flow velocity is then calculated from the Doppler frequency shift when backscattered light from moving particles either adds or subtracts from the fixed Doppler frequency [186]. Hemodynamic and functional cardiac data can be easily measured from OCT structural and Doppler flow data to assess response to surgical interventions intended to alter blood flow conditions such as banding [62].

The studies in this chapter used Doppler OCT to measure blood flow velocity in the outflow tract after banding over a measured range of band constrictions and in control embryos. Wall shear rate (*WSR*), stroke volume (*SV*) and normalized time of flow (percentage of the cardiac cycle in which blood flows through the outflow tract) were also calculated from the Doppler velocity and structural data to evaluate the immediate hemodynamic response to banding. This study is novel because we assessed the varied hemodynamic responses due to measured degrees of band constriction, revealing how the developing system reacts over a range of loads. Characterization of the hemodynamics induced by banding will help elucidate whether the wide spectrum of heart defects observed after banding may partly represent the range of hemodynamic changes, and thus the potentially different mechanisms by which biomechanical forces affect cardiac development. While *WSR* (which depends on blood flow velocities) is a major trigger of cardiovascular endothelial-cell response, *SV* and time of flow serve as measures of cardiac efficiency and function. We present here, for the first time, how blood flow conditions (peak blood flow velocity, *WSR*, *SV*, and time of flow) are dependent on the degree of band tightness.

4.3 Methods

4.3.1 Chick embryo preparation and hemodynamic intervention

Fertilized White Leghorn chicken eggs were incubated blunt end up at 37.5 °C and 80% humidity until they reached stage HH18 (~3 days) [37]. Tweezers were used to remove a small section of the blunt-end shell and then the inner shell membrane directly over the embryo heart. Any embryos that bled upon membrane removal, had obvious structural defects, or were not at the correct developmental stage were discarded.

Three groups of embryos were studied: 1) normal group (NL), in which no interventions were performed; 2) sham control group (CON), in which a 10-0 nylon suture was passed under the outflow tract but not tightened; 3) outflow tract banded group (OTB), in which a 10-0 nylon suture was passed under the outflow tract and tied in a knot around the mid-section of the outflow tract to constrict the lumen cross-sectional area (Figure 4-1). A range of loose bands to very tight bands were studied in the banded group. Following interventions, the sham and banded group eggs were sealed with saran wrap and incubated for an additional 2 hours before OCT data acquisition. The banded group was imaged with OCT immediately prior to banding and after 2 hours of banding to calculate band tightness:

$$Band\ tightness = 1 - \frac{D_a}{D_b} \tag{4.1}$$

where D_a is the maximum external diameter of the outflow tract at the band site after banding, and D_b is the maximum external diameter of the outflow tract at the approximate band site location before banding.

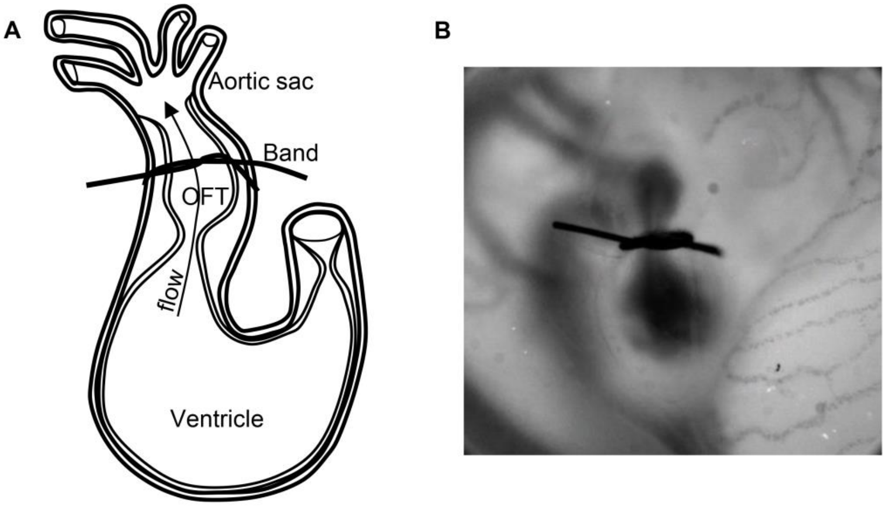

Figure 4-1. Outflow tract banding of the chick embryo heart at HH18. (**A**) Sketch showing part of the embryonic tubular heart at HH18: the outflow tract is downstream of the primitive ventricle and upstream of the aortic sac. The band is placed around the midsection of the outflow tract. (**B**) Representative photograph of an embryo right-side up, immediately after banding. OFT, outflow tract.

4.3.2 OCT image acquisition

A custom-made OCT system was used in this study. The system has a spectral domain configuration consisting of a superluminescent diode centered at 1325 nm from Thorlabs

Inc (Newton, NJ) and a 1024 pixel, 92 kHz maximal line-scan rate infrared InGaAs line-scan camera from Goodrich Inc (Charlotte, NC). This system allowed acquisition of 512 x 512 pixel (512 A-scans) 2D images at approximately 140 frames per second with <10 μm resolution. In addition to structural images, this system can generate simultaneous Doppler flow phase images in post-processing by calculating the phase differences between two adjacent A-scans in a B-scan. Our group has previously used a similar system to image the embryonic chicken heart motion and blood flow dynamics [52, 62, 64, 157]. Temperature during acquisition was maintained with a thermocouple-controlled heating pad surrounding the egg in a ceramic cup filled with water that was enclosed in a plastic box. This apparatus kept the embryo near the normal physiological temperature of 37.5 °C so that the heart rate remained close to the HH18 normal of 400 ms/beat, with variations of less than 40 ms/beat (~10% of cardiac cycle).

Each embryo was positioned within the OCT system so that a longitudinal section down the center of the outflow tract was obtained. It was verified that the lumen completely filled the outflow tract at maximum expansion and made a silt-like shape in the center of the outflow tract at maximum contraction [64, 159]. 200 sequential B-scan longitudinal section frames were acquired for each embryo (~ 3-4 cardiac cycles).

4.3.3 Structural and Doppler OCT image analyses

Simultaneous structural and Doppler phase image data sets were extracted from the acquired OCT raw data, using a custom Matlab code (The MathWorks, Inc. Natick, MA), to obtain an integrated view of blood flow and outflow tract wall movement (Figure 4-2). The overall analysis process is shown in Figure 4-3. Standards were imaged to calibrate conversion of pixel measurements to length measurements for all structural analyses. A flow-rate-controlled syringe pump was used to push milk through a glass capillary tube, which confirmed Doppler velocities within 10.7% of theoretical values after flow angle adjustment (Supplemental Figure 4-7).

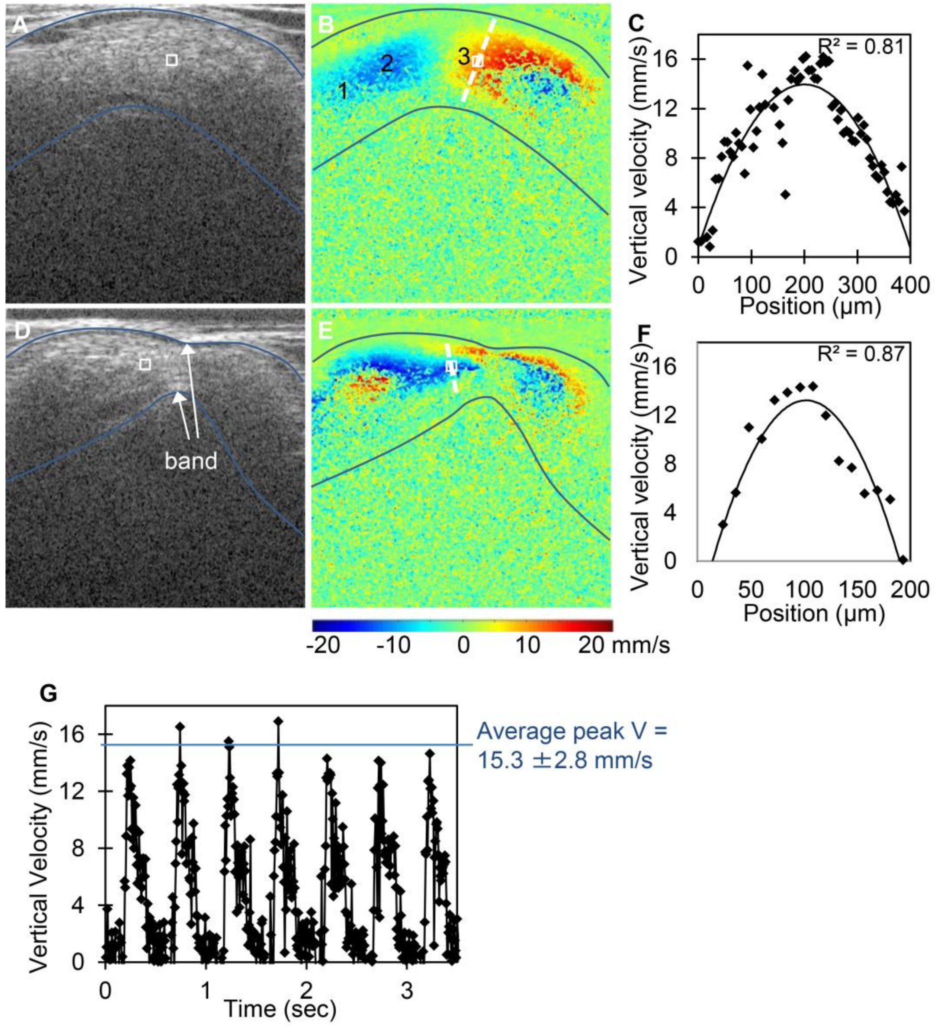

Figure 4-2. Representative OCT images of the HH18 chick heart outflow tract before and after banding at maximum expansion. (**A**) Structural image of a normal outflow tract. (**B**) Corresponding Doppler flow image of a normal outflow tract. Locations labeled 1, 2, and 3 along with the sampling area were chosen to compare maximum flow rate throughout the outflow tract, with comparable values (average maximum flow rate of 3.8 ± 0.1 mm^3/s) obtained. The myocardium is outlined on the structural image, and overlaid on the Doppler flow image, in blue. The approximate velocity sampling area is outlined by a white box in the Doppler flow images, and overlaid on the structural images. (**C**) Vertical velocity along dashed cross-sectional line in (**B**) showing a parabolic-like flow profile through the outflow tract under normal conditions. Experimental data is fit to a polynomial function with corresponding R^2 value. (**D**) Structural image of the same embryo 2 hours after banding. (**E**) Corresponding Doppler flow image 2 hours after banding. (**F**) Vertical velocity along the dashed cross-sectional line in (**E**) showing a parabolic-like flow profile through the outflow tract under banded conditions. Less experimental data is given for the banded embryos since the diameter is reduced compared to before banding. (**G**) Vertical velocity versus time plot over several cardiac cycles.

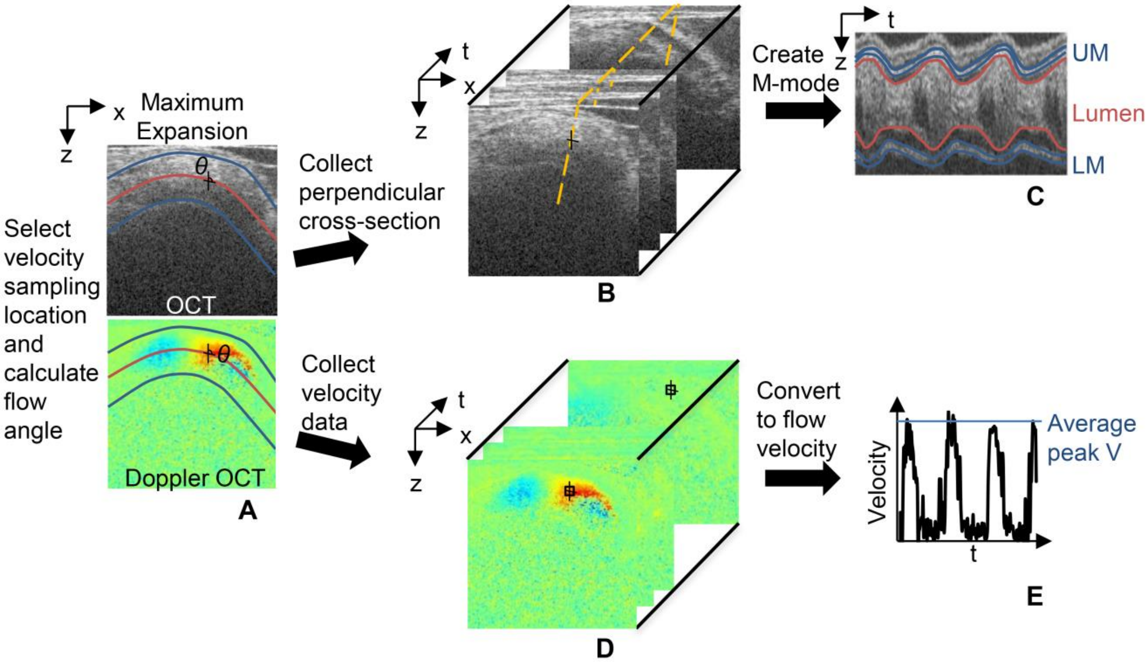

Figure 4-3. Flow chart of OCT image analysis. (**A**) Flow angle was measured by first outlining the myocardium walls in the 2D structural image at maximum expansion, in blue, to calculate the outflow tract centerline, in red. The trace was then overlaid on the corresponding Doppler image and θ calulated. (**B**) The outflow tract cross-section perpendicular to flow at the velocity measurement location was identified, shown as the dashed-line. (**C**) An M-mode image was extracted from the B scan dataset along the perpendicular dashed-line for *WSR* and *SV* analysis. (**D**) Velocity data was extracted from the 2D Doppler data set from a 3x3 pixel area at the selected measurement location. (**E**) Vertical velocity from each 2D frame was converted to the absolute flow velocity using θ to calculate peak V.

Phase wrapping was evident in the Doppler images of longitudinal scans (B-mode scans), when the phase shift exceeded ±π, which corresponded to vertical velocities higher than ± 23.4 mm/s. Since the velocity flow profile in the outflow tract at HH18 is parabolic-like [62, 157], the fastest flow frequently wraps in the center of the outflow tract (negative phase enclosed by positive phase or vice versa depending on direction of flow), while the slowest/non-wrapped flow is present near the walls (Figure 4-2). Areas with wrapped flow at peak blood velocities in the cardiac cycle were not chosen for the measurement location to avoid pixel-averaging errors associated with phase wrapping and corresponding unwrapping algorithms. Consistently located non-wrapped flow regions were identified and used for flow comparisons.

A velocity sampling area was selected in the region of non-wrapped flow along the outflow tract centerline near the middle of the outflow tract in all embryo groups (Figure 4-2). The “dog leg” bend geometry of the outflow tract has a region of ‘upward’ flow followed by a region of ‘downward’ flow, which creates a perfect region for non-wrapped flow in control embryos near the position in which the band was placed in banded embryos. The presence of the band in the banded embryos slightly lifted the outflow tract so that flow approached the band at an angle, passed through it horizontally, and then flowed downstream, with high vertical velocity flow on either side of the band. This geometry again created a non-wrapped, parabolic flow region, just upstream of the band. This velocity measurement location was chosen in the banded group to be the most representative of changes due to band constriction, as well as consistent with the location within the outflow tract across all embryo groups. We have further confirmed that the analysis technique measures similar flow rates throughout the length of the outflow tract. For example, the normal embryo shown in Figure 4-2,B has an average maximum flow rate of 3.8 ± 0.1 mm^3/s measured from 4 different locations along the centerline. For comparisons among embryos, however, velocities from just one consistent location are compared.

To compute flow velocities from phase shift data ($\Delta\phi$), the measured $\Delta\phi$ was converted to the vertical component of blood flow velocity (V_z) [64, 157]:

$$V_z = \frac{\lambda_0 \, \Delta\phi}{4\pi \, n \, \tau} \tag{4.2}$$

where λ_0 is the central wavelength, n is the refractive index of the tissue (~1.35), and τ is the time difference between two adjacent A-scans. To reduce noise while minimally affecting flow velocity measurements, at each pixel $\Delta\phi$ was calculated as the average of a 9 pixel (3x3 box) sampling area. Then, the vertical velocity (obtained from Equation

4.2) at the sampling point over time was further averaged within the cycle and filtered in 2 iterations, excluding values more than 1.3 standard deviations away from the updated mean at each iteration. We then calculated the magnitude of the 3D blood flow velocity (*V*):

$$V = \frac{V_z}{\cos\theta} \tag{4.3}$$

where θ is the angle of the outflow tract centerline tangent with the vertical direction (the direction of V_z). The average peak *V* in the cardiac cycle was compared across all embryos.

A custom Matlab program was used to measure the angle θ. While θ is commonly set by operator estimation, our procedure calculates the angle by first computing the tangent to the curved outflow tract centerline at the selected velocity measurement location in a maximum expansion frame. Doppler flow and structural images show that blood flow follows the contour of the outflow tract in a parabolic-like profile, with the maximum velocity at the axial center of the tube, consistent with a low Reynolds (Re <6) and Womersley (W <0.5) numbers, and viscous forces dominating blood flow (Figure 4-2). To obtain the outflow tract centerline, first the upper and lower myocardium walls were manually outlined on the structural image and then the centerline was computed as the middle position in the z-direction at each pixel along the outflow tract length in the x-direction (Figure 4-3). The myocardium was outlined for the angle calculation as it is better defined in longitudinal frames, and since at maximum expansion the lumen fills the outflow tract and is roughly circular like the myocardium. The structural outlines were then overlaid on the corresponding Doppler flow image for the user to select the velocity measurement position along the centerline. Finally, the angle of the line tangent to the centerline with respect to the vertical direction at the measurement location was calculated to find θ and calculate *V*.

Outflow tract characteristic diameters were measured from M-mode image analysis. M-modes are used to show cardiac wall motion over time, by displaying gray scales from a single line of every structural B-mode frame in a data set. This organization results in cardiac structure along the selected line shown in the vertical direction versus time in the horizontal direction (Figure 4-3). M-modes were generated from a line at the point along the outflow tract centerline that was chosen for velocity measurement or band tightness measurement and at an angle perpendicular to the centerline. The upper and lower myocardium or lumen interfaces in the M-mode were traced to calculate the outflow tract diameter of interest over the entire cardiac cycle.

WSR variation from banded altered velocity was then evaluated. Shear rate at the wall was calculated using

$$WSR = \frac{dV}{dr} \tag{4.4}$$

where ***V*** is the velocity vector, ***r*** is a vector normal to the lumen-wall surface, and d**V**/d**r** is the velocity gradient in the direction normal (perpendicular) to the lumen-wall surface, see e.g. [165, 169, 187, 188]. Equation 4.5 can be derived from the Haagen-Poisseuille equation,

$$WSR = \frac{4\,v_c}{D} \tag{4.5}$$

where v_c is the outflow tract centerline velocity *V*, and *D* is the outflow tract lumen diameter at a single point in the cardiac cycle, see e.g.[165, 166]. A parabolic-like velocity profile in the outflow tract at HH18 [62, 157] (Figure 4-2) make this approximation valid. While adult mammalian blood is non-Newtonian with biconcave red blood cells, embryonic chick blood has spherical red blood cells that are less deformable in flow [189] resulting in a fairly constant viscosity in the physiological shear rate range [167] and thus WSR should be proportional to wall shear stress. The *WSR* during peak *V* in the cardiac cycle was compared across all embryos.

SV was measured to assess cardiac function over a range of band tightness. *SV* was estimated using the centerline blood flow velocity over an entire cardiac cycle, and the diameter of the lumen walls in each frame at the selected measurement location. The volumetric flow rate corresponding to each frame was calculated using a form of the Poiseuille equation derived for a parabolic flow profile as the product of the mean centerline velocity and the cross-sectional area of the lumen [163, 164]:

$$Q = \frac{\pi D^2 v_c}{8} \tag{4.6}$$

where *Q* is the blood flow rate through the outflow tract and *D* is the outflow tract lumen diameter. This approximation assumes that blood is homogeneous, and that blood flow is parabolic and laminar, with zero velocity at the outflow tract lumen wall. Since the outflow tract cross-sectional area (and thus *D*) and the centerline blood velocity change over the cardiac cycle, the flow rate was divided by the image acquisition rate to estimate the volume of blood passing in between each 2D image acquired. *SV* was estimated by summing the blood volume calculated from each frame during blood flow in a full cardiac cycle:

$$SV = \sum_{i=1}^{N} Q_i \, \Delta t \tag{4.7}$$

where Δt = 1/frame rate (140 fps for our system), *Q* is the blood flow rate calculated from each frame, and the sum takes into account one cardiac cycle (*N* approximately 25 frames, depending on actual cardiac cycle period and time of flow). The average *SV* value from 2-3 cardiac cycles was used to compare embryos.

To further characterize the relationship between blood flow and outflow tract wall dynamics, time of flow was measured in all embryo groups. Time of flow was defined as the average percentage of time in the cardiac cycle when blood was flowing through the measurement location in the outflow tract. The presence of flow was determined from the blood flow velocity versus time trace as clear peaks above the background noise level.

4.3.4 Statistical and uncertainty analyses

Embryo group data was analyzed as the mean ± standard deviation. Statistical significance was determined with a two-sample Student's t-test, reporting two-tail p-values, and assuming significance with p-values <0.05. 2D OCT image analysis involves many assumptions that can introduce error into the final variable estimates. Maximum error was calculated with uncertainties for each variable involved in the approximation for peak blood flow velocity, *WSR*, and *SV.* Assuming typical values and average variation, maximum possible error was estimated by,

$$F = F(D, \theta, V_z)$$

$$dF = \left.\frac{\delta F}{\delta D}\right|_{D_0,\theta_0,V_{z0}} \Delta D \; + \; \left.\frac{\delta F}{\delta \theta}\right|_{D_0,\theta_0,V_{z0}} \Delta\theta \; + \; \left.\frac{\delta F}{\delta V_z}\right|_{D_0,\theta_0,V_{z0}} \Delta V_z \qquad (4.8)$$

where *F* is the variable in question (peak *V, WSR, SV*), and *dF* is the summation of individual partial derivative errors; D_o, θ_0, and V_{z0} are typical reference values of 450 μm outflow tract diameter, 70 ° flow angle with respect to the vertical direction, and 15 mm/s vertical velocity, respectively; ΔD, $\Delta\theta$, are ΔV_z are average variations of 50 μm outflow tract diameter, 5 ° flow angle with respect to the vertical direction, and 2.8 mm/s vertical velocity (Figure 4-2G), respectively. Typical reference and variation values were determined as averages from repeated measurements.

4.4 Results

Both the normal and sham control groups were comparable, with no significant differences across all measures (n=8 for each group; p-values: 0.92 for peak velocity, 0.91 for *WSR*, 0.19 for *SV,* 0.83 for time of flow), indicating that any changes after banding are from the constriction of the outflow tract and not due to the surgical manipulation. Banding constriction ranged between 0-64% band tightness.

4.4.1 Peak blood flow velocity response to banding

Maximum blood flow velocity through the outflow tract near the band site (Figure 4-2) was analyzed for all embryos (n=41). Average peak blood flow velocity for normal and control groups was 40.2±5.7 mm/s and 40.4±3.1 mm/s, respectively which corresponds to previously published values at HH18 [64, 157, 162, 172]. Peak velocity was increased in banded embryos, consistent with previous studies [62, 63], but was also dependent on degree of band tightness with the largest increase of 2.5-fold near 40% band constriction. Peak velocity increased approximately linearly with band tightness between 0-40% constriction (R^2=0.91), and then plateaued near 40-50% band tightness. Above 50% constriction, peak velocity decreased with band tightness, while still remaining higher than normal and control groups (Figure 4-4 and Table 4-1). Peak velocities from all ranges of banded embryos tested were significantly higher than control groups (OTB n=25; p-value=2.2×10^{-4} for <20% OTB, n=6; p-value=2.7×10^{-18} for 20-40% OTB, n=12; and p-value= 5.3×10^{-6} for >40% OTB, n=7). Figure 4-4,B additionally includes one embryo that was severely compromised with 81% band tightness (OCT imaged immediately after banding), to demonstrate that a tight band that allowed little blood flow through the lumen caused the peak velocity to decrease below that of control embryos.

Table 4-1. Summary of average outflow tract flow parameters for normal (NL), control (CON), and banded (OTB) groups separated by band tightness range. Data presented as means ± standard deviation. * denotes statistically significant difference from control groups with p-value<0.05.

Embryo Group	**Velocity** (mm/s)	*WSR* (s^{-1})	**SV** (mm^3/ beat)	**Time of Flow** (%)
NL	40.2+5.7	302.1±73.2	0.51±0.17	53.1±6.4
CON	40.4±3.1	305.5±33.2	0.41±0.10	52.5±5.9
OTB(<20%)	66.0±7.5*	572.3±101.7*	0.51±0.19	52.2±7.0
OTB(20-40%)	89.9±5.1*	797.5±104.4*	0.45±0.17	43.9±5.0*
OTB(>40%)	83.9±8.9*	783.0±121.4*	0.39±0.11	32.9±2.7*

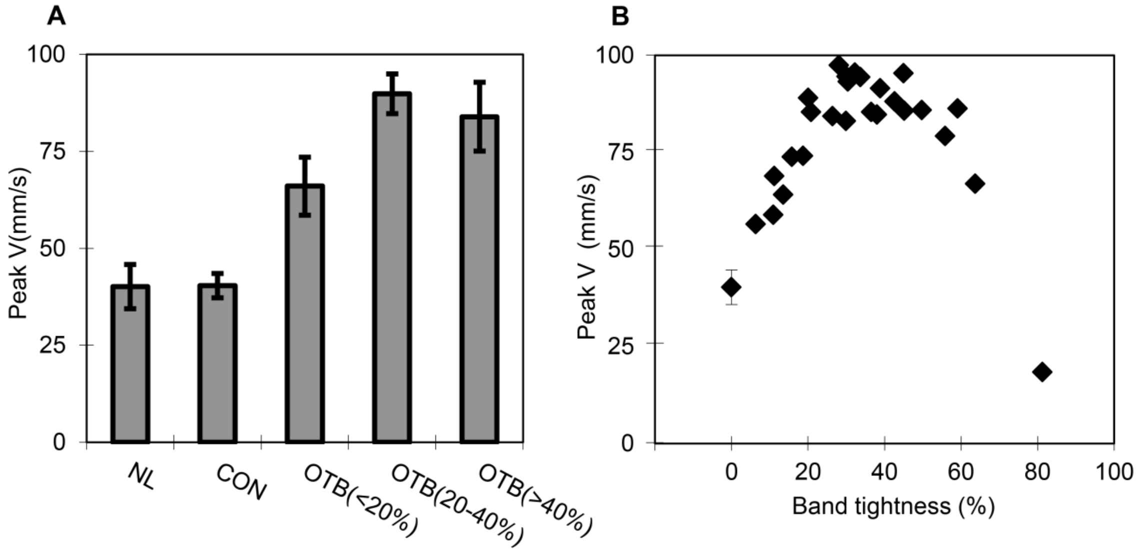

Figure 4-4. Blood flow peak velocity response to band tightness. (**A**) Comparison of average peak velocity of the normal (NL, n=8), control (CON, n=8), and the banded group (OTB) split between those embryos with bands <20% constriction (n=6), 20-40% constriction (n=12), and >40% constriction (n=7). Data presented as mean with standard deviation shown as error bars. (**B**) Individual average peak velocity response over a range of 0-81% band tightness, with NL and CON groups shown with 0% band tightness.

Considering uncertainties in the measurements, the maximum possible error for the peak blood flow velocity calculation was 18.6 mm/s, with the largest error contribution from the θ estimation (see Table 4-2 and Equation 4.8). Since the θ estimation in this study was based on the outline of the myocardium walls from OCT structural images (instead of standard ultrasound angle measuring procedures where θ is manually set by the operator), angle estimations were likely very consistent.

Table 4-2. Summary of maximum error calculations for total error (d*F*) and each error component (δ*F*/δ*x*).

Error	***F*=*V*** (mm/s)	***F*=*WSR*** (s^{-1})	***F*=*SV*** (mm^3/beat)
d*F*	18.6	208.8	2.2×10^{-2}
δ*F*/δ*D*	N/A	43.3	1.1×10^{-2}
δ*F*/dθ	10.5	93.5	6.0×10^{-3}
δ*F*/d*Vz*	8.1	72.0	5.0×10^{-3}

4.4.2 WSR response to banding

WSR at peak blood flow velocity near the band site (Figure 4-2) was calculated across the range of band tightness (n=40). Average maximum *WSR* across normal and control embryos was 302.1±73.2 s^{-1} and 305.5±33.2 s^{-1}, respectively which is within previously published experimental and computational fluid dynamics model estimates in the chick embryo outflow tract [64, 170]. Results are summarized in Figure 4-5,A and Table 4-1. Error propagation analysis showed that the largest error contribution to *WSR* was from the θ estimation (see Table 4-2 and Equation 4.8). While the maximum hypothetical error could be large (208.8 s^{-1}) compared to the mean of control embryos, our computed standard deviations are relatively low (24% and 11% of the mean for normal and control groups, respectively). Since velocity is one of the main variables in this estimation (see Equation 4.5), the *WSR* from the banded group follows the general trend of the velocity versus band tightness curve (Figure 4-5,A) but does not begin to decrease until 60% band constriction. The *WSR* estimations in the banded group were significantly higher than the control groups, across all banded sub-divisions (OTB n=24; p-value=8.5×10^{-4}

for <20% OTB, n=6; p-value=8.9×10^{-10} for 20-40% OTB, n=11; and p-value=2.1×10^{-5} for >40% OTB, n=7). The range of band tightness studied therefore generated a range of *WSR* on cardiac tissues just upstream of the band at the chosen measurement location (Figure 4-2).

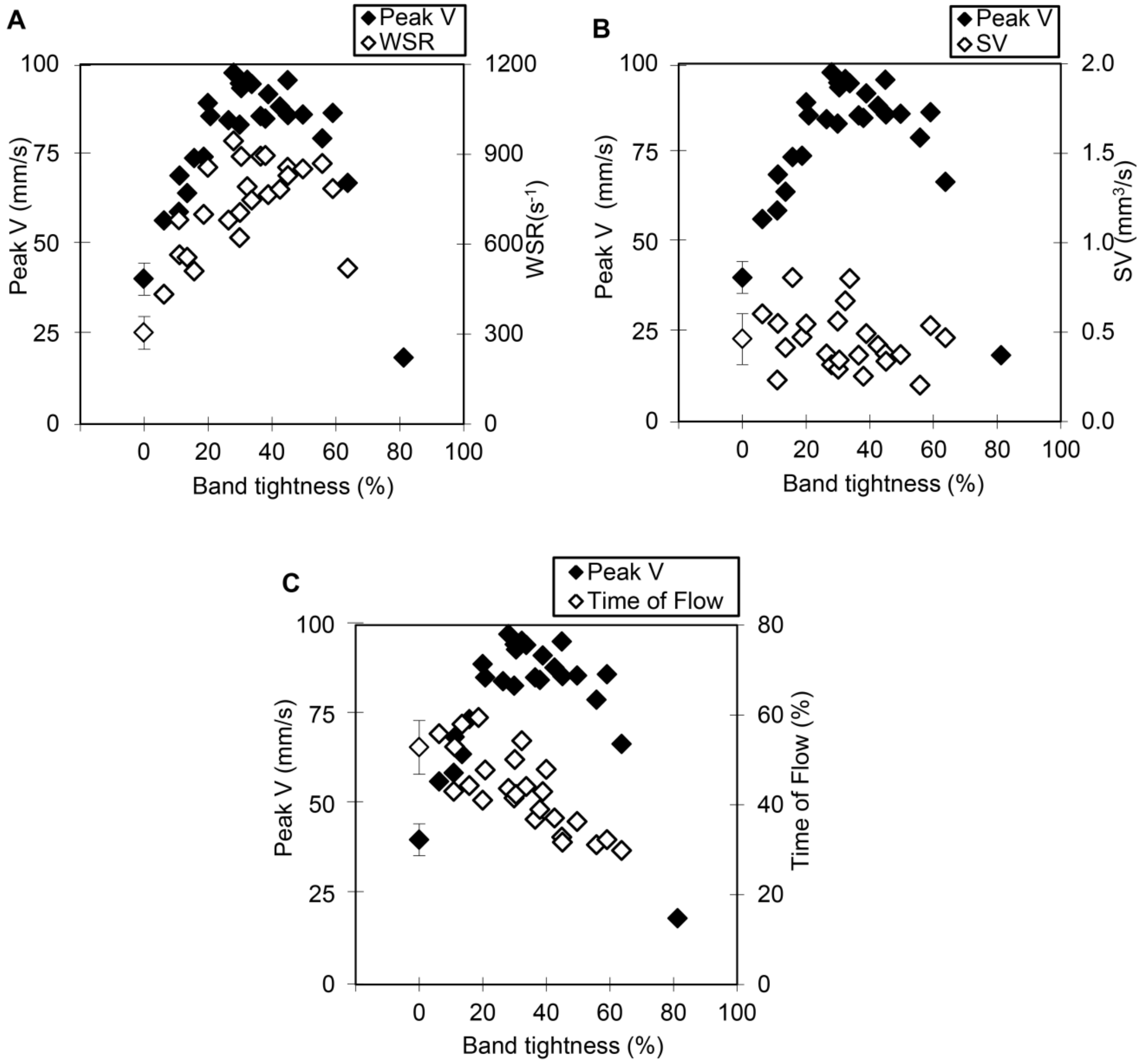

Figure 4-5. Hemodynamic measures as a function of band tightness compared to the average peak blood flow velocity response over a 0-64% constriction range. (**A**) WSR (s^{-1}) response, banded n=24. (**B**) *SV* (mm^3/beat) response, banded n=24. (**C**) Time of flow (%) response, banded n=25. Normal (n=8) and control (n=8) embryo data shown at 0% band tightness averaged together with standard deviation shown as error bars.

4.4.3 SV response to banding

SV was measured over the range of band tightness (n=40). Average *SV* values for normal and control groups were 0.51±0.17 mm^3/beat and 0.41±0.10 mm^3/beat, respectively which is comparable to previously published data estimated with prolate spheroid ventricular volumes [153] and dorsal aortic flow [48, 190]. *SV* in banded embryos stayed approximately constant within the range of control groups, with no significant differences across all banded sub-divisions (OTB n=24; p-value=0.59 for <20% OTB, n=6; p-value=0.91 for 20-40% OTB, n=11; and p-value=0.18 for >40% OTB, n=7). Results are summarized in Figure 4-5,B and Table 4-1. Considering uncertainties in the *SV* calculation, the maximum error for the *SV* calculation was 2.2×10^{-2} mm^3/beat, with the largest error contribution from the outflow tract diameter estimation (see Table 4-2 and Equation 4.8). While not measured over a range of band constriction, others have previously found that *SV* did not clearly differ between control and banded embryos [63, 191].

4.4.4 Time of flow response to banding

The time of flow was measured for all embryos that had clearly distinguishable periods of blood flow in the velocity versus time trace (n=41). Time of flow, the percentage of time in the cardiac cycle when blood was flowing, for normal and control groups was approximately half of the cardiac cycle, consistent with our previous observations [64]. Differences in time of flow were not significant between control groups and the banded embryos with <20% band tightness (p-value=0.86, n=6). Banded embryos with >20% band tightness had significantly lower time of flows (OTB n=25; p-value=3.3×10^{-4} for 20-40% OTB, n=11; and p-value=5.6×10^{-6} for >40% OTB, n=8). Figure 4-5,C shows that time of flow decreased with increasing band tightness, and average values are summarized in Table 4-1.

Control and loosely banded embryos (<30% constriction) consistently had an initial surge of blood flow through the outflow tract prior to the main flow of the cardiac cycle, shown in Figure 4-6,A with an arrow. The initial flow surge was not evident in banded embryos with >30% band tightness, consistent with the measured decrease in time of flow. Figure 4-6,B shows the relationship between the minimum external outflow tract diameter in the cardiac cycle at the band site (D_{min}) and band tightness. While band tightness is measured from maximum outflow tract diameters (see Equation 4.1), the ratio of minimum outflow tract diameter after banding compared to before banding (*A/B ratio*) was decreased in bands tighter than 40% constriction, indicating the outflow tract is constricted beyond its normal contraction geometry with tight bands. The range of band tightness with decreased D_{min} was also consistent with the observed decrease in time of flow.

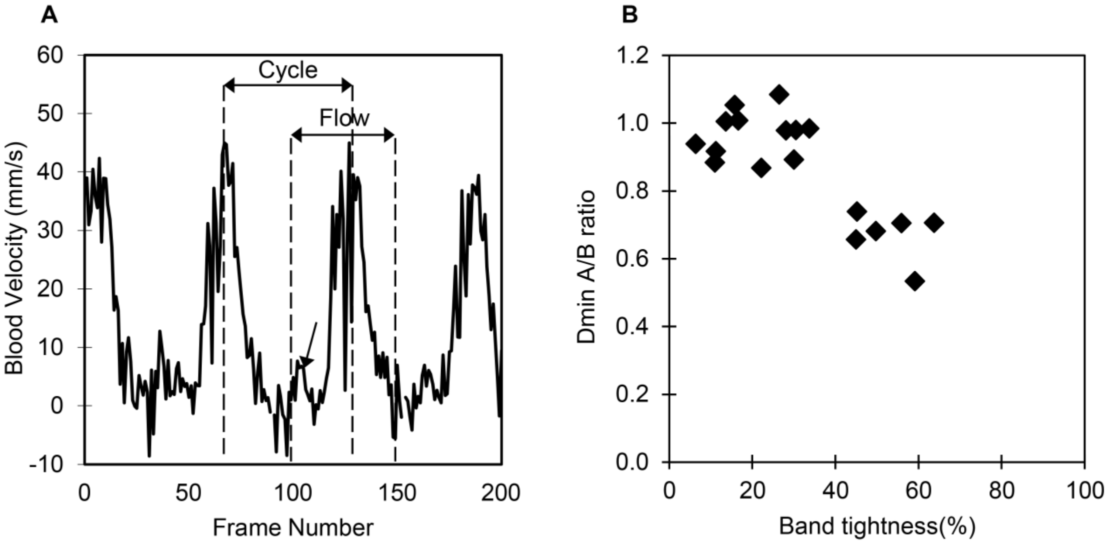

Figure 4-6. Time of flow versus band tightness. (**A**) Blood flow velocity trace over ~4 cardiac cycles for an example normal embryo. The arrow designates the initial flow surge seen before the main flow of the cardiac cycle in loosely banded embryos. (**B**) Outflow tract D_{min} ratios at banding site (after/before banding) versus band tightness. Diameters were measured only from M-mode images which clearly showed the upper and lower myocardium walls (n=18).

4.5 Discussion

These results show the immediate hemodynamic response due to initial banding mechanical stimuli. Since the embryonic cardiovascular system cannot fully remodel within 2 hours, our hemodynamic assessment of banded embryonic hearts characterizes the initial flow alterations which have been shown to stimulate myocardial and endocardial layer response and tissue remodeling to cause cardiac defects [7-10, 51]. Hemodynamic assessment is the first step in elucidating the mechanisms that cause altered blood flow to lead to cardiac malformations. We found that peak blood flow velocity increased with band tightness until near 40% constriction, where the velocity plateaued and then decreased with very tight bands, while the corresponding *WSR* followed a similar trend. *SV* remained constant with band tightness, while time of flow (the percentage of time with blood flow in the cardiac cycle) decreased with band tightness >20% constriction. The combination of these results suggests that immediate adaptations to banding promote the preservation of cardiac function.

Recent 4D OCT analyses have been employed to accurately track the dynamics of myocardial tissue and blood flow over time using similar OCT systems that acquire multiple 2D cross-sectional data sets before synchronization and 4D reconstruction [64, 157, 173]. While 4D analyses of the heart allow for accurate 2D cross-sectional image generation and dynamic wall motion visualization, the simpler 2D longitudinal images acquired in this study permit velocity comparisons across a large banded sample group in a relatively easy and fast way. 2D acquisition is significantly faster than 4D acquisition, and therefore can also be routinely used to scan embryos before performing other analyses (e.g. before tissue fixation). The high reproducibility exhibited in the control groups showed that our analyses, while not straight-forward, were accurate enough to capture subtle changes in dynamic hemodynamic conditions that were not reported before.

4.5.1 Peak blood flow velocity response to banding

This study complements recent work from Shi et al [52], which assessed blood pressure changes due to a range of band constrictions. The study showed that as resistance to blood flow through the outflow tract increased with band tightness, so did blood pressure throughout the circulatory system. Not only did the ventricle, aortic sac, and dorsal aorta pressures increase after banding, but they were dependent on the relative band tightness. Both diastolic blood pressure (minimum pressure) and pulse pressure amplitude (and therefore systolic pressure) increased somewhat linearly with band tightness until near 40% band constriction, at which point pressure measures started to increase faster than linearly with band tightness. 40% band tightness also corresponded to a sharper decrease in pulse transit time through the outflow tract and a plateau in the increase of the time lag for pressure to peak after cardiac depolarization (obtained from ECG measurements). In this study, 40% band tightness represents the point in the velocity versus band tightness curve where the peak blood flow velocity stops increasing with band tightness. The faster pressure increase and pulse transit time decrease with band tightness may be related to the blood flow velocity plateau because of a combination banding effects, including decreased outflow tract active wall contraction at the band site, and afterload stretching of the ventricular cardiomyocytes.

Under normal conditions, blood is pushed through the outflow tract by a combination of pressure wave propagation after ventricular contraction and the active contraction of the outflow tract. The presence of active contraction through the outflow tract is supported by synchronized wall motion and pressure data, where the peak ventricular systolic pressure and peak aortic sac pressure occurs just prior to the maximum outflow tract inlet and outlet wall contraction, respectively [52, 64, 192]. Blood flow generated solely by ventricle contraction, followed by passive pressure wave propagation through the outflow tract, would instead cause the peak pressure to occur in phase with the maximum outflow tract expansion. Further, we observed that the HH18 heart outflow tract alone contracts in warmed Hank's balanced salt solution after being removed from the embryo and separated from the ventricle. Banding increases pressure wave propagation speed, while decreasing peristaltic-like patterns of outflow tract wall motion [52]. The banding suture physically anchors the outflow tract to surrounding membrane tissues, making the wall effectively stiffer and less compliant with increased band tightness. This lessens the contractile capacity of cardiomyocytes close to the band and thus decreases outflow tract active contraction. The diminishing effect banding has on active wall contraction, together with increased constriction, may contribute to the velocity versus band tightness curve plateau near 40% constriction. The peak blood flow velocities in this range are still much higher than those measured in control embryos because of increased pressure and pressure wave propagation speeds, but may stop increasing with band tightness partially due to the loss of active wall contraction against an increased resistance to flow.

Previous studies suggest the banding induced increase in cardiac afterload and resistance to ventricular ejection may extend the time for full myocardial force generation and increase the resultant ventricular contraction force [52, 191]. The Starling law establishes that the heart can change the force generated by contractile muscle fibers depending on the amount of overlap of the thin and thick myofilaments, with a reduced force generated with more or less fiber overlap than the optimal sarcomere length [180, 181]. Increased afterload (resistance to flow) due to banding may create greater contraction forces until a certain band tightness, where the optimal sarcomere length of ventricle muscle fibers is exceeded and additional ventricle load generates a diminished contraction force. Thus a balance is established in which increased resistance to flow induced by the band is compensated by increased ventricular contraction force, resulting in increased velocities through a narrower lumen area. Increases in afterload and myocardium force generation with band tightness, however, are not proportional, and the peak blood flow velocity levels off and begins decreasing with constriction >40% band tightness.

4.5.2 WSR response to banding

Four-dimensional computational fluid dynamics models have been developed to account for the curved, moving geometry of the outflow tract during the pulsatile flow in the cardiac cycle [64], which is not accounted for by our *WSR* estimation using Equation 4.5. The *WSR* estimation calculated from 2D longitudinal images in this study only compares values at one outflow tract position at one time point in the cardiac cycle. Further, Equation 4.5 assumes a circular lumen, which is a good approximation when the outflow tract walls are fully expanded [64, 159], and thus it is reasonable to compute *WSR* at peak blood flow velocity. Nevertheless, 2D longitudinal images are easier to acquire and analyze than the 4D motion of the outflow tract, resulting in an efficient (and relatively simple-to-implement) procedure to monitor the effect of increased band constriction on endocardial *WSR*.

The trend of maximum *WSR* loosely followed the velocity versus band tightness curve. This is somewhat expected as *WSR* is proportional to velocity and inversely proportional to lumen diameter (see Equation (4.5)). *WSR* increased with band tightness and started to decrease only at very tight band constrictions near 60% band tightness. This decrease occurred after the diminished velocity response (Figure 4-5A), when blood flow velocities were dramatically decreased. While the velocity versus band tightness curve plateaus near 40% constriction, the diameter at peak velocity continues to decrease with band tightness, which explains the continuous increase of *WSR* beyond 40% constriction and up to 60% band tightness.

4.5.3 SV response to banding

SV values reported here are likely overestimates, since the calculation assumes the outflow tract is a circular cylinder throughout the cardiac cycle. In reality, cross-sectional OCT images of the outflow tract show the myocardium undergoes concentric narrowing and widening over the cardiac cycle while the lumen has an ellipse-like shape at maximum expansion and a slit-like shape during contraction [64, 159]. While the dynamic and complex flow through the moving outflow tract is simplified in this estimation, the approach accounts for the velocity and outflow tract size changes over the cardiac cycle, and serves as a comparison across embryos over a range of band constriction.

SV remained constant under 0-64% band constriction conditions, even while the minimum outflow tract diameter and time of flow (portion of cardiac cycle with flow) decreased with band tightness. This conservation of SV indicates that the early embryonic cardiovascular system has a large range of functional adaptation in response to the increased afterload imposed by the band. The Starling law of the heart may be partly responsible for the conserved *SV* over a large range of band constrictions presented in this study. The greater ventricular force generation that results from increased afterload and sarcomere lengthening could contribute to the heart’s astonishing ability to preserve normal blood pumping even with tight band constrictions. The conservation of normal SV in embryos with band constriction greater than 50%, despite decreases in peak velocity and time of flow, is associated with an increased average flow rate (Supplemental Figure 4-8). Previous studies report a similar adaptive ability of the cardiovascular system to alter *SV* after end-diastolic volume infusions [137, 191]. The fact that the heart at this stage has no valves, and the nervous system has not yet been formed, supports the idea that the cardiovascular adjustment to banding conditions is mainly mechanical in nature.

While *SV* has been previously shown to be similar in control and banded embryos [63, 191], it has not before been investigated over a range of measured band tightness. Keller et al [191] used outflow tract banding to induce acute outflow tract occlusion using very tight bands alongside a volume infusion procedure, and calculated *SV* using ellipsoid ventricle volume estimations and pressure-volume loops. This *SV* measure demonstrated no striking difference between control and outflow tract occluded embryos with and without volume infusion at HH21. McQuinn et al [63] compared the hemodynamic environments of control and outflow tract banded embryos with high frequency ultrasound, and found no difference in *SV* at HH24 and HH27 when calculated by tracking particle movement in the dorsal aorta. This study shows evidence of similar *SV* compensation, while over a wider documented range of hemodynamic alterations than previously reported.

4.5.4 Time of flow response to banding

The time of flow (percentage time in which blood flows through the outflow tract in each cardiac cycle) significantly decreased with constriction >20% band tightness. This result was not obvious *a priori*. The velocity versus time traces showed an initial flow surge in control and loosely banded embryos (<30% constriction) that was not evident in tight bands (Figure 4-6,A). The initial surge may be caused by the opening event of the outflow tract cushions which allows blood into the outflow tract before the main ventricle contraction. This could also be explained by a dynamic suction pumping model [193]. The dynamic beating movement of the outflow tract may also introduce an artifact in the velocity versus time trace, since only a stationary 2D longitudinal plane is imaged. Tight bands anchor the outflow tract to surrounding membranes and tissues more than loose bands, which may cause the surge artifact to disappear in the tightly banded data. Further 4D OCT analysis is needed to capture the longitudinal movement of the outflow tract, and determine if the initial flow surge is present in the cardiac cycle or an artifact of the sample positioning. Nevertheless, the absence of the surge in tightly banded embryos contributed to the decreased time of flow.

Maximum outflow tract diameter decreased with band tightness while the minimum outflow tract diameter remained relatively constant with constrictions up to ~40% band tightness. In embryos with >40% band constriction, the myocardium was constricted beyond its minimum diameter prior to banding. This is likely explained by movement of the cardiac jelly layer away from the constricted region. When the band constricts the outflow tract myocardium beyond its normal contraction the lumen may remain closed for a larger portion of the cardiac cycle, and thus contribute to the decreased time of flow.

4.6 Conclusion

We have successfully measured blood flow triggers of tissue remodeling and cardiac function over an identified range of band constrictions using structural and Doppler OCT images. Peak blood flow velocity, *WSR*, and time of flow were significantly affected by banding with varied dependence on band tightness, while normal *SV* was preserved in banded embryos. Hemodynamic response assessment based on the degree of band tightness provides a novel view of functional adjustments and preservation in the early embryonic cardiovascular system, and advances understanding of the altered forces that affect cardiac development. The conservation of *SV* even under a dramatic range of band tightness highlights the adaptation capabilities present at this early stage of development. Further, these outcomes suggest that cardiac malformations caused by banding [3-5] result from a complex combination of altered ventricular function and blood flow resistance through the outflow tract. Moreover, the spectrum of cardiac malformations previously observed after banding may be partly explained by different band tightness that generated diverse biomechanical conditions and thus distinct cardiac tissue growth and remodeling effects. Future studies will be needed to correlate the initial altered hemodynamics to early cardiac adaptations and the different types of cardiac defects that result later in development.

4.7 Acknowledgements

This work has been supported by grants NIH R01 HL094570 and NSF DBI-1052688. The content is solely the responsibility of the authors and does not necessarily represent the official views of grant giving bodies.

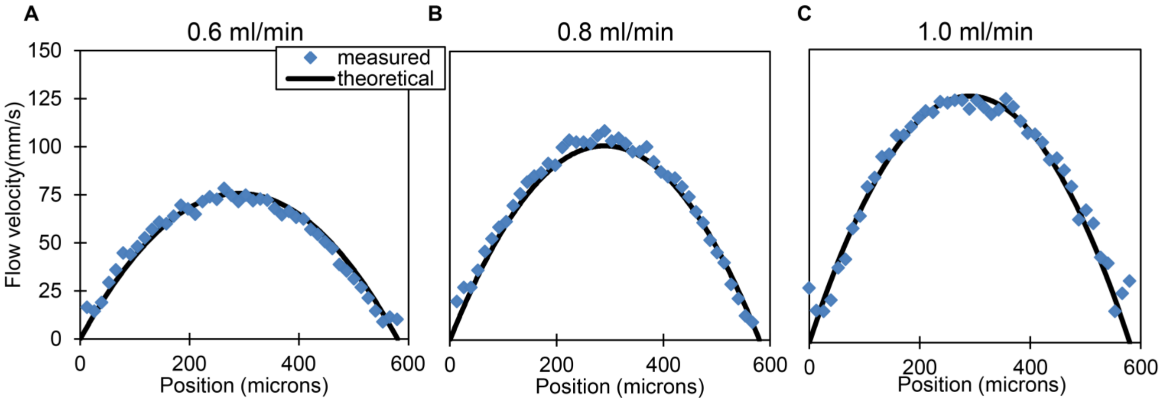

Supplemental Figure 4-7. Doppler OCT velocity verification. Doppler velocities measured from the OCT system were confirmed with a flow-rate-controlled syringe pump that pushed milk through a glass capillary tube set at (**A**) 0.6 ml/min, (**B**) 0.8 ml/min, and (**C**) 1.0 ml/min. Measured doppler velocites across the tube were compared to theoretical values.

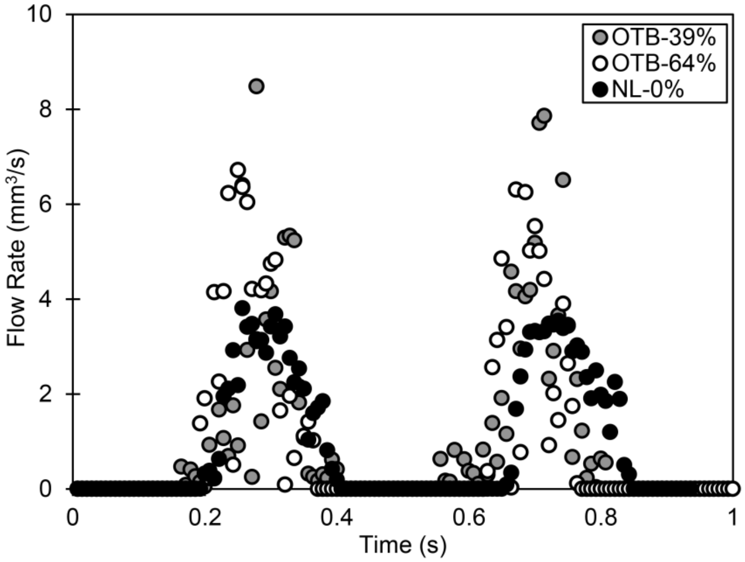

Supplemental Figure 4-8. Flow rate after outflow tract banding. Example flow rate vs. time curves over two cardiac cycles from a normal, a banded embryo with 39% banded tightness, and a banded embryo with 64% band tightness.

CHAPTER 5: Increased Hemodynamic Load in Early Embryonic Stages Alters Endocardial to Mesenchymal Transition

Madeline Midgett, Claudia S. López, Larry David, Sandra Rugonyi

5.1 Abstract

Normal blood flow is essential for proper heart formation during embryonic development, as abnormal hemodynamic load (blood pressure and shear stress) results in cardiac defects seen in congenital heart disease. However, the progressive detrimental remodeling processes that relate altered blood flow to cardiac defects remain unclear. Endothelial-mesenchymal cell transition is one of the many complex developmental events involved in transforming the early embryonic outflow tract into the aorta, pulmonary trunk, interventricular septum, and semilunar valves. This study elucidated the effects of increased hemodynamic load on endothelial-mesenchymal transition remodeling of the outflow tract cushions *in vivo*. Outflow tract banding was used to increase hemodynamic load in the chicken embryo heart between Hamburger and Hamilton stages 18 and 24. Increased hemodynamic load induced increased cell density in outflow tract cushions, fewer cells along the endocardial lining, endocardium junction disruption, and altered periostin expression as measured by confocal microscopy analysis. In addition, 3D focused ion beam scanning electron microscopy analysis determined that a portion of endocardial cells adopted a migratory shape after outflow tract banding that is more irregular, elongated, and with extensive cellular projections compared to normal cells. Proteomic mass-spectrometry analysis quantified altered protein composition after banding that is consistent with a more active stage of endothelial-mesenchymal transition. Outflow tract banding enhances the endothelial-mesenchymal transition phenotype during formation of the outflow tract cushions, suggesting that endothelial-mesenchymal transition is a critical developmental process that when disturbed by altered blood flow gives rise to cardiac malformation and defects.

5.2 Introduction

Congenital heart defects affect nearly 1% of newborns and are the leading cause of infant death in the United States [16, 194]. Additionally, surgical repair of congenital heart defects is associated with a yearly economic burden of approximately $2.2 billion [18] and long term consequences for patients. Blood flow dynamics play a critical role in regulating early heart development [39], as numerous studies have shown that surgically altered blood flow results in a spectrum of cardiac defects seen in human congenital heart disease (CHD) [7-10, 32, 33, 51, 195]**.** However, the ways in which altered blood flow triggers malformation that leads to cardiac defects remain unclear. Understanding the root causes of CHD and the initial dysregulation leading to it is essential for future prevention and treatment.

The heart is the first functional organ in the embryo, and starts beating and pumping blood as soon as the primitive heart tube is formed. Blood is ejected from the ventricle of the tubular heart into the arterial vessel system via the outflow tract. Early during cardiac development, endocardial cushions (localized thickenings of the wall) form in the outflow tract and atrioventricular canal, and eventually serve as primitive valves that block blood flow upon contraction of the myocardium. The endocardial cushions are initially composed of extracellular matrix (cardiac jelly), separated from blood by an endocardium monolayer, and collectively adapt to an ever-changing biomechanical environment as blood pressure and flow increase over development. The outflow tract cushions are frequently studied because they are very sensitive to hemodynamic perturbation and later transform into the interventricular septum and semilunar valves, which are often involved in congenital heart defects [3, 10, 38].

Endothelial mesenchymal transition (EMT) [196] is considered a hallmark process in the development of the endocardial cushions. EMT characterizes a complex process in endocardial cushion formation, where a portion of endocardial cells delaminate from the endocardium monolayer, invade the cardiac jelly, and then proliferate and differentiate into mesenchymal cells, leaving the disassembled endocardium to rearrange and form a new intact flattened layer [197, 198]. EMT in the outflow tract cushions ultimately leads to formation of the semilunar valves, and is regulated by complicated signaling pathways that include TGFβ, Notch, and Erbb3 [199, 200]. These EMT pathways depend on many extracellular matrix components, soluble growth factors, and various transcription factors that promote a mesenchymal phenotype by stimulating the disassembly of cell junction complexes and re-arrangement of actin cytoskeleton during EMT activation, as well as re-organization of extracellular matrix during cell invasion. While EMT is still not completely understood, *in vitro* culture systems, *ex vivo* cushion explant systems, and knockout mouse models have defined key factors governing EMT in the outflow tract and atrioventricular cushions [201]. Both sets of endocardial cushions follow similar developmental mechanisms, however outflow tract cushions lag behind in development and have an additional cellular contribution from neural crest cells in the cardiac jelly by HH21 [202, 203]. Cushion explant studies have revealed an important role of soluble growth factors within the extracellular matrix [204] and a unique cushion response to critical myocardial-derived differentiation signals [205], while mouse models have elucidated dozens of EMT signaling gene disruptions that alter valve phenotypes [206, 207]. In addition, several studies also indicated that mechanotransduction signaling is key to normal cushion development, where increased shear stress activates TGFβ-dependent Krüppel like factor 2 **(**KLF2) signaling in endothelial cells *in vitro* [208], contractile mechanical forces modulate EMT *ex vivo* [209], and misregulation of signaling pathways [210] and hemodynamic surgical interventions [195] lead to similar cardiac deficits. However, the modulating effects of blood flow on EMT have not been fully elucidated.

This study investigated the effects of increased hemodynamic load (blood pressure and wall shear stress) on outflow tract cushion EMT in early development. Hemodynamic forces exerted by blood flow on heart tissue walls trigger mechanotransduction mechanisms that lead to physical, chemical, and gene regulatory responses in cardiac tissue [147]. To alter blood flow through the heart, this study used a well-established hemodynamic intervention called outflow tract banding in the chicken embryo at Hamburger and Hamilton (HH) stage 18 (~3 days of incubation) [37]. Outflow tract banding increases peak ventricular pressure [51, 52] and blood flow velocities [62, 158] in the outflow cushion region. These hemodynamic changes are dependent on the degree of band tightness [158] and result in a wide spectrum of heart defects in the chicken embryo [7-10, 51]. We used chicken embryos as a model of human heart development (which is highly conserved among vertebrate species) to allow for ease of accessibility in the egg for surgical manipulation and *in vivo* imaging [52, 62, 63]. Banding was performed at the onset of EMT [197] in the outflow tract cushions in order to characterize changes in normal cushion development induced by increased hemodynamic load *in vivo*. Changes in shape and organization of cellular and extracellular matrix components of outflow tract tissue after banding were characterized with immunohistochemistry, confocal microscopy, 3D electron microscopy, and combined with proteomics analysis to characterize the ways in which normal tissue remodeling is detrimentally modified by increased hemodynamic load. Specifically, endocardial and cardiac jelly cell density and organization were quantified with DAPI and phalloidin staining, VE-cadherin endocardial junctions and extracellular matrix periostin organization were analyzed with immunolabeling, 3D endocardial cell arrangements were quantified with electron microscopy, and global changes in relative protein abundances were measured by mass spectrometry.

5.3 Methods

5.3.1 Hemodynamic intervention

Fertilized White Leghorn chicken eggs were incubated blunt end up at 38°C and 80% humidity until stage HH18 (~3 days) [37]. Embryo hemodynamics were altered with a 10-0 nylon suture passed under the outflow tract and tied in a knot around the mid-section of the outflow tract to constrict the cross-sectional area. A control group of embryos served as a surgical sham where the suture was passed under the outflow tract but not tightened. Following interventions, eggs were sealed with saran wrap and incubated until further evaluation.

5.3.2 Band tightness measurement with OCT

A custom-made optical coherence tomography (OCT) system was used to measure chick embryo band tightness *in vivo* as previously described [52, 62, 64, 157]. Briefly, the system has a spectral domain configuration with a superluminescent diode centered at 1325 nm from Thorlabs Inc. (Newton, NJ, USA) and a 1024 pixel, 92 kHz maximal line-scan rate infrared InGaAs line-scan camera from Goodrich Inc. (Charlotte, NC, USA). It acquired 512 x 512 pixel, 2D B-mode line-scan tomographic images at 140 frames per second with <10 µm resolution. Embryo temperature during acquisition was maintained at a normal physiological range (~38°C) with a thermocouple-controlled heating system. Each banded embryo was imaged immediately before and 2 hours after manipulation with OCT to acquire 200 tomographic frames (~3-4 cardiac cycles) of the longitudinal outflow tract in order to measure the change in outflow tract diameter and calculate the degree of band tightness with Equation 5.1,

$$\text{Band tightness} = 1\text{-}D_a/D_b \quad , \tag{5.1}$$

where D_a is the maximum external diameter of the outflow tract at the band site after banding, and D_b is the maximum external diameter of the outflow tract at the approximate band site location before banding. The measured band tightness of each banded embryo was used to define the hemodynamic environment, based on our previous characterization of the relationship between the degree of outflow tract band tightness and the specific blood pressure and velocity conditions induced [52, 158]. Band tightness in this study ranged from 0-60% constriction. After OCT imaging, the eggs were re-sealed with saran wrap and placed back in the incubator.

5.3.3 Confocal microscopy

Immunohistochemistry and confocal microscopy were performed to characterize cushion remodeling after banding flow conditions. Whole embryos were removed from the egg at HH24 (~24 hours after surgical manipulation at HH18) and fixed overnight in 4% paraformaldehyde at 4 °C and dehydrated in methanol. Samples were then transferred into methanol/DMSO/H_2O_2 to block endogenous peroxidase activity, rehydrated, blocked for 45 minutes with PBS +10% TritonX + 2% milk +4% goat sera, and treated with conjugated antibody (Alexa Fluor® 555 Antibody Labeling Kit, Life Technologies™) overnight at 4 °C. Immunohistochemistry was performed with 1:100 rabbit anti-human VE-Cadherin (abcam®, ab33168) to label endothelial cell-cell adhesions [196], and separately with 1:100 rabbit anti-mouse periostin (Aviva Systems Biology, OAPC00052) to label periostin fibers, which serve as a critical TGFβ signal transduction regulator and an EMT-stimulating scaffold for cell attachment and migration through the cardiac jelly [211, 212]. Separate embryos were stained to label F-actin with 66 nM Alexa Fluor® 568 Phalloidin (Molecular Probes™, A12380) in order to analyze cell organization within the outflow tract cushions. Normal (without intervention) embryo subsets were also stained with phalloidin and periostin between the stages of HH15 and HH25 in the outflow tract and the atrioventricular cushions to track F-actin and periostin remodeling changes during normal EMT progression. All samples were then extensively washed and co-stained with 10 nM DAPI (Life Technologies™, D1306) for 12 hours at 4 °C, before methanol dehydration and treatment with a clearing agent (1:2 benzyl alcohol: benzyl benzoate) prior to imaging. Confocal microscopy was performed with a Zeiss LSM 780 confocal laser scanning microscope (Carl Zeiss), and images were collected in a z-stack throughout the outflow cushions, spaced 10 μm apart.

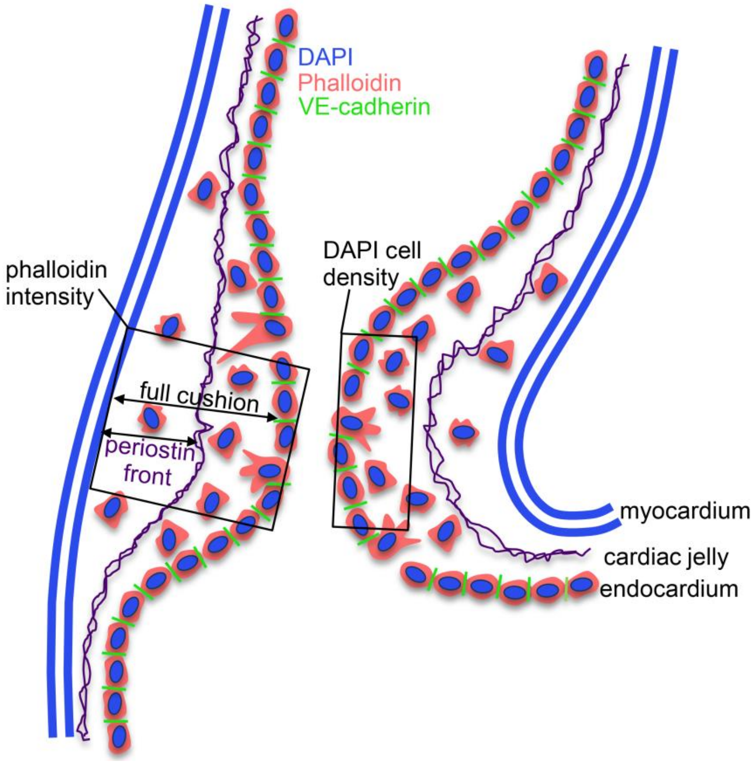

Figure 5-1. Schematic of outflow tract cushion analysis. The cushions are composed of an outer myocardium layer, a middle cardiac jelly layer, and an inner endocardium monolayer. VE-cadherin junctions connect endocardial cells and are lost when cells delaminate from the endocardium and invade the cardiac jelly region. Cushion cell density is measured using DAPI staining from an area that extends 10 microns into the cushion from the lumen edge, and cell organization is quantified using phalloidin staining from an area that extends across the whole width of the cushion from the lumen edge. Additionally, we measured phalloidin intensity from an area that only includes 25% of the cushion width from the lumen edge. Periostin fibers run through the cardiac jelly, where the fibers concentrate at a front that extends from the myocardium.

Fluorescent label patterns within the outflow tract cushions were quantified from confocal images using ImageJ (NIH), and characterized based on the degree of band constriction. Figure 5-1 shows a schematic of the outflow tract cushion analysis. F-actin was quantified by phalloidin fluorescence intensities across the center of the outflow tract cushions, from an area that extends across the whole width of the cushion from the lumen edge and additionally from an area that only includes 25% of the cushion width from the lumen edge. DAPI fluorescence signal was used to count cells and calculate cell density from an area 10 μm into the cushions from the lumen edge and cell count per endocardium length along the endocardium edge in each embryo. Average values from three confocal slices and both cushions are reported. Cell junctions labeled with VE-cadherin antibody were counted along the endocardium edge to calculate the number of junctions per endocardium length in each embryo. Periostin localization was quantified by measuring the distance between the myocardium edge and the periostin concentration front in the cardiac jelly and calculating the percentage of the cushion width in which the periostin front extended from the myocardium. VE-cadherin and periostin quantifications were measured from the largest, centered section of the outflow tract cushions, and averaged over the inner and outer cushions. Figure 5-2 shows example confocal images with quantification features marked for each measure.

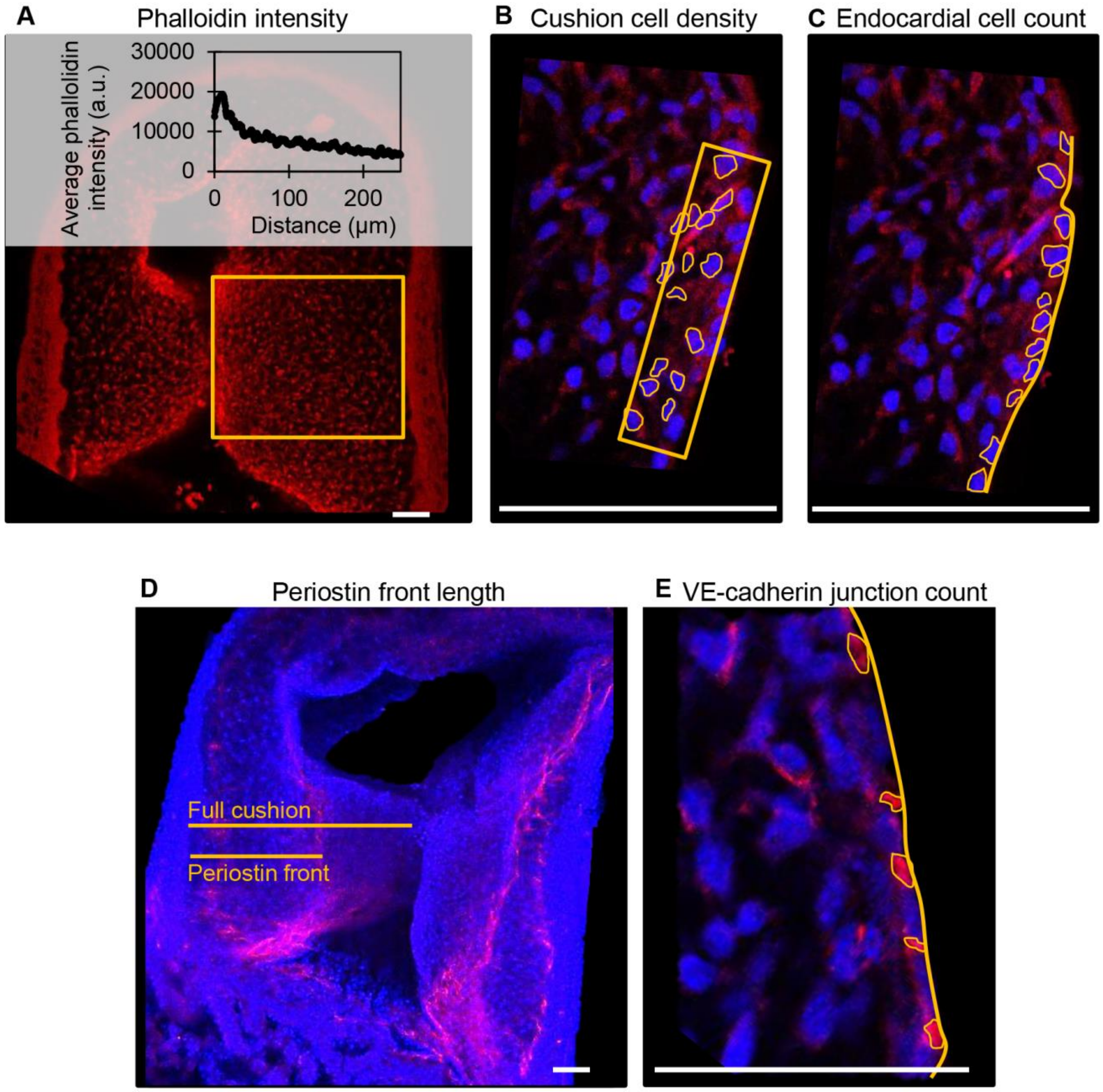

Figure 5-2. Example confocal fluorescent image quantifications from control embryos. (**A**) Phalloidin (red) stain fluorescence intensities from a full cushion, where the average fluorescent intensity at each distance position across the cushion is plotted. (**B**) Cushion cell density measured from the number of outlined DAPI-stained nuclei (blue) within an area 10 μm into the cushion from the lumen edge. (**C**) Cell count per endocardium length measured from the number of outlined DAPI-stained nuclei (blue) along a measured length of endocardium. (**D**) Periostin (red) front length measured as a percentage of the length of the full cushion. (**E**). VE-cadherin (red) junction per endocardium length measured from the number of outlined junctions along a measured length of endocardium. Scale bar = 50 microns.

5.3.4 Electron microscopy and quantification

Embryos with band tightness between 30-45% constriction were collected at HH24 (~24 hours after surgical manipulation at HH18) and processed for transmission electron microscopy (TEM) and focused ion beam scanning electron microscopy (FIB-SEM). The 30-45% band tightness range corresponds to a relatively constant and large increase in peak velocity and wall shear rate [158]. TEM and FIB-SEM imaging were performed on a FEI Tecnai 12 Spirit system interfaced to an Eagle™ 2K CCD multiscan camera and a FEI Helios 660 NanoLab™ DualBeam™, respectively. TEM images were acquired as 2048 × 2048 pixel, 16-bit gray scale files using the FEI's TEM Imaging & Analysis (TIA). Whole embryos were removed from the egg and immediately immersed in fixative (2.5% paraformaldehyde + 2.5% glutaraldehyde) to maximally preserve and contract the tissue [213, 214]. A portion of the outflow tract containing the cushions upstream of the banding location was then dissected from the embryo. The fixed tissue was stained and processed as previously described [214], and oriented longitudinally in the resin block face to contain a cross-section of the outflow tract and easily locate the region of interest for imaging. 100 nm sections were cut from the block face and imaged with the Tecnai™ TEM system to confirm adequate tissue contrast and fixation and identify areas of interest. The samples were then processed for Helios 660 NanoLab™ DualBeam™ FIB-SEM imaging to acquire serial (3D), high-resolution images, as previously described [214]. The FIB-SEM system alternated between imaging the block face with a scanning electron beam and milling away 10 nm thick sections with a focused ion beam, in order to collect a high-resolution 3D image volume. A maximum of 1000 slices through the endocardium were acquired, resulting in nearly the entire endocardium thickness with a region of interest width of 20 μm. Amira software was used to align the image stacks and manually segment endocardial cells in order to reconstruct and quantify the 3D cell shape and orientation.

3D endocardial cell shape and organization were quantified using a surface area-to-volume ratio, shape factor, and elongation factor for each segmented cell. Individual cells from three control and three banded samples were combined for the segmentation analysis ($n_{control}$=14, n_{banded}=26). The surface area-to-volume ratio serves as a measure of the degree of compactness and projections of each cell, and was calculated with Equation 5.2,

$$\text{surface area-to-volume ratio} = \frac{SA}{V}, \tag{5.2}$$

where *SA* is the surface area of the cell and *V* is total volume of the segmented portion of each individual cell. The shape factor is a measure of the degree of sphericity for each cell and was calculated with Equation 5.3,

$$\text{shape factor} = \frac{SA^3}{36\pi V^2}, \tag{5.3}$$

where a perfect sphere has a shape factor of 1. Only cells with a segmented cell volume greater than 100 μm^3 ($n_{control}$=6, n_{banded}=19) were included in the surface area-to-volume ratio and the shape factor analysis to avoid overly truncated segmented volumes when only small portions of cells were located within the image volume. Additionally, segmented endocardial cell volumes were quantified by an elongation factor that defines the degree of stretch of each cell using Equation 5.4,

$$\text{elongation factor} = {\lambda_{medium}}/{\lambda_{largest}}, \tag{5.4}$$

which is a ratio of the medium to the largest eigenvalue (λ) of the covariance matrix. A covariance matrix defines each 3D cell in space, and consists of three orthogonal eigenvectors that point in the direction that is stretched by the transformation. The eigenvalue is the factor by which the vector is stretched. Stretched objects have an elongation factor closer to zero when $\lambda_{largest}$ is significantly larger than λ_{medium}. Only cells that were centered in the image volume ($n_{control}$=10, n_{banded}=22) were included in the elongation factor analysis.

5.3.5 Mass spectrometry

After surgical manipulations at HH18, outflow tracts were dissected from the embryo at HH24 and rinsed in ultrapure water before pooling 8 outflow tracts for each sample. There were a total of 5 banded embryo samples (30-45% band tightness) and 5 sham control samples included in these experiments. Samples were suspended in 20 μl of 50 mM ammonium bicarbonate, 0.2% ProteaseMax™ detergent (ProMega, Madison, WI), shaken for 10 min, 80 μl of 50 mM ammonium bicarbonate added, and samples probe sonicated at a setting of 5 watts for 5 sec with 3 repeats on ice using a Sonic Dismembrator (Fisher Scientific). The protein content of each lysate was then determined using a BCA assay (Thermo Scientific) and BSA standard, 40 μg of protein removed, and the final volume of each sample set to 80.3 μl by addition of 50 mM ammonium bicarbonate, 0.04% ProteaseMax™ solution. Samples were then reduced by addition of 1 μl of 0.5M dithiothreitol and incubation at 56°C for 20 min, followed by alkylation by addition of 2.7 μl of 0.55 M iodoacetamide and incubation at room temperature for 15 min. Samples were then trypsinized by addition of 16 μl of 0.1 μg/ul sequencing grade modified trypsin (ProMega) and incubation for 4 hours at 37°C. Ten μl of 10% trifluoroacetic acid was then added, samples centrifuged at 16,000 x g for 10 min, and the supernatant solid phase extracted using MicroSpin™ C18 columns (The Nest Group, Southboro, MA).

Twenty µg portions of solid phase extracted digests were then dried by vacuum centrifugation and dissolved in 25 µl of 100 mM triethyl ammonium bicarbonate buffer. Two hundred µg of 10-plex tandem mass tagging (TMT) reagent (Thermo Scientific) freshly dissolved in 12.5 µl of anhydrous acetonitrile (ACN) was then added to each sample and incubated at room temperature for 1 hour. A short single LC-MS analysis was then performed to check for complete labeling and to determine the relative summed reporter ion intensities of each sample. This was accomplished by pooling 2 µl of each reaction mixture into 2 µl of 5% hydroxylamine, incubation at room temperature for 15 min, drying by vacuum centrifugation, dissolving in 5% formic acid, injection of 2 µg of pooled peptide mixture, and a single 2 hour LC-MS run as described below. This normalization run allowed confirmation of > 95% TMT labeling and generated preliminary summed reporter ion intensities for each TMT channel. Each of the original samples then had 2 µl of 5% hydroxylamine added and the 10 samples were pooled by adjusting each volume so that each would yield approximately equal summed reporter ion intensities when the final pooled mixture was analyzed by two-dimensional LC-MS as described below.

To increase numbers of quantified proteins, TMT labeled peptides were separated by two dimensions of reverse phase chromatography performed at both high and low pH. A Dionex NCS-3500RS UltiMate RSLCnano UPLC pump was used for sample loading and 2nd dimension reverse phase separation at low pH, and a Dionex NCP-3200RS UltiMate RSLCnano UPLC system for dilution of 1st dimension reverse phase eluents.Twenty µl samples containing 50 µg of pooled TMT-labeled digest were injected for 10 min onto a

NanoEase 5 µm particle XBridge BEH130 C18 300 µm x 50 mm column (Waters, Bedford, MA) at 3 µl/min in a mobile phase containing 10 mM ammonium formate (pH 9). Peptides were then eluted by sequential injection of 20 µl of 14, 17, 20, 21, 22, 23, 24, 25, 26, 27, 28, 29, 30, 35, 40, 50 and 90% ACN in 10 mM ammonium formate (pH 9) at a 3 ul/min flow rate using an autosampler. Eluted peptides at were then diluted at a tee with mobile phase containing 0.1% formic acid at a 24 µl/min flow rate. Peptides were then delivered to an Acclaim PepMap 100 µm x 2 cm NanoViper C18, 5 µm particle trap on a switching valve. After 10 min of loading, the trap column was switched on-line to a PepMap RSLC C18, 2 µm, 75 µm x 25 cm EasySpray column (Thermo Scientific). Peptides were then separated at low pH in the 2nd dimension using a 7.5–30% ACN gradient in mobile phase containing 0.1% formic acid at a 300 nl/min flow rate. Each 2nd dimension LC run required 2 hours for separation and reequilibration, so the entire LC/MS method required 34 hours for completion. Tandem mass spectrometry data was collected using an Orbitrap Fusion Tribrid instrument configured with an EasySpray NanoSource (Thermo Scientific). Survey scans were performed in the Orbitrap mass analyzer, and data-dependent MS2 scans in the linear ion trap using collision-induced dissociation following isolation with the instrument’s quadrupole. Reporter ion detection was performed in the Orbitrap mass analyzer using MS3 scans following synchronous precursor isolation of the top 10 most intense ions in the linear ion trap, and higher-energy collisional dissociation in the ion-routing multipole.

5.3.6 TMT data analysis

RAW instrument files were processed using Proteome Discoverer version 1.4.1.14 (Thermo Scientific) with SEQUEST HT software and a Gallus gallus Ensembl database containing 16,187 sequences. Searches were configured with static modifications for the TMT reagents (+229.163 peptide N-terminus and K residues) and iodoacetamide

(+57.021 C residues), variable oxidation (+15.995 M residues), parent ion tolerance of +/- 1.25 Da, fragment ion tolerance of 1.0 Da, monoisotopic masses, and trypsin cleavage (max 2 missed cleavages). Searches used a reversed sequence decoy strategy to control peptide false discovery and identifications were validated using Percolator software. Only peptides with q-values $\le$ 0.05, having mass errors <20 ppm, and matching only one protein entry in the database were used. Search results and TMT reporter ion intensities were exported as text files and processed using in-house scripts. After excluding the highest and lowest reporter ion intensities, an average intensity >500 was required for the remaining reporter ions to exclude the analysis of peptides with insufficient signal intensity. Reporter ions intensities with zero intensity also had values of 150 added to prevent errors during subsequent data analysis. Reporter ion intensities for peptides assigned to each protein were then summed to create an abundance measurement for each protein across the 10 samples simultaneously analyzed.

5.3.7 Statistical analysis

To compare significant changes among outflow tract banded embryos compared to controls, confocal data was analyzed for the entire banded and control groups and separated based on the degree of band tightness. Linear regression analysis was used with cell density and periostin front length parameters to show band-tightness dependence. FIB-SEM samples and TMT samples were selected with a relatively tight range of band tightness (30-45%), and therefore differences between samples with varying band tightness were not analyzed. Statistical significance between banded and control groups during image analysis were determined with a two-sample Student's t-test, assuming significance with two-tail p-values of less than 0.05. Differential protein abundance was determined in the TMT experiment by comparing the summed peptide reporter ion intensities for each protein across samples (5 control, and 5 banded) using the R software (v 3.1.1) package edgeR, which performed data normalization, Benjamini-Hochberg multiple test correction, and calculation of false discovery rates during tests for differential abundance for each protein compared between banded and control samples.

5.4 Results

5.4.1 Cell infiltration occurs at different developmental times in outflow tract and atrioventricular cushions

F-actin staining with phalloidin at HH15, HH18, and HH24 in both the outflow and atrioventricular segments of control hearts displayed the progression of cell activation and invasion into the cushion cardiac jelly during EMT (Figure 5-3). At HH15, F-actin labeling extended from the endocardium into the cardiac jelly in atrioventricular cushions but not outflow tract cushions, demonstrating EMT initiation in the atrioventricular canal prior to the outflow tract. These F-actin strands are likely filopodia that extend for long distances into the cardiac jelly at the onset of EMT before invasion, as described by Kinsella and Fitzharris [215]. EMT had begun in the outflow tract by HH18 with a few strands of F-actin stain that extended from the center of the cushion endocardium, which coincided with a more disbursed configuration of F-actin staining along the entire length of the cushions in the atrioventricular canal. F-actin staining at HH24 showed an influx of cell material in outflow cushions, and a much denser layer of F-actin along the endocardium in atrioventricular cushions, indicating that EMT is more progressed in atrioventricular cushions compared to outflow tract cushions at HH24.

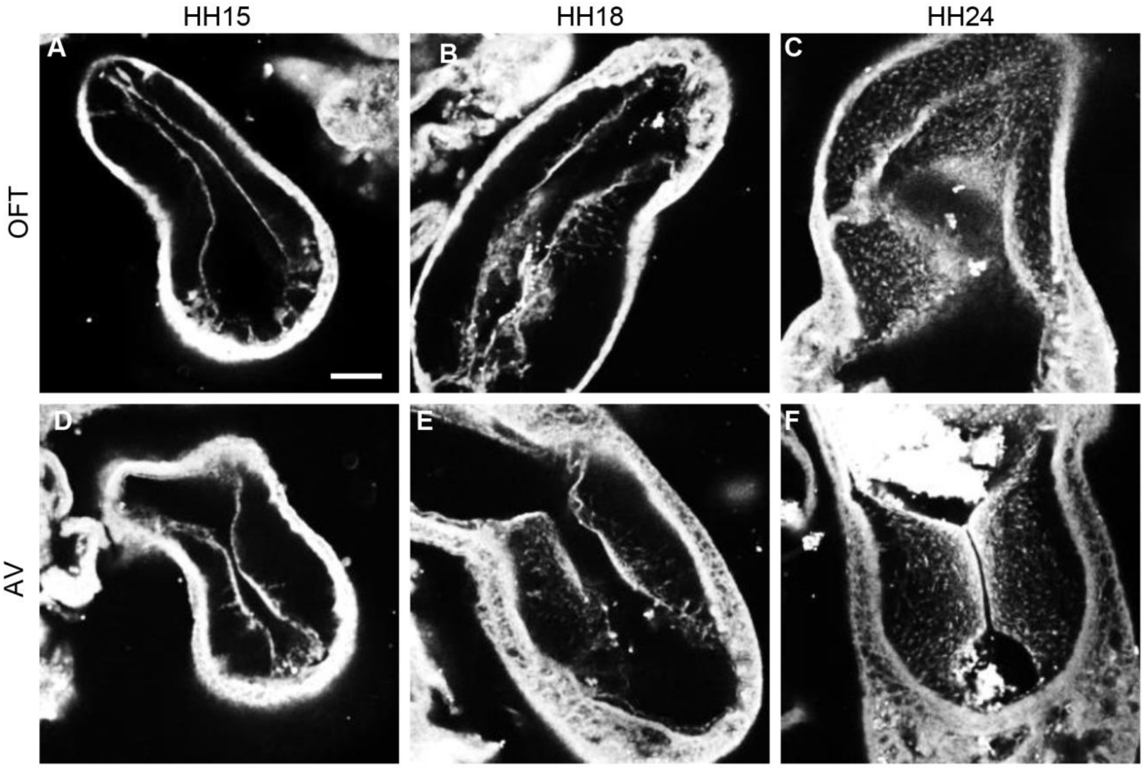

Figure 5-3. Phalloidin confocal fluorescent image analysis. Confocal fluorescent images at 20x from whole embryo hearts stained with phalloidin at HH15 (**A&D**), HH18 (**B&E**), and HH24 (**C&F**) at the outflow tract cushions (**A-C**) and the atrioventricular cushions (**D-F**). Scale bar = 100 microns. AV, atrioventricular canal; OFT, outflow tract.

5.4.2 Increased hemodynamic load induces changes in cardiac jelly remodeling

Confocal microscopy image analysis showed significantly more cells in outflow tract cushions of banded samples compared to controls at HH24. The largest increase in phalloidin fluorescence intensities was in the innermost 25% of the cushion adjacent to the endocardium (p-value<0.05, n=8) (Figure 5-4,A-C). Tightly banded samples displayed a dense region of high phalloidin fluorescence intensities bordering the endocardium, which resembled the more advanced EMT phenotype displayed in atrioventricular cushions of control embryos at HH24. DAPI staining and analysis determined that cell density in the outflow tract cushion region neighboring the endocardium (an area 10 μm into the cushions from the lumen edge) was significantly increased in banded embryos compared to controls (p-value<0.01, n=8) (Figure 5-4,D-

F). Further, this cell density increased with band constriction somewhat linearly with a linear regression R^2 value of 0.63, indicating that mechanisms that increase cell density after banding depend on the specific hemodynamic conditions.

Immunohistochemistry labeling for periostin showed a distinct fibrous periostin expression pattern which localized at the endocardium and around a subset of immediately adjacent mesenchymal cells at HH15, HH18, and HH21. In later stages at HH24 and HH25, the expression front within the outflow tract cushions ran parallel to the myocardium and endocardium layers near the middle of the outflow tract cushions (equidistant from the myocardium and endocardium) and along the cardiac jelly/myocardium interface (Supplemental Figure 5-7). While periostin was expressed near the middle of the outflow tract cushions in control samples, the expression front instead appeared closer to the endocardium in banded samples at HH24 (Figure 5-4,G-I). The percentage of the cushion width that the periostin front length extended from the myocardium was significantly higher in banded embryos compared to controls (p-value<0.001, n=8). The extension of the periostin front also tended to increase with band constriction, however with a low linear regression R^2 value of 0.46. DAPI, phalloidin, and perisotin quantifications did not significantly vary between outer and inner cushions (Supplemental Figure 5-8).

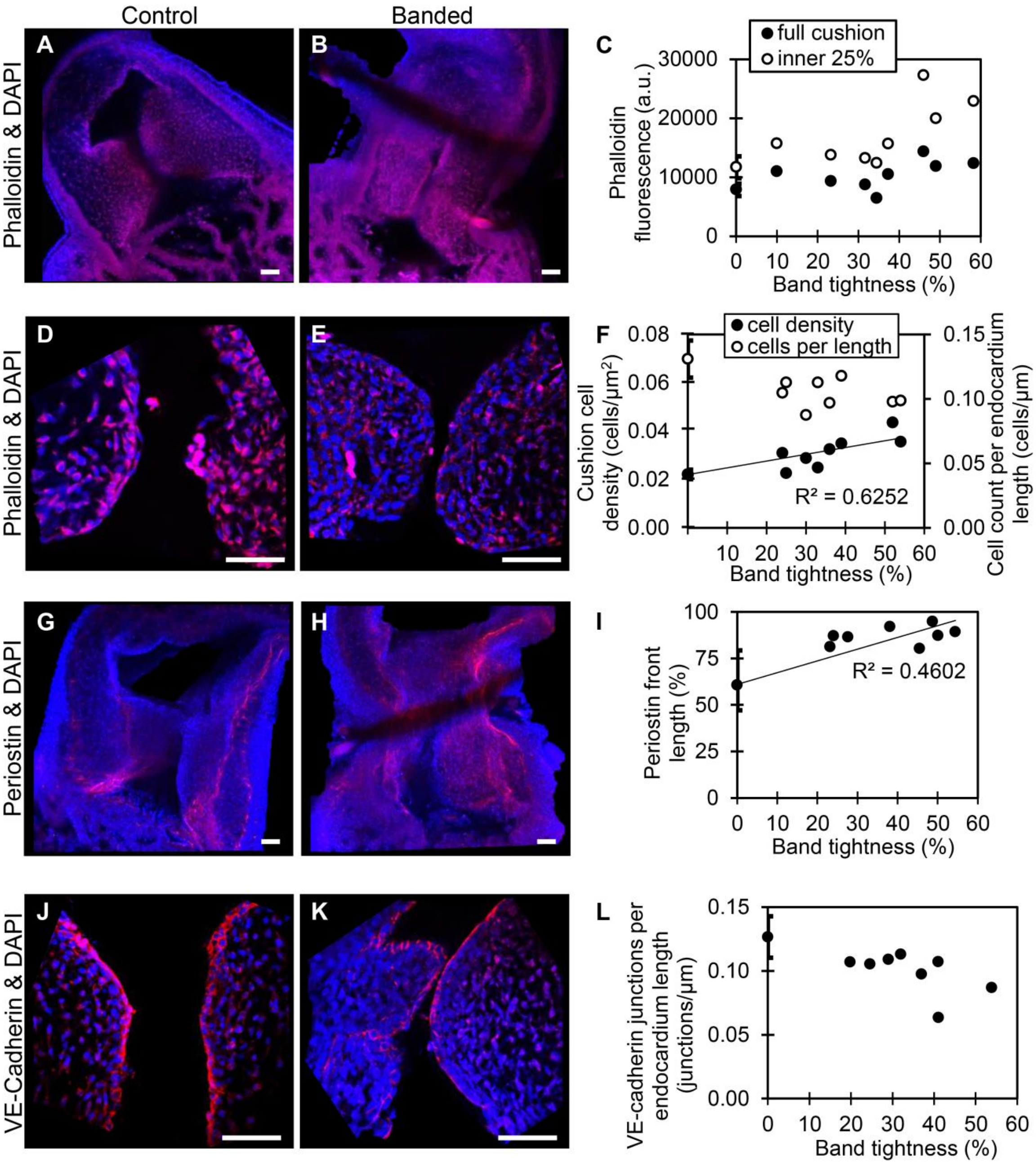

Figure 5-4. Confocal fluorescent image analysis with banding. Phalloidin (red) stain at 20x in a control (**A**) and banded outflow tract with 52% band tightness (**B**), with phallodin fluorescence intensities quantitated in (**C**). Phalloidin (red) stain at 63x in a control (**D**) and banded outflow tract with 52% band tightness (**E**), with cushion cell density and cell count per endocardium length quantitated from DAPI stain (**F**). Periostin (red) labeling at 20x in a control (**G**) and banded outflow tract with 49% band tightness (**H**), with periostin front length quantitated in (**I**). VE-cadherin (red) labeling at 63x in a control (**J**) and banded outflow tract with 41% band tightness (**K**), with endocardial cell junctions per endocardium length quantitated in (**L**). Each sample is also stained with DAPI (blue). Scale bar = 50 microns.

5.4.3 Increased hemodynamic load leads to altered endocardium arrangement

Confocal microscopy analysis determined that the increased hemodynamic load after banding not only influenced cardiac jelly remodeling but also endocardium organization. There was significantly fewer DAPI stained cells along the cushion endocardium in banded embryos compared to controls at HH24 ($p\text{-value}<0.001$, $n=8$) (Figure 5-4,D-F). Further, immunohistochemistry labeling for VE-Cadherin and confocal microscopy image analysis showed significantly fewer cell junctions along the cushion endocardium in banded embryos compared to controls ($p\text{-value}<0.01$, $n=8$) (Figure 5-4,J-L). Tightly banded hearts had the lowest number of cell junctions per endocardium length, however there was not a strong linear correlation between cell junctions per length and band tightness. DAPI and VE-Cadherin quantifications did not significantly vary between outer and inner cushions (Supplemental Figure 5-8).

TEM images displayed a disrupted outflow tract cushion endocardium upstream of the banding site in banded embryos compared to controls at HH24. Control embryo cushions had tightly arranged endocardium with mostly plump and round cells, while banded embryo endocardial cells were more loosely organized with projections that invaded the cardiac jelly ($n=8$) (Figure 5-5,A-B). FIB-SEM was then used to acquire serial, high-resolution images through the endocardium and create ~0.8 mm^3 isotropic image volumes ($n=3$). Endocardial cell reconstructions display dramatic cell filopodia projections and chaotic layer organization in banded tissue compared to controls (Figure 5-5,C-F). The translucent cell view of the lumen edge of the endocardium shows that control endocardial cells were tightly packed with minimal cell overlap, while the banded sample included irregular and stretched cells that overlay each other with many cell projections. The example endocardial segmentations that are oriented to view the cardiac jelly interface edge show that the control layer is mostly spherical and intact, while the banded sample interface is covered with projections that extend into the cardiac jelly. The surface area-to-volume ratio, shape factor, and elongation factor were quantified using Amira software for each 3D segmented cell volume. Box plots in Figure 5-5,G-I show that cells from banded samples have more projections, are less spherical, and are more elongated. The average surface area-to-volume ratio and shape factor were significantly increased in banded endocardial cells compared to controls by a factor of 1.5 and 4.1, respectively (p-values<0.01; $n_{control}$=6, n_{banded}=19). The elongation factor significantly decreased in banded endocardial cells compared to controls by a factor of 1.6 (p-value<0.01; $n_{control}$=10, n_{banded}=22). The standard deviation of the surface area-to-volume ratio, shape factor, and elongation factor among cells was increased in the banded group compared to control by a factor of 3.1, 14.5, and 1.7, respectively.

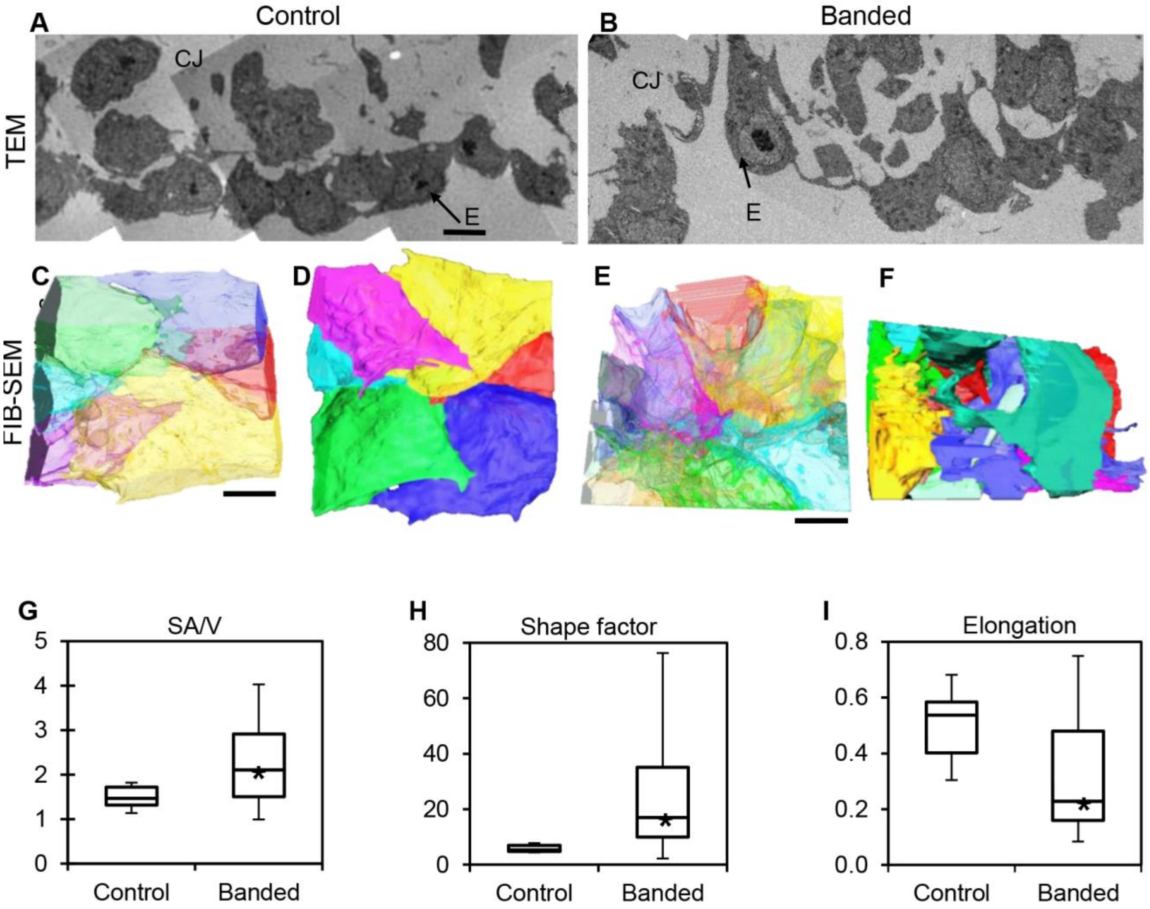

Figure 5-5. Electron microscopy analysis of endocardium remodeling. Stitched TEM images of the endocardium and adjacent cardiac jelly at 1700x (**A-B**), and corresponding 3D FIB-SEM reconstructions of endocardial cell segmentations from image stacks (**C-F**). Reconstructions display each cell in a different color and are orientated to view the endocardial-lumen edge with translucently colored cells (**C&E**) and the endocardial-cardiac jelly interface edge with opaquely colored cells (**D&F**) from an example control embryo (**A,C,D**) and an example banded embryo (**B,E,F**). Box plots showing differences in endocardial cell geometry, quantified from 3D segmentations of FIB-SEM images, with surface area-to-volume ratio, SA/V (**G**), shape factor (**H**), and elongation factor (**I**). Boxes mark the upper and lower quartiles and whiskers mark the maximum and minimum values for each parameter. Asterisks denotes statistically significant differences between experimental and control samples ($p<0.01$). CJ, cardiac jelly; E, endocardium. Scale bar = 5 μm.

5.4.4 Increased hemodynamic load triggers EMT-related proteomic response

TMT based mass spectrometry provided a proteome-wide assessment of changes in the relative abundance of specific proteins induced by increased hemodynamic load. Specifically, we examined changes in proteins known to be markers of EMT. A total of 5330 proteins were detected in the outflow tract samples, where the abundance of 606 proteins significantly differed between banded and control samples (p-value <0.1). Of those proteins that were significantly up or downregulated, 38 proteins were related to a form of EMT, and 21 were directly related to EMT in the endocardial cushions. All EMT-related proteins had at least 2 peptide-spectrum matches with reporter ion signal used in quantitation among our samples, with the exception of mucin 6 and myocyte enhancer factor-2 that only had a single peptide for quantification. These two proteins however also had relatively high overall reporter intensity of at least 11,100 in each sample. The main protein changes include extracellular matrix components, cell type markers, and other EMT regulators (Figure 5-6). Table 5-1 lists changes in proteins related to EMT in endocardial cushions and Table 5-2 lists changes in proteins linked to other forms of EMT, such as in tumorigenesis and gastrulation. Each table gives the protein fold changes between control and banded samples and lists their functions related to EMT. Most fold-changes in EMT-related protein abundances are relatively small (1.2-1.5 fold), which may reflect the relatively small cushion portion of the entire outflow tract sample that is undergoing EMT.

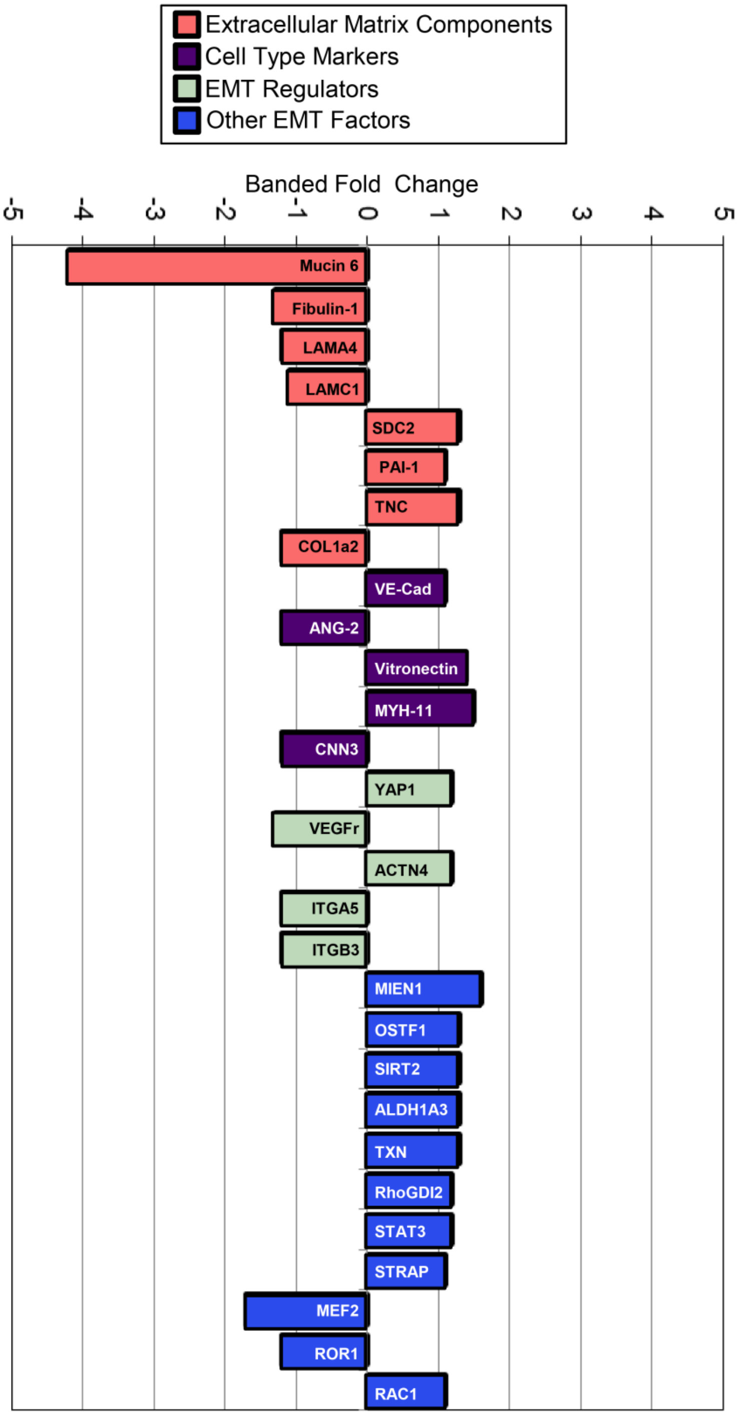

Figure 5-6. Fold changes in mass-spectrometry measured protein abundances in banded samples compared to controls that are associated with EMT. Extracellular matrix proteins, cell type markers, EMT regulators, and factors associated with other types of EMT are shown, with positive and negative fold changes representing protein upregulation and downregulation, respectively. Protein abbreviations are listed in Tables 5-1 and 5-2.

Table 5-1. EMT-cardiac cushion associated proteins

ECM Proteins		**Banded Fold Change**	**p-value**	**Function**
ECM Proteins	Mucin 6	- 4.2x	0.01	Glycoprotein indicative of glycosaminoglycans in the heart [216], where mucins are secreted by endothelial cells and play a role in cell differentiation. Mucin 6 specifically inhibits cell adhesion to the extracellular matrix and hinders cell invasion [217].
	Fibulin-1	- 1.3x	<0.01	Glycoprotein that suppresses EMT in the proximal outflow tract during valve morphogenesis, specifically by repressing TGFβ2 and Snail1 levels [218].
	Laminin α 4 (LAMA4)	-1.2x	0.02	Cushion basal lamina component that stabilizes the endothelium and acts as a barrier to migratory cells [219], and becomes intermittently distributed along the endocardium and myocardium after EMT onset [220].
	Laminin γ1 (LAMC1)	- 1.1x	0.07	
	Syndecan 2 (SDC2)	+1.3x	0.01	Heparin sulfate proteoglycan which can interact with and concentrate glycoproteins, collagens, and growth factors ligands found in extracellular matrix [221].
	Plasminogen activator 1 (PAI-1)	+1.1x	0.10	Enzyme that degrades basal lamina so that endocardial cells can invade the cardiac jelly, before other migration-inducing proteins fill the cushions [222].
	Tenascin C (TNC)	-1.3x*	0.01	Glycoprotein that stimulates the TGFβ pathway, and is closely associated with EMT in cushion tissue [223].
	Collagen 1, α2 (COL1a2)	-1.2x*	0.08	Type I collagen that has been associated with EMT activation [219].
Cell Type Markers	VE-Cadherin (VE-Cad)	+1.1x*	0.10	Endocardial junction marker [197].
	Angiopoietin 2 (ANG-2)	-1.2x	0.04	Endothelial marker; member of the VEGF family and largely specific for vascular endothelium[224].
	Vitronectin	+1.4x	<0.01	Mesenchymal marker that is activated by Snail [225].
	Myosin-11 (MYH-11)	+1.5x	0.04	Late myogenic differentiation marker. Myosin-11 is a smooth muscle myosin belonging to the myosin heavy chain family. A portion of mesenchymal transitioned cells further differentiate into smooth muscle cells [226].
	Calponin 3 (CNN3)	-1.2x*	0.04	Mesenchymal marker [227].
EMT Regulators	YAP1	+1.2x	0.06	Transcription factor that promotes TGFβ-induced upregulation of Snail, Twist1, and Slug during cardiac cushion development [228].
	Vascular endothelial growth factor receptor (VEGFr)	-1.3x	0.03	Receptor for VEGF ligand whose expression suppresses EMT during early valvulogenesis [229].
	α actinin 4 (ACTN4)	+1.2x	0.04	Microfilament protein associated with assembly and maintenance of the actin cytoskeleton in developing valves [230], that promotes EMT through Snail signaling in cervical cancer [231].
	Integrin α5 (ITGA5)	-1.2x	0.03	Integrins that mediate cell-matrix adhesion, where a change in the level of expression (an integrin switch) often reflects alterations in cell-matrix interactions [232].
	Integrin β3 (ITGB3)	-1.2x	0.06	

* Fold change does not follow the expected direction

Table 5-2. Proteins associated with other types of EMT (tumorigenesis, gastrulation)

Other Proteins	**Banded Fold Change**	**p-value**	**Associated Process**	**Function**
Migration and invasion enhancer 1 (MIEN1)	+1.6x	<0.01	tumorigenesis	Promotes cell migration by inducing filopodia formation at the leading edge of migrating cells, and is predominantly overexpressed in Her-2 and luminal B subtypes of breast tumors [233].
Osteoclast stimulating factor 1 (OSTF1)	+1.3x	0.01	tumorigenesis	Transcription factor that promotes migration with modulation of EMT in human embryonic kidney cells [234].
Sirtuin 2 (SIRT2)	+1.3x	<0.01	tumorigenesis	Overexpression in hepatocellular carcinoma mediates EMT by protein kinase B/glycogen synthase kinase-3β/β-catenin signaling [235].
Aldehyde dehydrogenase 1 family, member A3 (ALDH1A3)	+1.3x	0.01	tumorigenesis	Mesenchymal marker in gliomas, where ALDH1A3 overexpression was significantly associated with tumor cell invasion [236].
Thioredoxin (TXN)	+1.3x	0.09	tumorigenesis	Mediates TGF-β-induced EMT in salivary adenoid cystic carcinoma (SACC), where higher expressions of TXN were present in human metastatic SACC compared to non-metastatic SACC tissues [237].
Rho GDP-dissociation inhibitor 2 (RhoGDI2)	+1.2x	0.05	tumorigenesis	Overexpression stimulates EMT through the expression of Snail in gastric cancer cells, but not other family members such as Slug or Twist [238].
Signal transducer and activator Of transcription 3 (STAT3)	+1.2x	0.03	tumorigenesis	Induces TWIST1 to drive EMT and further activates AKT contributing to acquisition and metastatic maintenance [239].
Serine/Threonine Kinase Receptor Associated Protein (STRAP)	+1.1x	0.06	tumorigenesis	Promotes TGFβ-dependent EMT and metastasis of neoplastic cancer cells [240].
Myocyte enhancer factor-2 (MEF2)	-1.7x*	0.01	tumorigenesis	Promotes EMT and invasiveness of hepatocellular carcinoma through TGFβ1 autoregulation circuitry [241].
Receptor Tyrosine Kinase-Like Orphan Receptor 1 (ROR1)	-1.2x*	0.03	tumorigenesis	Reduces expression of E-cadherin, but enhanced the expression of SNAIL-1/2 and vimentin [242].
Ras-related C3 botulinum toxin substrate 1(RAC1)	+1.1x*	0.06	gastrulation	Small GTPase that induces EMT by regulating cell migration through control of actin polymerization [243].

5.5 Discussion

Precise spatial and temporal regulation of EMT is required for proper cardiac morphogenesis as alterations in cushion development lead to significant impairment of cardiac formation and function. Here we used outflow tract banding to alter blood flow at the onset of EMT in the outflow tract in order to investigate the effects of increased hemodynamic load on the mesenchymal transition in the outflow tract cushions. Variations in normal EMT in the outflow tract cushions are complex to unravel *in vivo*, because of multifaceted regulation of EMT through several signaling cascades, overlapping stages of EMT activation and invasion, and the simultaneous invasion of neural crest cells into the outflow tract. Despite these challenges, we analyzed changes in cushion cell density and EMT marker organization with confocal microscopy, characterized 3D structural variations of the endocardium assembly with FIB-SEM, and quantitated alterations in EMT-related protein abundance with mass-spectrometry after outflow tract banding. These results taken together indicate that increased hemodynamic load enhances the EMT phenotype, which is characterized by endocardial loss of cell-cell junctions, acquisition of invasive and migratory cellular properties, and mesenchymal population of the cardiac jelly.

We employed the chicken embryo model to investigate the effects of dynamic increases in hemodynamic load produced by outflow tract banding *in vivo*, which reflect insights gained from previous in vitro experiments. Egorova et al showed that increased shear stress near the outflow tract cushions activates TGFβ signaling, which is required for shear stress-induced KLF2 expression in endothelial cells [208]. Accordingly, the elevated shear stress in our model is likely also utilizing KLF2 and TGFβ cross-talk to increase EMT. Sewell-Loftin et al demonstrated that mechanical forces affect EMT regulation in a hydrogel explant model with varied gel deformation and strain, and determined that weaker myocardial contractions reduced atrioventricular cushion EMT [209]. Our previous work suggests that a compensatory pumping mechanism maintains normal stroke volume under highly elevated pressure conditions [52, 158], which may involve stronger myocardial contractions in the ventricle that may be associated with the promotion of EMT.

Confocal image analysis determined that banding induced an increase in cardiac jelly cell density and F-actin near the endocardium combined with fewer cells along the endocardial lining in the outflow tract cushions. In addition, immunohistochemistry labeling of VE-cadherin, an endothelial cell adheren junction molecule that is lost when endocardial cells delaminate and undergo EMT [196], showed interrupted expression along the endocardium of the outflow tract cushions in banded samples. This configuration supports an active stage of EMT when the endocardium lacks integrity of intracellular junctions and tightly connected cells, and a greater portion of endocardial cells have left the endocardium and invaded the cardiac jelly. This study also found altered expression of periostin, a TGFβ superfamily-responsive matricellular protein, that is expressed in a temporospatial pattern during cardiac development. Periostin mediates extracellular matrix remodeling, and provides a fibrous framework for the attachment and spreading of cells undergoing EMT [199, 211, 244, 245]. Periostin fibers extend through the cardiac cushions with the strongest expression concentrated at the endocardial lining of the outflow tract cushions during active stages of EMT at HH15, HH18, and HH21, and moves towards the middle of the outflow tract cushions in later developmental stages at HH24 and HH25. Our data suggests that the hemodynamics induced by outflow tract banding alter periostin expression patterns so that the fibers are organized closer to the endocardium in banded samples compared to controls at HH24. This change indicates that increased hemodynamic load induces an active stage of EMT in the outflow tract at HH24.

3D FIB-SEM endocardial cell segmentations of banded samples correspond with previous electron microscopy characterizations of the morphologic changes of cells undergoing EMT, while controls display a more immature endocardium configuration [9, 198, 246]. Structural descriptions of EMT detail how a portion of endocardial cells in the cardiac cushions lose their orientation as individual cells change shape, flatten, and extend filopodial and lamellipodial projections over neighboring endocardial cells and into the cardiac jelly. As cells migrate into the cardiac jelly, the remaining endocardial cells reorganize and establish new contacts to create an intact layer. These hallmarks of EMT are displayed in TEM and FIB-SEM images of our banded samples, where overall quantified changes in the average cell surface area-to-volume ratio, shape factor, and elongation from FIB-SEM data sets suggest that banding increases EMT in the outflow tract cushions. Large standard deviations associated with the quantification measures of cells from banded embryos compared to controls reflect that only a portion of endocardial cells undergo EMT and vary in shape and organization. Even though the entire volume of each cell was rarely acquired within the FIB-SEM image volume, the small standard deviations of the control cells compared to the banded show that the quantification measures detected valid differences in cell shape and elucidate the ways in which the endocardial cells change after banding.

We used mass-spectrometry to detect global changes in protein abundances after banding to reflect the overall dynamic regulation balance between transcription, localization, modification and programmed destruction of protein during EMT. The proteomic analysis corroborates the confocal and FIB-SEM evaluations in this chapter, further indicating that the hemodynamics induced by banding enhances EMT in the outflow tract. The TMT results do not show significant changes in TGFβ ligand between control and banded samples. However, the EMT-related proteins that are up or downregulated in banded samples include extracellular matrix components, cell type markers, and EMT transcription factors, indicating that the increased hemodynamic load interferes with EMT signaling pathways downstream of growth factor binding. The compositional extracellular matrix reorganization in banded samples promotes EMT cell migration and TGFβ regulation, with an overall decrease in early matrix components that inhibit EMT and stabilize the endocardium (mucin, laminin, and fibulin). This remodeling may encourage cell migration along EMT-stimulating matrix components, such as hyaluronic acid and versican, and allow for more efficient secretion and binding of growth factors released from the myocardium. Overall, significant changes in cell type marker protein counts in banded samples compared to controls also correlate with more progressed EMT, with decreased endothelial markers (angiopoietin 2) and increased mesenchymal markers (vitronectin, myosin-11). Small changes and discrepancies in endothelial markers, such as a slight increase in VE-Cadherin protein in banded samples (+1.1x, p-value=0.1) may reflect the relatively small portion of endocardial cells in the whole outflow tract samples. The small increase in VE-cadherin protein abundance may also reflect the reformation of cell-cell adhesion junctions between the majority of cells that remain in the endocardial layer after EMT. The other EMT regulator proteins that are altered in banded samples (YAP1, VEGFr, α actinin 4, integrins) promote EMT through TGFβ and VEGF pathways. Even though the protein variations listed in Table 5-2 have only been implicated in other types of EMT, such as in tumorigenesis and gastrulation, these changes are likely associated with cardiac cushion EMT in the banded samples since major elements of EMT regulation are reiterated among various embryonic development events and adult pathologies. The majority of these protein changes linked with other types of EMT promote EMT through TGFβ and β-catenin pathways. While there were no significant changes in TGFβ ligand protein in the TMT analysis, these significant changes indicate that increased hemodynamic load alters the downstream EMT proteins regulated by this signaling pathway.

Recently, Menon et al created 3D hematoxylin and eosin image reconstructions of the outflow tract after banding the ventricle/outflow tract junction at HH16-17, and measured decreased cushion volume with fewer cells in the cardiac jelly after banding (n=3) [247]. There are a few key differences between this report and the current study that may explain the varied cushion remodeling outcomes. First, Menon et al banded the outflow tract *ex ovo* at HH16-17 instead of at HH18. Second and likely most importantly, their results reflect the effects of altered hemodynamics downstream of the outflow tract/ventricle junction band site, while our study investigated cushion remodeling upstream of the mid-section outflow tract band site. This is due to different placement of the band in each study. The hemodynamic variations due to band placement may account for the differences in the number of cells in the outflow tract cushions.

The imaging and proteomic data taken together indicate the hemodynamic forces induced by banding interfere with normal developmental cushion formation by increasing EMT in the outflow tract cushions. While our analysis did not discriminate between mesenchymal cells arising from EMT and those derived from the neural crest or proliferation, increased cell density in the cardiac jelly was accompanied by a loosely packed endocardium in phalloidin and DAPI stained confocal images, VE-cadherin junction disruption in immunohistochemically labeled confocal images, elongated and less-spherical endocardial cells with more projections in FIB-SEM image volumes, and periostin expression closer to the endocardium in immunohistochemically labeled confocal images. In addition, our proteomic analysis indicated a reorganization of the extracellular matrix and increased TGFβ-related signaling. Heart development is a finely regulated process with several remodeling mechanisms acting in parallel during the looping heart stages. This study indicates that EMT is one of the initial processes affected by increased hemodynamic load that triggers a detrimental cascade of events that eventually leads to cardiac defects.

5.6 Acknowledgements

Electron microscopy was performed at the Multi-scale Microscopy Core (MMC) with technical support from the OHSU-FEI Living Lab and the OHSU Center for Spatial Systems Biomedicine. Confocal fluorescent microscopy was performed at the OHSU Advanced Light Microscopy Core. Proteomic mass-spectrometry experiments were performed at the OHSU Proteomic Shared Resource with the assistance of John Klimek, Ashok Ready, and Phillip Wilmarth.

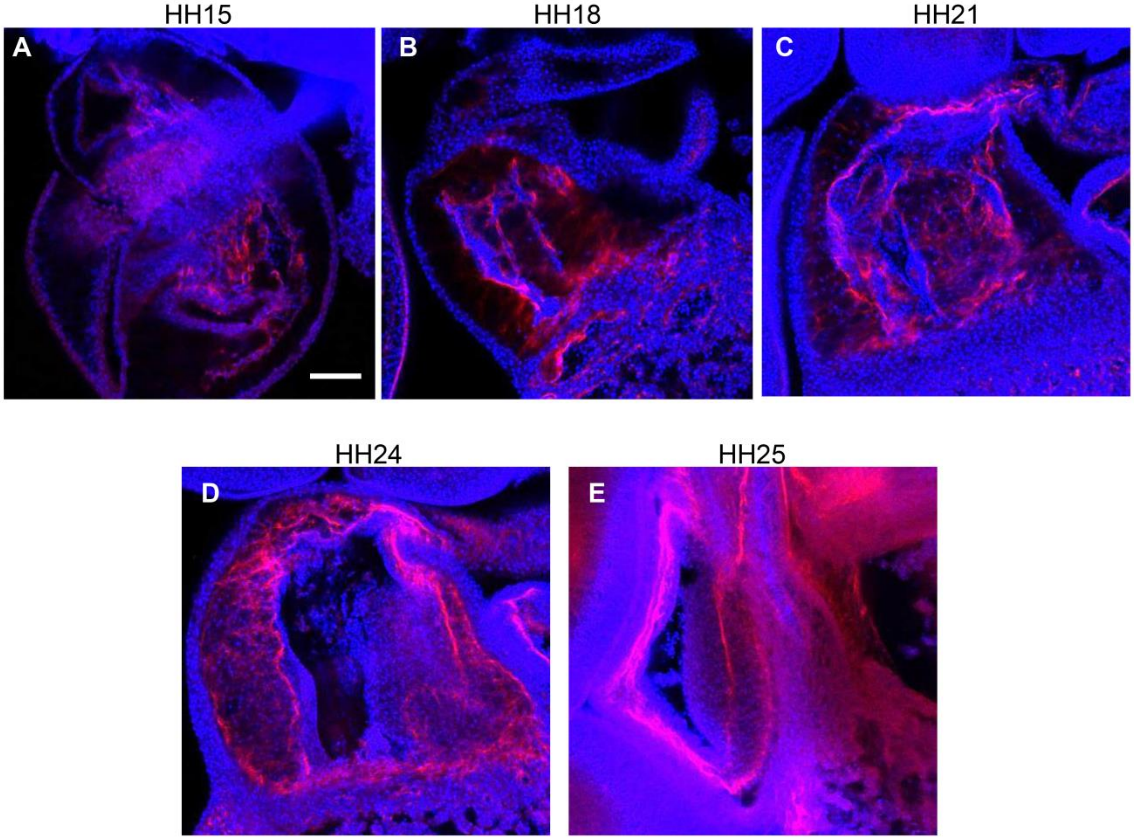

Supplemental Figure 5-7. Normal periostin expression in outflow tract cushions. Confocal fluorescent images at 20x from whole embryo hearts labeled with periostin (red) and DAPI (blue) at progressing developmental stages, (**A**) HH15, (**B**) HH18, (**C**) HH21, (**D**) HH24, and (**E**) HH25. Scale bar = 100 microns.

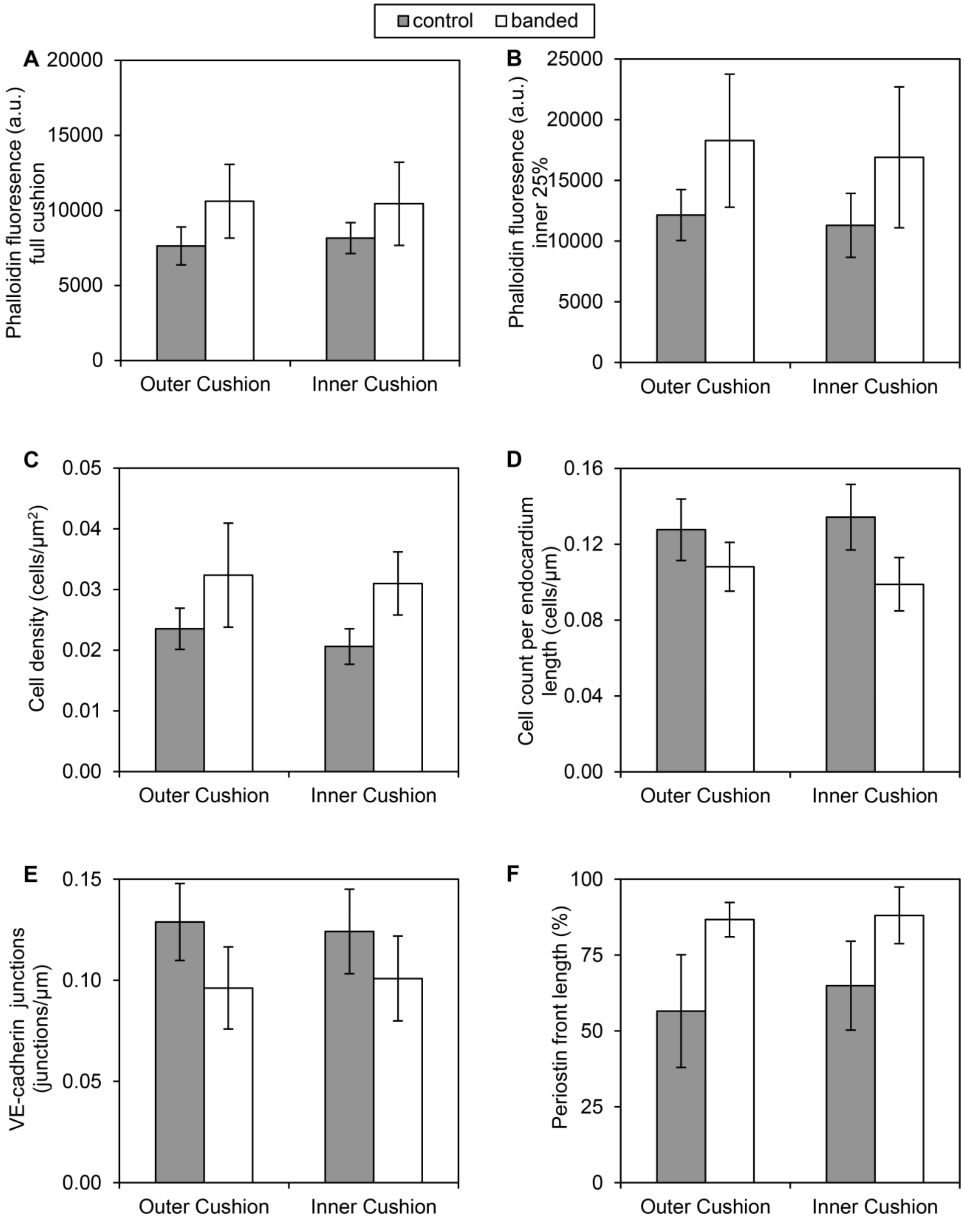

Supplemental Figure 5-8. Quantification comparisons between outer and inner cushions. Phalloidin stain quantifications (**A-B**), DAPI stain quantifications (**C-D**), VE-cadherin label quantification (**E**), and periostin label quantification (**F**). All control and banded comparisons between outer and inner cushions were not significantly different (p-value >0.05).

CHAPTER 6: Blood Flow Patterns Underlie Developmental Heart Defects

Madeline Midgett, Kent Thornburg, Sandra Rugonyi

6.1 Abstract

Although cardiac malformations at birth are typically associated with genetic anomalies, blood flow dynamics also play a crucial role in heart formation. However, the relationship between blood flow patterns in the early embryo and later cardiovascular malformation has not been determined. We used the chicken embryo model to quantify the extent to which anomalous blood flow patterns predict cardiac defects that resemble those in humans, and found that restricting either the inflow or the outflow to the heart led to reproducible abnormalities with a dose-response type relationship between blood flow mechanical stimuli and the expression of cardiac phenotypes. Constricting the outflow tract by 10-35% led predominantly to ventricular septal defects whereas constricting by 35-60%, most often led to double outlet right ventricle. Ligation of the vitelline vein caused mostly pharyngeal arch artery malformations. We show that both cardiac inflow reduction and graded outflow constriction strongly influence the development of specific and persistent abnormal cardiac structure and function. Moreover, the hemodynamic-associated cardiac defects recapitulate those caused by genetic disorders. Thus, these experiments demonstrate the importance of investigating embryonic blood flow conditions to understand the root causes of congenital heart disease as a prerequisite to future prevention and treatment.

6.2 Introduction

The genesis of heart defects during embryonic development is rooted in complex and unexplained dysregulation of normal heart formation. Congenital heart disease (CHD) is the most common and lethal structural disease present at birth in newborns [15]. Although several genetic disorders have been associated with congenital heart defects, less than 20% of defects are clearly linked to specific human gene mutations [19]. Furthermore, even known cardiac-defect inducing genetic mutations do not affect individuals equally and are typically associated with a range of anatomical outcomes. Cardiogenesis is a finely orchestrated interplay between both genetic and environmental factors, including exposure to teratogens and abnormal blood flow. Nevertheless, scientists investigating the underlying causes of CHD often neglect the confounding effects of blood flow alterations in favor of signaling pathways derived from gene anomalies. Meanwhile, the multifactorial combination of environmental and genetic influences is attracting ever increasing attention as the explanation for complex congenital heart defects [15, 20], but individual effects are difficult to tease apart. Here, we focus on the effects of altered blood flow patterns alone.

Hemodynamic forces associated with blood flow play an important role in early embryonic cardiac morphogenesis [2, 3] as well as in structural features of the mature heart [4-6]. In the embryo, the heart is the first functional organ, and starts beating as soon as a primitive tubular heart is formed. Once beating, pump-derived blood pressure and shear (frictional) forces exerted on tissue walls trigger nascent mechanotransduction mechanisms that lead to physical, biochemical, and gene regulatory responses within the heart and blood vessels [3, 39]. The embryonic cardiovascular system quickly responds to abnormal mechanical cues (due to blood flow) by passively altering contractile function [50, 51], which is followed by abnormal tissue composition remodeling that eventually leads to subtle or overt cardiac defects [3, 7-14]. Genetic anomalies and environmental exposures can alter blood flow in human embryos and fetuses by inducing structural cardiovascular malformation, contractile deficiencies, and inadequate vascularization of the placental and vitelline beds (Figure 6-1,A). For example, intrauterine growth restriction is associated with decreased placental and fetal blood flow [28], while maternal smoking during pregnancy increases fetal vascular resistance and umbilical artery blood velocity [248]. Although it is clear that hemodynamic forces are crucial components of heart development, the relationship between altered hemodynamic conditions and cardiac malformation phenotypes remain unclear.

Previous studies have found a spectrum of congenital heart defects after hemodynamic interventions [7-10, 51, 195], suggesting that multifactorial CHD may be the result of genetic factors compounded by hemodynamic signals. In such studies, however, altered hemodynamics induced by surgical interventions have only been investigated as a group and the possibly large range of hemodynamic change within the group has been neglected. Previous studies, therefore, have not investigated whether different levels of hemodynamic perturbation may lead to distinct cardiac defects. Herein, using chicken embryo models of cardiac development, we show that specific, reproducible, congenital heart defect phenotypes can be induced by precisely controlled blood flow patterns during early cardiac development. We thus demonstrate that congenital cardiac malformations are finely regulated by the specific hemodynamic environment. Future diagnostic imaging of early embryonic/fetal circulation will be critical to help guide management decisions during pregnancy to possibly revert or prevent cardiac malformations.

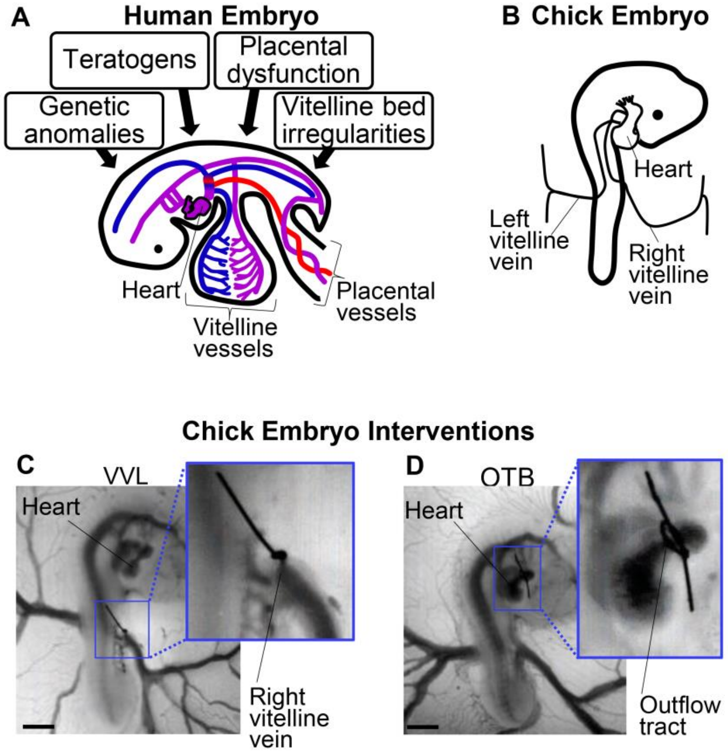

Figure 6-1. Abnormal hemodynamics. (**A**) Human embryonic circulation with factors contributing to hemodynamic perturbations. (**B**) Schematic of a normal chick embryo at day 3 (HH18), corresponding to about 4 weeks in human development. Example optical images of chick embryos at HH18, after surgical interventions used to alter blood flow with (**C**) vitelline vein ligation (VVL) and (**D**) outflow tract banding (OTB). Scale bar = 1 mm.

6.3 Methods

6.3.1 Experimental design

The experiments outlined in this chapter were designed to determine the extent to which different blood flow conditions at early stages of cardiac development lead to distinct cardiac phenotype, heart defect incidence, and cardiac functional abnormalities. To conduct the studies, we used chicken embryo models of heart development, since it is relatively easy to surgically manipulate blood flow conditions in chicken embryos *in ovo*, while minimally disrupting other physiological processes. Results were compared between embryo groups that were selected based on hemodynamic (blood flow) alteration. Embryo groups included a normal group (no intervention), a surgical sham group (intervention control), and 5 surgical intervention groups, with distinct blood flow conditions. The hemodynamic interventions were performed at early embryonic stages of cardiac development, about day 3 of incubation (HH18) out of 21 days to hatching, when the heart is tubular with no valves nor chambers but is already pumping blood. Two hours after surgical intervention, the embryonic hearts were monitored with optical coherence tomography (OCT) *in ovo* to precisely determine the level of hemodynamic alteration in each embryo. Altered blood flow conditions lasted at most 24 hours during tubular stages. Embryos that survived to about day 12 of incubation (HH38) had their hearts imaged with high-frequency ultrasound *in vivo* for functional analysis, and then excised for imaging using micro-computed tomography for detailed structural analysis.

6.3.2 Hemodynamic intervention

Fertilized White Leghorn chicken eggs were incubated blunt end up at 38 °C and 80% humidity until HH18. Embryos that bled or had obvious structural defects at HH18 were discarded. Four types of embryo groups were included in this study: 1. normal group (NL), no interventions were performed; 2. control group (CON), a 10-0 nylon suture was passed under the heart outflow tract but not tightened; 3. outflow tract banded groups (OTB), a 10-0 nylon suture was passed under the heart outflow tract and tied in a knot around the mid-section of the outflow tract (downstream of the cushion and near the flat portion of the outflow tract) to constrict the tract cross-sectional area; and 4. right vitelline vein ligation group (VVL), a 10-0 nylon suture was tied in a knot around the right vitelline vein close to the embryo body to acutely stop venous return flow through that vein (reducing flow to the heart in about half for about 5 hours [66, 195]), before blood flow is later restored by angiogenesis. Band tightness ranged from 0-60%. Following interventions, windowed eggs were sealed with saran wrap and incubated until further evaluation. The band was removed from the outflow tract in the banded group ~24 hours after placement when the embryo reached HH24 to increase survival to later stages, and then the embryo was allowed to develop to HH38 when the heart is nearly fully developed with four chambers and valves. The suture knot in the vein ligated group remained on the vein until the final evaluation at HH38.

6.3.3 Band tightness measurement with OCT

A custom-made OCT system was used to measure chick embryo band tightness as previously described [62, 64, 157, 195]. Briefly, the system has a spectral domain configuration with a superluminescent diode centered at 1325 nm and a 1024 pixel, 92 kHz maximal line-scan rate infrared InGaAs line-scan camera. It acquires 512 x 512 pixel, 2D B-mode line-scan tomographic images at 140 frames per second with <10 μm resolution. Normal physiological temperature (38 °C) was maintained during imaging with a thermocouple-controlled heating system. 200 frames (~3-4 cardiac cycles) of the longitudinal outflow tract were acquired for each banded embryo before and after manipulation in order to measure the change in outflow tract diameter (D), calculate the degree of band tightness ($\Delta D/D$), and measure blood flow velocity in the outflow tract, thus establishing the level of hemodynamic alteration.

6.3.4 Intervention velocity analysis

A subset of embryos were imaged with Doppler OCT at HH18 and high frequency ultrasound at HH24 to analyze changes in blood flow after hemodynamic surgical interventions. Peak blood flow velocity at HH18 was measured with Doppler OCT, 2 hours after each manipulation. The 2 hour time period after performing the sham surgery in the control embryos, the banding in the banded embryos, or the ligation in the vein ligated embryos allowed the embryo to warm back to physiological temperature in the incubator, and physiologically respond to the intervention. A velocity sampling area was selected in the region of non-wrapped flow along the centerline and near the middle of the outflow tract to be most representative of changes due to band constriction in banded embryos, as well as consistent with the location within the outflow tract across all embryo groups (see our previous publication for a more detailed explanation [158]). Peak blood flow velocity was then measured in the same embryos and outflow tract location at HH24 with our Vevo 2100 ultrasound system. The positioning of the embryo and heart in the egg at HH18 allows us to employ the high spatial resolution of OCT imaging, however by HH24 the embryo starts to sink in the egg and can no longer be imaged with OCT. Ultrasound provided enough tissue penetration and spatial resolution to observe cardiac wall features and blood flow at HH24. See Echocardiography section for more ultrasound details. This dataset included two groups of banded embryos: one that did not have the band removed at HH24, to assess the effect of banding after 24 hours; and a second group that had the band removed 2 hours prior to velocity measurement at HH24, to assess the effect of band removal on hemodynamics. The two groups were needed because flow measurements at HH24 are invasive and thus might affect the embryos, preventing longitudinal studies.

6.3.5 Echocardiography

Blood flow velocity at HH24 and cardiac function of the mature heart at HH38 was evaluated with high frequency ultrasound (Supplemental Figure 6-6). The windowed eggs were submerged in physiological temperature-controlled Hank's Balanced Salt Solution to make contact with the transducer probe. A 32-56 MHz linear array transducer probe was used with the smaller cardiac structures at HH24, and a 18-38 MHz ultrasound linear array transducer probe was used to image the heart at HH38. Our high frequency ultrasound Vevo 2100 system acquires images at 100 fps, with an axial resolution of ~30 μm. A complete 2-dimensional B-mode (structure), Doppler velocity, and Tissue Doppler Imaging (TDI) echocardiographic examination was performed for each embryo to assess structural heart integrity and cardiac function at HH38. Peak blood flow velocity, velocity time integral, and heart rate were averaged over 2-3 cardiac cycles from the Doppler velocity signal from the left ventricular outflow tract. The flow angle was set during acquisition, so that Doppler velocities were automatically corrected for the direction of flow. Stroke volume, cardiac output, and left ventricular ejection fraction (*LVEF*) were calculated using the modified Simpson's rule with 4-chamber and 2-chamber B-mode images [249-251]. Additionally, TDI was used to record systolic (*S'*) and early diastolic (*E'*) peak radial and longitudinal myocardial velocities at the mitral lateral annulus from a 4-chamber view. Please note that while longitudinal velocities are more widely used clinically [252, 253], the heart orientation required to measure longitudinal velocities was difficult to achieve with the embryo in the egg, and this reduced the functioning sample size. Color Doppler high frequency ultrasound was used to identify VSD flow through the ventricular septum.

6.3.6 Micro-CT

After ultrasound imaging at HH38, each heart was collected for micro-computed tomography (micro-CT) to identify structural defects and analyze structural geometry. The heart was arrested at end-diastolic phase by injecting chick ringer solution containing 60 mM KCL, 0.5 mM verapamil, and 0.5 mM EGTA [43], collected, and stained with 100% Lugol's solution for 16 hours to enhance tissue contrast. A Caliper Quantum FX Micro-CT system was used with a 10 mm field of view, 140 μA current, and 90 kV voltage to acquire high resolution (~10 μm), 3D heart scans. Scans were discretely sampled using the Amira (FEI, Hillsboro, OR) software platform to generate 2D image stacks and identify major cardiac defects. Double outlet right ventricle (DORV) was identified from micro-CT images as dextroposition of the aorta with alignment of both great arteries with the right ventricle, always combined with a ventricular septal defect (VSD). VSDs were confirmed by Doppler ultrasound, a feature that enables color-coded identification of flow from ultrasound images. Tetralogy of Fallot (TOF), like DORV had dextroposition of the aorta, but was separately characterized by unequal outflow sizes with a large aorta and small pulmonary artery, combined with a large VSD. Cardiac defects were mainly identified from micro-CT images and identification was aided by ultrasound.

Micro-CT images were also used to measure aortic arch diameter, compact and trabeculated myocardium thickness, septal thickness, and ventricle cavity diameters and length. These dimensions were measured from micro-CT images to ensure comparable measurement locations across embryos and to have adequate image resolution for fine measurements. Wall thicknesses and chamber diameters were measured at a midportion slice which contained both ventricles, just below the muscular rim of the tricuspid valve. Compact and trabeculated myocardium thicknesses were measured from the lateral segments of each ventricle wall. Relative wall thickness was calculated for each ventricle (posterior + septal wall thickness/end-diastolic cavity diameter) in order to categorize wall thickening and chamber dilation patterns of response. Diameters of the pharyngeal arch arteries were also measured from micro-CT images, where the base diameters of the aortic root, pulmonary root, right and left aortic arches, right and left brachiocephalic arteries, and right and left pulmonary arteries were compared to the sum of the aortic and pulmonary roots to allow for any differences in embryo size [7]. A sphericity index was calculated for each ventricle (ventricle base-to-apex length/basal diameter) from a 4-chambered image view [254]. The sphericity index was used to detect elongation and shortened ventricles, where elongated and globular hearts were defined as having a sphericity index higher or lower than the average mean of the control group ± 2 standard deviations, respectively.

6.3.7 Statistical analysis

To compare significant changes among embryo groups, banded embryos were divided into 4 different band tightness ranges to capture distinct hemodynamic conditions induced by the intervention: 11-20%, 21-35%, 36-45%, and 46-60% band tightness. The chi-squared statistic (X^2) was used to compare proportions of embryos that survived to stage HH38 in each group to the normal group, assuming significance with corresponding two-tail *p*-values of less than 0.05. All surviving embryos in banded groups and the vein ligated group were compared to control groups, and analyzed as the mean ± standard deviation. Statistical significance between functional and structural parameters were determined with a two-sample Student's *t*-test, assuming significance with two-tail *p*-values of less than 0.05. Because the defects that arise in late stages create separate and dissimilar hemodynamic conditions, only embryos without major defects (at least 3 embryos with no major structural defects per group) were compared to controls to evaluate changes in cardiac function and structure after hemodynamic manipulation in seemingly normal hearts.

6.4 Results

6.4.1 Altered hemodynamics

We altered cardiac hemodynamics in the early chicken embryo using two well-established interventions: 1. outflow tract banding (OTB) [7-9, 51]; and 2. right vitelline vein ligation (VVL) [10, 62] (Figure 6-1,B-D). Both interventions were performed at approximately 3 days of incubation at Hamburger and Hamilton stage 18 (HH18) [37], an early stage of embryonic development when the heart is a looped tubular structure, with atrium, ventricle, and outflow tract connected in series. The heart at this stage is sensitive to hemodynamic changes that affect later septation and valve formation [3, 10, 38], and the interventions lead to heart defects seen in human babies. Outflow tract banding (referred to as ‘banding’ for simplicity) was used to reduce the diameter of the early embryonic heart outflow tract and increase hemodynamic load on cardiac tissues [51, 52, 62, 158]. A contrasting blood flow alteration, vitelline vein ligation (referred to as ‘vein ligation’ for simplicity), was used to generate an acute reduction in hemodynamic load by decreasing venous return to the heart [66, 195].

While vein ligation resulted in a consistent flow decrease through the embryonic heart, the degree to which blood pressure and flow velocity increased following banding varied widely. Doppler OCT and servo-null pressure characterization of the immediate blood flow response after banding revealed that the altered hemodynamic conditions are defined by the degree of diameter constriction in the outflow tract, also referred as band tightness (Figure 6-2) [52, 158]. Peak blood flow velocity increased with constriction up to ~35% band tightness, above which it plateaued and decreased. Peak ventricular pressure increased approximately exponentially with constriction. We thus considered five embryo groups according to the level of hemodynamic alteration at HH18: one vein ligated embryo group (the VVL group) and four outflow tract banded embryo groups (OTB groups), with different degrees of band tightness (Figure 6-2, vertical lines separate groups). The first banded group (OTB 10-20%) exhibited almost normal blood pressures, but had increased outflow tract velocity and thus wall shear stress (friction exerted by flowing blood on the endocardial tissue). The second banded group (OTB 21-35%) was characterized by maximum outflow tract velocity and increased wall shear stress, while blood pressure was only moderately elevated. The third group (OTB 36-45%) exhibited maximum outflow tract velocity and increased wall shear stress, as well as high blood pressure levels. In contrast, the fourth group (OTB 46-60%) had reduced outflow tract velocity and wall shear stress (with respect to maximum in the banding intervention), but highly elevated blood pressure levels. As shown later, the level of hemodynamic alteration strongly influences cardiac outcomes.

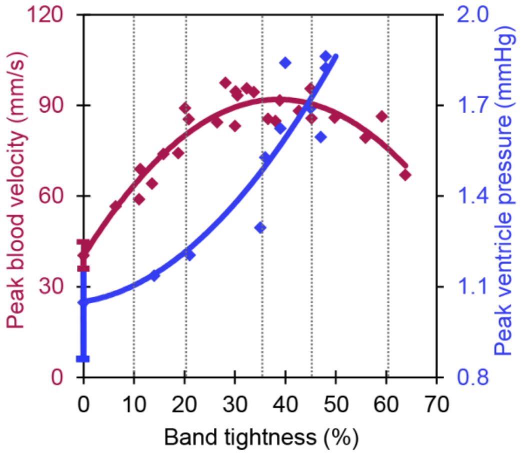

Figure 6-2. Altered hemodynamics after outflow tract banding. Hemodynamic response to outflow tract band tightness, produced from previously published data [52, 158]. Vertical lines outline ranges of constriction used for analysis, and standard deviation of controls are displayed as error bars.

The time period of perturbed flow in this study was limited to 24 hours from HH18 to HH24. Two hours after intervention at HH18, peak blood flow velocity in the outflow tract was significantly increased in the banded group, and significantly decreased in the vein ligated group compared to control embryos. By HH24, peak velocities in the outflow tract remained significantly elevated in the banded embryos with the band in place with respect to controls, but returned to control levels after band removal. Similarly, peak velocities in vein ligated embryos were restored to control levels at HH24 (Figure 6-3).

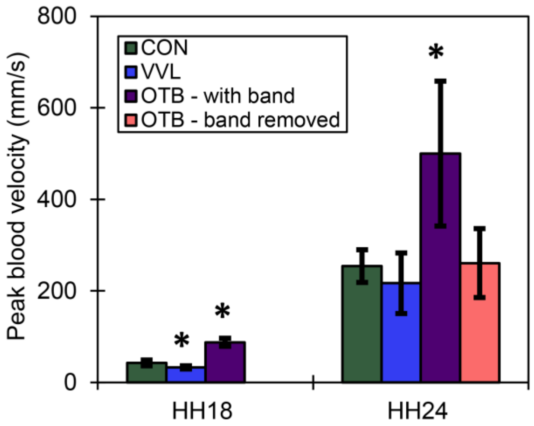

Figure 6-3. Maximum blood velocity after interventions. Interventions performed at HH18; band removed at HH24. Standard deviation is displayed as error bars. Asterisk, statistically significant differences between experimental and control embryos (n=8, p<0.05); CON, surgical sham control; VVL, vitelline vein ligated; OTB, outflow tract banded.

6.4.2 Embryo survival and cardiac defects

We characterized the effects of altered early stage hemodynamics by comparing banded and vein ligated groups, to surgical sham control and normal embryos at HH38 once the heart is four-chambered with valves. Rates of embryo survival to HH38 (~12 days of incubation) varied by group (Supplemental Figure 6-7). Roughly half of all embryos in normal (55%) and control (50%) groups survived to HH38, while the percentage of banded embryos that survived to HH38 decreased to about 38% in the band tightness ranges between 10 and 45%. Lowest survival rates corresponded to the highest peak velocity (and therefore wall shear stress) ranges of the banding alteration, OTB 21-35% group, with the proportion of embryos that survived to HH38 in this group significantly below normal survival (X_1^2=4.07, p=0.044). Conversely, survival rate increased to within control variability in the tightest banded range (OTB 46-60%; X_1^2=0.087, p=0.768) at the point where the peak velocity curve began to decrease while the pressure continued to increase with increased constriction. Vein ligated embryos also had high survival rates that were comparable to controls (X_1^2=0.475, p=0.491).

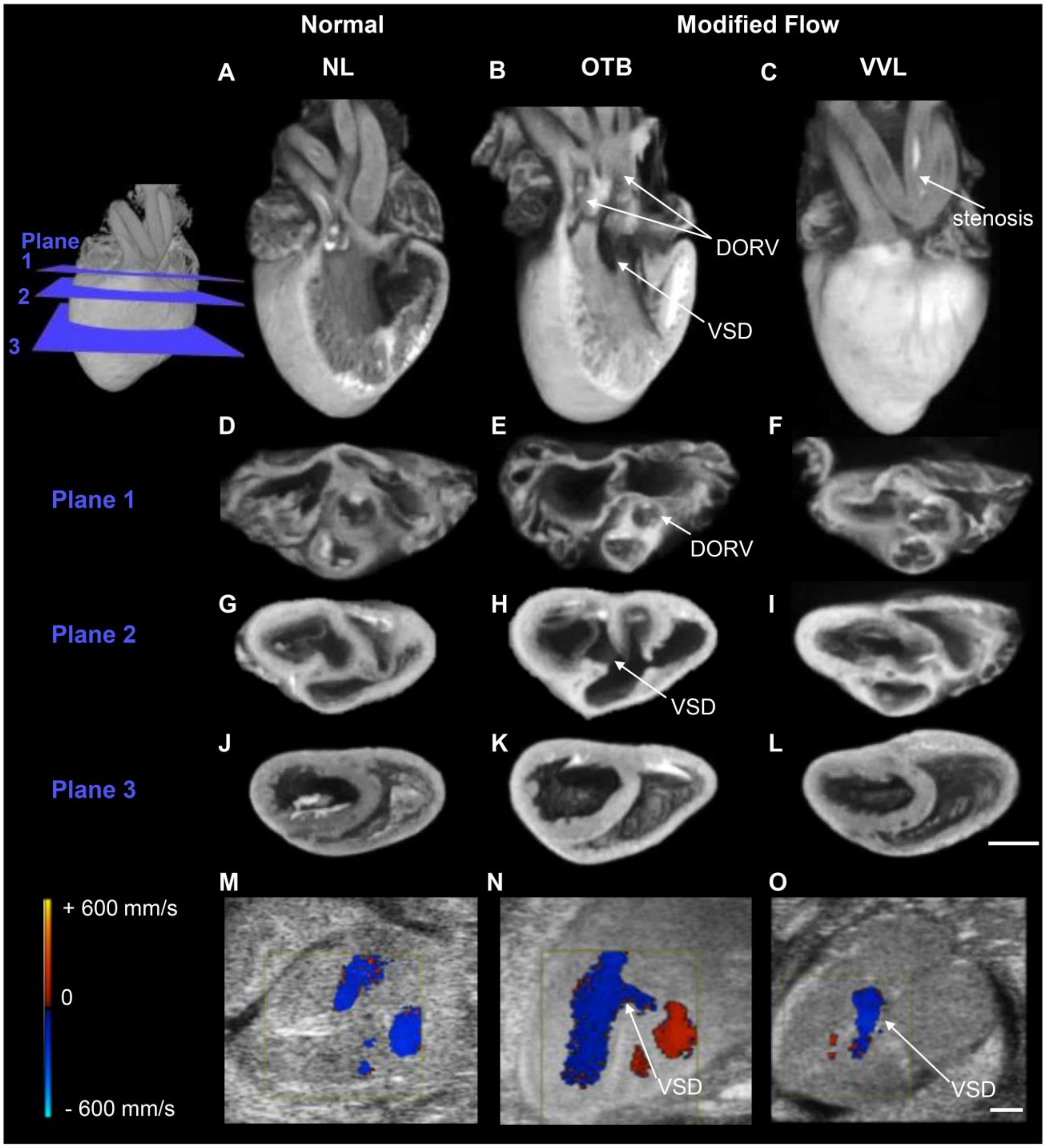

Figure 6-4. Cardiac defects at HH38. Example micro-CT images of a normal (**A,D,G,J**), banded (**B,E,H,K**), and vein ligated (**C,F,I,L**), depicting 3D reconstructions (**A-C**) and three cross-sectional planes (**D-L**). Plane 1 intersects the semilunar valves (**D-F**), plane 2 intersects the atrioventricular valves (**G-I**), and plane 3 intersects the ventricle midpoint (**J-L**). DORV in the banded embryo displayed with aortic valve rotated outward (**E**), along with both outflows from the RV and a perimembranous VSD (**B, H**). The vein ligated embryo displayed stenosis of the right brachiocephalic artery (**C**). Example Ultrasound Color Doppler images (**M-O**) with detection of ventricular septal defect (VSD) flow after both interventions (**N,O**). Scale bars = 1 mm. NL, normal; VVL, vitelline vein ligated; OTB, outflow tract banded.

Fully formed hearts were imaged with high frequency ultrasound and micro-computed tomography (micro-CT) in late development at HH38 to determine the effects of varied early hemodynamics on cardiac function and structure (Figure 6-4). Major defects included ventricular VSDs that were further divided according to where the ventricular septum was disrupted, including conoventricular VSD (section of the ventricular septum just below the semilunar valves), perimembranous VSD (upper section of the ventricular septum), and muscular VSD (lower, muscular section of the ventricular septum). Other defects included DORV, TOF, and pharyngeal arch artery (PAA) malformation. DORV and TOF defect combinations were sometimes accompanied with PAA malformation, with persistence of the left 4th aortic arch, stenosis interruption of the left brachiocephalic artery, and tubular hypoplasia of right pulmonary artery. PAA malformation that developed without DORV or TOF included stenosis interruption of the right and left brachiocephalic arteries and pulmonary root, and tubular hypoplasia of the right pulmonary artery.

Importantly, defect type and incidence of major structural cardiac malformation identified at HH38 depended on the distinct hemodynamic conditions in each group (Figure 6-5). The number of surviving embryos in each group ranged from 10-16, where the percentage of surviving banded embryos with major cardiac defects remained higher than 50% in all ranges above 20% band tightness, compared to only 10% of hearts with defects in the loosely constricted range (10-20% tightness), 33% in the ligated embryos, 8% in normal embryos, and no control hearts with defects. Defect incidence also varied with band tightness. DORV mostly occurred in hearts with greater than 36% band constriction while perimembranous VSD only occurred in the ranges below 36% band constriction. Contrastingly, the vein ligated group exhibited a lower overall cardiac defect incidence compared to the banded groups with more than 20% band tightness. Further, unlike the outflow banded groups, the vein ligated group exhibited PAA malformations without DORV or TOF. Even though TOF and muscular VSD only occurred in a small subset of embryos, the distribution of defects uniquely depended on each embryo group. Thus, the various early hemodynamic conditions translated into distinct cardiac phenotypes.

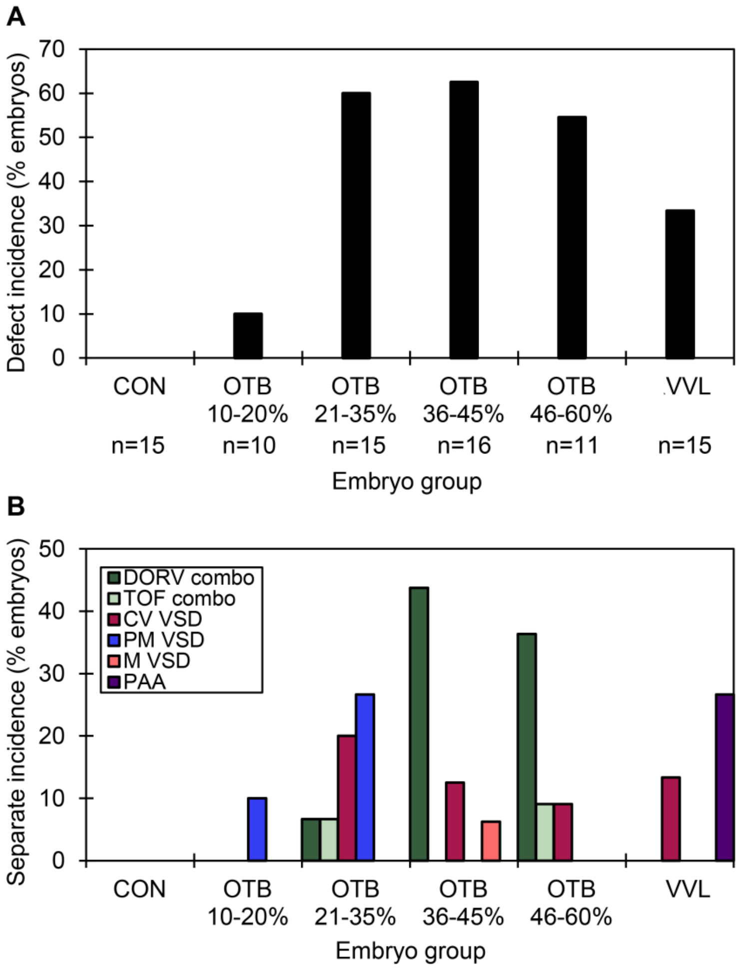

Figure 6-5. Cardiac defects depend on intervention group. (**A**) Overall defect incidence among surviving embryos. (**B**) Separate defect type incidence among surviving embryos. CON, surgical sham control; VVL, vitelline vein ligated; OTB, outflow tract banded; DORV, double outlet right ventricle; TOF, Tetralogy of Fallot; CV VSD, conoventricular ventricular septal defect; PM VSD, perimembranous ventricular septal defect; M VSD, muscular ventricular septal defect; PAA, pharyngeal arch arteries malformation.

Additionally, Tissue Doppler Imaging (TDI) was used to identify impaired pumping function. TDI recorded systolic (*S'*) and early diastolic (*E'*) peak radial and longitudinal myocardial wall velocities at the mitral lateral annulus [255]. As stroke volume is dependent on myocardial contractile function [256], our TDI analysis showed that longitudinal *E'* and *S'* was positively correlated with cardiac output across all embryos, most notably in DORV and TOF hearts (Supplemental Figure 6-8,A-B) .

Cardiac defects following interventions produced diverse functional and structural outcomes. This is likely due to the cyclical relationship between altered hemodynamic forces and subsequent cardiac remodeling. Defects that result from the initial hemodynamic changes impact blood flow patterns, which in turn influence further anatomic changes.

6.4.3 Hearts with no major defects

Functional and structural parameters measured from hearts with only minor structural defects were compared to determine the more subtle effects of altered hemodynamic forces induced by outflow tract banding and vitelline vein ligation alone and when unaccompanied by secondary flow modification (Table 6-1). Despite having no major defects at HH38, functional anomalies persisted in the embryos that were hemodynamically altered, especially in the most severely constricted banded group (OTB 46-60%). This group had a decreased diastolic radial wall velocity (*E')* and increased aortic outflow velocity. The latter was combined with decreased aortic arch diameter and therefore increased aortic wall shear stress, while stroke volumes remained similar to controls. Since ventricular wall thickness is decreased in this same group, the reduction in *E'* is perhaps associated with less compliant walls that inhibit chamber filling. The OTB 46-60% group had a decrease in posterior ventricle wall thickness while ventricle cavity diameter remained similar to controls. Lateral compact myocardium thickness also decreased in both OTB 36-45% (right ventricle) and 46-60% (left and right ventricles) groups. The compact myocardium adapts to physiologically increased load by thickening during development, initially by increased cell proliferation, and then followed by compaction of trabeculae and invasion of vasculature from the epicardium (a cell layer that covers the external myocardium after cardiac looping) [257-259]. Multilayered compact myocardium is important for force generation, and noncompaction of the myocardium (thin compact myocardium syndrome) presents severe consequences for the developing heart [260]. While compact myocardial thickness decreased with tight bands in this study, trabecular thickness remained similar to controls, suggesting that the differences in compaction were not due to disturbed trabeculae compaction. Previous works have shown that continuous banding between HH21 and HH34 results in compact myocardium thickening and advanced trabeculation [8], however our study suggests that the increased load in tightly banded embryos between HH18 and HH24 interferes with cell proliferation and epicardial vasculature invasion processes that contribute to normal myocardium compaction. The decrease in compact myocardium thickness was not accompanied by any changes in septum thickness. Nevertheless, the septum thickness was significantly decreased in OTB 21-35% and vein ligated groups. Vein ligated embryos without major structural defects had an elevated left ventricular ejection fraction (*LVEF)* compared to controls, which has been previously linked to high mortality and sudden cardiac death in humans [261]. Since no hypertrophy (increase in cell volume) was observed in vein ligated hearts, this compensation is likely due to input/output impedance mismatch [262]. Even in hearts without major structural defects, deviations from normal physiology and morphology strongly depend on the level of early hemodynamic alteration.

A sphericity index was used to define ventricle shape, which highlights alterations in muscle fiber architecture [82, 263] and pumping efficiency [254]. Hearts with no major structural defects across all groups displayed a loose correlation between stroke volume and left ventricle sphericity index (Supplemental Figure 6-8,C), where decreased sphericity (more globular heart) was associated with decreased stroke volume. While examples of elongated and globular hearts developed in most experimental groups, differences in the overall sphericity indices compared to control indices were not significant.

Relative diameters of the pharyngeal arch arteries were measured as an index of altered blood flow. The only significant difference in banded group hearts without overt malformations was an increased left pulmonary artery diameter in both 10-20% and 21-35% tightness groups. Vein ligated embryos displayed decreased aortic arch base and increased pulmonary root base diameter compared to controls. These results indicate that the distribution of flow to the arch arteries depend on the early hemodynamic intervention performed.

Table 6-1. Functional and structural parameter evaluation of hearts without defects.

Parameter	NL	CON	OTB 11-20%	OTB 21-35%	OTB 36-45%	OTB 46-60%	VVL
Blood flow parameters	n=11	n=11	n=9	n=6	n=5	n=4	n=8
heart rate (BPM)	156 ± 17	151 ± 23	154 ± 40	160 ± 32	147 ± 31	168 ± 24	182 ± 49
stroke volume (mm^3)	9.7 ± 2.1	9.6 ± 2.5	10.2 ± 5.8	8.1 ± 1.9	9.7 ± 4.2	10.9 ± 3.0	9.2 ± 4.5
cardiac output (mL/min)	1.5 ± 0.4	1.4 ± 0.4	1.6 ± 1.0	1.3 ± 0.4	1.4 ± 0.6	1.8 ± 0.6	1.9 ± 1.2
LVEF (%)	53.4 ± 9.9	64.4 ± 16.1	56.6 ± 15.1	52.6 ± 2.1	56.5 ± 17.0	62.2 ± 6.4	**70.9 ± 12.4***
peak velocity (mm/s)	423 ± 120	414 ± 166	425 ± 191	411 ± 170	369 ± 167	**669 ± 209***	378 ± 142
velocity time integral (mm)	34.8 ± 7.7	38.6 ± 17.2	34.7 ± 16.0	33.7 ± 14.5	31.7 ± 14.7	53.5 ± 22.8	35.9 ± 12.0
TDI radial annular velocities	n=11	n=9	n=7	n=4	n=4	n=3	n=7
E' (mm/s)	27.7 ± 14.6	22.6 ± 9.0	32.8 ± 32.8	25.3 ± 17.8	21.4 ± 14.3	**17.6 ± 3.2***	21.7 ± 8.1
S' (mm/s)	16.5 ± 6.9	13.2 ± 5.1	20.1 ± 11.5	17.4 ± 9.7	13.5 ± 3.3	12.5 ± 2.4	18.3 ± 7.4
TDI longitudinal annular velocities	n=3	n=2	n=2	n=1	n=0	n=3	n=2
E' (mm/s)	25.7 ± 6.0	32.7 ± 3.1	35.1 ± 2.1	14.9		24.8 ± 3.3	35.8 ± 12.6
S' (mm/s)	10.2 ± 2.0	17.2 ± 2.5	16.0 ± 0.7	8.3		13.1 ± 2.3	26.5 ± 2.2
LV structure	n=10	n=14	n=9	n=7	n=6	n=5	n=10
relative wall thickness	0.58 ± 0.08	0.61 ± 0.13	0.58 ± 0.11	0.52 ± 0.13	0.65 ± 0.10	**0.47 ± 0.09***	0.57 ± 0.14
compact myocardium thickness (μm)	257 ± 34	241 ± 38	231 ± 44	229 ± 51	231 ± 48	**159 ± 20***	226 ± 57
trabecular myocardium thickness (μm)	160 ± 51	149 ± 53	158 ± 47	152 ± 97	164 ± 27	158 ± 63	146 ± 62
sphericity	2.03 ± 0.14	2.06 ± 0.14	2.05 ± 0.21	2.08 ± 0.27	2.01 ± 0.24	1.99 ± 0.32	1.97 ± 0.19
RV structure	n=10	n=14	n=9	n=7	n=6	n=5	n=10
relative wall thickness	0.73 ± 0.08	0.77 ± 0.12	0.82 ± 0.12	0.73 ± 0.19	0.94 ± 0.43	**0.64 ± 0.07***	0.81 ± 0.10
compact myocardium thickness (μm)	168 ± 44	182 ± 57	177 ± 45	178 ± 34	**136 ± 27***	**118 ± 30***	161 ± 55
trabecular myocardium thickness (μm)	164 ± 40	195 ± 54	183 ± 30	218 ± 60	168 ± 60	159 ± 10	201 ± 74
sphericity	1.55 ± 0.09	1.60 ± 0.27	1.59 ± 0.22	1.50 ± 0.20	1.54 ± 0.19	1.61 ± 0.46	1.66 ± 0.18
Septal thickness (μm)	653 ± 86	635 ± 104	616 ± 68	**536 ± 47***	623 ± 150	547 ± 90	**534 ± 133 ***
Relative great vessel diameters	n=10	n=14	n=9	n=7	n=6	n=5	n=10
aortic root	0.50 ± 0.03	0.52 ± 0.04	0.50 ± 0.05	0.46 ± 0.06	0.48 ± 0.03	0.44 ± 0.08	**0.45 ± 0.07***
pulmonary root	0.50 ± 0.03	0.48 ± 0.04	0.50 ± 0.05	0.54 ± 0.06	0.52 ± 0.03	0.56 ± 0.08	**0.55 ± 0.07***
right aortic arch	0.40 ± 0.09	0.47 ± 0.10	0.45 ± 0.06	0.47 ± 0.14	0.44 ± 0.06	0.52 ± 0.08	0.42 ± 0.11
right brachiocephalic artery	0.40 ± 0.06	0.39 ± 0.07	0.45 ± 0.07	0.37 ± 0.11	0.43 ± 0.06	0.42 ± 0.09	0.43 ± 0.10
left brachiocephalic artery	0.35 ± 0.05	0.35 ± 0.04	0.39 ± 0.06	0.35 ± 0.08	0.37 ± 0.10	0.36 ± 0.08	0.38 ± 0.07
right pulmonary artery	0.43 ± 0.08	0.41 ± 0.10	0.46 ± 0.11	0.41 ± 0.10	0.49 ± 0.11	0.48 ± 0.07	0.48 ± 0.12
left pulmonary artery	0.46 ± 0.09	0.50 ± 0.05	**0.59 ± 0.07***	**0.60 ± 0.11***	0.56 ± 0.13	0.53 ± 0.05	0.53 ± 0.10

Data represented as mean ± standard deviation. Asterisks indicate significant difference from control groups; P<0.05.

6.5 Discussion

Hemodynamic intervention models were used to mimic perturbed blood flow conditions in human embryos that can be induced by genetic anomalies, teratogens, or irregular placental or vitelline circulations. In this study, the short initial period of altered hemodynamics during tubular heart stages triggered a detrimental growth and remodeling cascade that eventually led to major cardiac malformations. These results further support the notion that abnormal hemodynamics may be the main regulator of malformation in many CHD cases that develop following transient exposure to teratogens or other environmental conditions that are known to alter blood flow, considering that similar heart defects were induced after only a short-term developmental period of perturbed blood flow. Previous studies have reported cardiac malformations and abnormal remodeling in a number of embryonic heart models following blood flow perturbations [195] , however, the degree of hemodynamic change was not assessed. This study is the first to show that the level of hemodynamic alteration predicts distinct abnormalities in the maturing heart. Even hearts that did not show overt structural anomalies, exhibited more subtle structural (myocardium thickness, septal thickness, great vessel diameter) and functional (peak velocity, *E'*, *LVEF*) challenges, which depended on early hemodynamic modifications with varied and distinct dependence on intervention group. Thus, even in seemingly normal hearts, exposure to altered blood flow in early development may increase the risk for cardiac dysfunction and cardiovascular disease later in life. More importantly, this study demonstrates a ‘dose-response’ type of relationship between mechanical stimuli and the expression of cardiac phenotypes, where in malformed hearts the frequency and severity of cardiac defects also depended on the level of flow alteration. The highest incidence of DORV occurred in the hemodynamic groups corresponding to the highest pressure, which perhaps is less commonly achieved in humans and reflects the relatively rare occurrence of DORV in 1-3% of babies with CHD [264]. VSDs, a common defect that affects about 50% of children with CHD [100], also frequently occurred in our study with the highest incidence in the OTB 21-35% tightness group. The incidence of TOF, a complex CHD that appears in about 1 in 3000 live births [265], was also low in our studies. PAA defects not associated with DORV or TOF, in contrast, only developed in the vein ligated group. Not only did the overall malformation incidence depend on intervention group, each defect phenotype uniquely occurred in response to separate hemodynamic alterations.

Our data emphasize that altered hemodynamics and cardiac defects are linked, with cardiac malformations dictated by early blood flow patterns. Future therapies for CHD should address the altered blood flow conditions produced alone or as part of genetic anomalies and environmental exposure, as the adverse outcomes of congenital heart defects may be largely propagated by the associated blood flow conditions. This finding suggests the need for new avenues for prevention, early diagnostic, and treatment of cardiac defects.

6.6 Acknowledgments

This work was funded by a grant from US National Institutes of Health, NIH R01HL094570. We thank Dr. J. Lindner for providing guidance on high frequency ultrasound evaluation of cardiac function and Tissue Doppler Imaging.

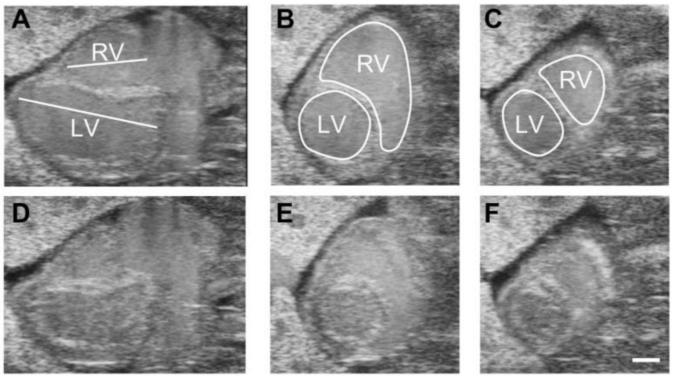

Supplemental Figure 6-6. High frequency ultrasound imaging at HH38. Example images from a normal embryo in diastole (**A-C**) and systole (**D-F**) at four-chamber (**A,D**), cross-sectional mitral valve (**B,E**), and cross-sectional papillary muscle (**C,F**) views. Ventricle lengths in the long-axis view are noted in **A**, and ventricles perimeters are outlined in short-axis views in **B** and **C**. RV, right ventricle; LV, left ventricle. Scale bar = 1mm.

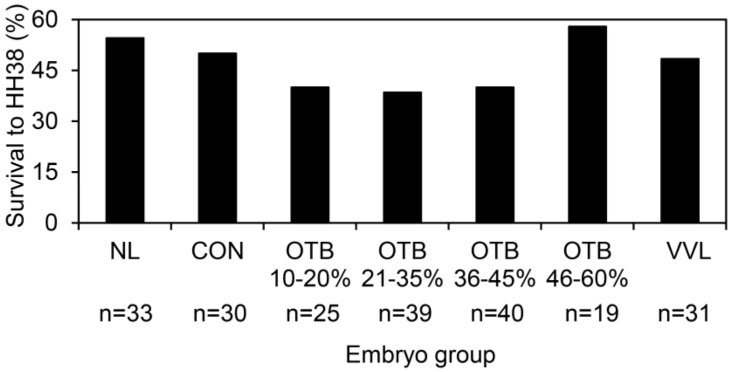

Supplemental Figure 6-7. Embryo survival to HH38 depended on intervention group.

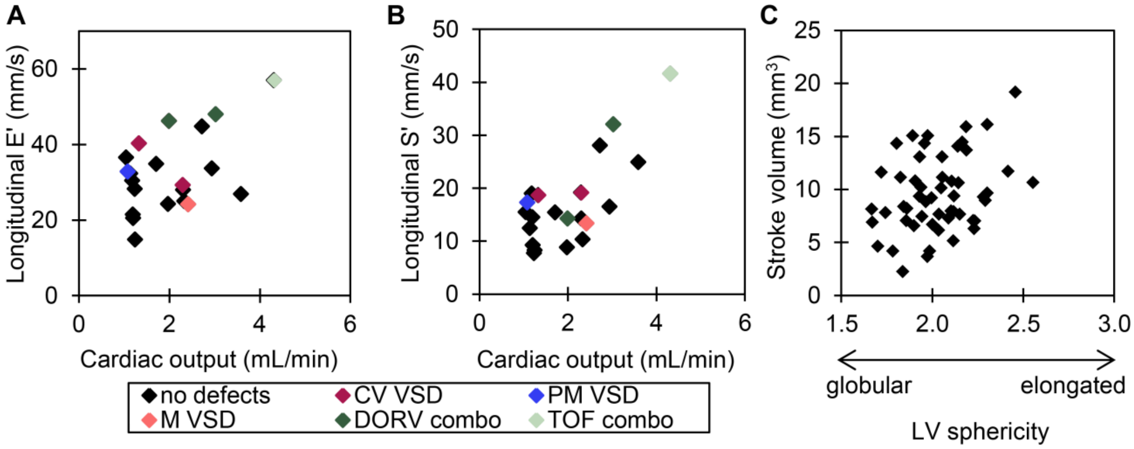

Supplemental Figure 6-8. Functional comparisons from UBM and micro-CT evaluations. **A**, LV stroke volume with respect to LV sphericity for all non-defected embryos. **B,** TDI longitudinal *E'* and **C**, *S'* velocities for all non-defected embryos.

Chapter 7: Conclusions and future directions

7.1 Dissertation conclusions

The studies presented in Chapters 3-6 lead to further understanding of the complex relationship between abnormal embryonic blood flow and cardiac malformation. The results demonstrate that detrimental cardiac remodeling and the development of cardiac defects are finely regulated by the specific hemodynamic environment. These investigations revealed the following main findings: tightly controlled patterns of hemodynamic change accompany normal structural remodeling in the cardiac outflow tract during looping stages (Chapter 3); shear-induced vasodilation likely acts to maintain normal shear stress levels in the outflow tract during normal development (Chapter 3); hemodynamics induced by outflow tract banding strongly depend on band tightness, where peak blood flow velocity and wall shear rate increase with constriction up to 35% band tightness above which they plateau and decrease (Chapter 4); while hemodynamics significantly vary based on the degree of outflow tract band tightness, conserved normal stroke volume in banded embryos suggest functional preservation in the early embryonic cardiovascular system (Chapter 4); increased hemodynamic load between HH18 and HH24 perturbs normal tissue remodeling by enhancing the EMT phenotype in the outflow tract cushions (Chapter 5); frequency and severity of major cardiac defects strongly depend on the level of blood flow mechanical stimuli in early development, and defect phenotypes uniquely occur in response to separate hemodynamic conditions (Chapter 6); even hearts that do not show overt defects following early hemodynamic modifications exhibit subtle structural and functional challenges with varied and distinct dependence on hemodynamic alteration (Chapter6).

Proposed future research directions would extend the studies presented in this dissertation and investigate 1) myocardial remodeling after increased hemodynamic load, 2) global transcriptome and proteome changes induced by increased hemodynamic load, 3) early outflow tract remodeling triggered by decreased hemodynamic load, and 4) tissue remodeling abnormalities presented with cardiac defects. Preliminary studies performed in these areas as well as future methods that will be developed are discussed in the following sections.

7.2 Myocardium remodeling following increased hemodynamic load

Future work aims to quantify myocardial changes following altered hemodynamics in the chicken embryo heart outflow tract (which later gives rise to the aorta, pulmonary trunk, interventricular septum, and semilunar valves), in order to elucidate the mechanisms that relate altered blood flow to abnormal myocardial remodeling. Preliminary work has focused on variations in myofibril and apoptotic remodeling after outflow tract banding between stages HH18 and HH24, which will be expanded to also investigate mitochondrial and proliferative remodeling after banding. This work will elucidate effects of altered hemodynamics on early myocardial remodeling that ultimately leads to cardiac defects. This knowledge could be essential in future prevention and treatment of congenital heart disease (CHD).

7.2.1 Myofibril remodeling

The heart is the first functional organ in the embryo, and starts beating with the help of primitive myofibril bundles as soon as the early heart tube is formed at approximately HH10 [266]. These premature myofibril bundles are not regularly oriented as in the mature heart. Instead, disarrayed myofibril-like structures are distributed throughout the cytoplasm and lack alignment and packing. Throughout normal development, more fibrils are formed, the fibril to cytoplasm volume fraction increases, bundle thickness increases, and bundles align to the circumferential axis of the myocyte in an orderly pattern [267-269]. These developmental changes take place in order to contribute to optimal force transfer and contraction in the outflow tract and the rest of the heart [270]. Mature myofibrils emerge by HH41, which are characterized by an organized repeated pattern of thick (actin) and thin (myosin) filaments that are connected by sarcoplasmic-derived Z-discs [267].

Preliminary FIB-SEM data shows that at HH24, control outflow tract myocytes contained immature myofibril structures (Figure 7-1), indicating that the development of the outflow tract heart muscle is still ongoing at this stage. Immature myofibril organization was displayed by overall lack of myofibril alignment and instances where more than one fibril radiated from the same z-band center. In addition, while most myofibrils inserted into intercalated disks at nearly right angles as they do in mature tissue, some oblique insertions were still visible in control tissue.

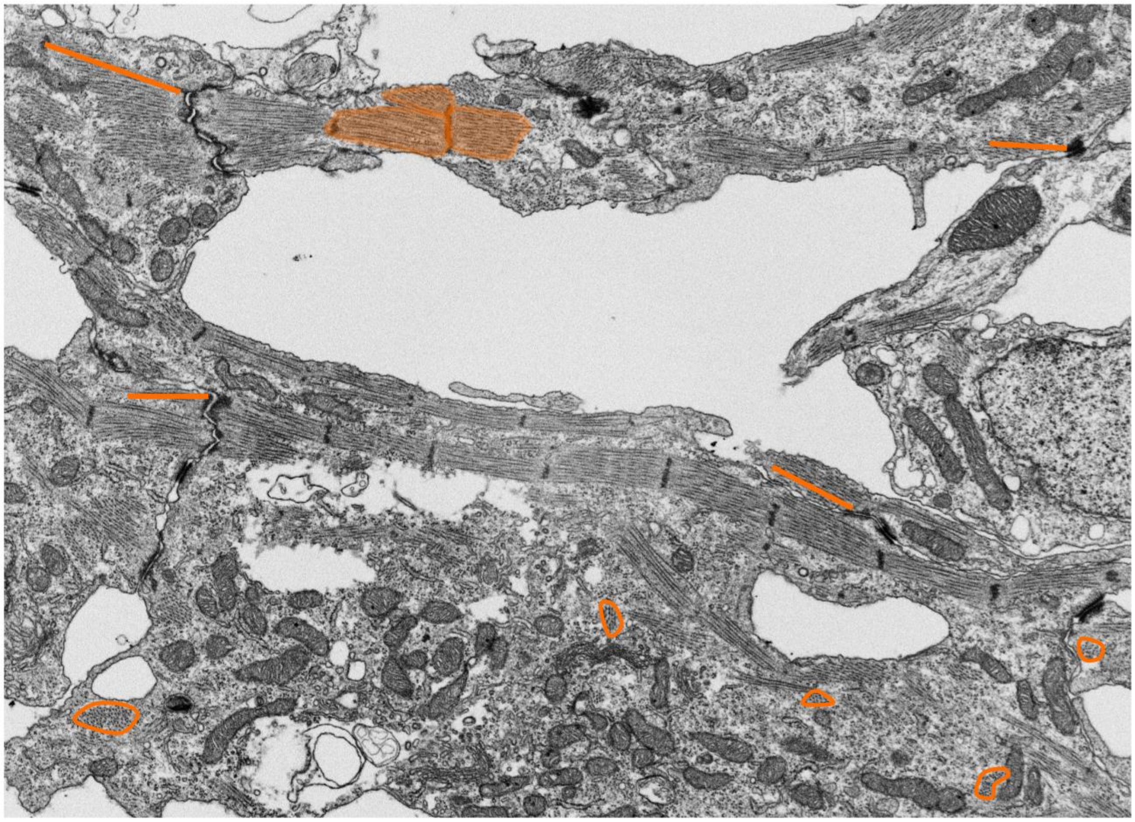

Figure 7-1. Example FIB-SEM image showing myofibrils in control outflow tract myocardium tissue. Several myofibril orientations are displayed, where the tissue mostly consists of longitudinally oriented bundles arranged circumferentially around the outflow tract. Radially oriented bundles are marked by empty orange outlines. Fibril bundles that insert into intercalated disks at oblique angles are marked by orange lines that align with the bundle. An example of a group of fibril bundles that radiate from the same z-band center is marked by shaded orange outlines.

To quantify alterations in myofibril size and organization after outflow tract banding, myofibrils were segmented from high-resolution image volumes of HH24 outflow tract tissue acquired using FIB-SEM, as described in section 5.3.4 [214]. 3D FIB-SEM reconstructions of myofibril bundle segmentations were used to calculate myofibril volume fraction in the cell cytoplasm, fibril bundle orientation, and bundle thickness (Figure 7-2). Myofibril bundle orientation was quantified in terms of angles φ and θ, where φ is the angle of the fibril bundle in the xy plane (circumferential plane of the outflow tract), and θ is the angle of the fibril bundle in the xz plane (radial plane of the outflow tract). While myofibril volume fraction and fibril orientation angles in the radial plane were unchanged after banding, fibril bundles were more clustered, fibril orientation angles were more disbursed in the circumferential plane, and fibril bundles were thicker following increased hemodynamic load.

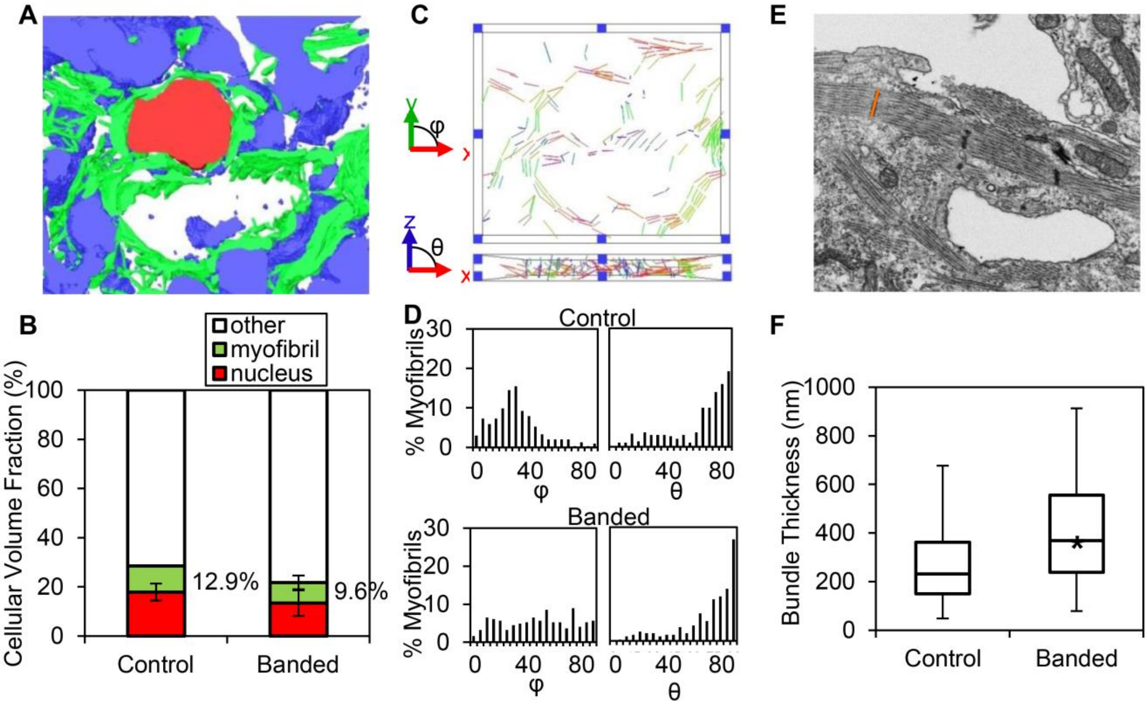

Figure 7-2. Myofibril segmentation quantification summary. (A) Example 3D myocardium segmentation reconstruction with myofibrils, nucleus, and extracellular material displayed in green, red, and blue, respectively. (B) Average cellular volume fraction quantification from 3D reconstructions (n=3). Myofibril/cytoplasmic volume fraction is shown next to the cellular volume display. (C) Example myofibril bundle orientation display where each bundle is shown colored based on the orientation in the xy and xz planes. (D) Example myofibril bundle orientation angle histograms for a control and banded embryo. (E) Example FIB-SEM image with an example bundle thickness measurement length at a z-band shown in orange. (F) Bundle thickness quantification box plots displaying the average, with boxes that mark the upper and lower quartiles and whiskers that mark the maximum and minimum values (n=3). The asterisk designates a significantly higher bundle thickness average in banded samples compared to controls (p-value<0.05).

Although previous studies have thoroughly characterized myofibril morphology during development, the mechanisms of myofibril formation and alignment are still poorly understood [271]. It has been postulated, however, that fibrils align in specific regions of the heart in response to mechanical contraction stresses that increase throughout development [267]. Raeker et al suggested that fibril bundles slide to align z-disks as well as dismantle and reassemble fibrils to aid in bundling small myofibril clusters to form larger bundle units in skeletal muscle. Further, they concluded that degradation in myofibril organization and reorganization of bundles during development seemed to occur when the offset between z-disks was too great to permit intact integration [270]. Differences in φ distributions in our samples may be due to similar shifting of myofibrils to cluster and align, which results in thicker bundles. These changes in myofibril organization and size suggest that the increased hemodynamic load induced by banding may accelerate the normal myocardial maturation process. It is possible that overdeveloped myofibrils in select portions of the heart become more abnormal as development progresses and contribute to the development of cardiac defects.

7.2.2 Myocardial apoptosis remodeling

Programmed cell death plays a role in embryonic heart development by selectively removing and sculpting the myocardium [272]. Apoptosis regulation in the outflow tract of the early embryonic heart is critical for normal morphogenesis, since genetic or environmental perturbation of apoptotic remodeling leads to conotruncal heart anomalies [273-276]. Studies in chick have shown that the elimination of myocytes by programmed cell death is one of the mechanisms by which the outflow tract myocardium remodels to form portions of the mature heart, specifically by shortening the outflow tract during looping and septation stages [277].

Preliminary data used outflow tract banding and apoptosis labeling techniques to determine the effects of increased hemodynamic load between HH18-HH24 on apoptotic remodeling of the outflow tract. Size and spatial distributions of apoptotic regions were analyzed at HH24 using terminal deoxynucleotidyl transferase dUTP nick end (TUNEL) and LysoTracker Red (LTR) staining. While TUNEL staining directly detected apoptotic cells, the technique was limited to thin histological sections to allow for permeability of a terminal transferase. In contrast, LysoTracker Red dye was highly soluble, retained in active subcellular lysosomal compartments, and used to correlate lysosomal activity to increased cell death in whole heart samples. Increased hemodynamic load induced larger apoptotic regions in the myocardium at the ventricle/outflow tract junction (upstream of the band) and in downstream portions of outflow tract (downstream of the band), where LysoTracker Red particle counts from confocal image stacks were most increased following high hemodynamic load conditions induced by tight bands. This apoptotic remodeling pattern was confirmed with TUNEL-stained sample image analysis. This preliminary data suggests that normal programmed cell death remodeling of the outflow tract is accelerated after banding, which may contribute to the malformation that leads to defects.

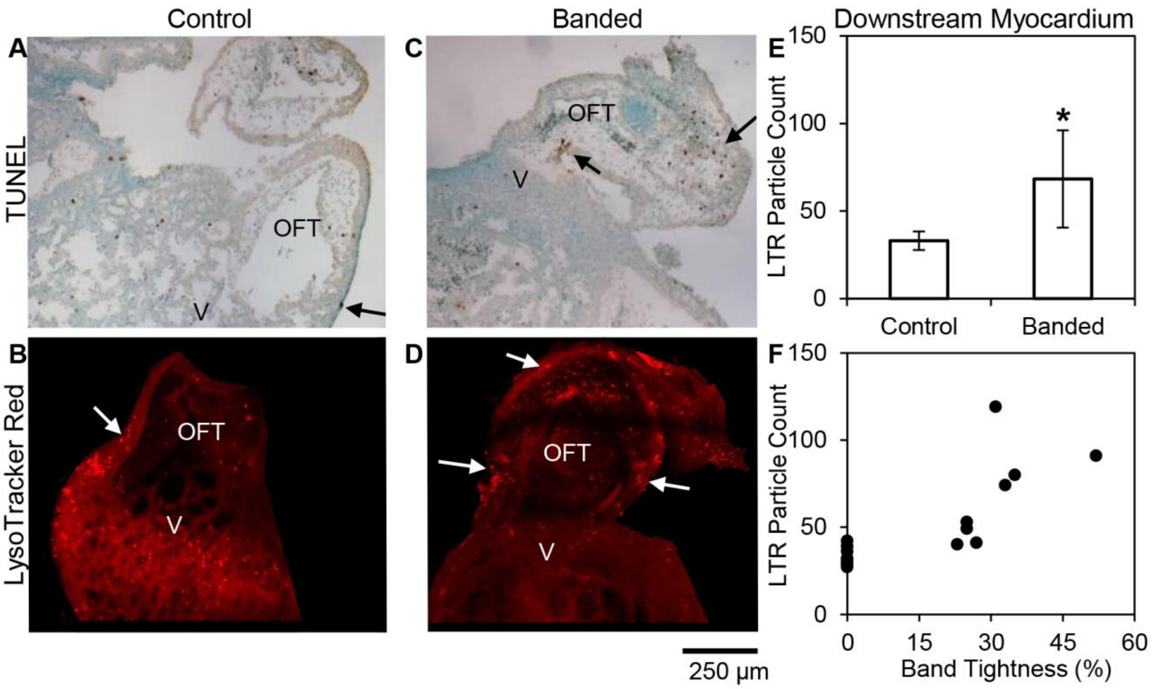

Figure 7-3. Apoptosis quantification summary. Example TUNEL-stained (A) and LTR-stained (B) tissue from control samples. Example TUNEL-stained (C) and LTR-stained (D) tissue from banded samples. (E) Average LTR particle counts in portions of the outflow tract downstream of the ventricle/outflow tract junction with error bars that display standard deviation (n=8). The asterisk designates a significantly higher LTR particle count average in banded samples compared to controls (p-value<0.05). (F) Individual LTR particle count values based on band tightness. Arrows in A-D mark areas of apoptosis. OFT, outflow tract; V, ventricle.

7.2.3 Myocardial proliferation remodeling

Cell proliferation is another remodeling mechanism that is affected by mechanical loading [213], and when perturbed may contribute to the development of cardiac defects. Proliferative activity in the embryonic heart increases organ mass to meet the increasing circulatory demands of the growing embryo. Additionally, regional differences in proliferative cell activity work in concert with differentiation, migration, and cell death to shape the developing heart [146]. Future studies will use outflow tract banding and cell proliferation labeling techniques to determine the effects of increased hemodynamic load between HH18-HH24 on proliferative cell remodeling of the outflow tract. Proliferating cells in the outflow tract will be DNA labeled with a Click-iT EdU kit that detects a thymidine analog in the intact double-stranded DNA, as described by Scott-Dreschel et al [278]. Similar to the methods described in section 5.3.3, the whole heart of outflow tract banded and control samples will be labeled, imaged with confocal microscopy, and the images reconstructed to create a 3D proliferation analysis of the outflow tract. A ratio of proliferating cells versus non-proliferating cells will be calculated from the image stack. This study will help determine the effects of increased hemodynamic load on myocardial proliferative remodeling of the heart. Any perturbation to the finely-tuned coordination of mechanisms involved in cardiac morphogenesis may lead to the development of cardiac defects.

7.2.4 Myocardial mitochondrial remodeling

Developing myocardial mitochondria serve the crucial role of supplying energy to contractile myofibrils. Mitochondria are initially dispersed throughout the cytoplasm in developing myocytes [279], and over development increase in volume fraction and arrange in an organized pattern [280]. In adult and late fetal periods, myocardial mitochondria are stacked in orderly rows between a myofibrillar lattice, and form contacts with surrounding ATP consumption sites to aid in contraction [281, 282]. The preliminary FIB-SEM image in Figure 7-4 shows mitochondria with clear cristae and ribosomes scattered throughout the cytoplasm. Future work will focus on segmenting mitochondria from the FIB-SEM image stacks, in order to reconstruct 3D mitochondrial structures and analyze the 3D architecture of mitochondrial-myofibril networks. Mitochondrial stacking, clustering, and cellular volume fraction will be evaluated in outflow tract banded and control tissue in order to elucidate the effects of increased hemodynamic load on mitochondrial organization. Changes in normal mitochondrial development may help reveal the ways in which altered hemodynamics trigger cardiac malformation.

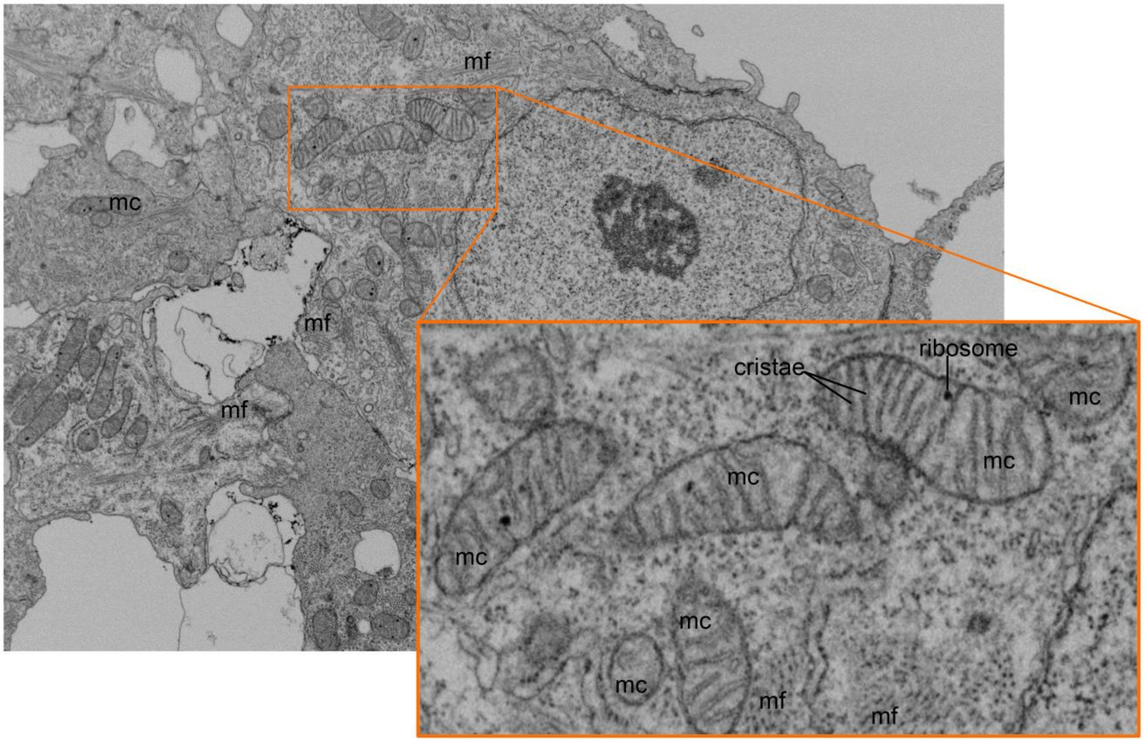

Figure 7-4. Example FIB-SEM image showing mitochondria in control outflow tract myocardium tissue. The enlarged region shows a cluster of mitochondria with clearly visible cristae and ribosomes. mc, mitochondria; mf, myofibril.

7.3 Global transcriptome and proteome changes induced by increased hemodynamic load

Future studies are planned to characterize global changes in transcriptome and proteome expression in outflow tract banded samples in order to determine how developmental signaling pathways are modified by abnormal hemodynamic load. The ways in which blood flow forces perturb normal cardiac morphogenesis and trigger cardiac malformation likely involve several, intricate regulatory pathways. These finely-tuned signaling networks are excessively complex to unravel by analyzing expression changes in small groups of genes with traditional PCR. Thus we plan to use shotgun analysis by RNASeq and mass-spectrometry to sensitively and accurately measure changes in comprehensive regulatory control by analyzing the whole transcriptome and proteome, respectively. This analysis will complement the results presented in this dissertation, to better understand the role of early genotype changes in the expression of cardiac phenotypes.

After outflow tract banding at HH18 and outflow tract tissue collection at HH24, RNASeq analysis will be used to detect changes in gene expression and mass spectrometry will be used to identify differences in protein abundance in banded samples compared to controls. RNASeq and analysis will be performed by OHSU's Massively Parallel Sequencing Shared Resource core facility. Some mass spectrometry data, performed by OHSU's Proteomics Shared Resource core facility, is presented in Chapter 5. Several protein markers of EMT significantly varied in abundance between banded and control samples. However, there was also an additional 568 significant changes in proteins levels after banding that were not directly related to EMT, which are likely involved in other key cardiac morphogenesis processes, including proliferation, apoptosis, differentiation, and migration. These global changes require a thorough pathway analysis by bioinformatics experts in the core facilities to determine how control of cardiac development is affected by altered blood flow. Network analysis will be used to identify functionally upregulated or downregulated signaling pathways in banded samples, by comparing components with altered levels of expression to a database of those genes/proteins known to have regulatory influence. Pathway investigation results from both the RNASeq and mass-spectrometry will also be compared to gain insights into regulatory control differences between the gene and protein levels. Furthermore, alterations in signaling hubs and the most relevant interactions determined by bioinformatics pathway analysis can be used to identify the most promising candidates for further investigations of the effects of altered hemodynamic loads.

7.4 Early outflow tract remodeling following decreased hemodynamic load

The work in this dissertation explores the effects of altered hemodynamics on cardiac remodeling and malformation by mainly employing the outflow tract banding surgical intervention. This intervention is extremely valuable since we have shown that the blood flow conditions induced by banding can be precisely controlled by the degree of band tightness (Chapter 4), and the different hemodynamic levels lead to specific cardiac defect phenotypes (Chapter 6). Even though outflow tract banding produces a range of hemodynamic change, the intervention always increases hemodynamic load on the developing heart. Contrastingly, the late stage defect study in Chapter 6 also included the vitelline vein ligation intervention to investigate the effects of decreased hemodynamic load on cardiac morphogenesis. Future work will incorporate the vitelline vein ligation as well as the left atrium ligation into investigations of detrimental early tissue remodeling. Vitelline vein ligation will serve as a model of an acute decrease in hemodynamic load, since the returning blood that is blocked by the ligation is redirected back to the heart after approximately 5 hours [40, 67-69]. Left atrium ligation instead serves as a chronic model of decreased hemodynamic load that is created by restricting blood flow entering the primitive ventricle [8, 12]. Specifically, future studies are planned to determine the effect of decreased hemodynamic load on EMT and myocardial remodeling. The EMT study will mirror the methods explained in Chapter 5, which strongly suggests that increased hemodynamic load from outflow tract banding enhances the EMT phenotype in the outflow tract cushions. We hypothesize that decreased hemodynamic load induced by vitelline vein ligation and left atrial ligation may halt or slow EMT in the outflow tract. The effects of decreased hemodynamic load on normal myocardial remodeling will closely follow the studies outlined for future outflow tract banding studies in section 7.2. Expansion of the range of hemodynamic change will aid in elucidating the complex triggers of CHD.

7.5 Tissue remodeling abnormalities presented with cardiac defects

The work presented in Chapter 6 determined that defined blood flow patterns induced in early cardiogenesis lead to specific and unique heart defects in later development. This characterization of overall cardiac structure and function clearly demonstrated that abnormal hemodynamics underlie cardiac malformations that are similar to CHD cases in humans. Future work is planned to investigate the compositional changes in cardiac tissue once major heart defects are formed, in order to further elucidate the detrimental remodeling processes involved in specific defect phenotypes. Several defects were induced in our chick model after varied constriction ranges of outflow tract banding in early development, including ventricular septal defect (VSD), double outlet right ventricle (DORV), Tetralogy of Fallot (TOF), and pharyngeal arch artery malformation. Initial changes in hemodynamics after banding and the subsequent altered blood flow patterns induced by the structural malformation likely trigger a unique tissue remodeling response in each defect scenario. Hence, tissue remodeling abnormalities specific to TOF and DORV defects will be investigated with histology. Considering fetal sheep models have shown that increased hemodynamic load during late gestational periods induces abnormal cardiomyocyte growth and proliferation in otherwise normal hearts [283-285], this future work will begin with similar investigations of tissue remodeling. Following the methods presented in Chapter 6, after outflow tract banding at HH18, embryo hearts with TOF and DORV defects at HH38 will be collected and prepared for histology. Histology sections from the right and left ventricle will be processed for immunohistochemistry labeling of cardiac troponin I to quantify cell shape and size, Masson’s trichrome staining to additionally identify areas of fibrosis, and immunohistochemistry labeling of Ki-67 to mark and quantify cell proliferation. This model has the potential to serve as a valuable tool to better understand not only the structural abnormalities of heart defects but also tissue remodeling implications of CHD.

References

1. Martinsen, B.J., *Reference guide to the stages of chick heart embryology.* Dev Dyn, 2005. **233**(4): p. 1217-37.
2. Goenezen, S., M.Y. Rennie, and S. Rugonyi, *Biomechanics of Early Cardiac Development.* Biomech Model Mechanobiol, 2012. **11**(8): p. 1187-1204.
3. Hove, J.R., R.W. Koster, A.S. Forouhar, G. Acevedo-Bolton, S.E. Fraser, and M. Gharib, *Intracardiac fluid forces are an essential epigenetic factor for embryonic cardiogenesis.* Nature, 2003. **421**(6919): p. 172-7.
4. Goodwin, R.L., T. Nesbitt, R.L. Price, J.C. Wells, M.J. Yost, and J.D. Potts, *Three-dimensional model system of valvulogenesis.* Dev Dyn, 2005. **233**(1): p. 122-9.
5. Campbell, S.G. and A.D. McCulloch, *Multi-scale computational models of familial hypertrophic cardiomyopathy: genotype to phenotype.* J R Soc Interface, 2011. **8**(64): p. 1550-61.
6. Humphrey, J.D., *Mechanisms of arterial remodeling in hypertension: coupled roles of wall shear and intramural stress.* Hypertension, 2008. **52**(2): p. 195-200.
7. Clark, E.B. and G.C. Rosenquist, *Spectrum of cardiovascular anomalies following cardiac loop constriction in the chick embryo.* Birth Defects Orig Artic Ser, 1978. **14**(7): p. 431-42.
8. Sedmera, D., T. Pexieder, V. Rychterova, N. Hu, and E.B. Clark, *Remodeling of chick embryonic ventricular myoarchitecture under experimentally changed loading conditions.* Anat Rec, 1999. **254**(2): p. 238-52.
9. Clark, E.B., N. Hu, P. Frommelt, G.K. Vandekieft, J.L. Dummett, and R.J. Tomanek, *Effect of increased pressure on ventricular growth in stage 21 chick embryos.* Am J Physiol, 1989. **257**(1 Pt 2): p. H55-61.

10. Hogers, B., M.C. DeRuiter, A.C. Gittenberger-de Groot, and R.E. Poelmann, *Unilateral vitelline vein ligation alters intracardiac blood flow patterns and morphogenesis in the chick embryo.* Circ Res, 1997. **80**(4): p. 473-81.

11. Harh, J.Y., M.H. Paul, W.J. Gallen, D.Z. Friedberg, and S. Kaplan, *Experimental production of hypoplastic left heart syndrome in the chick embryo.* Am J Cardiol, 1973. **31**(1): p. 51-6.

12. Tobita, K. and B.B. Keller, *Right and left ventricular wall deformation patterns in normal and left heart hypoplasia chick embryos.* Am J Physiol Heart Circ Physiol, 2000. **279**(3): p. H959-69.

13. Fisher, A.B., S. Chien, A.I. Barakat, and R.M. Nerem, *Endothelial cellular response to altered shear stress.* Am J Physiol Lung Cell Mol Physiol, 2001. **281**(3): p. L529-33.

14. Omens, J.H., *Stress and strain as regulators of myocardial growth.* Prog Biophys Mol Biol, 1998. **69**(2-3): p. 559-72.

15. Fahed, A.C., B.D. Gelb, J.G. Seidman, and C.E. Seidman, *Genetics of congenital heart disease: the glass half empty.* Circ Res, 2013. **112**(4): p. 707-20.

16. Hoffman, J.I. and S. Kaplan, *The incidence of congenital heart disease.* J Am Coll Cardiol, 2002. **39**(12): p. 1890-900.

17. Yang, M., L.A. Taber, and E.B. Clark, *A nonliner poroelastic model for the trabecular embryonic heart.* J Biomech Eng, 1994. **116**(2): p. 213-23.

18. Russo, C.A. and A. Elixhauser, *Hospitalizations for Birth Defects, 2004: Statistical Brief #24*, in *Healthcare Cost and Utilization Project (HCUP) Statistical Briefs*. 2006, Agency for Healthcare Research and Quality (US): Rockville (MD).

19. Roos-Hesselink, J.W., W.S. Kerstjens-Frederikse, F.J. Meijboom, and P.G. Pieper, *Inheritance of congenital heart disease.* Neth Heart J, 2005. **13**(3): p. 88-91.

20. Richards, A.A. and V. Garg, *Genetics of Congenital Heart Disease.* Curr Cardiol Rev, 2010. **6**(2): p. 91-7.

21. Gilboa, S.M., A. Correa, L.D. Botto, S.A. Rasmussen, D.K. Waller, C.A. Hobbs, M.A. Cleves, and T.J. Riehle-Colarusso, *Association between prepregnancy body mass index and congenital heart defects.* Am J Obstet Gynecol, 2010. **202**(1): p. 51.e1-51.e10.

22. Correa, A., S.M. Gilboa, L.M. Besser, L.D. Botto, C.A. Moore, C.A. Hobbs, M.A. Cleves, T.J. Riehle-Colarusso, D.K. Waller, and E.A. Reece, *Diabetes mellitus and birth defects.* Am J Obstet Gynecol, 2008. **199**(3): p. 237.e1-9.

23. Malik, S., M.A. Cleves, M.A. Honein, P.A. Romitti, L.D. Botto, S. Yang, and C.A. Hobbs, *Maternal smoking and congenital heart defects.* Pediatrics, 2008. **121**(4): p. e810-6.

24. Kim, S.Y., P.M. Dietz, L. England, B. Morrow, and W.M. Callaghan, *Trends in pre-pregnancy obesity in nine states, 1993-2003.* Obesity (Silver Spring), 2007. **15**(4): p. 986-93.

25. Nohr, E.A., B.H. Bech, M.J. Davies, M. Frydenberg, T.B. Henriksen, and J. Olsen, *Prepregnancy obesity and fetal death: a study within the Danish National Birth Cohort.* Obstet Gynecol, 2005. **106**(2): p. 250-9.

26. Frias, A.E., T.K. Morgan, A.E. Evans, J. Rasanen, K.Y. Oh, K.L. Thornburg, and K.L. Grove, *Maternal high-fat diet disturbs uteroplacental hemodynamics and increases the frequency of stillbirth in a nonhuman primate model of excess nutrition.* Endocrinology, 2011. **152**(6): p. 2456-64.

27. Huang, L., J. Liu, L. Feng, Y. Chen, J. Zhang, and W. Wang, *Maternal prepregnancy obesity is associated with higher risk of placental pathological lesions.* Placenta, 2014. **35**(8): p. 563-9.

28. Bellotti, M., G. Pennati, C. De Gasperi, M. Bozzo, F.C. Battaglia, and E. Ferrazzi, *Simultaneous measurements of umbilical venous, fetal hepatic, and ductus venosus blood flow in growth-restricted human fetuses.* Am J Obstet Gynecol, 2004. **190**(5): p. 1347-58.

29. Cohen, E., F.Y. Wong, R.S. Horne, and S.R. Yiallourou, *Intrauterine growth restriction: impact on cardiovascular development and function throughout infancy.* Pediatr Res, 2016. **79**(6): p. 821-30.

30. Thornburg, K.L., P.F. O'Tierney, and S. Louey, *Review: The placenta is a programming agent for cardiovascular disease.* Placenta, 2010. **31 Suppl**: p. S54-9.

31. Kiserud, T., C. Ebbing, J. Kessler, and S. Rasmussen, *Fetal cardiac output, distribution to the placenta and impact of placental compromise.* Ultrasound Obstet Gynecol, 2006. **28**(2): p. 126-36.

32. Hogers, B., M.C. DeRuiter, A.C. Gittenberger-de Groot, and R.E. Poelmann, *Extraembryonic venous obstructions lead to cardiovascular malformations and can be embryolethal.* Cardiovasc Res, 1999. **41**(1): p. 87-99.

33. Hu, N., D.A. Christensen, A.K. Agrawal, C. Beaumont, E.B. Clark, and J.A. Hawkins, *Dependence of aortic arch morphogenesis on intracardiac blood flow in the left atrial ligated chick embryo.* Anat Rec (Hoboken), 2009. **292**(5): p. 652-60.

34. Hutson, M.R. and M.L. Kirby, *Model systems for the study of heart development and disease: Cardiac neural crest and conotruncal malformations.* Seminars in Cell & Developmental Biology, 2007. **18**(1): p. 101-110.

35. Ruijtenbeek, K., J.G.R. De Mey, and C.E. Blanco, *The Chicken Embryo in Developmental Physiology of the Cardiovascular System: A Traditional Model with New Possibilities.* Am J Physiol Regul Integr Comp Physiol, 2002. **283**(2): p. R549-R551.

36. Crossley, D., 2nd and J. Altimiras, *Ontogeny of cholinergic and adrenergic cardiovascular regulation in the domestic chicken (Gallus gallus).* Am J Physiol Regul Integr Comp Physiol, 2000. **279**(3): p. R1091-8.

37. Hamburger, V. and H.L. Hamilton, *A series of normal stages in the development of the chick embryo. 1951.* Dev Dyn, 1992. **195**(4): p. 231-72.

38. Gittenberger-de Groot, A.C., M.M. Bartelings, M.C. Deruiter, and R.E. Poelmann, *Basics of cardiac development for the understanding of congenital heart malformations.* Pediatr Res, 2005. **57**(2): p. 169-76.

39. Culver, J.C. and M.E. Dickinson, *The effects of hemodynamic force on embryonic development.* Microcirculation, 2010. **17**(3): p. 164-78.

40. Broekhuizen, M.L., B. Hogers, M.C. DeRuiter, R.E. Poelmann, A.C. Gittenberger-de Groot, and J.W. Wladimiroff, *Altered hemodynamics in chick embryos after extraembryonic venous obstruction.* Ultrasound Obstet Gynecol, 1999. **13**(6): p. 437-45.

41. Oscar, C., *Hemodynamic Factors in the Development of the Chick Embryo Heart.* Anat Rec, 1965. **151**: p. 69-76.

42. Icardo, J.M., *Developmental biology of the vertebrate heart.* J Exp Zool, 1996. **275**(2-3): p. 144-61.

43. Tobita, K., J.B. Garrison, L.J. Liu, J.P. Tinney, and B.B. Keller, *Three-dimensional myofiber architecture of the embryonic left ventricle during normal development and altered mechanical loads.* Anat Rec A Discov Mol Cell Evol Biol, 2005. **283**(1): p. 193-201.

44. deAlmeida, A., T. McQuinn, and D. Sedmera, *Increased ventricular preload is compensated by myocyte proliferation in normal and hypoplastic fetal chick left ventricle.* Circ Res, 2007. **100**(9): p. 1363-70.

45. Rychter, Z., *Experimental morphology of the aortic arches and the heart loop in chick embryos.* Adv Morphogen, 1962. **2**: p. 333-371.

46. Sedmera, D., N. Hu, K.M. Weiss, B.B. Keller, S. Denslow, and R.P. Thompson, *Cellular changes in experimental left heart hypoplasia.* Anat Rec, 2002. **267**(2): p. 137-45.

47. Clark, E.B., N. Hu, and G.C. Rosenquist, *Effect of conotruncal constriction on aortic-mitral valve continuity in the stage 18, 21 and 24 chick embryo.* Am J Cardiol, 1984. **53**(2): p. 324-7.

48. Hu, N. and E.B. Clark, *Hemodynamics of the stage 12 to stage 29 chick embryo.* Circ Res, 1989. **65**(6): p. 1665-70.

49. Van der Heiden, K., B.C. Groenendijk, B.P. Hierck, B. Hogers, H.K. Koerten, A.M. Mommaas, A.C. Gittenberger-de Groot, and R.E. Poelmann, *Monocilia on chicken embryonic endocardium in low shear stress areas.* Dev Dyn, 2006. **235**(1): p. 19-28.

50. Keller, B., *Function and Biomechanics of Developing Cardiovascular Systems*, in *Formation of the Heart and Its Regulation*, R. Tomanek and R. Runyan, Editors. 2001, Birkhäuser Boston. p. 251-271.

51. Tobita, K., E.A. Schroder, J.P. Tinney, J.B. Garrison, and B.B. Keller, *Regional passive ventricular stress-strain relations during development of altered loads in chick embryo.* Am J Physiol Heart Circ Physiol, 2002. **282**(6): p. H2386-96.

52. Shi, L., S. Goenezen, S. Haller, M.T. Hinds, K.L. Thornburg, and S. Rugonyi, *Alterations in pulse wave propagation reflect the degree of outflow tract banding in HH18 chicken embryos.* Am J Physiol Heart Circ Physiol, 2013. **305**(3): p. H386-96.

53. Groenendijk, B.C., K. Van der Heiden, B.P. Hierck, and R.E. Poelmann, *The role of shear stress on ET-1, KLF2, and NOS-3 expression in the developing cardiovascular system of chicken embryos in a venous ligation model.* Physiology (Bethesda), 2007. **22**: p. 380-9.

54. Bruneau, B.G., *The developmental genetics of congenital heart disease.* Nature, 2008. **451**(7181): p. 943-8.

55. Phoon, C.K., R.P. Ji, O. Aristizabal, D.M. Worrad, B. Zhou, H.S. Baldwin, and D.H. Turnbull, *Embryonic heart failure in NFATc1-/- mice: novel mechanistic insights from in utero ultrasound biomicroscopy.* Circ Res, 2004. **95**(1): p. 92-9.

56. Zhou, Y.Q., F.S. Foster, D.W. Qu, M. Zhang, K.A. Harasiewicz, and S.L. Adamson, *Applications for multifrequency ultrasound biomicroscopy in mice from implantation to adulthood.* Physiol Genomics, 2002. **10**(2): p. 113-26.

57. James, J.F., T.E. Hewett, and J. Robbins, *Cardiac physiology in transgenic mice.* Circ Res, 1998. **82**(4): p. 407-15.

58. Yu, Q., L. Leatherbury, X. Tian, and C.W. Lo, *Cardiovascular assessment of fetal mice by in utero echocardiography.* Ultrasound Med Biol, 2008. **34**(5): p. 741-52.

59. Piliszek, A., G. Kwon, and A.-K. Hadjantonakis, *Ex Utero Culture and Live Imaging of Mouse Embryos*, in *Vertebrate Embryogenesis*, F.J. Pelegri, Editor. 2011, Humana Press. p. 243-257.

60. Miura, G.I. and D. Yelon, *A guide to analysis of cardiac phenotypes in the zebrafish embryo.* Methods Cell Biol, 2011. **101**: p. 161-80.

61. Jenkins, M.W., L. Peterson, S. Gu, M. Gargesha, D.L. Wilson, M. Watanabe, and A.M. Rollins, *Measuring hemodynamics in the developing heart tube with four-dimensional gated Doppler optical coherence tomography.* J Biomed Opt, 2010. **15**(6): p. 066022.

62. Rugonyi, S., C. Shaut, A. Liu, K. Thornburg, and R.K. Wang, *Changes in wall motion and blood flow in the outflow tract of chick embryonic hearts observed with optical coherence tomography after outflow tract banding and vitelline-vein ligation.* Phys Med Biol, 2008. **53**(18): p. 5077-91.

63. McQuinn, T.C., M. Bratoeva, A. Dealmeida, M. Remond, R.P. Thompson, and D. Sedmera, *High-frequency ultrasonographic imaging of avian cardiovascular development.* Dev Dyn, 2007. **236**(12): p. 3503-13.

64. Liu, A., X. Yin, L. Shi, P. Li, K.L. Thornburg, R. Wang, and S. Rugonyi, *Biomechanics of the Chick Embryonic Heart Outflow Tract at HH18 Using 4D Optical Coherence Tomography Imaging and Computational Modeling.* PLoS ONE, 2012. **7**(7): p. e40869.

65. Peterson, L.M., M.W. Jenkins, S. Gu, L. Barwick, M. Watanabe, and A.M. Rollins, *4D shear stress maps of the developing heart using Doppler optical coherencetomography.* Biomed Opt Express, 2012. **3**(11): p. 3022-3032.

66. Stekelenburg-de Vos, S., N.T. Ursem, W.C. Hop, J.W. Wladimiroff, A.C. Gittenberger-de Groot, and R.E. Poelmann, *Acutely altered hemodynamics following venous obstruction in the early chick embryo.* J Exp Biol, 2003. **206**(Pt 6): p. 1051-7.

67. Ursem, N.T., S. Stekelenburg-de Vos, J.W. Wladimiroff, R.E. Poelmann, A.C. Gittenberger-de Groot, N. Hu, and E.B. Clark, *Ventricular diastolic filling characteristics in stage-24 chick embryos after extra-embryonic venous obstruction.* J Exp Biol, 2004. **207**(Pt 9): p. 1487-90.

68. Stekelenburg-de Vos, S., P. Steendijk, N.T. Ursem, J.W. Wladimiroff, R. Delfos, and R.E. Poelmann, *Systolic and diastolic ventricular function assessed by pressure-volume loops in the stage 21 venous clipped chick embryo.* Pediatr Res, 2005. **57**(1): p. 16-21.

69. Stekelenburg-de Vos, S., P. Steendijk, N.T. Ursem, J.W. Wladimiroff, and R.E. Poelmann, *Systolic and diastolic ventricular function in the normal and extra-embryonic venous clipped chicken embryo of stage 24: a pressure-volume loop assessment.* Ultrasound Obstet Gynecol, 2007. **30**(3): p. 325-31.

70. Lucitti, J.L., K. Tobita, and B.B. Keller, *Arterial hemodynamics and mechanical properties after circulatory intervention in the chick embryo.* J Exp Biol, 2005. **208**(Pt 10): p. 1877-85.

71. Manner, J., *Cardiac looping in the chick embryo: a morphological review with special reference to terminological and biomechanical aspects of the looping process.* Anat Rec, 2000. **259**(3): p. 248-62.

72. Oppenheimer-Dekker, A., R.J. Moene, A.J. Moulaert, and A.C. Gittenberger-de Groot, *Teratogenetic Considerations Regarding Aortic Arch Anomalies Associated with Cardiovascular Malformations*, in *Perspectives in Cardiovascular Research: Mechanisms of Cardiac Morphogenesis and Teratogenesis*, T. Pexieder, Editor. 1981, Raven Press: New York. p. 485-500.

73. Dyer, L.A. and M.L. Kirby, *The role of secondary heart field in cardiac development.* Dev Biol, 2009. **336**(2): p. 137-44.

74. Kelly, R.G., N.A. Brown, and M.E. Buckingham, *The arterial pole of the mouse heart forms from Fgf10-expressing cells in pharyngeal mesoderm.* Dev Cell, 2001. **1**(3): p. 435-40.

75. Mjaatvedt, C.H., T. Nakaoka, R. Moreno-Rodriguez, R.A. Norris, M.J. Kern, C.A. Eisenberg, D. Turner, and R.R. Markwald, *The outflow tract of the heart is recruited from a novel heart-forming field.* Dev Biol, 2001. **238**(1): p. 97-109.

76. Waldo, K.L., D.H. Kumiski, K.T. Wallis, H.A. Stadt, M.R. Hutson, D.H. Platt, and M.L. Kirby, *Conotruncal myocardium arises from a secondary heart field.* Development, 2001. **128**(16): p. 3179-88.

77. Kelly, R.G., *Chapter two - The Second Heart Field*, in *Current Topics in Developmental Biology*, G.B. Benoit, Editor. 2012, Academic Press. p. 33-65.

78. de la Cruz, M.V., C. Sanchez-Gomez, and M.A. Palomino, *The primitive cardiac regions in the straight tube heart (Stage 9-) and their anatomical expression in the mature heart.* Journal of Anatomy, 1989. **165**(121-131).

79. Mercola, M. and M. Levin, *Left-right asymmetry determination in vertebrates.* Annu Rev Cell Dev Biol, 2001. **17**: p. 779-805.

80. Baker, K., N.G. Holtzman, and R.D. Burdine, *Direct and indirect roles for Nodal signaling in two axis conversions during asymmetric morphogenesis of the zebrafish heart.* Proc Natl Acad Sci U S A, 2008. **105**(37): p. 13924-9.

81. Stalsberg, H., *Development and ultrastructure of the embryonic heart. II. Mechanism of dextral looping of the embryonic heart.* Am J Cardiol, 1970. **25**(3): p. 265-71.

82. Taber, L.A., *Mechanical aspects of cardiac development.* Prog Biophys Mol Biol, 1998. **69**(2–3): p. 237-255.

83. Voronov, D.A., P.W. Alford, G. Xu, and L.A. Taber, *The role of mechanical forces in dextral rotation during cardiac looping in the chick embryo.* Dev Biol, 2004. **272**(2): p. 339-50.

84. Voronov, D.A. and L.A. Taber, *Cardiac looping in experimental conditions: effects of extraembryonic forces.* Dev Dyn, 2002. **224**(4): p. 413-21.

85. Manner, J., L. Thrane, K. Norozi, and T.M. Yelbuz, *In vivo imaging of the cyclic changes in cross-sectional shape of the ventricular segment of pulsating embryonic chick hearts at stages 14 to 17: a contribution to the understanding of the ontogenesis of cardiac pumping function.* Dev Dyn, 2009. **238**(12): p. 3273-84.

86. Sedmera, D., T. Pexieder, N. Hu, and E.B. Clark, *Developmental changes in the myocardial architecture of the chick.* Anat Rec, 1997. **248**(3): p. 421-32.

87. Ben-Shachar, G., R.A. Arcilla, R.V. Lucas, and F.J. Manasek, *Ventricular trabeculations in the chick embryo heart and their contribution to ventricular and muscular septal development.* Circ Res, 1985. **57**(5): p. 759-66.

88. Challice, C.E. and S. Viragh, *The architectural development of the early mammalian heart.* Tissue Cell, 1974. **6**(3): p. 447-62.

89. Taber, L.A., *On a nonlinear theory for muscle shells: Part II--Application to the beating left ventricle.* J Biomech Eng, 1991. **113**(1): p. 63-71.

90. Wang, Y., O. Dur, M.J. Patrick, J.P. Tinney, K. Tobita, B.B. Keller, and K. Pekkan, *Aortic arch morphogenesis and flow modeling in the chick embryo.* Ann Biomed Eng, 2009. **37**(6): p. 1069-81.

91. Hiruma, T. and R. Hirakow, *Formation of the pharyngeal arch arteries in the chick embryo. Observations of corrosion casts by scanning electron microscopy.* Anat Embryol (Berl), 1995. **191**(5): p. 415-23.

92. Keller, B.B., L.J. Liu, J.P. Tinney, and K. Tobita, *Cardiovascular developmental insights from embryos.* Ann N Y Acad Sci, 2007. **1101**: p. 377-88.

93. Pekkan, K., L.P. Dasi, P. Nourparvar, S. Yerneni, K. Tobita, M.A. Fogel, B. Keller, and A. Yoganathan, *In vitro hemodynamic investigation of the embryonic aortic arch at late gestation.* J Biomech, 2008. **41**(8): p. 1697-706.

94. Kowalski, W.J., O. Dur, Y. Wang, M.J. Patrick, J.P. Tinney, B.B. Keller, and K. Pekkan, *Critical transitions in early embryonic aortic arch patterning and hemodynamics.* PLoS ONE, 2013. **8**(3): p. e60271.

95. Lamers, W.H. and A.F. Moorman, *Cardiac septation: a late contribution of the embryonic primary myocardium to heart morphogenesis.* Circ Res, 2002. **91**(2): p. 93-103.

96. van den Berg, G. and A.F. Moorman, *Concepts of cardiac development in retrospect.* Pediatr Cardiol, 2009. **30**(5): p. 580-7.

97. Hendrix, M.J.C. and D.E. Morse, *Atrial septation: I. Scanning electron microscopy in the chick.* Dev Biol, 1977. **57**(2): p. 345-363.

98. Rychter Z, R.V., *Angio- and myoarchitecture of the heart wall under normal and experimentally changed conditions*. Perspectives in cardiovascular research, Vol. 5, Mechanisms of cardiac morphogenesis and teratogenesis., ed. P. T. Vol. 5. 1981, New York: Raven Press.

99. Hoffman, J.I., *Incidence of congenital heart disease: I. Postnatal incidence.* Pediatr Cardiol, 1995. **16**(3): p. 103-13.

100. Minette, M.S. and D.J. Sahn, *Ventricular septal defects.* Circulation, 2006. **114**(20): p. 2190-7.

101. Penny, D.J. and G.W.I. Vick, *Ventricular septal defect.* The Lancet, 2011. **377**(9771): p. 1103-1112.

102. Hoffman, J.I., *Incidence of congenital heart disease: II. Prenatal incidence.* Pediatr Cardiol, 1995. **16**(4): p. 155-65.

103. Arora, R., V. Trehan, A.K. Thakur, V. Mehta, P.P. Sengupta, and M. Nigam, *Transcatheter closure of congenital muscular ventricular septal defect.* J Interv Cardiol, 2004. **17**(2): p. 109-15.

104. Fu, Y.C., J. Bass, Z. Amin, W. Radtke, J.P. Cheatham, W.E. Hellenbrand, D. Balzer, Q.L. Cao, and Z.M. Hijazi, *Transcatheter closure of perimembranous ventricular septal defects using the new Amplatzer membranous VSD occluder: results of the U.S. phase I trial.* J Am Coll Cardiol, 2006. **47**(2): p. 319-25.

105. Türkvatan, A., Büyükbayraktar, FG, Cumhur, T, *Congenital Anomalies of the Aortic Arch: Evaluation with the Use of Multidetector Computed Tomography.* Korean Journal of Radiology, 2009. **10**(2): p. 176-184.

106. Kellenberger, C., *Aortic arch malformations.* Pediatr Radiol, 2010. **40**(6): p. 876-884.

107. Gross, R.E., *Arterial malformations which cause compression of the trachea or esophagus.* Circulation, 1955. **11**(1): p. 124-34.

108. Schneider, D.J. and J.W. Moore, *Patent ductus arteriosus.* Circulation, 2006. **114**(17): p. 1873-82.

109. Lloyd, T.R. and R.H.I. Beekman, *Clinically silent patent ductus arteriosus.* Am Heart J, 1994. **127**: p. 1664-1665.

110. Mitchell, S.C., S.B. Korones, and H.W. Berendes, *Congenital heart disease in 56,109 births. Incidence and natural history.* Circulation, 1971. **43**(3): p. 323-32.

111. Slomp, J., J.C. van Munsteren, R.E. Poelmann, E.G. de Reeder, A.J. Bogers, and A.C. Gittenberger-de Groot, *Formation of intimal cushions in the ductus arteriosus as a model for vascular intimal thickening. An immunohistochemical study of changes in extracellular matrix components.* Atherosclerosis, 1992. **93**(1-2): p. 25-39.

112. Marshall, R., *Persistent Truncas Arteriosus.* Br Heart J., 1943. **5**(4): p. 194-196.

113. Ferdman, B. and G. Singh, *Persistent truncus arteriosus.* Current Treatment Options in Cardiovascular Medicine, 2003. **5**(5): p. 429-438.

114. Rapaport, E., *Natural history of aortic and mitral valve disease.* Am J Cardiol, 1975. **35**(2): p. 221-227.

115. Kappetein, A.P., A.C. Gittenberger-de Groot, A.H. Zwinderman, J. Rohmer, R.E. Poelmann, and H.A. Huysmans, *The neural crest as a possible pathogenetic factor in coarctation of the aorta and bicuspid aortic valve.* J Thorac Cardiovasc Surg, 1991. **102**(6): p. 830-6.

116. Arrington, C.B., C.T. Sower, N. Chuckwuk, J. Stevens, M.F. Leppert, A.T. Yetman, and N.E. Bowles, *Absence of TGFBR1 and TGFBR2 mutations in patients with bicuspid aortic valve and aortic dilation.* Am J Cardiol, 2008. **102**(5): p. 629-31.

117. Perloff, J.K. and J.S. Child, *Clinical and epidemiologic issues in mitral valve prolapse: overview and perspective.* Am Heart J, 1987. **113**(5): p. 1324-32.

118. Devereux, R.B., R. Kramer-Fox, M.K. Shear, P. Kligfield, R. Pini, and D.D. Savage, *Diagnosis and classification of severity of mitral valve prolapse: methodologic, biologic, and prognostic considerations.* Am Heart J, 1987. **113**(5): p. 1265-80.

119. Freed, L.A., D. Levy, R.A. Levine, M.G. Larson, J.C. Evans, D.L. Fuller, B. Lehman, and E.J. Benjamin, *Prevalence and clinical outcome of mitral-valve prolapse.* N Engl J Med, 1999. **341**(1): p. 1-7.

120. Devereux, R.B., R. Kramer-Fox, and P. Kligfield, *Mitral valve prolapse: causes, clinical manifestations, and management.* Ann Intern Med, 1989. **111**(4): p. 305-17.

121. Corno, A., *Double outlet right ventricle*, in *Congenital Heart Defects*. 2004, Steinkopff. p. 141-155.

122. Kurosawa, H. and A. Becker, *Double-Outlet Right Ventricle*, in *Atrioventricular Conduction in Congenital Heart Disease*. 1987, Springer Japan. p. 145-173.

123. Walters III, H.L., C. Mavroudis, C.I. Tchervenkov, J.P. Jacobs, F. Lacour-Gayet, and M.L. Jacobs, *Congenital Heart Surgery Nomenclature and Database Project: double outlet right ventricle.* The Annals of Thoracic Surgery, 2000. **69**(3, Supplement 1): p. 249-263.

124. Bradely, S., *Neonatal repair and dealing with a single ventricle.* J S C Med Assoc, 1999. **95**: p. 335-338.

125. Tworetzky, W., D.B. McElhinney, V.M. Reddy, M.M. Brook, F.L. Hanley, and N.H. Silverman, *Improved surgical outcome after fetal diagnosis of hypoplastic left heart syndrome.* Circulation, 2001. **103**(9): p. 1269-73.

126. Norwood, W.I., H.K. Kirklin, and S.P. Sanders, *Hypoplastic left heart syndrome: Experience with palliative surgery.* Am J Cardiol, 1980. **45**(1): p. 87-91.

127. Norwood, W.I., P. Lang, and D.D. Hansen, *Physiologic repair of aortic atresia-hypoplastic left heart syndrome.* N Engl J Med, 1983. **308**(1): p. 23-6.

128. Prsa, M., C.D. Holly, F.A. Carnevale, H. Justino, and C.V. Rohlicek, *Attitudes and practices of cardiologists and surgeons who manage HLHS.* Pediatrics, 2010. **125**(3): p. e625-30.

129. Davies, P.F. and S.C. Tripathi, *Mechanical stress mechanisms and the cell. An endothelial paradigm.* Circ Res, 1993. **72**(2): p. 239-45.

130. Nerem, R.M., M.J. Levesque, and J.F. Cornhill, *Vascular endothelial morphology as an indicator of the pattern of blood flow.* J Biomech Eng, 1981. **103**(3): p. 172-6.

131. Malek, A. and S. Izumo, *Molecular aspects of signal transduction of shear stress in the endothelial cell*, in *Molecular Reviews in Cardiovascular Medicine*, K. Lindpaintner and D. Ganten, Editors. 1996, Springer Netherlands. p. 183-193.

132. Icardo, J.M., *Endocardial cell arrangement: Role of hemodynamics.* Anat Rec, 1989. **225**(2): p. 150-155.

133. Schroder, E.A., K. Tobita, J.P. Tinney, J.K. Foldes, and B.B. Keller, *Microtubule involvement in the adaptation to altered mechanical load in developing chick myocardium.* Circ Res, 2002. **91**(4): p. 353-9.

134. Hogers, B., A.C. Gittenberger-de Groot, M.C. DeRuiter, M.M.T. Mentink, and R.E. Poelmann, *Cardiac inflow malformations are more lethal and precede cardiac outflow malformations. Chick embryonic venous clip model.*, in *The Role of Blood Flow in Normal and Abnormal Heart Development*, B. Hogers, Editor. 1998, Ponsen & Looijen BV: Wageningen. p. 79-100.

135. Friedman, W.F., *The intrinsic physiologic properties of the developing heart.* Prog Cardiovasc Dis, 1972. **15**(1): p. 87-111.

136. Keller, B.B., J.P. Tinney, and N. Hu, *Embryonic ventricular diastolic and systo¥c pressure-volunle relations.* Cardiol Young, 1994. **4**(1): p. 19-27.

137. Yoshigi, M., N. Hu, and B.B. Keller, *Dorsal aortic impedance in stage 24 chick embryo following acute changes in circulating blood volume.* Am J Physiol, 1996. **270**(5 Pt 2): p. H1597-606.

138. Itasaki, N., H. Nakamura, and M. Yasuda, *Changes in the arrangement of actin bundles during heart looping in the chick embryo.* Anat Embryol (Berl), 1989. **180**(5): p. 413-20.

139. Shiraishi, I., T. Takamatsu, T. Minamikawa, and S. Fujita, *3-D observation of actin filaments during cardiac myofibrinogenesis in chick embryo using a confocal laser scanning microscope.* Anat Embryol (Berl), 1992. **185**(4): p. 401-8.

140. Miller, C.E., C.L. Wong, and D. Sedmera, *Pressure overload alters stress-strain properties of the developing chick heart.* Am J Physiol Heart Circ Physiol, 2003. **285**(5): p. H1849-H1856.

141. Hutchins, G.M., B.H. Bulkley, G.W. Moore, M.A. Piasio, and F.T. Lohr, *Shape of the human cardiac ventricles.* Am J Cardiol, 1978. **41**(4): p. 646-654.

142. Biechler, S.V., J.D. Potts, M.J. Yost, L. Junor, R.L. Goodwin, and J.W. Weidner, *Mathematical modeling of flow-generated forces in an in vitro system of cardiac valve development.* Ann Biomed Eng, 2010. **38**(1): p. 109-17.

143. Tan, H., S. Biechler, L. Junor, M.J. Yost, D. Dean, J. Li, J.D. Potts, and R.L. Goodwin, *Fluid flow forces and rhoA regulate fibrous development of the atrioventricular valves.* Dev Biol, 2013. **374**(2): p. 345-56.

144. Yalcin, H.C., A. Shekhar, T.C. McQuinn, and J.T. Butcher, *Hemodynamic patterning of the avian atrioventricular valve.* Dev Dyn, 2011. **240**(1): p. 23-35.

145. Buskohl, P.R., J.T. Jenkins, and J.T. Butcher, *Computational simulation of hemodynamic-driven growth and remodeling of embryonic atrioventricular valves.* Biomech Model Mechanobiol, 2012. **11**(8): p. 1205-17.

146. Sedmera, D. and R.P. Thompson, *Myocyte proliferation in the developing heart.* Dev Dyn, 2011. **240**(6): p. 1322-34.

147. Davies, P.F., *Flow-mediated endothelial mechanotransduction.* Physiol Rev, 1995. **75**(3): p. 519-60.

148. Reckova, M., C. Rosengarten, A. deAlmeida, C.P. Stanley, A. Wessels, R.G. Gourdie, R.P. Thompson, and D. Sedmera, *Hemodynamics is a key epigenetic factor in development of the cardiac conduction system.* Circ Res, 2003. **93**(1): p. 77-85.

149. Patten, B.M., *The formation of the cardiac loop in the chick.* American Journal of Anatomy, 1922. **30**(3): p. 373-397.

150. Stalsberg, H., *Regional mitotic activity in the precardiac mesoderm and differentiating heart tube in the chick embryo.* Dev Biol, 1969. **20**(1): p. 18-45.

151. Itasaki, N., H. Nakamura, H. Sumida, and M. Yasuda, *Actin bundles on the right side in the caudal part of the heart tube play a role in dextro-looping in the embryonic chick heart.* Anat Embryol (Berl), 1991. **183**(1): p. 29-39.

152. Taber, L.A., N. Hu, T. Pexieder, E.B. Clark, and B.B. Keller, *Residual strain in the ventricle of the stage 16-24 chick embryo.* Circ Res, 1993. **72**(2): p. 455-62.

153. Keller, B.B., N. Hu, and E.B. Clark, *Correlation of ventricular area, perimeter, and conotruncal diameter with ventricular mass and function in the chick embryo from stages 12 to 24.* Circ Res, 1990. **66**(1): p. 109-14.

154. Faber, J.J., T.J. Green, and K.L. Thornburg, *Embryonic stroke volume and cardiac output in the chick.* Dev Biol, 1974. **41**(1): p. 14-21.

155. Hu, N., D.M. Connuck, B.B. Keller, and E.B. Clark, *Diastolic filling characteristics in the stage 12 to 27 chick embryo ventricle.* Pediatr Res, 1991. **29**(4 Pt 1): p. 334-7.

156. Hu, N. and B.B. Keller, *Relationship of simultaneous atrial and ventricular pressures in stage 16-27 chick embryos.* Am J Physiol, 1995. **269**(4 Pt 2): p. H1359-62.

157. Ma, Z., A. Liu, X. Yin, A. Troyer, K. Thornburg, R.K. Wang, and S. Rugonyi, *Measurement of absolute blood flow velocity in outflow tract of HH18 chicken embryo based on 4D reconstruction using spectral domain optical coherence tomography.* Biomed Opt Express, 2010. **1**(3): p. 798-811.

158. Midgett, M., S. Goenezen, and S. Rugonyi, *Blood flow dynamics reflect degree of outflow tract banding in Hamburger-Hamilton stage 18 chicken embryos.* J R Soc Interface, 2014. **11**(100): p. 20140643.

159. Manner, J., L. Thrane, K. Norozi, and T.M. Yelbuz, *High-resolution in vivo imaging of the cross-sectional deformations of contracting embryonic heart loops using optical coherence tomography.* Dev Dyn, 2008. **237**(4): p. 953-61.

160. Liu, A., R. Wang, K.L. Thornburg, and S. Rugonyi, *Efficient postacquisition synchronization of 4-D nongated cardiac images obtained from optical coherence tomography: application to 4-D reconstruction of the chick embryonic heart.* J Biomed Opt, 2009. **14**(4): p. 044020.

161. Yin, X., A. Liu, K.L. Thornburg, R.K. Wang, and S. Rugonyi, *Extracting cardiac shapes and motion of the chick embryo heart outflow tract from four-dimensional optical coherence tomography images.* J Biomed Opt, 2012. **17**(9): p. 96005-1.

162. Liu, A., A. Nickerson, A. Troyer, X. Yin, R. Cary, K. Thornburg, R. Wang, and S. Rugonyi, *Quantifying blood flow and wall shear stresses in the outflow tract of chick embryonic hearts.* Comput Struct, 2011. **89**(11-12): p. 855-867.

163. Nicholas, W.W., M.F. O'Rourke, and C. Vlachopoulos, *McDonald's Blood Flow in Arteries: Theoretical, experimental, and clinical principles*. 6 ed. 2011, London: Hodder & Arnold.

164. Phoon, C.K., O. Aristizabal, and D.H. Turnbull, *Spatial velocity profile in mouse embryonic aorta and Doppler-derived volumetric flow: a preliminary model.* Am J Physiol Heart Circ Physiol, 2002. **283**(3): p. H908-16.

165. Katritsis, D., L. Kaiktsis, A. Chaniotis, J. Pantos, E.P. Efstathopoulos, and V. Marmarelis, *Wall shear stress: theoretical considerations and methods of measurement.* Prog Cardiovasc Dis, 2007. **49**(5): p. 307-29.

166. Welty, J., C.E. Wicks, G.L. Rorrer, and R.E. Wilson, *Fundamentals of Momentum, Heat and Mass Transfer*. 5 ed. 2008, Hoboken: John Wiley & Sons, Inc.

167. Al-Roubaie, S., E.D. Jahnsen, M. Mohammed, C. Henderson-Toth, and E.A. Jones, *Rheology of embryonic avian blood.* Am J Physiol Heart Circ Physiol, 2011. **301**(6): p. H2473-81.

168. Goenezen, S., V.K. Chivukula, M. Midgett, L. Phan, and S. Rugonyi, *4D Subject-Specific Inverse Modeling of the Chick Embryonic Heart Outflow Tract Hemodynamics.* Biomech Model Mechanobiol, 2015.

169. Vennemann, P., K.T. Kiger, R. Lindken, B.C. Groenendijk, S. Stekelenburg-de Vos, T.L. ten Hagen, N.T. Ursem, R.E. Poelmann, J. Westerweel, and B.P. Hierck, *In vivo micro particle image velocimetry measurements of blood-plasma in the embryonic avian heart.* J Biomech, 2006. **39**(7): p. 1191-200.

170. Poelma, C., K. Van der Heiden, B.P. Hierck, R.E. Poelmann, and J. Westerweel, *Measurements of the wall shear stress distribution in the outflow tract of an embryonic chicken heart.* J R Soc Interface, 2010. **7**(42): p. 91-103.

171. Butcher, J.T., T.C. McQuinn, D. Sedmera, D. Turner, and R.R. Markwald, *Transitions in early embryonic atrioventricular valvular function correspond with changes in cushion biomechanics that are predictable by tissue composition.* Circ Res, 2007. **100**(10): p. 1503-11.

172. Oosterbaan, A.M., N.T. Ursem, P.C. Struijk, J.G. Bosch, A.F. van der Steen, and E.A. Steegers, *Doppler flow velocity waveforms in the embryonic chicken heart at developmental stages corresponding to 5-8 weeks of human gestation.* Ultrasound Obstet Gynecol, 2009. **33**(6): p. 638-44.

173. Happel, C.M., J. Thommes, L. Thrane, J. Manner, T. Ortmaier, B. Heimann, and T.M. Yelbuz, *Rotationally acquired four-dimensional optical coherence tomography of embryonic chick hearts using retrospective gating on the common central A-scan.* J Biomed Opt, 2011. **16**(9): p. 096007.

174. Koller, A. and G. Kaley, *Flow velocity-dependent regulation of microvascular resistance in vivo.* Microcirc Endothelium Lymphatics, 1989. **5**(6): p. 519-29.

175. Castier, Y., R.P. Brandes, G. Leseche, A. Tedgui, and S. Lehoux, *p47phox-dependent NADPH oxidase regulates flow-induced vascular remodeling.* Circ Res, 2005. **97**(6): p. 533-40.

176. Dekker, R.J., S. van Soest, R.D. Fontijn, S. Salamanca, P.G. de Groot, E. VanBavel, H. Pannekoek, and A.J. Horrevoets, *Prolonged fluid shear stress induces a distinct set of endothelial cell genes, most specifically lung Kruppel-like factor (KLF2).* Blood, 2002. **100**(5): p. 1689-98.

177. Groenendijk, B.C., B.P. Hierck, A.C. Gittenberger-De Groot, and R.E. Poelmann, *Development-related changes in the expression of shear stress responsive genes KLF-2, ET-1, and NOS-3 in the developing cardiovascular system of chicken embryos.* Dev Dyn, 2004. **230**(1): p. 57-68.

178. Phelan, C.M., S.F. Hughes, and D.W. Benson, Jr., *Heart rate-dependent characteristics of diastolic ventricular filling in the developing chick embryo.* Pediatr Res, 1995. **37**(3): p. 289-93.

179. Vermot, J., A.S. Forouhar, M. Liebling, D. Wu, D. Plummer, M. Gharib, and S.E. Fraser, *Reversing Blood Flows Act through <italic>klf2a</italic> to Ensure Normal Valvulogenesis in the Developing Heart.* PLoS Biol, 2009. **7**(11): p. e1000246.

180. Gordon, A.M., A.F. Huxley, and F.J. Julian, *The variation in isometric tension with sarcomere length in vertebrate muscle fibres.* J Physiol, 1966. **184**(1): p. 170-92.

181. Ramsey, R.W. and S.F. Street, *The isometric length-tension diagram of isolated skeletal muscle fibers of the frog.* J Cell Comp Physiol, 1940. **15**(1): p. 11-34.

182. Furst, B., *Hemodynamics of the Early Embryo Circulation*, in *The Heart and Circulation*. 2014, Springer London. p. 21-29.

183. Clark, E.B., N. Hu, J.L. Dummett, G.K. Vandekieft, C. Olson, and R. Tomanek, *Ventricular function and morphology in chick embryo from stages 18 to 29.* Am J Physiol, 1986. **250**(3 Pt 2): p. H407-13.

184. Chen, Z., T.E. Milner, D. Dave, and J.S. Nelson, *Optical Doppler tomographic imaging of fluid flow velocity in highly scattering media.* Optics Letters, 1997. **22**(1): p. 64-66.

185. Ma, Z., L. Du, Q. Wang, Z. Chu, X. Zang, F. Wang, and R.K. Wang. *Changes in strain and blood flow in the outflow tract of chicken embryo hearts observed with spectral domain optical coherence tomography after outflow tract banding*. 2013.

186. Wang, R., *High-resolution visualization of fluid dynamics with Doppler optical coherence tomography.* Meas Sci Technol, 2004. **15**(4).

187. Hierck, B.P., K. Van der Heiden, C. Poelma, J. Westerweel, and R.E. Poelmann, *Fluid shear stress and inner curvature remodeling of the embryonic heart. Choosing the right lane!* ScientificWorldJournal, 2008. **8**: p. 212-22.

188. Poelma, C., P. Vennemann, R. Lindken, and J. Westerweel, *In vivo blood flow and wall shear stress measurements in the vitelline network.* Experiments in Fluids, 2008. **45**(4): p. 703-713.

189. Gaehtgens, P., F. Schmidt, and G. Will, *Comparative rheology of nucleated and non-nucleated red blood cells. I. Microrheology of avian erythrocytes during capillary flow.* Pflugers Arch, 1981. **390**(3): p. 278-82.

190. Cuneo, B., S. Hughes, and D.W. Benson, Jr., *Heart rate perturbation in the stage 17-27 chick embryo: effect on stroke volume and aortic flow.* Am J Physiol, 1993. **264**(3 Pt 2): p. H755-9.

191. Keller, B.B., M. Yoshigi, and J.P. Tinney, *Ventricular-vascular uncoupling by acute conotruncal occlusion in the stage 21 chick embryo.* Am J Physiol, 1997. **273**(6 Pt 2): p. H2861-6.

192. Liu, A., S. Rugonyi, J.O. Pentecost, and K.L. Thornburg, *Finite element modeling of blood flow-induced mechanical forces in the outflow tract of chick embryonic hearts.* Compt Struct, 2007. **85**(11-14).

193. Forouhar, A.S., M. Liebling, A. Hickerson, A. Nasiraei-Moghaddam, H.J. Tsai, J.R. Hove, S.E. Fraser, M.E. Dickinson, and M. Gharib, *The embryonic vertebrate heart tube is a dynamic suction pump.* Science, 2006. **312**(5774): p. 751-3.

194. Yang, Q., H. Chen, A. Correa, O. Devine, T.J. Mathews, and M.A. Honein, *Racial differences in infant mortality attributable to birth defects in the United States, 1989–2002.* Birth Defects Research Part A: Clinical and Molecular Teratology, 2006. **76**(10): p. 706-713.

195. Midgett, M. and S. Rugonyi, *Congenital heart malformations induced by hemodynamic altering surgical interventions.* Front Physiol, 2014. **5**: p. 287.

196. Runyan, R.B., R.L. Heimark, T.D. Camenisch, and S.E. Klewer, *Epithelial-Mesenchymal Transformation in the Embryonic Heart. In: Madame Curie Bioscience Database [Internet].* 2000, Austin (TX): Landes Bioscience.

197. Person, A.D., S.E. Klewer, and R.B. Runyan, *Cell biology of cardiac cushion development.* Int Rev Cytol, 2005. **243**: p. 287-335.

198. Icardo, J., *Changes in endocardial cell morphology during development of the endocardial cushions.* Anatomy and Embryology, 1989. **179**(5): p. 443-448.

199. Lencinas, A., A.L. Tavares, J.V. Barnett, and R.B. Runyan, *Collagen gel analysis of epithelial-mesenchymal transition in the embryo heart: an in vitro model system for the analysis of tissue interaction, signal transduction, and environmental effects.* Birth Defects Res C Embryo Today, 2011. **93**(4): p. 298-311.

200. Lim, J. and J.P. Thiery, *Epithelial-mesenchymal transitions: insights from development.* Development, 2012. **139**(19): p. 3471-3486.

201. Armstrong, E.J. and J. Bischoff, *Heart Valve Development: Endothelial Cell Signaling and Differentiation.* Circ Res, 2004. **95**(5): p. 459-470.

202. Hinton, R.B. and K.E. Yutzey, *Heart valve structure and function in development and disease.* Annu Rev Physiol, 2011. **73**: p. 29-46.

203. Webb, S., S.R. Qayyum, R.H. Anderson, W.H. Lamers, and M.K. Richardson, *Septation and separation within the outflow tract of the developing heart.* Journal of Anatomy, 2003. **202**(4): p. 327-342.

204. Eisenberg, L.M. and R.R. Markwald, *Molecular regulation of atrioventricular valvuloseptal morphogenesis.* Circ Res, 1995. **77**(1): p. 1-6.

205. Runyan, R.B. and R.R. Markwald, *Invasion of mesenchyme into three-dimensional collagen gels: a regional and temporal analysis of interaction in embryonic heart tissue.* Dev Biol, 1983. **95**(1): p. 108-14.

206. Schroeder, J.A., L.F. Jackson, D.C. Lee, and T.D. Camenisch, *Form and function of developing heart valves: coordination by extracellular matrix and growth factor signaling.* J Mol Med (Berl), 2003. **81**(7): p. 392-403.

207. Gitler, A.D., M.M. Lu, Y.Q. Jiang, J.A. Epstein, and P.J. Gruber, *Molecular markers of cardiac endocardial cushion development.* Dev Dyn, 2003. **228**(4): p. 643-50.

208. Egorova, A.D., K. Van der Heiden, S. Van de Pas, P. Vennemann, C. Poelma, M.C. DeRuiter, M.J. Goumans, A.C. Gittenberger-de Groot, P. ten Dijke, R.E. Poelmann, and B.P. Hierck, *Tgfbeta/Alk5 signaling is required for shear stress induced klf2 expression in embryonic endothelial cells.* Dev Dyn, 2011. **240**(7): p. 1670-80.

209. Sewell-Loftin, M.K., D.M. DeLaughter, J.R. Peacock, C.B. Brown, H.S. Baldwin, J.V. Barnett, and W.D. Merryman, *Myocardial contraction and hyaluronic acid mechanotransduction in epithelial-to-mesenchymal transformation of endocardial cells.* Biomaterials, 2014. **35**(9): p. 2809-15.

210. Hinton, R.B., Jr., J. Lincoln, G.H. Deutsch, H. Osinska, P.B. Manning, D.W. Benson, and K.E. Yutzey, *Extracellular matrix remodeling and organization in developing and diseased aortic valves.* Circ Res, 2006. **98**(11): p. 1431-8.

211. Kern, C.B., S. Hoffman, R. Moreno, B.J. Damon, R.A. Norris, E.L. Krug, R.R. Markwald, and C.H. Mjaatvedt, *Immunolocalization of chick periostin protein in the developing heart.* Anat Rec A Discov Mol Cell Evol Biol, 2005. **284**(1): p. 415-23.

212. Nakajima, Y., T. Yamagishi, S. Hokari, and H. Nakamura, *Mechanisms involved in valvuloseptal endocardial cushion formation in early cardiogenesis: roles of transforming growth factor (TGF)-beta and bone morphogenetic protein (BMP).* Anat Rec, 2000. **258**(2): p. 119-27.

213. Damon, B.J., M.C. Remond, M.R. Bigelow, T.C. Trusk, W. Xie, R. Perucchio, D. Sedmera, S. Denslow, and R.P. Thompson, *Patterns of muscular strain in the embryonic heart wall.* Dev Dyn, 2009. **238**(6): p. 1535-46.

214. Rennie, M.Y., C.G. Gahan, C.S. Lopez, K.L. Thornburg, and S. Rugonyi, *3D imaging of the early embryonic chicken heart with focused ion beam scanning electron microscopy.* Microsc Microanal, 2014. **20**(4): p. 1111-9.

215. Kinsella, M.G. and T.P. Fitzharris, *Origin of cushion tissue in the developing chick heart: cinematographic recordings of in situ formation.* Science, 1980. **207**(4437): p. 1359-60.

216. Coram, R.J., S.J. Stillwagon, A. Guggilam, M.W. Jenkins, M.S. Swanson, and A.N. Ladd, *Muscleblind-like 1 is required for normal heart valve development in vivo.* BMC Dev Biol, 2015. **15**(1): p. 1-20.

217. Leir, S.H. and A. Harris, *MUC6 mucin expression inhibits tumor cell invasion.* Exp Cell Res, 2011. **317**(17): p. 2408-19.

218. Harikrishnan, K., M.A. Cooley, Y. Sugi, J.L. Barth, L.M. Rasmussen, C.B. Kern, K.M. Argraves, and W.S. Argraves, *Fibulin-1 suppresses endothelial to mesenchymal transition in the proximal outflow tract.* Mech Dev, 2015. **136**: p. 123-32.

219. Medici, D. and R. Kalluri, *Endothelial-mesenchymal transition and its contribution to the emergence of stem cell phenotype.* Seminars in cancer biology, 2012. **22**(5-6): p. 379-384.

220. Nakajima, Y., M. Morishima, M. Nakazawa, K. Momma, and H. Nakamura, *Distribution of fibronectin, type I collagen, type IV collagen, and laminin in the cardiac jelly of the mouse embryonic heart with retinoic acid-induced complete transposition of the great arteries.* Anat Rec, 1997. **249**(4): p. 478-85.

221. Lockhart, M., E. Wirrig, A. Phelps, and A. Wessels, *Extracellular Matrix and Heart Development.* Birth defects research. Part A, Clinical and molecular teratology, 2011. **91**(6): p. 535-550.

222. McGuire, P.G. and S.M. Alexander, *Inhibition of urokinase synthesis and cell surface binding alters the motile behavior of embryonic endocardial-derived mesenchymal cells in vitro.* Development, 1993. **118**(3): p. 931-9.

223. Imanaka-Yoshida, K. and H. Aoki, *Tenascin-C and mechanotransduction in the development and diseases of cardiovascular system.* Front Physiol, 2014. **5**: p. 283.

224. Vijayaraj, P., A. Le Bras, N. Mitchell, M. Kondo, S. Juliao, M. Wasserman, D. Beeler, K. Spokes, W.C. Aird, H.S. Baldwin, and P. Oettgen, *Erg is a crucial regulator of endocardial-mesenchymal transformation during cardiac valve morphogenesis.* Development, 2012. **139**(21): p. 3973-85.

225. Xu, J., S. Lamouille, and R. Derynck, *TGF-beta-induced epithelial to mesenchymal transition.* Cell Res, 2009. **19**(2): p. 156-72.

226. Lin, F., N. Wang, and T.C. Zhang, *The role of endothelial-mesenchymal transition in development and pathological process.* IUBMB Life, 2012. **64**(9): p. 717-23.

227. Moonen, J.R., E.S. Lee, M. Schmidt, M. Maleszewska, J.A. Koerts, L.A. Brouwer, T.G. van Kooten, M.J. van Luyn, C.J. Zeebregts, G. Krenning, and M.C. Harmsen, *Endothelial-to-mesenchymal transition contributes to fibro-proliferative vascular disease and is modulated by fluid shear stress.* Cardiovasc Res, 2015. **108**(3): p. 377-86.

228. Zhang, H., A. von Gise, Q. Liu, T. Hu, X. Tian, L. He, W. Pu, X. Huang, L. He, C.L. Cai, F.D. Camargo, W.T. Pu, and B. Zhou, *Yap1 is required for endothelial to mesenchymal transition of the atrioventricular cushion.* J Biol Chem, 2014. **289**(27): p. 18681-92.

229. Wang, Z., B. Calpe, J. Zerdani, Y. Lee, J. Oh, H. Bae, A. Khademhosseini, and K. Kim, *High-throughput investigation of endothelial-to-mesenchymal transformation (EndMT) with combinatorial cellular microarrays.* Biotechnol Bioeng, 2015.

230. Barnette, D.N., M. VandeKopple, Y. Wu, D.A. Willoughby, and J. Lincoln, *RNA-seq analysis to identify novel roles of scleraxis during embryonic mouse heart valve remodeling.* PLoS One, 2014. **9**(7): p. e101425.

231. An, H.T., S. Yoo, and J. Ko, *alpha-Actinin-4 induces the epithelial-to-mesenchymal transition and tumorigenesis via regulation of Snail expression and beta-catenin stabilization in cervical cancer.* Oncogene, 2016.

232. Zeisberg, M. and E.G. Neilson, *Biomarkers for epithelial-mesenchymal transitions.* J Clin Invest, 2009. **119**(6): p. 1429-37.

233. Kpetemey, M., S. Dasgupta, S. Rajendiran, S. Das, L.D. Gibbs, P. Shetty, Z. Gryczynski, and J.K. Vishwanatha, *MIEN1, a novel interactor of Annexin A2, promotes tumor cell migration by enhancing AnxA2 cell surface expression.* Mol Cancer, 2015. **14**: p. 156.

234. Lai, K.P., A.Y. Law, M.C. Lau, Y. Takei, W.K. Tse, and C.K. Wong, *Osmotic stress transcription factor 1b (Ostf1b) promotes migration properties with the modulation of epithelial mesenchymal transition (EMT) phenotype in human embryonic kidney cell.* Int J Biochem Cell Biol, 2013. **45**(8): p. 1921-6.

235. Chen, J., A.W. Chan, K.F. To, W. Chen, Z. Zhang, J. Ren, C. Song, Y.S. Cheung, P.B. Lai, S.H. Cheng, M.H. Ng, A. Huang, and B.C. Ko, *SIRT2 overexpression in hepatocellular carcinoma mediates epithelial to mesenchymal transition by protein kinase B/glycogen synthase kinase-3beta/beta-catenin signaling.* Hepatology, 2013. **57**(6): p. 2287-98.

236. Zhang, W., Y. Liu, H. Hu, H. Huang, Z. Bao, P. Yang, Y. Wang, G. You, W. Yan, T. Jiang, J. Wang, and W. Zhang, *ALDH1A3: A Marker of Mesenchymal Phenotype in Gliomas Associated with Cell Invasion.* PLoS One, 2015. **10**(11): p. e0142856.

237. Jiang, Y., X. Feng, L. Zheng, S.-L. Li, X.-Y. Ge, and J.-G. Zhang, *Thioredoxin 1 mediates TGF-β-induced epithelial-mesenchymal transition in salivary adenoid cystic carcinoma.* Oncotarget, 2015. **6**(28): p. 25506-25519.

238. Cho, H.J., S.M. Park, I.K. Kim, I.K. Nam, K.E. Baek, M.J. Im, J.M. Yoo, S.H. Park, K.J. Ryu, H.T. Han, H.J. Kim, S.C. Hong, K.D. Kim, Y. Pak, J.W. Kim, C.W. Lee, and J. Yoo, *RhoGDI2 promotes epithelial-mesenchymal transition via induction of Snail in gastric cancer cells.* Oncotarget, 2014. **5**(6): p. 1554-64.

239. Zhao, D., A.H. Besser, S.A. Wander, J. Sun, and W. Zhou, *Cytoplasmic p27 promotes epithelial-mesenchymal transition and tumor metastasis via STAT3-mediated Twist1 upregulation.* 2015. **34**(43): p. 5447-59.

240. Reiner, J.E. and P.K. Datta *TGF-beta-dependent and -independent roles of STRAP in cancer*. Frontiers in bioscience (Landmark edition), 2011. **16**, 105-115.

241. Yu, W., C. Huang, Q. Wang, T. Huang, Y. Ding, C. Ma, H. Ma, and W. Chen, *MEF2 transcription factors promotes EMT and invasiveness of hepatocellular carcinoma through TGF-beta1 autoregulation circuitry.* Tumour Biol, 2014. **35**(11): p. 10943-51.

242. Cui, B., S. Zhang, L. Chen, J. Yu, G.F. Widhopf, 2nd, J.F. Fecteau, L.Z. Rassenti, and T.J. Kipps, *Targeting ROR1 inhibits epithelial-mesenchymal transition and metastasis.* Cancer Res, 2013. **73**(12): p. 3649-60.

243. Lee, J.M., S. Dedhar, R. Kalluri, and E.W. Thompson, *The epithelial-mesenchymal transition: new insights in signaling, development, and disease.* J Cell Biol, 2006. **172**(7): p. 973-81.

244. Butcher, J.T., R.A. Norris, S. Hoffman, C.H. Mjaatvedt, and R.R. Markwald, *Periostin promotes atrioventricular mesenchyme matrix invasion and remodeling mediated by integrin signaling through Rho/PI 3-kinase.* Dev Biol, 2007. **302**(1): p. 256-66.

245. Norris, R.A., C.B. Kern, A. Wessels, E.I. Moralez, R.R. Markwald, and C.H. Mjaatvedt, *Identification and detection of the periostin gene in cardiac development.* Anat Rec A Discov Mol Cell Evol Biol, 2004. **281**(2): p. 1227-33.

246. Markwald, R.R., T.P. Fitzharris, and W.N. Smith, *Sturctural analysis of endocardial cytodifferentiation.* Dev Biol, 1975. **42**(1): p. 160-80.

247. Menon, V., J. Eberth, R. Goodwin, and J. Potts, *Altered Hemodynamics in the Embryonic Heart Affects Outflow Valve Development doi:10.3390/jcdd2020108.* J Cardiovasc Dev Dis 2308-3425, 2015. **2**(2): p. 108.

248. Morrow, R.J., J.W. Ritchie, and S.B. Bull, *Maternal cigarette smoking: the effects on umbilical and uterine blood flow velocity.* Am J Obstet Gynecol, 1988. **159**(5): p. 1069-71.

249. Lang, R.M., M. Bierig, R.B. Devereux, F.A. Flachskampf, E. Foster, P.A. Pellikka, M.H. Picard, M.J. Roman, J. Seward, J. Shanewise, S. Solomon, K.T. Spencer, M. St John Sutton, and W. Stewart, *Recommendations for chamber quantification.* Eur J Echocardiogr, 2006. **7**(2): p. 79-108.

250. Hahn, R.T., T. Abraham, M.S. Adams, C.J. Bruce, K.E. Glas, R.M. Lang, S.T. Reeves, J.S. Shanewise, S.C. Siu, W. Stewart, and M.H. Picard, *Guidelines for performing a comprehensive transesophageal echocardiographic examination: recommendations from the American Society of Echocardiography and the Society of Cardiovascular Anesthesiologists.* Anesth Analg, 2014. **118**(1): p. 21-68.

251. Mor-Avi, V., R.M. Lang, L.P. Badano, M. Belohlavek, N.M. Cardim, G. Derumeaux, M. Galderisi, T. Marwick, S.F. Nagueh, P.P. Sengupta, R. Sicari, O.A. Smiseth, B. Smulevitz, M. Takeuchi, J.D. Thomas, M. Vannan, J.U. Voigt, and J.L. Zamorano, *Current and evolving echocardiographic techniques for the quantitative evaluation of cardiac mechanics: ASE/EAE consensus statement on methodology and indications endorsed by the Japanese Society of Echocardiography.* Eur. J. Echocardiogr., 2011. **12**(3): p. 167-205.

252. Henein, M., C. Anagnostopoulos, S. Das, C. O'Sullivan, S. Underwood, and D. Gibson, *Left ventricular long axis disturbances as predictors for thallium perfusion defects in patients with known peripheral vascular disease.* Heart, 1998. **79**(3): p. 295-300.

253. Bolognesi, R., D. Tsialtas, A.L. Barilli, C. Manca, R. Zeppellini, A. Javernaro, and F. Cucchini, *Detection of early abnormalities of left ventricular function by hemodynamic, echo-tissue Doppler imaging, and mitral Doppler flow techniques in patients with coronary artery disease and normal ejection fraction.* J Am Soc Echocardiogr, 2001. **14**(8): p. 764-772.

254. Crispi, F., B. Bijnens, F. Figueras, J. Bartrons, E. Eixarch, F. Le Noble, A. Ahmed, and E. Gratacós, *Fetal Growth Restriction Results in Remodeled and Less Efficient Hearts in Children.* Circulation, 2010. **121**(22): p. 2427-2436.

255. Nikitin, N.P., K.K. Witte, S.D. Thackray, R. de Silva, A.L. Clark, and J.G. Cleland, *Longitudinal ventricular function: normal values of atrioventricular annular and myocardial velocities measured with quantitative two-dimensional color Doppler tissue imaging.* J Am Soc Echocardiogr, 2003. **16**(9): p. 906-21.

256. Teshima, K., K. Asano, Y. Sasaki, Y. Kato, K. Kutara, K. Edamura, A. Hasegawa, and S. Tanaka, *Assessment of Left Ventricular Function Using Pulsed Tissue Doppler Imaging in Healthy Dogs and Dogs with Spontaneous Mitral Regurgitation.* J Vet Med Sci, 2005. **67**(12): p. 1207-1215.

257. Perez-Pomares, J.M., A. Phelps, M. Sedmerova, R. Carmona, M. Gonzalez-Iriarte, R. Munoz-Chapuli, and A. Wessels, *Experimental studies on the spatiotemporal expression of WT1 and RALDH2 in the embryonic avian heart: a model for the regulation of myocardial and valvuloseptal development by epicardially derived cells (EPDCs).* Dev Biol, 2002. **247**(2): p. 307-26.

258. Männer, J., *Microsurgical Procedures for Studying the Developmental Significance of the Proepicardium and Epicardium in Avian Embryos: PE-Blocking, PE-Photoablation, and PE-Grafting.* J Dev Biol, 2013. **1**: p. 47-63.

259. Sedmera, D. and T. McQuinn, *Embryogenesis of heart muscle.* Heart failure clinics, 2008. **4**(3): p. 235-245.

260. Sucov, H.M., E. Dyson, C.L. Gumeringer, J. Price, K.R. Chien, and R.M. Evans, *RXR alpha mutant mice establish a genetic basis for vitamin A signaling in heart morphogenesis.* Genes Dev, 1994. **8**(9): p. 1007-18.

261. Bahrami, H., M. McConnell, and P. Heidenreich, *High left ventricle ejection fraction is associated with worse outsomes in patients with and without heart failure* J Am Coll Cardiol, 2014. **63**(12_S).

262. Asanoi, H., S. Sasayama, and T. Kameyama, *Ventriculoarterial coupling in normal and failing heart in humans.* Circ Res, 1989. **65**(2): p. 483-93.

263. Arts, T., F.W. Prinzen, L.H. Snoeckx, J.M. Rijcken, and R.S. Reneman, *Adaptation of cardiac structure by mechanical feedback in the environment of the cell: a model study.* Biophys J, 1994. **66**(4): p. 953-61.

264. Allen, H.D., H.P. Gutgesell, E.B. Clark, and D.J. Driscoll, *Moss and Adam's Heart Disease in Infants, Children, and Adolescents: Including the Fetus and Young Adult*. 7th ed. 2008, Baltimore, MD: Lippincott Williams & Wilkins.

265. Eldadah, Z.A., A. Hamosh, N.J. Biery, R.A. Montgomery, M. Duke, R. Elkins, and H.C. Dietz, *Familial Tetralogy of Fallot caused by mutation in the jagged1 gene.* Hum Mol Genet, 2001. **10**(2): p. 163-9.

266. Wainrach, S. and J.R. Sotelo, *Electron microscope study of the developing chick embryo heart.* Zeitschrift für Zellforschung und Mikroskopische Anatomie, 1961. **55**(5): p. 622-634.

267. Manasek, F.J., *Histogenesis of the embryonic myocardium.* Am J Cardiol, 1970. **25**(2): p. 149-68.

268. Rai, R., C.C.L. Wong, T. Xu, N.A. Leu, D.W. Dong, C. Guo, K.J. McLaughlin, J.R. Yates, and A. Kashina, *Arginyltransferase regulates alpha cardiac actin function, myofibril formation and contractility during heart development.* Development, 2008. **135**(23): p. 3881-3889.

269. Fischman, D.A., *An electron microscope study of myofibril formation in embryonic chick skeletal muscle.* J Cell Biol, 1967. **32**(3): p. 557-75.

270. Raeker, M.Ö., J.A. Shavit, J.J. Dowling, D.E. Michele, and M.W. Russell, *Membrane-myofibril cross-talk in myofibrillogenesis and in muscular dystrophy pathogenesis: lessons from the zebrafish.* Front Physiol, 2014. **5**: p. 14.

271. Sanger, J.W., S. Kang, C.C. Siebrands, N. Freeman, A. Du, J. Wang, A.L. Stout, and J.M. Sanger, *How to build a myofibril.* J Muscle Res Cell Motil, 2005. **26**(6-8): p. 343-54.

272. Barbosky, L., D.K. Lawrence, G. Karunamuni, J.C. Wikenheiser, Y.Q. Doughman, R.P. Visconti, J.B. Burch, and M. Watanabe, *Apoptosis in the developing mouse heart.* Dev Dyn, 2006. **235**(9): p. 2592-602.

273. Watanabe, M., A. Jafri, and S.A. Fisher, *Apoptosis is required for the proper formation of the ventriculo-arterial connections.* Dev Biol, 2001. **240**(1): p. 274-88.

274. Sallee, D., Y. Qiu, J. Liu, M. Watanabe, and S.A. Fisher, *Fas ligand gene transfer to the embryonic heart induces programmed cell death and outflow tract defects.* Dev Biol, 2004. **267**(2): p. 309-19.

275. Sugishita, Y., D.W. Leifer, F. Agani, M. Watanabe, and S.A. Fisher, *Hypoxia-responsive signaling regulates the apoptosis-dependent remodeling of the embryonic avian cardiac outflow tract.* Dev Biol, 2004. **273**(2): p. 285-96.

276. Sugishita, Y., M. Watanabe, and S.A. Fisher, *Role of myocardial hypoxia in the remodeling of the embryonic avian cardiac outflow tract.* Dev Biol, 2004. **267**(2): p. 294-308.

277. Schaefer, K.S., Y.Q. Doughman, S.A. Fisher, and M. Watanabe, *Dynamic patterns of apoptosis in the developing chicken heart.* Dev Dyn, 2004. **229**(3): p. 489-499.

278. Scott-Drechsel, D.E., S. Rugonyi, D.L. Marks, K.L. Thornburg, and M.T. Hinds, *Hyperglycemia Slows Embryonic Growth and Suppresses Cell Cycle via Cyclin D1 and p21.* Diabetes, 2013. **62**(1): p. 234-242.

279. Smolich, J.J., *Ultrastructural and functional features of the developing mammalian heart: a brief overview.* Reprod Fertil Dev, 1995. **7**(3): p. 451-61.

280. Brook, W.H., S. Connell, J. Cannata, J.E. Maloney, and A.M. Walker, *Ultrastructure of the myocardium during development from early fetal life to adult life in sheep.* J Anat, 1983. **137**(Pt 4): p. 729-741.

281. Vendelin, M., N. Beraud, K. Guerrero, T. Andrienko, A.V. Kuznetsov, J. Olivares, L. Kay, and V.A. Saks, *Mitochondrial regular arrangement in muscle cells: a "crystal-like" pattern.* Am J Physiol Cell Physiol, 2005. **288**(3): p. C757-67.

282. Roberts, D.E., L.T. Hersh, and A.M. Scher, *Influence of cardiac fiber orientation on wavefront voltage, conduction velocity, and tissue resistivity in the dog.* Circ Res, 1979. **44**(5): p. 701-12.

283. Barbera, A., G.D. Giraud, M.D. Reller, J. Maylie, M.J. Morton, and K.L. Thornburg, *Right ventricular systolic pressure load alters myocyte maturation in fetal sheep.* Am J Physiol Regul Integr Comp Physiol, 2000. **279**(4): p. R1157-64.

284. Tibayan, F.A., S. Louey, S. Jonker, H. Espinoza, N. Chattergoon, F. You, K.L. Thornburg, and G. Giraud, *Increased systolic load causes adverse remodeling of fetal aortic and mitral valves.* Am J Physiol Regul Integr Comp Physiol, 2015. **309**(12): p. R1490-8.

285. Jonker, S.S., J.J. Faber, D.F. Anderson, K.L. Thornburg, S. Louey, and G.D. Giraud, *Sequential growth of fetal sheep cardiac myocytes in response to simultaneous arterial and venous hypertension.* Am J Physiol Regul Integr Comp Physiol, 2007. **292**(2): p. R913-9.

Biographical Sketch

Madeline Midgett was born on June 15, 1988 in Portland, Oregon to Joe and Jeanine Midgett. She was married to Ryan Stillwell on August 15, 2015.

Madeline “Maddie” attended Woodrow Wilson High School in Portland, Oregon, and enrolled at Oregon State Univeristy (OSU) with a full-scholarship upon graduation. During her undergraduate studies, she became involved in student activities in the School of Chemical, Biological, and Environmental Engineering, served as fundraising coordinator and co-president for the student chapter, and planned and attended American Chemical Engineering Society Conferences. She also participated in Multiple Engineering Cooperative Program (MECOP) with industrial internships at Oregon Freeze Dry and Cellphire, Inc. Maddie gained research experience during her undergraduate studies from internships in the laboratories of Dr. Owen McCarty at Oregon Health & Science University (OHSU) and Dr. Patrick Rousche at the University of Illinois at Chicago. In June of 2011, she earned her Bachelor of Science degree in Bioengineering.

After graduation from OSU, Maddie worked in industry for about 2 years as a Product Development Technician with Oregon Freeze Dry and Cellphire, Inc., and as an Associate Scientist with MolecularMD. She continued her education at OHSU, joining the lab of Dr. Sandra Rugonyi in the Department of Biomedical Engineering in February 2013. After her first year of graduate school, she received the Charles Patrick Memorial Scholarship from the Biomedical Engineering Department. During her time at OHSU, Maddie was awarded funding for a predoctoral American Heart Association fellowship that ranked in the top 1%, was awarded funding for a NRSA F31 predoctoral fellowship from the NIH, received the student oral presentation award at OHSU Research Week 2015, and received a Fellowship to attend a short course in Morphogenesis & Spatial Dynamics Systems Biology at University of California Irvine Center for Complex Biological Systems. Maddie’s research has been published in a number of peer-reviewed journals, and also presented as oral and poster presentations at academic conferences including the Weinstein Cardiovascular Development, Biomechanics, Bioengineering and Biotransport, and Microscopy and Microanalysis Meetings. Current publications and presentations are listed below.

Selected Peer-reviewed Publications

Midgett, Madeline, Rugonyi, Sandra. Analysis of 4D Myocardial Wall Motion during Early Stages of Chick Heart Development. Methods in Molecular Biology, 2015; 1299.

Midgett, Madeline, Chivukula, Venkat, Dorn, Calder, Wallace, Samantha, Rugonyi, Sandra. Acute Blood Flow Changes Through the Embryonic Outflow Tract During Cardiac Looping in HH13-HH18 Chicken Embryos. Journal of the Royal Society Interface, 2015; 12(111).

Midgett, Madeline, Goenezen, Sevan, Rugonyi, Sandra. Blood Flow Dynamics Reflect Degree of Outflow Tract Banding in HH18 Chicken Embryos. Journal of the Royal Society Interface. 2014; 11(100).

Midgett, Madeline, Rugonyi, Sandra. Congenital Heart Malformations Induced by Hemodynamic Altering Surgical Interventions. Frontiers in Physiology. 2014; 5(287).

Goenezen Sevan, Chivukula Venkat Keshav, **Midgett** M, Phan Li, Rugonyi Sandra. 4D subject-specific inverse modeling of the chick embryonic heart outflow tract hemodynamics. Biomechanics and Modeling in Mechanobiology, 2016; 15(3).

Selected Conference Abstracts

Midgett, Madeline, Thornburg, Kent, Rugonyi, Sandra. “Early embryonic hemodynamic load is a strong determinant of cardiac malformation” platform presentation at the Weinstein Cardiovascular Development Conference, Durham, NC, May 2016.

Midgett, Madeline, Lopez, Claudia, Rugonyi, Sandra. “3D Imaging of the Early Embryonic Chicken Heart After Altered Blood Flow with Focused Ion Beam Scanning Electron Microscopy” poster presentation at the Microscopy and Microanalysis Conference, Portland, OR August 2015.

Midgett, Madeline, Rugonyi, Sandra. “The Degree of Outflow Tract Banding Predicts Cardiac Remodeling in Chicken Embryos” platform presentation at the Summer Biomechanics, Bioengineering and Biotransport Conference, Snowbird Resort, UT, June 2015.

Midgett, Madeline, Rugonyi, Sandra. “The Degree of Hemodynamic Perturbation Predicts Cardiac Remodeling in Chicken Embryos” poster at the Weinstein Cardiovascular Development Conference, Boston, MA, April 2015.

Midgett, Madeline, Cowin, Brianna, Goenezen, Sevan, Rennie, Monique, Rugonyi, Sandra. “Blood Flow Dynamics Reflect Degree of Outflow Tract Banding in HH18 Chicken Embryos” presentation at Oregon Health & Science University Cell, Developmental, & Cancer Biology and Center for Spatial Systems Biomedicine Joint Retreat, Skamania, WA, July 2014.

Midgett, Madeline, Goenezen, Sevan, Rugonyi, Sandra. “Blood Flow Dynamics Reflect Degree of Outflow Tract Banding in HH18 Chicken Embryos” platform presentation at Oregon Health & Science University Research Week 2014, Portland, OR, April 2014.

Midgett, Madeline, Walt, Pebley, Dee, Josh, Fitzpatrick, Mike. “Combination of freeze-dry microscopy, differential scanning calorimetry, and election microscopy analysis as a guide for lyophilization cycle optimization to enhance Thrombosome function” platform presentation at the Society for Cryobiology Meeting, Corvallis, OR, July, 2011.

Midgett, Madeline, Rousche, Patrick. “Chronic Electrophysiological and Behavioral Response in Rats due to Cerebral Ischemic Stroke in the Motor Cortex” poster at the Annual Biomedical Engineering Society Conference, St. Louis, MO, October 2008.